

**Efficient uncertainty  
quantification in computational  
fluid dynamics**

Copyright ©2010 by G.J.A. Loeven

All rights reserved. No part of the material protected by this copyright notice may be reproduced or utilized in any form or by any means, electronic or mechanical, including photocopying, recording or by any other information storage and retrieval system, without permission from the author.

Printed by Proefschriftmaken.nl, Oisterwijk, The Netherlands

ISBN: 978-90-8891-171-2

# Efficient uncertainty quantification in computational fluid dynamics

PROEFSCHRIFT

ter verkrijging van de graad van doctor aan de Technische Universiteit Delft,  
op gezag van de Rector Magnificus prof. ir. K.C.A.M. Luyben,  
voorzitter van het College voor Promoties,  
in het openbaar te verdedigen  
op maandag 7 juni 2010 om 12:30 uur

door

Gerhardus Joseph Alex LOEVEN

ingenieur luchtvaart en ruimtevaart  
geboren te Steenwijk

Dit proefschrift is goedgekeurd door de promotor:  
Prof. dr. ir. drs. H. Bijl

Samenstelling promotiecommissie:

Rector Magnificus	voorzitter
Prof. dr. ir. drs. H. Bijl	Technische Universiteit Delft, promotor
Prof. dr. ir. C. Vuik	Technische Universiteit Delft
Prof. dr. ir. C. Lacor	Vrije Universteit Brussel
Prof. dr. ir. S. Vandewalle	Katholieke Universiteit Leuven
Prof. dr. V. Schulz	Universität Trier
Dr. R.P. Dwight	Technische Universiteit Delft
Dr. D. Büche	MAN Turbo AG Schweiz
Prof. dr. ir. G.A.M. van Kuik	Technische Universiteit Delft, reservelid

The presented work was supported (partly) by the NODESIM-CFD project (Non-Deterministic Simulation for CFD based design methodologies); a collaborative project funded by the European Commission, Research Directorate-General in the 6th Framework Programme, under contract AST5-CT-2006-030959.

*To my wife Marieke*



---

# Summary

---

When modeling physical systems, several sources of uncertainty are present. For example, variability in boundary conditions like free stream velocity or ambient pressure are always present. Furthermore, uncertainties in geometry arise from production tolerances, wear or unknown deformations under loading. Uncertainties in computational fluid dynamics (CFD) simulations can have a significant impact on the computed aerodynamic performance. Since CFD simulations are computationally intensive, an efficient uncertainty quantification approach is required.

The main objective of this research is to obtain an efficient approach for uncertainty quantification in CFD simulations. This was achieved by focusing on efficient uncertainty propagation and the practical applicability to a wide range of test cases.

The Probabilistic Collocation method was developed as an efficient non-intrusive uncertainty propagation method. It is based on the polynomial chaos framework and shows spectral convergence with respect to the polynomial chaos order. Its effectiveness was demonstrated on several flow cases using a commercial CFD solver.

For cases with a discontinuous response or involving long time integration, modifications of the Probabilistic Collocation method were used to efficiently propagate the uncertainties. A multi-element formulation was successfully applied to capture the discontinuous response of a stall flutter problem. Furthermore, a time-independent parameterization was used to efficiently propagate uncertainties in case of vortex shedding behind a circular cylinder, which required long time integration.

Geometric uncertainties were shown to have a significant influence on the aerodynamic performance. Since geometric uncertainties affect the shape, a new computational grid should be computed for every collocation point in the Probabilistic Collocation

## Summary

method. To efficiently treat geometric uncertainties in CFD, a grid deformation technique was used.

Most CFD simulations in this thesis involved solving the Reynolds-averaged Navier-Stokes equations. This required a turbulence model to close the system of equations. Turbulence models often contain several parameters that are tuned to computed or measured simplified flow problems, which introduces uncertainty in the model. Uncertainty quantification was applied to the parameters of the  $k$ - $\epsilon$  turbulence model in combination with wall functions in the cases of flow over a flat plate and flow around a NACA0012 airfoil. The drag coefficient showed a coefficient of variation of 3-4% for both cases. The wall function parameters  $\kappa$  and  $C$  and the model parameter  $C_\mu$  proved to affect the solution most. General conclusions require more test cases, like a shear layer and an expanding jet.

Compressor rotors are components of a gasturbine that are highly sensitive to operational and geometrical uncertainties. Operational uncertainties like static outlet pressure and the total pressure profile at the inlet of the rotor were considered. The Probabilistic Collocation method was validated using a Monte Carlo simulation using 10,000 Latin Hypercube samples. It was shown that the mass flow was most sensitive to the uncertainty in the total pressure profile at the inlet.

Multiple uncertainties were shown to be effectively handled using a two-step approach. The first step was a screening of the parameters. A sensitivity analysis was used to identify the most important parameters of the problem. Here it was assumed that all parameters are independent and have no combined effects. Secondly, the probability density functions of the most important parameters are propagated using the Probabilistic Collocation method.

The Probabilistic Radial Basis Function approach was developed as an alternative efficient approach for multiple uncertain parameters. To obtain an accuracy of  $10^{-2}$ - $10^{-3}$  for the mean and variance, the CFD test cases required 10-35 support points for 3 uncertain parameters. Close agreement between the Probabilistic Radial Basis Function approach and a Monte Carlo simulation using 10,000 Latin Hypercube samples was shown for flow around a RAE2822 airfoil with three uncertain parameters.

It can be concluded that the Probabilistic Collocation method and adapted versions are capable of efficiently propagating uncertainties in CFD simulations. The development of the Probabilistic Radial Basis Function approach provided an efficient alternative for cases with multiple uncertain parameters. From the test cases it became clear that there is not a single method that is most efficient for all possible cases.

Uncertainty quantification increases the reliability of CFD computations, since the effect of uncertain parameters on the output of interest is quantified. It was shown that small coefficients of variation of uncertain parameters can lead to a significant variability of the aerodynamic performance. Taking uncertainties into account in CFD simulation is therefore of great importance and with the current state of technology feasible for many real world applications.



---

# Contents

---

<b>Summary</b>	<b>i</b>
<b>1 Introduction</b>	<b>1</b>
1.1 Uncertainty quantification . . . . .	2
1.2 Objectives and the approach to achieve them . . . . .	5
1.3 Outline of this thesis . . . . .	5
<b>2 The Probabilistic Collocation method</b>	<b>7</b>
2.1 Literature review . . . . .	7
2.2 Theory based on the polynomial chaos framework . . . . .	10
2.2.1 The Galerkin Polynomial Chaos method . . . . .	10
2.2.2 The Probabilistic Collocation formulation . . . . .	12
2.3 Comparison between methods for one uncertain parameter . . . . .	17
2.4 Summary . . . . .	23
<b>3 Flow applications of the Probabilistic Collocation method</b>	<b>25</b>
3.1 Subsonic flow around a NACA0012 airfoil . . . . .	26
3.2 Transonic flow around a RAE2822 airfoil . . . . .	31

## Contents

3.2.1	Deterministic test case description . . . . .	31
3.2.2	Uncertain parameters . . . . .	31
3.2.3	Results Probabilistic Collocation method . . . . .	33
3.3	Summary . . . . .	40
<b>4</b>	<b>Modifications of the Probabilistic Collocation method</b>	<b>43</b>
4.1	Multi-Element formulation applied to stall flutter . . . . .	44
4.1.1	Multi-Element Probabilistic Collocation . . . . .	44
4.1.2	Deterministic stall flutter model . . . . .	45
4.1.3	Uncertainty quantification for the dynamic stall flutter problem	47
4.2	Unsteady flow around a cylinder . . . . .	55
4.2.1	Probabilistic Collocation method for period-1 oscillations . . .	55
4.2.2	Deterministic solution . . . . .	56
4.2.3	Stochastic analysis . . . . .	59
4.2.4	Stochastic results . . . . .	59
4.3	Summary . . . . .	63
<b>5</b>	<b>Geometric uncertainties</b>	<b>67</b>
5.1	NACA5412 results using JavaFOIL . . . . .	68
5.2	Grid deformation for geometrical uncertainties . . . . .	73
5.3	A NACA0012 airfoil with uncertain camber and thickness . . . . .	73
5.3.1	Subsonic flow at $M=0.3$ . . . . .	75
5.3.2	Transonic flow at $M=0.8$ . . . . .	76
5.4	Summary . . . . .	79
<b>6</b>	<b>Uncertainty analysis of the <math>k</math>-<math>\epsilon</math> turbulence model parameters</b>	<b>81</b>
6.1	Turbulence modeling . . . . .	82
6.1.1	Incompressible Reynolds-averaged Navier Stokes equations . .	82
6.1.2	The $k$ - $\epsilon$ model . . . . .	85
6.2	Probability distributions of the model parameters . . . . .	86
6.3	Turbulent flow over a flat plate . . . . .	92
6.3.1	Deterministic test case description . . . . .	93
6.3.2	Comparing the different parameters . . . . .	95

6.4	Flow around a NACA0012 airfoil . . . . .	101
6.4.1	Deterministic test case description . . . . .	102
6.4.2	Influence of each individual parameter . . . . .	104
6.5	Summary . . . . .	109
<b>7</b>	<b>Operational uncertainties for a transonic compressor rotor</b>	<b>111</b>
7.1	Deterministic test case description . . . . .	113
7.1.1	Computational settings . . . . .	113
7.1.2	Deterministic solution . . . . .	115
7.2	Validation using a quasi-3D simulation . . . . .	117
7.2.1	Uncertain static pressure at the outlet . . . . .	120
7.2.2	Stochastic results for the quasi-3D rotor . . . . .	120
7.2.3	Conclusions of the validation . . . . .	123
7.3	NASA Rotor 37, 3D simulations . . . . .	124
7.3.1	Uncertain total pressure profile at the inlet . . . . .	124
7.3.2	Stochastic results for the 3D simulations . . . . .	124
7.4	Summary . . . . .	129
<b>8</b>	<b>Two-step approach for multiple uncertain parameters</b>	<b>131</b>
8.1	Sensitivity analysis using the Probabilistic Collocation method . . . . .	132
8.2	Flow around a NACA0012 airfoil with 8 uncertain parameters . . . . .	134
8.2.1	Step I: Identifying the most important parameter . . . . .	136
8.2.2	Step II: Propagating the probability distributions . . . . .	138
8.3	Summary . . . . .	143
<b>9</b>	<b>A Probabilistic Radial Basis Function approach</b>	<b>145</b>
9.1	Probabilistic Radial Basis Function Approach . . . . .	146
9.1.1	Radial Basis Functions in a probabilistic framework . . . . .	146
9.1.2	Error estimation . . . . .	148
9.1.3	Sampling of the support points . . . . .	150
9.2	Evaluation of the radial basis functions and sampling techniques . . . . .	151
9.2.1	Mass-spring problem . . . . .	152
9.2.2	Evaluation up to 5 uncertain parameters . . . . .	155

*Contents*

9.3 Flow around a NACA0012 airfoil with 4 uncertain parameters . . . . . 156

9.4 Transonic flow around a RAE2822 airfoil with 3 uncertain parameters 157

    9.4.1 Test case settings . . . . . 160

    9.4.2 Results of the Probabilistic Radial Basis Function approach . . 160

9.5 Summary . . . . . 161

**10 Conclusions 163**

    10.1 General conclusions . . . . . 163

    10.2 Conclusions based on each chapter . . . . . 165

**11 Recommendations 171**

**A Commonly used probability distributions 175**

**B Uncertainty propagation methods 179**

    B.1 Galerkin Polynomial Chaos method . . . . . 179

    B.2 Non-Intrusive Polynomial Chaos/Spectral Projection . . . . . 181

    B.3 Probabilistic Collocation . . . . . 182

    B.4 Probabilistic Collocation (T) . . . . . 183

    B.5 Stochastic Collocation (MH) . . . . . 184

**C Figures turbulent flate plate 187**

**D NASA Rotor 37 blade sections 193**

**E Convergence plots PRBF and PC 195**

**References 199**

**List of publications 211**

**Samenvatting 215**

**Acknowledgements 217**

**Curriculum Vitae 219**

# CHAPTER 1

---

## Introduction

---

In this thesis an efficient approach for uncertainty quantification in computational fluid dynamics (CFD) is investigated. Due to increasing computing power and advancing algorithms deterministic computations can be very accurate. However, by treating the parameters that describe a physical system as fixed values, uncertainties and errors are introduced. To increase the reliability of CFD, a lot of research is performed to quantify these uncertainties and errors.

This research is performed in the NODESIM-CFD project [Hirsch and Dinescu (2007)], represented by a consortium of 17 partners. Among these are industrial partners from the aerospace and power generation industry, research institutes and universities. The acronym stands for Non-Deterministic simulations for CFD-based design methodologies. The goal of the project is to identify sources of uncertainty, develop efficient uncertainty propagation methods, perform non-deterministic simulations for CFD test cases, and to disseminate the gained knowledge.

A more elaborate introduction on uncertainty quantification and its application to CFD is given in section 1.1. After that the objectives of this thesis and the approach to meet them are formulated in section 1.2. An outline is provided in section 1.3.

## 1.1 Uncertainty quantification

To avoid confusion between uncertainty and error, the definitions used in this thesis are written below. The following definition of error is stated by the American Institute of Aeronautics and Astronautics (AIAA, G-077-1998):

Error:

*A **recognizable** deficiency in any phase or activity of modeling and simulation that is **not due to lack of knowledge**.*

This definition was extended by Oberkampf et al. (2000) to *acknowledged* and *unacknowledged* errors. Acknowledged errors include round-off error, discretization error or the error due to an oversimplified model of a physical process. Procedures exist to remove or estimate these errors. Unacknowledged errors are mistakes like programming errors or wrong use of the code. Procedures can be effective in addressing unacknowledged errors, but due to the human factor there is no guarantee that they are not present.

Uncertainty is divided in two categories [Cullen and Frey (1999); Oberkampf et al. (2000)]:

Epistemic uncertainty:

*A **potential** deficiency in any phase or activity of the modeling process that is **due to the lack of knowledge**.*

Aleatory uncertainty:

*The **physical variation** present in the system being analyzed or its environment.*

The epistemic uncertainty is also called reducible uncertainty because by increasing knowledge the uncertainty can be reduced. The epistemic uncertainties contain some vagueness, for these uncertainties no probability density function can be specified. Examples are insufficient experimental data or physical knowledge of the system being analyzed. Epistemic uncertainties are characteristic for the analyst.

The aleatory uncertainty can be found in literature as irreducible uncertainty, variability and inherent uncertainty, this uncertainty is the natural variability that is inherently present. Examples of aleatory uncertainty appear among others in the boundary conditions or the geometrical description of the model. The variability of boundary conditions and geometrical parameters will always be present because of natural variability and limited accuracy of for example production processes. Aleatory are characteristic for the system being analyzed.

Figure 1.1 shows three measures of uncertainty [Zang et al. (2002)], ordered with respect to the amount of information that is known of the uncertain parameter. The first is the uncertainty of which least information is known, which is a typical epistemic uncertainty. The only information of the uncertain parameter is the interval in

## 1.1 Uncertainty quantification

which the parameter lies. Interval analysis [Moore and Yang (1959); Kearfott (1996)] is a tool to quantify these uncertainties. A uniform distribution is typically used to propagate the interval, but no conclusions can be drawn on the probability or mean and variance of the solution in that case. A bit more information is given when the membership function of the parameter is known. Membership functions are used in possibility analysis, where fuzzy logic is used to propagate the uncertainty [Moens and Vandepitte (2002); Wilcox and Ayyub (2003)]. Membership functions indicate the membership of a parameter to a fuzzy set. For a value of 1, the parameter is definitely a member of the set and if the membership function is 0, the parameter is definitely not a member of the set. Each value in between, corresponds to an interval, which can be propagated using interval arithmetic. The last one is the uncertainty of which the complete probability density function is known. This is a typical aleatory uncertainty which is considered in this thesis. The probability density function is put into the model and propagated using an uncertainty propagation method. The solution is computed including its probability density function. Methods to propagate are among others the commonly used Monte Carlo method [Kelvin (1901); Metropolis and Ulam (1949)], the more recent Galerkin Polynomial Chaos method [Ghanem and Spanos (1991); Xiu and Karniadakis (2002)] and the Probabilistic Collocation method [Babuška et al. (2007); Loeven, Witteveen and Bijl (2007a)].

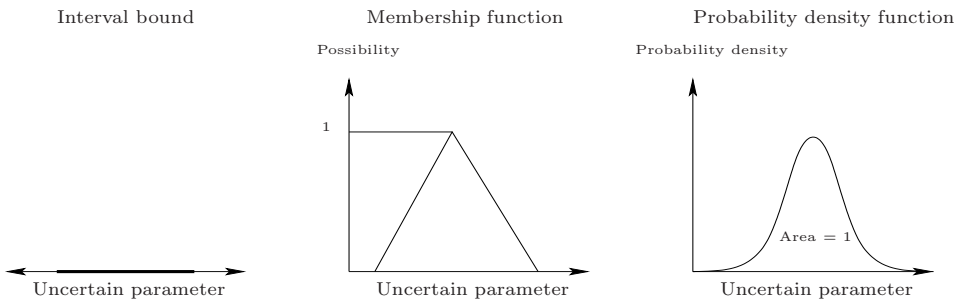


**Figure 1.1:** Three different measures of uncertainty (from Zang et al. (2002)).

Several sources of uncertainty are present in CFD simulations. Operational uncertainties, geometric uncertainties, and model uncertainties are commonly encountered by engineers when designing new products. Examples of operational uncertainties include free stream conditions like pressure, velocity, temperature or angle of incidence. Due to physical variability, these are always present when considering a real life process. By measurements one should be able to find probability density functions for these parameters. These uncertainties are in general aleatory. Geometrical uncertainties arise among others from production tolerance, wear of the product, or unknown deformations under loading. Uncertainties like production tolerance can be reduced by better production methods, but will never be zero. Furthermore, production tolerance are often a trade-off between the costs and the quality of the product. By measuring the final products a probability density function of the geometrical pa-

## Chapter 1: Introduction

parameters can be found. Uncertainty quantification can be used to quantify the effect of this aleatory production tolerance on the performance of a product. The unknown deformation under loading is a source of epistemic uncertainty and can be reduced by increasing the knowledge or otherwise be quantified by, for example, interval analysis. A more difficult form of uncertainty is the model uncertainty. Questions that may rise are: “Are the Euler equations suitable to solve my problem?”, “Is the SST  $k-\omega$  turbulence model right for this type of flow?”, or “Are the model coefficients set to the right values?”. These quantification of uncertainties that come with these questions often are epistemic and treated as such. If there is a physical background and probability density functions can be found to describe the uncertainty, it is aleatory and uncertainty propagation methods as described in this thesis can be employed.

In practice many problems will contain a mix of aleatory and epistemic uncertainties [Oberkampf and Ferson (2007)]. A mix of probabilistic methods and possibilistic methods has to be used to come up with estimates of the statistics of the output of interest. The result is a so-called probability box, which represents an interval of cumulative distribution functions.

The focus of this thesis is on uncertainty propagation used for aleatory uncertainties. It is assumed that the probability distribution functions of the uncertain parameters are known. Key issue is then to propagate that uncertainty through the system to obtain the statistics of the output of interest. Since our main interest is in uncertainty quantification in CFD problems, the efficiency of the uncertainty propagation method is of utmost importance. A deterministic CFD computation can take days or even weeks to compute. Therefore, the additional computational costs for non-deterministic simulations may only be the equivalent of several deterministic solves. If an engineer has to spend for example 100 times as much computational effort compared to a deterministic computation, the added value of the computation should be significant. Application of uncertainty quantification methods in CFD can be found in the work of among others Godfrey and Cliff (2001), Walters and Huyse (2002), Xiu et al. (2002), Hosder et al. (2006), and Witteveen (2009).

The main added value of uncertainty quantification is the increase of reliability of a simulation. When a user specifies probability density functions of uncertain parameters, the effect on the performance is obtained. This will lead to a more robust design, since the performance can be optimized in a mean sense, while the variability of the performance is minimized. Furthermore, uncertainty quantification can be used for more reliable model validation with experiments, see for example the work of Ferson et al. (2008) and Ghanem et al. (2008).



## 1.2 Objectives and the approach to achieve them

The main objective of this research is to obtain an efficient approach for uncertainty quantification in computational fluid dynamics simulations.

The focus is on efficient uncertainty propagation and the practical application to a wide range of test cases. This implies that the uncertainty quantification approach is preferably non-intrusive. Non-intrusive means that the deterministic solver can be used as a black box. Any (commercial) solver can then be used for uncertainty quantification.

This pursued efficient approach deals with the efficient propagations of uncertainties to minimize the computational effort. Many test cases are performed to demonstrate the efficiency of the uncertainty propagation method and to identify possible difficulties. Cases involve a smooth response, a discontinuous response (or a discontinuous derivative), long time integration (where the response surface becomes more nonlinear in time) and multiple uncertain parameters.

Operational and geometric uncertainties are considered. Operational uncertainties are treated as parameteric uncertainties, which appear mainly in the boundary conditions. Geometric uncertainties require a special treatment, since in CFD a change in geometry requires a different computational grid. Geometric uncertainties directly influence the aerodynamic performance. Therefore, they are of great interest, especially for industry.

A secondary objective is to apply the efficient uncertainty quantification approach to some interesting test cases. Two test cases are considered, which are known to be sensitive to uncertainties and have not been studied using probability density functions. The first case involves the quantification of uncertainties in the  $k$ - $\epsilon$  turbulence model parameters. Secondly, analysis of the effect of operational uncertainties on the performance of a transonic axial flow compressor in a gasturbine is performed.

## 1.3 Outline of this thesis

This thesis is divided in the following chapters:

*Chapter 2: The Probabilistic Collocation method.*

This chapter derives and explains the theory of the Probabilistic Collocation method. A comparison with existing methods is shown for one uncertain parameter.

*Chapter 3: Flow applications of the Probabilistic Collocation method.*

Firstly, subsonic flow around a NACA0012 with one uncertain parameter is analyzed. Secondly, transonic flow around a RAE2822 airfoil with three uncertain parameters is investigated.

## **Chapter 1: Introduction**

### *Chapter 4: Modifications of the Probabilistic Collocation method.*

The standard Probabilistic Collocation approximation fails in cases with discontinuous responses or unsteady problems. Slight modifications of the method enable efficient use for these cases as well. First a multi-element formulation is applied to a stall flutter problem with a discontinuous response. Secondly, a period-1 parameterization is used to compute the statistics of a low Reynolds number flow around a cylinder.

### *Chapter 5: Geometrical uncertainties.*

Due to manufacturing tolerances, unknown deformations under loading or wear and tear, the actual geometry is often different from the designed geometry. The Probabilistic Collocation method is employed to analyse the effect of geometrical uncertainties on the performance of airfoil.

### *Chapter 6: Uncertainty analysis of the $k$ - $\epsilon$ turbulence model parameters.*

The  $k$ - $\epsilon$  turbulence model and wall functions parameters are often tuned or empirically determined using simplified flows. This introduces uncertainties, which are often neglected. Flow over a flat plate and a NACA0012 airfoil are used to analyse the effect of the uncertainties in the model parameter on the solutions.

### *Chapter 7: Operational uncertainties for a transonic compressor rotor.*

The compressor rotor is one of the most sensitive components of a gasturbine. This chapter demonstrates how the Probabilistic Collocation is used to efficiently analyse the effect of operational uncertainties on the performance of the rotor.

### *Chapter 8: Two-Step approach for multiple uncertain parameters.*

To use the Probabilistic Collocation method in an efficient framework for multiple uncertain parameters, a two-step approach is employed. The first step identifies the most important parameter(s) by a sensitivity analysis. Secondly, the probability density functions of the most important parameters are propagated using a higher order Probabilistic Collocation approximation.

### *Chapter 9: A Probabilistic Radial Basis Function approach.*

Since radial basis functions are known to be efficient interpolants in high dimensional spaces, they are written in a probabilistic framework to efficiently propagate multiple uncertain parameters.

### *Chapter 10: Conclusions.*

Conclusions on each chapter and the complete thesis are presented.

### *Chapter 11: Recommendations.*

Recommendations for further research are presented in the final chapter.

---

# The Probabilistic Collocation method

---

Computational Fluid Dynamics (CFD) simulations are often computationally intensive. Typically a simulation runs for hours, even days. Since uncertainty propagation increases the computational effort, an efficient method is required. In this chapter the Probabilistic Collocation method is introduced. It is a non-intrusive uncertainty propagation method, which shows spectral convergence with respect to the order of approximation.

The chapter is organized as follows: it starts with a literature review in section 2.1. Section 2.2 introduces the Probabilistic Collocation method, where first the polynomial chaos framework is explained in section 2.2.1. Section 2.3 compares the efficiency of the Probabilistic Collocation method with some existing uncertainty propagation methods using numerical results for the one dimensional piston problem for one uncertain parameter.

## 2.1 Literature review

Since Monte Carlo simulations typically use thousands of samples, it is not feasible for CFD simulations. Many uncertainty propagation methods have been developed to reduce the computational effort. Efficient methods are based on the polynomial chaos framework [Ghanem and Spanos (1991)]. They exist in intrusive and non-intrusive variants. Intrusive means that the uncertainty propagation method requires the source

## **Chapter 2: The Probabilistic Collocation method**

code for implementation, since the resulting set of equations is coupled. Non-intrusive methods on the other hand, use the deterministic solver as a black-box for uncertainty propagation.

### **Intrusive polynomial chaos method**

The Galerkin Polynomial Chaos method [Ghanem and Spanos (1991); Ghanem (1999); Xiu and Karniadakis (2002)] is an intrusive uncertainty propagation method. It is based on the homogeneous chaos theory of Wiener (1938), who constructed a chaos expansion using Hermite polynomials. Ghanem and Spanos (1991) provided the basis for the current spectral stochastic finite element methods [Ghanem (1999)] like the Generalized Polynomial Chaos method [Xiu and Karniadakis (2002)] and the Gram-Schmidt Polynomial Chaos method [Witteveen and Bijl (2006*a*)]. A Galerkin projection is used to obtain the polynomial chaos coefficients, therefore, these methods are referred to as Galerkin Polynomial Chaos methods. It is successfully applied to fluid mechanics problems by Xiu et al. (2002) and Walters and Huyse (2002).

However, to be able to apply this method, the source code of the solver has to be available. It is not trivial to implement the Galerkin Polynomial Chaos method efficiently in an existing CFD solver. All variables need to be written as a polynomial chaos expansion. For a Reynolds-averaged Navier-Stokes solver, this means that apart from the flow variables, also the turbulent quantities need to be expanded for each possible turbulence model. Applications with a commercial CFD solver has been shown by Lacor and Smirnov (2007, 2008) and Dinescu et al. (2010).

### **Non-intrusive polynomial chaos methods**

To enable application of uncertainty propagation methods in combination with a commercial or inhouse CFD solver, non-intrusive methods have been developed. Similar to Monte Carlo simulation, the non-intrusive methods use the deterministic solver as a black-box.

To benefit from the efficiency of the Galerkin Polynomial Chaos method, Walters (2003) and Hosder et al. (2006) developed the Non-Intrusive Polynomial Chaos method and applied it to computational fluid dynamics problems. Both methods use sampling to estimate the coefficients of the polynomial chaos expansion. The number of samples required for the same accuracy is much less than for a full Monte Carlo simulation. A similar approach is followed by Reagan et al. (2003), which they call Non-Intrusive Spectral Projection.

Another class of non-intrusive uncertainty propagation methods are the Stochastic or Probabilistic Collocation methods [Tatang et al. (1997); Mathelin and Hussaini (2003); Babuška et al. (2007); Loeven, Witteveen and Bijl (2007*a*)]. There are, however, different choices of collocation points and polynomials, which results in a different performance of the collocation methods.

First the Probabilistic Collocation method of Tatang et al. (1997) starts with the same polynomial chaos expansion as the Galerkin Polynomial Chaos method. Since the approach is different from the method used in this thesis, it is denoted as the Probabilistic Collocation (T) method. The resulting equations that have to be solved are similar to the Non-Intrusive Polynomial Chaos method of Walters (2003). The sampling points are, however, taken to be collocation points corresponding to Gauss quadrature points weighted with the probability density function of the uncertain parameter. A detailed description of the Probabilistic Collocation (T) method can be found in appendix B.

Next Mathelin and Hussaini (2003) developed the Stochastic Collocation method based on Lagrange polynomials. To avoid confusion on the name, this approach is denoted as the Stochastic Collocation (MH) method. The probability distribution of the uncertain parameter forms the basis of a transformation to an artificial space on  $[-1,1]$ , which is different from the chaos transformation of the Galerkin Polynomial Chaos method. For the collocation points, in this artificial space Gauss-Legendre points are chosen. With Lagrange interpolation the probability distribution of the solution is constructed. A Galerkin projection is applied to compute the expansion coefficients, which is computed using Gaussian quadrature. The Stochastic Collocation (MH) method results in a set of decoupled deterministic equations, which makes the method non-intrusive. Mathelin et al. (2005) showed a significant decrease in computational time compared to the Galerkin Polynomial Chaos method for a quasi-1D nozzle flow.

### The Probabilistic Collocation method

In section 2.2 the Probabilistic Collocation method is presented as it was developed by Loeven, Witteveen and Bijl (2007a). This method combines the idea of a chaos transformation like in the Galerkin Polynomial Chaos method and the decoupled approach of the Stochastic Collocation (MH) method. A previous study [Loeven et al. (2006b,a); Loeven, Witteveen and Bijl (2007a)] showed that the Stochastic Collocation (MH) method only shows spectral convergence for uniformly distributed uncertain parameters. The Probabilistic Collocation method is a generalization of the Stochastic Collocation (MH) method, it converges spectrally for arbitrarily distributed uncertain parameters.

The collocation points with corresponding weights are computed based on the probability density function of the uncertain parameter to obtain spectral convergence with respect to the polynomial order for arbitrary probability distributions. The basis of the Probabilistic Collocation method is formed by Lagrange interpolation and Gaussian quadrature, with the same chaos transformation as the Galerkin Polynomial Chaos method. A major advantage is that the Probabilistic Collocation method can be used for all kinds of non-linearities where the Galerkin Polynomial Chaos method might show difficulties [Debusschere et al. (2001); Mathelin et al. (2005); Witteveen and Bijl (2006b); Sarkar et al. (2009)]. In the mathematics community

## Chapter 2: The Probabilistic Collocation method

the Probabilistic Collocation method was independently developed by Babuška et al. (2007), who proved that for elliptic partial differential equations the Probabilistic Collocation method is equivalent to the Galerkin Polynomial Chaos method.

### 2.2 Theory based on the polynomial chaos framework

The Probabilistic Collocation method as it is found in the work of Babuška et al. (2007) and Loeven, Witteveen and Bijl (2007a) is derived in this section. Since the method is based on the Galerkin Polynomial Chaos method [Ghanem and Spanos (1991); Xiu and Karniadakis (2002)], the polynomial chaos framework is first explained. The following general stochastic differential equation is used to demonstrate how the methods are applied:

$$\mathcal{L}(\mathbf{x}, t, \omega; u(\mathbf{x}, t, \omega)) = S(\mathbf{x}, t, \omega), \quad (2.1)$$

where  $u(\mathbf{x}, t, \omega)$  is the solution and  $\mathcal{L}$  is a (possibly nonlinear) differential operator which contains space and time derivatives and can be stochastic, indicated by  $\omega$ . The solution  $u(\mathbf{x}, t, \omega)$  is a function of space  $\mathbf{x} \in D \subset \mathbb{R}^n$ , time  $t$  and the random event  $\omega \in \Omega$ . The complete probability space is given by  $(\Omega, \mathcal{F}, P)$ , where  $\Omega$  is the set of outcomes,  $\mathcal{F} \subset 2^\Omega$  is the  $\sigma$ -algebra of events and  $P : \mathcal{F} \rightarrow [0, 1]$  is a probability measure.  $S(\mathbf{x}, t, \omega)$  is a space and time dependent source term, which can also depend on the random event. The random event  $\omega$  is introduced by the presence of one or several uncertain parameter in the differential operator, source term, boundary and/or initial conditions.

#### 2.2.1 The Galerkin Polynomial Chaos method

The Galerkin Polynomial Chaos method results in a spectral representation of the stochastic response of the solution and high order approximations of the mean and variance. Based on the Homogeneous Chaos theory of Wiener (1938) the original Galerkin Polynomial Chaos method was developed by Ghanem and Spanos (1991). A polynomial chaos is a polynomial of random variables instead of ordinary variables. The term chaos in this context originates from the paper of Wiener (1938), and should not be confused with deterministic chaos of dynamical systems. Later the Polynomial Chaos framework has been extended to obtain spectral convergence for arbitrary distributions [Xiu and Karniadakis (2002); Wan and Karniadakis (2005); Witteveen and Bijl (2006a)] using numerical techniques to construct a set of polynomials that are orthogonal with respect to the probability density function of the uncertain parameter. The method has successfully been applied to fluid mechanics by Walters and Huyse (2002) and Xiu et al. (2002). An advantage of the Polynomial Chaos method is the spectral convergence with respect to the polynomial order, a disadvantage is the intrusiveness due to the coupled system of deterministic equations that has to be solved.

## 2.2 Theory based on the polynomial chaos framework

In the probabilistic framework, the solution and the uncertain parameter(s) become random variables. The solution is approximated by the following polynomial chaos representation [Ghanem and Spanos (1991)]:

$$u(\mathbf{x}, t, \omega) \approx \sum_{i=0}^M \bar{u}_i(\mathbf{x}, t) \Psi_i(\boldsymbol{\xi}(\omega)). \quad (2.2)$$

This expansion is a spectral expansion in the vector of independent basis random variables  $\boldsymbol{\xi}(\omega)$  with the random polynomial basis  $\{\Psi_i\}$ . Equation (2.2) divides the random variable  $u(\mathbf{x}, t, \omega)$  into a deterministic part, the coefficients  $\bar{u}_i(\mathbf{x}, t)$  and a stochastic part, the polynomial chaos  $\Psi_i(\boldsymbol{\xi}(\omega))$ . The vector  $\boldsymbol{\xi}$  consists of  $d$  independent random variables  $\{\xi_1, \dots, \xi_d\}$ , which are linear transformations of the  $d$  uncertain parameters. The expansion is truncated to  $M + 1$  terms, which is determined by  $d$  and the highest order  $p$  of the polynomials  $\{\Psi_i\}$ :

$$M + 1 = \frac{(d + p)!}{d!p!}. \quad (2.3)$$

The basis  $\{\Psi_i\}$  is a set of polynomials that are orthogonal with respect to the probability density function of the input uncertainty. For some standard distributions corresponding polynomials exist, for example Hermite polynomials correspond to a Normal distribution. The standard distribution and corresponding polynomials can be found in the Askey scheme [Xiu and Karniadakis (2002)]. For other commonly used distributions like the lognormal, truncated normal, and arbitrary unnamed distributions no corresponding standard polynomials exist. To handle arbitrarily distributed uncertain parameters, the corresponding orthogonal polynomials can be constructed using the Gram-Schmidt algorithm (Witteveen and Bijl (2006a)).

Substituting the polynomial chaos expansion (2.2) into the differential equation (2.1) results in:

$$\mathcal{L} \left( \mathbf{x}, t, \omega; \sum_{i=0}^M \bar{u}_i(\mathbf{x}, t) \Psi_i(\boldsymbol{\xi}(\omega)) \right) \approx S(\mathbf{x}, t, \omega). \quad (2.4)$$

A Galerkin projection on each basis polynomial  $\{\Psi_k\}$  is applied, to ensure that the truncation error is orthogonal to the functional space spanned by  $\{\Psi_i\}$ :

$$\left( \mathcal{L} \left( \mathbf{x}, t, \omega; \sum_{i=0}^M \bar{u}_i(\mathbf{x}, t) \Psi_i \right), \Psi_k \right) = (S(\mathbf{x}, t, \omega), \Psi_k), \quad k = 0, 1, \dots, M, \quad (2.5)$$

where  $(\cdot, \cdot)$  denotes the inner product. This set of  $M + 1$  deterministic equations is coupled and can be solved using standard numerical techniques. The inner product  $(\cdot, \cdot)$  is defined as:

$$(f(\boldsymbol{\xi}), g(\boldsymbol{\xi})) = \int f(\boldsymbol{\xi})g(\boldsymbol{\xi})w(\boldsymbol{\xi})d\boldsymbol{\xi}, \quad (2.6)$$

## Chapter 2: The Probabilistic Collocation method

where the weighting function  $w(\boldsymbol{\xi})$  is equal to the probability density functions of the uncertain parameters. For orthogonal polynomials, the following orthogonality relation holds:

$$(\Psi_i, \Psi_j) = (\Psi_i^2) \delta_{ij}, \quad (2.7)$$

where  $\delta_{ij}$  is the Kronecker delta. When the coefficients  $\bar{u}_i(\mathbf{x}, t)$  are known, the probability distribution of the solution can be constructed using equation (2.2). The mean and variance are given by

$$\mu_u = \bar{u}_0(\mathbf{x}, t), \quad (2.8)$$

$$\sigma_u^2 = \sum_{i=1}^M \bar{u}_i(\mathbf{x}, t)^2 (\Psi_i^2). \quad (2.9)$$

These relations follow from the definition of the mean and variance. A total of  $M + 1$  coefficients need to be computed. To benefit from the block structure of the matrix, a Block-Gauss-Seidel algorithm can be used. Typically, 2–5 iterations are required to solve for the coefficients, depending on the required accuracy. The total amount of work is therefore in the order of 2–5 times  $M + 1$  deterministic computations.

### 2.2.2 The Probabilistic Collocation formulation

In the Probabilistic Collocation method a polynomial chaos expansion similar to the expansion in equation (2.2) is used. The difference is that instead of polynomials orthogonal with respect to the probability density function of the uncertain parameters, Lagrange polynomials are used. The coefficients are the collocation points, which correspond to the Gauss quadrature points weighted with the probability density function of the uncertain parameters. By using Gauss quadrature a decoupled set of equations is obtained and the approximated distribution is integrated exactly to obtain the mean and variance.

#### Probabilistic Collocation expansion

The uncertain parameters and solution become random variables in the probabilistic framework, just like in the polynomial chaos method. The solution is expanded, similar to the expansion in equation (2.2), as follows:

$$u(\mathbf{x}, t, \omega) \approx \sum_{i=1}^{N_p} u_i(\mathbf{x}, t) L_i(\boldsymbol{\xi}(\omega)), \quad (2.10)$$

where  $u(\mathbf{x}, t, \omega)$  is a space  $\mathbf{x}$  and time  $t$  dependent random variable. The randomness is introduced by the random event  $\omega \in \Omega$ . The number of collocation points is  $N_p$ . The coefficients  $u_i(\mathbf{x}, t)$  are the solutions  $u(\mathbf{x}, t, \omega)$  at the collocation points  $\omega_i$ ;  $L_i$  are the Lagrange interpolating polynomial chaoses corresponding to the collocation



## 2.2 Theory based on the polynomial chaos framework

points  $\omega_i$ ;  $\boldsymbol{\xi}$  is the (multi-dimensional) random basis  $\boldsymbol{\xi} = \{\xi_1, \xi_2, \dots, \xi_d\}$  for  $d$  uncertain parameters. Key difference between expansions (2.2) and (2.10) is the choice of polynomials and coefficients. The Galerkin Polynomial Chaos expansion (2.2) uses polynomials which are orthogonal with respect to the probability density function of the uncertain parameters. The Probabilistic Collocation expansion (2.10), however, uses Lagrange polynomials. Here the choice of collocation points is crucial, as they should be equal to Gauss quadrature points weighted with the probability density function of the uncertain parameters. The Lagrange polynomial chaoses are given by:

$$L_i(\boldsymbol{\xi}(\omega)) = \prod_{\substack{j=1 \\ j \neq i}}^{N_p} \frac{\boldsymbol{\xi}(\omega) - \boldsymbol{\xi}(\omega_j)}{\boldsymbol{\xi}(\omega_i) - \boldsymbol{\xi}(\omega_j)}, \quad (2.11)$$

with  $L_i(\boldsymbol{\xi}(\omega_j)) = \delta_{ij}$ . The Lagrange interpolating polynomial chaos is the polynomial chaos  $L_i(\boldsymbol{\xi}(\omega))$  that passes through the  $N_p$  collocation points. The random variables  $\boldsymbol{\xi}(\omega)$  are chosen such that the uncertain input parameter is a linear transformation of  $\boldsymbol{\xi}(\omega)$ .

The collocation points are chosen such that they correspond to the Gauss quadrature points used to integrate the function  $u(\mathbf{x}, t, \omega)$  in the  $\omega$  domain. This ensures spectral convergence of the Probabilistic Collocation method [Babuška et al. (2007)]. For convenience of notation the argument  $\omega$  is omitted from here on. The solution is integrated to obtain the mean or variance.

When multiple uncertain parameters are present, the collocation points are obtained from tensor products of one dimensional points. The number of collocation points  $N_p$  then becomes  $N_p = (p+1)^d$ , where  $p$  is the order of approximation and  $d$  then dimension of the stochastic problem (i.e. number of uncertain parameters). The amount of computational work is equal to  $N_p$  deterministic solves, for every collocation point a deterministic simulation has to be performed. To find the suitable Gauss quadrature points and weights numerically, the Golub-Welsch algorithm [Golub and Welsch (1969)] described below is employed.

### Computing Gauss quadrature points with corresponding weights

A powerful method to compute Gauss quadrature rules is the Golub-Welsch algorithm [Golub and Welsch (1969)]. This algorithm needs as an input the recurrence coefficients [Gautschi (2005)] of polynomials which are orthogonal with respect to the weighting function of the integration. For the Probabilistic Collocation method, spectral convergence for arbitrary probability distributions is obtained when the polynomials are orthogonal with respect to the probability density function of  $\boldsymbol{\xi}$ , so  $w(\boldsymbol{\xi}) = f_{\boldsymbol{\xi}}(\boldsymbol{\xi})$ . In case of multiple uncertain parameters, this is done for each  $\xi_j$ ,  $j = 1, \dots, d$  separately.

The Golub-Welsch algorithm requires the recurrence coefficients of the orthogonal polynomials. The recurrence coefficients are computed using the discretized Stieltjes

## Chapter 2: The Probabilistic Collocation method

procedure [Gander and Karp (2001)]. The Stieltjes procedure may become unstable [Gragg and Harrod (1984)]. Gragg and Harrod (1984), however, show that it only becomes a problem at very high quadrature orders (much higher than  $p = 100$ ), which are not used in uncertainty quantification for CFD in practice. When problems with stability occur, an improved Stieltjes algorithm and the Lanczos algorithm are available [Gragg and Harrod (1984); Gautschi (2005)].

Orthogonal polynomials satisfy the following three-term recurrence relation:

$$\begin{aligned}\Psi_{i+1}(\xi) &= (\xi - \alpha_i)\Psi_i(\xi) - \beta_i\Psi_{i-1} & i = 1, 2, \dots, N_p, \\ \Psi_0(\xi) &= 0, \quad \Psi_1(\xi) = 1,\end{aligned}\tag{2.12}$$

where  $\alpha_i$  and  $\beta_i$  are the recurrence coefficients determined by the weighting function  $w(\xi)$  and  $\{\Psi_i(\xi)\}_{i=1}^{N_p}$  is a set of (monic) orthogonal polynomials with  $\Psi_i(\xi) = \xi^i + \mathcal{O}(\xi^{i-1})$ ,  $i = 1, 2, \dots, N_p$ . The recurrence coefficients are given by the Darboux's formulae [Gautschi (2005)]:

$$\begin{aligned}\alpha_i &= \frac{(\xi\Psi_i, \Psi_i)}{(\Psi_i, \Psi_i)} & i = 1, 2, \dots, N_p, \\ \beta_i &= \frac{(\Psi_i, \Psi_i)}{(\Psi_{i-1}, \Psi_{i-1})} & i = 2, 3, \dots, N_p,\end{aligned}\tag{2.13}$$

where  $(\cdot, \cdot)$  denotes an inner product, defined by equation (2.6). The first coefficient  $\beta_1$  is given by  $(\Psi_1, \Psi_1)$ .

Stieltjes' procedure is used to obtain the recurrence coefficients, it starts with  $i = 1$ . With equation (2.13) the first coefficient  $\alpha_1$  is computed. Now  $\Psi_2(\xi)$  is computed by equation (2.12) using  $\alpha_1$  and  $\beta_1$ . This is repeated for  $i = 2, 3, \dots, N_p$ .

The Golub-Welsch algorithm [Golub and Welsch (1969)] can now be employed to compute the collocation points  $\xi_i$  and corresponding weights  $w_i$  from the recurrence coefficients  $\alpha_i$  and  $\beta_i$ ,  $i = 1, 2, \dots, N_p$ . With the recurrence coefficients the following Jacobi matrix is constructed:

$$J = \begin{bmatrix} \alpha_1 & \sqrt{\beta_2} & & & & \\ \sqrt{\beta_2} & \alpha_2 & \sqrt{\beta_3} & & & \\ & \sqrt{\beta_3} & \alpha_3 & \sqrt{\beta_4} & & \\ & & \ddots & \ddots & \ddots & \\ & \emptyset & & \sqrt{\beta_{N_p-1}} & \alpha_{N_p-1} & \sqrt{\beta_{N_p}} \\ & & & \sqrt{\beta_{N_p}} & \alpha_{N_p} & \end{bmatrix}.\tag{2.14}$$

The collocation points  $\xi_i$ ,  $i = 1, \dots, N_p$  are the eigenvalues of  $J$ . The eigenvalues of  $J$  are the roots of the polynomial of order  $N_p$  from the set of the constructed orthogonal polynomials. The weights are found by  $w_i = \beta_1 v_{1,i}^2$ ,  $i = 1, \dots, N_p$ , where  $v_{1,i}$  is the first component of the normalized eigenvector corresponding to eigenvalue  $\xi_i$ .

Now the collocation points  $\xi_i$  in the  $\xi$ -domain are known. The collocation points  $\omega_i$  are found by using the distribution function of  $\xi$ :

$$\omega_i = F_\xi(\xi_i), \quad i = 1, \dots, N_p.\tag{2.15}$$

## 2.2 Theory based on the polynomial chaos framework

If multiple uncertain parameters are present, the collocation points are found using tensor products of the one dimensional vectors containing the collocation points. To reduce the number of collocation points a sparse grid approach [Xiu and Hesthaven (2005); Ganapathysubramanian and Zabarar (2007)] can be used. The tensor products lead to a trivial implementation of anisotropic Probabilistic Collocation expansions. For some parameters a second order approximation may suffice, while other require a third or fourth order expansion.

### Application to a general model

The application of Probabilistic Collocation method to a general model is shown. It is demonstrated how the method is used when the parameter of interest is a functional of the solution, like the lift coefficient of an airfoil. The expansion in equation (2.10) is substituted into the general model given by equation (2.1):

$$\mathcal{L} \left( \mathbf{x}, t, \omega; \sum_{i=1}^{N_p} u_i(\mathbf{x}, t) L_i(\boldsymbol{\xi}(\omega)) \right) = S(\mathbf{x}, t, \omega). \quad (2.1)$$

A Galerkin projection on each basis  $\{L_k(\boldsymbol{\xi}(\omega))\}$  is applied to ensure that the error is orthogonal to space spanned by expansion (2.10):

$$\left( \mathcal{L} \left( \mathbf{x}, t, \omega; \sum_{i=1}^{N_p} u_i(\mathbf{x}, t) L_i \right), L_k \right) = (S(\mathbf{x}, t, \omega), L_k), \quad k = 1, \dots, N_p. \quad (2.16)$$

This projection is approximated using Gaussian quadrature as in equation (2.6), with collocation points and corresponding weights based on the probability density function of the uncertain parameter. The result is a fully decoupled system of equations, similar to the deterministic equation (2.1):

$$\mathcal{L}(\mathbf{x}, t, \omega_k; u_k(\mathbf{x}, t, \omega_k)) = S(\mathbf{x}, t, \omega_k), \quad k = 1, \dots, N_p. \quad (2.17)$$

The distribution function is obtained from equation (2.10). From the distribution the probability density function or probability intervals can be extracted. The mean and variance of the solution are found by

$$\mu_u = \sum_{i=1}^{N_p} u_i(\mathbf{x}, t) w_i, \quad (2.18)$$

$$\sigma_u^2 = \sum_{i=1}^{N_p} \left[ (u_i(\mathbf{x}, t) - \mu_u)^2 \right] w_i, \quad (2.19)$$

where  $w_i$  are the weights corresponding to the collocation points  $\omega_i$ . These relations are derived from the definition of the mean and variance. Similar expressions can also be derived for higher moments like skewness and kurtosis.

## Chapter 2: The Probabilistic Collocation method

### Output of interest

Often the output of interest is a functional of the solution, like the lift coefficient of an airfoil. The flow around the airfoil is computed and integration of the pressure coefficient on the surface of the airfoil yields the lift coefficient. Due to the uncertainty present in the system, the lift coefficient becomes a random variable as well. The lift coefficient is written as a Probabilistic Collocation expansion as follows

$$C_L(\omega) = \sum_{i=1}^{N_p} C_{L_i} L_i(\xi(\omega)), \quad (2.20)$$

where  $C_{L_i}$  is the lift coefficient for collocation point  $\omega_i$ .  $C_{L_i}$  follows from the deterministic computations for every collocation point. The distribution function of the lift coefficient  $C_L$  is then constructed using equation (2.20), the mean and variance are obtained using equations (2.18) and (2.19). For the Galerkin Polynomial Chaos method the functionals have to be applied to the reconstructed solution  $u(\mathbf{x}, t, \omega)$ , which can give troubles [Loeven, Sarkar, Witteveen and Bijl (2007); Sarkar et al. (2009)].

The error of the approximation is estimated using an one order higher approximation [Tatang et al. (1997)]. The estimated error of the lift coefficient for a  $p^{\text{th}}$  order approximation is given by

$$\epsilon_{C_L} = \frac{\sqrt{\frac{1}{N_{p+1}} \sum_{i=1}^{N_{p+1}} w_i \left( C_{L_i}^{p+1} - \hat{C}_{L_i} \right)^2}}{\frac{1}{N_{p+1}} \sum_{i=1}^{N_{p+1}} \hat{C}_{L_i}}, \quad (2.21)$$

where  $N_{p+1}$  is the number of collocation points,  $C_{L_i}^{p+1}$  are the lift forces for the collocation points, all corresponding to a  $(p+1)^{\text{th}}$  order approximation.  $\hat{C}_{L_i}$  are the estimated lift forces at the collocation points of the  $(p+1)^{\text{th}}$  order approximation using a  $p^{\text{th}}$  order approximation.

A stochastic computation is now performed as follows:

1. *Specify input distributions* for every uncertain parameter by providing the probability density function.
2. *Compute collocation points and weights* based on the probability density functions of the uncertain parameter(s), using equations (2.13), (2.14), and (2.15).
3. *Perform deterministic computations* for every collocation point. These computations can be performed in parallel.
4. *Construct the stochastic solution* using all obtained deterministic solutions, e.g. mean/variance fields, uncertainty bars or probability density functions, using equations (2.10), (2.18), and (2.19).

## 2.3 Comparison between methods for one uncertain parameter

In this section the efficiency of the Probabilistic Collocation method [Babuška et al. (2007); Loeven, Witteveen and Bijl (2007a)] is compared with the efficiency of the Galerkin Polynomial Chaos method [Ghanem and Spanos (1991)], Non-Intrusive Polynomial Chaos method [Walters (2003)] and the Stochastic Collocation (MH) method [Mathelin et al. (2005)] for the linear piston problem [Loeven et al. (2006b)] indicated in figure 2.1(a).

### Linear 1D piston problem

The linear piston is chosen since it is a test problem which is easily evaluated, but it includes a nonlinear dependence between the solution and the uncertain parameter.

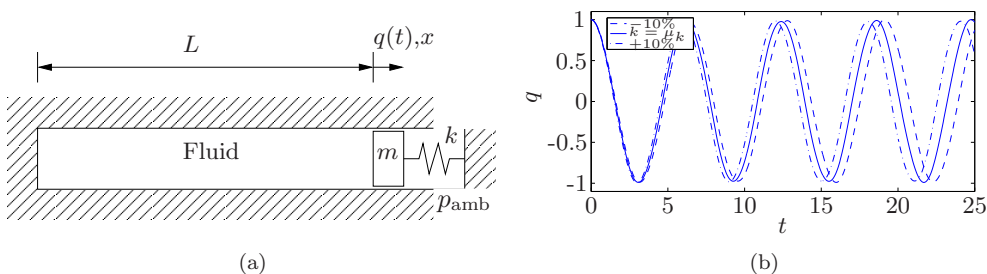


**Figure 2.1:** The linear piston problem (a) and realizations (b) using different values for the spring stiffness  $k$  of the linear piston problem for  $k = \mu_k = 1.429$  and  $k = \mu_k \pm 10\%$ .

It consists of a one-dimensional fluid domain on one side bounded by a mass which is attached to a spring. The fluid is modeled using the linearized isentropic Euler equations. The piston position  $q(t)$  and velocity  $\dot{q}(t)$  are determined by the mass of the piston  $m$ , the spring stiffness  $k$ , the length of the fluid domain  $L$ , the fluid state  $U = (\rho, \rho u)^T$ , the ambient pressure  $p_{\text{amb}}$ , and the initial conditions. The cross-sectional area is  $A = 1$ . The piston problem is considered for small deviations from the equilibrium only, therefore the fluid state vector can be split into two parts:

$$U = U_0 + U',$$

with  $U_0$  the equilibrium state and  $U'$  the small deviation. The governing equations for the perturbations become:

$$\frac{\partial U'}{\partial t} = - \begin{bmatrix} 0 & 1 \\ c_0^2 & 0 \end{bmatrix} \frac{\partial U'}{\partial x}, \quad (2.22)$$

## Chapter 2: The Probabilistic Collocation method

with  $c_0$  the speed of sound. The structure is governed by:

$$m\ddot{q} + kq = p_{x=L} - p_{\text{amb}}, \quad (2.23)$$

where  $q$  is the displacement of the piston,  $p_{x=L}$  is the pressure acting from the fluid on the piston and  $p_{\text{amb}}$  is the ambient pressure surrounding the piston. The flow and structure equations (2.22) and (2.23) are made dimensionless using the following substitutions:

$$\bar{t} = \frac{c_0}{L}t, \quad \bar{x} = \frac{x}{L}, \quad \bar{q} = \frac{q}{L}, \quad \bar{\rho} = \frac{\rho}{\rho_0}, \quad \bar{u} = \frac{u}{c_0}, \quad \bar{m} = \frac{m}{\rho_0 L}, \quad \bar{k} = \frac{kL}{\rho_0 c_0^2} \quad \text{and} \quad \bar{U} = \begin{bmatrix} \bar{\rho} \\ \bar{\rho}u \end{bmatrix}.$$

The resulting non-dimensional set of equations becomes:

$$\frac{\partial \bar{U}'}{\partial \bar{t}} = - \begin{bmatrix} 0 & 1 \\ 1 & 0 \end{bmatrix} \frac{\partial \bar{U}'}{\partial \bar{x}}, \quad (2.24)$$

$$\bar{m}\ddot{\bar{q}}' + \bar{k}\bar{q}' = \bar{\rho}'. \quad (2.25)$$

The coupling at the boundary  $\bar{x} = 1$  is governed by:

$$\bar{u}'(\bar{x} = 1) = \dot{\bar{q}}', \quad (2.26)$$

the other boundary condition for the fluid is a fixed wall:

$$\bar{u}'(\bar{x} = 0) = 0. \quad (2.27)$$

From now the bar and prime to indicate non-dimensionality and small deviations are omitted for convenience of notation.

### Fluid domain spatial discretization and time integration

The fluid domain is divided into  $N$  cells and the equations are discretized using a second order central finite volume discretization. Introducing two ghost-cells, at  $x = 0$  and  $x = 1$ , this results in the following equations:

$$\frac{dU_i}{dt} = - \begin{bmatrix} 0 & 1 \\ 1 & 0 \end{bmatrix} \left( \frac{U_{i+1} - U_{i-1}}{2\Delta x} \right) \quad i = 1, \dots, N, \quad (2.28)$$

with use of the boundary conditions the properties of the ghost cells are given by:

$$U_0 = \begin{bmatrix} \rho_0 \\ \rho u_0 \end{bmatrix} = \begin{bmatrix} \rho_1 \\ -\rho u_1 \end{bmatrix} \quad \text{and} \quad U_{N+1} = \begin{bmatrix} \rho_{N+1} \\ \rho u_{N+1} \end{bmatrix} = \begin{bmatrix} \rho_N - \Delta x \ddot{q} \\ 2\dot{q} - \rho u_N \end{bmatrix}. \quad (2.29)$$

The parameter values of the piston problem are given in Table 2.1. These values are chosen similar to the paper of van Zuijlen and Bijl (2004). This is done to be able to verify the deterministic solution. The choice of  $m$  and  $k$  are such that the fluid has a

### 2.3 Comparison between methods for one uncertain parameter

**Table 2.1:** Parameter values for the piston problem.

Property	Symbol	Value
Mean spring stiffness	$\mu_k$	1.429
Mean piston mass	$\mu_m$	2
Amount of uncertainty	$\varsigma$	0.1
Number of fluid cells	$N$	64
Initial position	$q(0)$	1
Initial velocity	$\dot{q}(0)$	0
Time step	$\Delta t$	0.1

strong influence on the structural motion without dominating the structure dynamics. With  $N = 64$  the term  $\Delta x \ddot{q}$  is small compared to  $\rho_N$ .  $\Delta x \ddot{q}$  is therefore left out of the calculations. The equations for structure are written as:

$$\frac{dQ}{dt} = \begin{bmatrix} 0 & 1 \\ -\frac{k}{m} & 0 \end{bmatrix} Q + \begin{bmatrix} 0 \\ \frac{\rho_{N+1/2}}{m} \end{bmatrix}, \quad (2.30)$$

with  $Q = \begin{bmatrix} q \\ \dot{q} \end{bmatrix}$  and  $\rho_{N+1/2} = \frac{\rho_{N+1} - \rho_N}{2}$ . Equations (2.28) and (2.30) are combined to one system which is solved monolithically. The monolithic system is written as:

$$\frac{d\mathbf{x}}{dt} = A\mathbf{x}, \quad (2.31)$$

in which

$$\mathbf{x} = \begin{bmatrix} \mathbf{x}_f \\ \mathbf{x}_s \end{bmatrix} \text{ and } A = \begin{bmatrix} A_f & A_{fs} \\ A_{sf} & A_s \end{bmatrix},$$

where  $\mathbf{x}_f$  contains the fluid properties  $U_i$  of all finite volume cells and  $\mathbf{x}_s = Q$ . The matrices  $A_{fs}$  and  $A_{sf}$  provide the coupling between the fluid and the structure.

At  $t = 0$  the fluid is at rest and the piston state is  $q(0)=1$  and  $\dot{q}(0)=0$ . Time integration is performed using an ESDIRK-4 scheme [van Zuijlen and Bijl (2004)].

#### Uncertain spring stiffness $k$

The mean value for  $k$  is  $\mu_k=1.429$ , the variance is set to  $\sigma_k^2=6.8068 \times 10^{-3}$ , and corresponding to  $U(\mu_k \pm 10\%)$  for a uniform distribution. Figure 2.1(b) shows that for a 10% variation of  $k$  a significant change of the solution is present. Further results are for the piston position at  $t=10$ .

The Probabilistic Collocation method is compared with the Galerkin and Non-Intrusive Polynomial Chaos methods and the Stochastic Collocation (MH) method. The error

## Chapter 2: The Probabilistic Collocation method

convergence with respect to the amount of computational work is used to compare the efficiency. The errors are defined by

$$\varepsilon_{\mu_u} = \left| \frac{\mu_u - \mu_{u,\text{ref}}}{\mu_{u,\text{ref}}} \right| \quad \text{and} \quad \varepsilon_{\sigma_u^2} = \left| \frac{\sigma_u^2 - \sigma_{u,\text{ref}}^2}{\sigma_{u,\text{ref}}^2} \right|, \quad (2.32)$$

where the subscript  $u,\text{ref}$  indicates the reference solution. The reference solution is a 20<sup>th</sup> order polynomial chaos computation. The method was validated for lower orders using a Monte Carlo simulation with  $10^6$  samples. The convergence of the methods is much faster than Monte Carlo simulation, therefore very quickly the accuracy is better than the accuracy of the Monte Carlo simulation. The work is expressed as the number of times a deterministic problem needs to be solved. For the Galerkin Polynomial Chaos method the amount of work is  $I \times (M + 1)$  where  $M$  is the number of polynomial chaos expansion terms of the approximation (equation (2.2)) and  $I$  the number of Block-Gauss-Seidel iterations required to obtain the polynomial coefficients. The Block-Gauss-Seidel algorithm makes use of the structure of the resulting matrix. The stopping criterion for the iterations is a residual of  $10^{-8}$ . For the computations in this paper about 2–5 iterations were required. The Non-Intrusive Polynomial Chaos method requires  $M + 1$  deterministic solves to approximate the coefficients. The Stochastic Collocation (MH) and Probabilistic Collocation method both use one deterministic computation for every collocation point. The implementation of the uncertainty propagation methods for the piston problem is shown in appendix B.

### Probabilistic Collocation versus Galerkin Polynomial Chaos

First the Probabilistic Collocation method is compared with the Galerkin Polynomial Chaos method to demonstrate the spectral convergence with respect to the polynomial chaos order and the increase in efficiency due to the decoupling of the equations. Figure 2.2(a) shows the convergence of both methods with respect to polynomial chaos order. The convergence is the same for both methods, which holds for arbitrarily distributed uncertain parameters, since the polynomial basis is constructed based on the probability density function of the uncertain parameter.

Figure 2.2(b) shows the convergence with respect to the amount of computational work, expressed in the number of deterministic solves. When the computational work is considered, the strength of the Probabilistic Collocation approach comes forward. The amount of work is equal to the number of collocation points, while for the Galerkin Polynomial Chaos method a coupled system of equations has to be solved. In the figure the amount of work for the Galerkin Polynomial Chaos is set to  $2 \times (M + 1)$ , where  $M$  is the number of polynomial chaos coefficients. This is the minimal computational effort required to solve the system of equations. In practice 2–5 Block-Gauss-Seidel iterations are required.

This is, however, a test problem which does not contain any non-polynomial nonlinearities. For problems with nonlinearities (especially non-polynomial) in the equations, the Galerkin Polynomial Chaos method can become inefficient [Witteveen and Bijl



### 2.3 Comparison between methods for one uncertain parameter

(2006b)]. In the case of polynomial nonlinearities, products of the polynomial chaos expansions can still be evaluated analytically. For non-polynomial nonlinearities one has to integrate the terms in the Galerkin projection (2.5) numerically, which can become computationally intensive [Sarkar et al. (2009)]. The Probabilistic Collocation method has no problems with nonlinear equations, since the problem is solved deterministically for each collocation point. The amount of work for the Probabilistic Collocation method is the same for linear and nonlinear systems of equations.

It must be noted that the conclusions based on these results hold for one uncertain parameter. Due to the tensor product approach for multiple uncertain parameters, the amount of work for the Probabilistic Collocation method scales with  $N_p = (p+1)^d$ , with  $p$  the order of approximation and  $d$  the number of uncertain parameters. So for a large number of uncertain parameters, the Galerkin Polynomial Chaos can become more efficient.

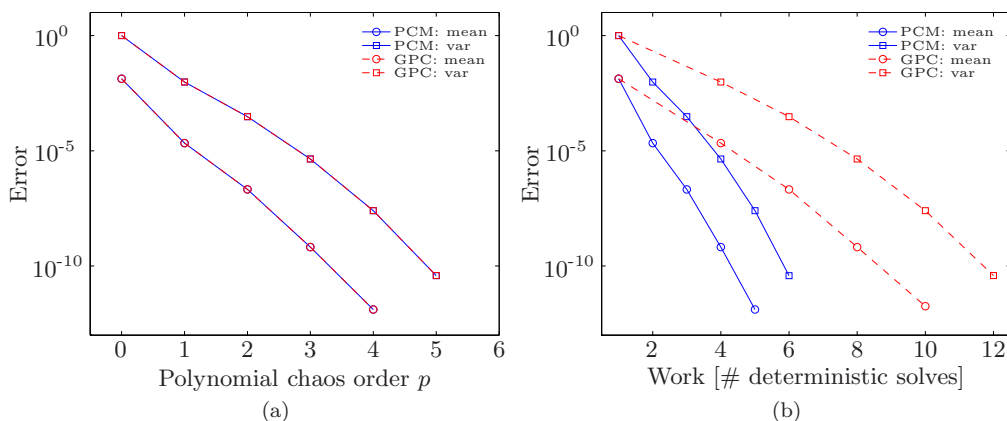


**Figure 2.2:** Convergence for the Probabilistic Collocation method (PCM) and the Galerkin Polynomial Chaos method (GPC), with respect to the polynomial chaos order (a) and the computational work (b) for one arbitrarily distributed uncertain parameter.

In order to show that the Probabilistic Collocation method results in exactly the same polynomial chaos approximation as the Galerkin Polynomial Chaos, the monomial coefficients  $\hat{u}_i$  of the expansions are compared.

$$\sum_{i=1}^{N_p} u_i(\omega_i) L_i(\xi(\omega)) = \sum_{i=0}^M \bar{u}_i \Phi_i(\xi(\omega)) = \hat{u}_0 + \hat{u}_1 \xi(\omega) + \hat{u}_2 \xi(\omega)^2 + \dots + \hat{u}_P \xi(\omega)^P \quad (2.33)$$

Table 2.2 shows the monomial coefficients of the expansion for the piston position at  $t = 10$ . It can be seen that the Galerkin Polynomial Chaos and the Probabilistic Collocation method result in the same monomial coefficients. The Non-Intrusive Polynomial Chaos, however, computes the coefficients based on some samples, so

## Chapter 2: The Probabilistic Collocation method

that an error is introduced. The magnitude of this error is case dependent. For this case, the coefficients are approximated reasonably well. The effect of the error in the coefficients on the mean and variance are discussed below. To compute the coefficients of the polynomial chaos method exactly, the system of equations is solved directly here. For general use of the Galerkin Polynomial Chaos the system is solved iteratively, using the Block-Gauss-Seidel algorithm.

**Table 2.2:** The monomial coefficients of the 4<sup>th</sup> order expansion (2.33) of the piston position at  $t = 10$  obtained from the Galerkin Polynomial Chaos method, the Probabilistic Collocation method, and the Non-Intrusive Polynomial Chaos method.

Coefficient	Galerkin Polynomial Chaos	Probabilistic Collocation	Non-Intrusive Polynomial Chaos
$\hat{u}_0$	-0.73204167739370	-0.73204167739370	-0.73204167739370
$\hat{u}_1$	0.11007272407613	0.11007272407613	0.11008631168539
$\hat{u}_2$	0.00969183126072	0.00969183126072	0.00969155246323
$\hat{u}_3$	-0.00069309123364	-0.00069309123364	-0.00069926645535
$\hat{u}_4$	-0.00000788645601	-0.00000788645601	-0.00000775982742

### Probabilistic Collocation versus Non-Intrusive Polynomial Chaos

The Non-Intrusive Polynomial Chaos method results in approximations of the polynomial chaos coefficients. Section B.2 shows a detailed description of the Non-Intrusive Polynomial Chaos method. The convergence cannot be better than the Probabilistic Collocation method, since this method yields the exact polynomial chaos coefficients. The approximated monomial coefficients for the piston position  $q$  at  $t = 10$  are included in table 2.2. The first coefficient is accurately approximated for this case. The other coefficients, however, show some discrepancies. The influence of these small differences between the exact and approximated coefficients on the convergence is clearly shown in figure 2.3, which shows the convergence of the error of the mean and variance with respect to the computational work for the Probabilistic Collocation method and the Non-Intrusive Polynomial Chaos method.

It must be stated that the convergence of the Non-Intrusive Polynomial Chaos method heavily depends on the choice of the sampling vector  $\xi$ . For this comparison the choice of Walters (2003) and Hosder et al. (2006) is followed. For the case of a normally distributed spring stiffness  $k$  the sampling vector is  $\xi = 0, 1, -1, 2, -2$ . Reagan et al. (2003) address the importance of the choice of the sampling vector as well. They are not convinced that  $M + 1$  samples are enough to accurately estimate the expansion coefficients. They, therefore, use significantly more samples computed using Latin Hypercube sampling. Later, Hosder et al. (2007) stated that  $2 \times (M + 1)$  samples in combination with regression is a more robust choice.

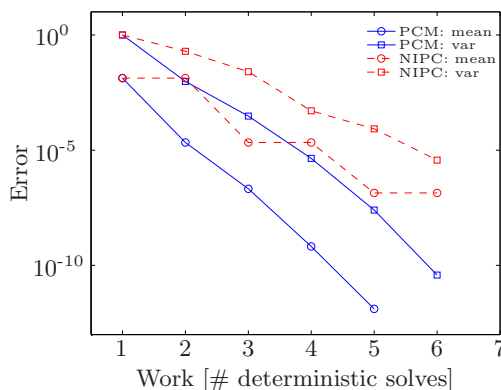


**Figure 2.3:** Convergence for the Probabilistic Collocation method (PCM) and the Non-Intrusive Polynomial Chaos method (NIPC) with respect to the computational work.

### Probabilistic Collocation versus Stochastic Collocation (MH)

The Stochastic Collocation (MH) method uses an artificial space instead of the chaos transformation. A detailed description of the Stochastic Collocation (MH) method can be found in section B.5. As a result, the Stochastic Collocation (MH) shows only spectral convergence for uniformly distributed input parameters. This is shown in figure 2.4, which shows the convergence of the error with respect to the amount of computational work. Figure 2.4(a) shows that when  $\xi(\omega)$  is taken uniformly distributed on  $[-1,1]$ , the Probabilistic Collocation is equivalent to the Stochastic Collocation (MH) method. This is due to the fact that the collocation points and corresponding weights are the in both cases the Gauss-Legendre points. Figure 2.4(b) shows the convergence for a lognormally distributed parameter. This is the general picture for a non-uniform distribution. For all non-uniform distributions, the Legendre collocation points of the Stochastic Collocation (MH) method are not the optimal choice. It can, therefore, be concluded that the Probabilistic Collocation method is a generalization of the Stochastic Collocation (MH) method, since spectral convergence is maintained for arbitrarily distributed parameters.

## 2.4 Summary

The Probabilistic Collocation method was developed to be an efficient and easy to use uncertainty propagation method. It is based on the polynomial chaos framework, maintaining spectral convergence with respect to the polynomial chaos order for arbitrarily distributed uncertain parameters. The Probabilistic Collocation method is non-intrusive, enabling the use of existing (commercial) CFD solvers. A big advantage with respect to the Galerkin Polynomial Chaos method is the fact that propagation

## Chapter 2: The Probabilistic Collocation method

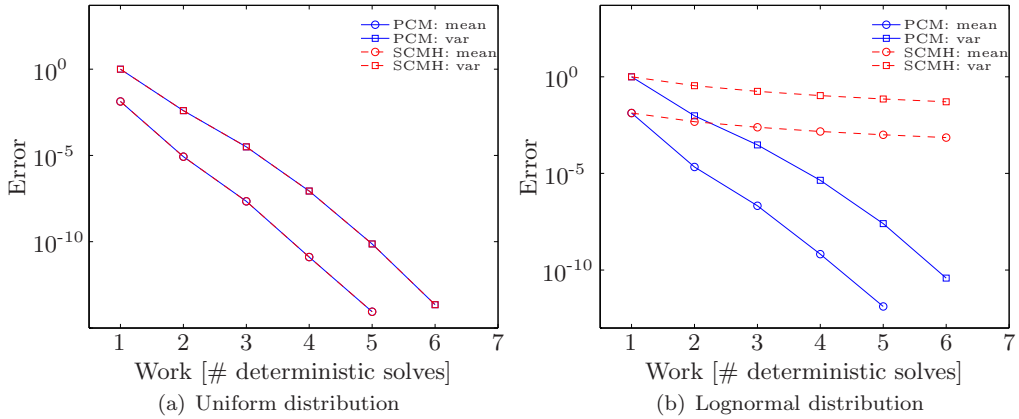


**Figure 2.4:** Convergence for the Probabilistic Collocation method (PCM) and the Stochastic Collocation (MH) method (SCMH) with respect to computational work for uniformly (a) and lognormally (b) distributed uncertain parameters. The result for the lognormal distribution is general for all non-uniform distributions.

through nonlinear models do not result in an increase of computational effort. Furthermore, functionals of the solution are trivially obtained.

A comparison of the Probabilistic Collocation method with some existing methods for one uncertain parameter demonstrated the spectral convergence with respect to the polynomial chaos order. The Galerkin Polynomial Chaos method showed exactly the same results as the Probabilistic Collocation method, however, at higher computational costs. The Non-Intrusive Polynomial Chaos method provides an approximation of the polynomial chaos coefficients. This results in a convergence that is not spectral and sensitive to the choice of sampling points. The Stochastic Collocation (MH) method of Mathelin et al. (2005) shows only spectral convergence for uniformly distributed uncertain parameters. The Probabilistic Collocation shows spectral convergence for arbitrarily distributed uncertain parameters if the response is  $C^{p+1}$ , where  $p$  is the order of approximation.

---

# Flow applications of the Probabilistic Collocation method

---

In order to demonstrate how uncertainties can efficiently be propagated, the Probabilistic Collocation method (see chapter 2) is used in combination with a commercial flow solver. Two flow test cases with different characteristics are shown in this chapter. A subsonic [Loeven, Witteveen and Bijl (2007*a*)] and transonic [Loeven and Bijl (2009*a*)] flow case are shown, which were computed using the FINE™/Hexa solver of Numeca International. Uncertainties are present in the free stream conditions, like Mach number and angle of attack. The transonic case also involves an uncertain relative thickness of the airfoil. The effect of the uncertainties on the solution (i.e. lift and drag of the airfoil) is shown.

Several ways of representing the stochastic solution are shown. For example, the probability density function of quantities of interest like drag or lift are shown. Furthermore, the mean and variance fields of flow quantities are computed to see in what part of the flow domain for example the pressure is most sensitive to an uncertain parameter. The mean skin friction and pressure on the airfoil surface are plotted with 99% uncertainty bars, which are obtained from the distribution function of the solutions.

### 3.1 Subsonic flow around a NACA0012 airfoil

The first test case is steady turbulent subsonic flow around a NACA0012 airfoil with uncertain Mach number. The airfoil is put at an angle of attack of  $5^\circ$ , with a Reynolds number of  $3 \times 10^6$ . The deterministic computations are performed on a grid of 42,902 cells, created with Hexpress™. At the surface approximately 800 cells are present with  $y^+ \leq 1$ . The grid layout is shown in figure 3.1.

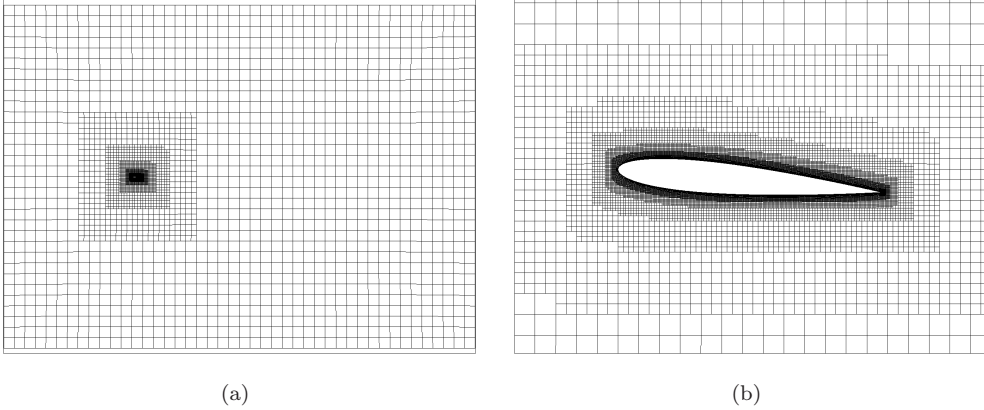


**Figure 3.1:** The computational mesh layout (a) and a detailed view of the airfoil (b).

The flow is modeled by the Reynolds-averaged Navier-Stokes equations using the Spalart-Allmaras turbulence model. The simulations are converged up to 5 digits for the lift and drag. The air properties are at 0m ISA. The free stream Mach number is assumed to be normally distributed, with mean  $\mu_M = 0.3$  and a coefficient of variation of 5%. Most probability is located around the mean and there is equal probability of a higher or lower Mach number. The coefficient of variation corresponds with a variations in Mach number of 0.015, which is approximately 5 m/s at sealevel. The coefficient of variation is defined as  $CV = \sigma/\mu$ , which results in a variance of  $\sigma_M^2 = 2.25 \times 10^{-4}$ .

The uncertainty is propagated using the Probabilistic Collocation method, which is described in chapter 2. The flow solver is run deterministically for every collocation point. The deterministic solutions are used to compute the mean, variance and distribution function of properties of interest according equations (2.10), (2.18), and (2.19). Convergence of the Probabilistic Collocation method is checked using equation (2.21). The collocation points and weights with the corresponding lift and drag for  $p = 0$  to 4 are given in table 3.1. The estimated error is plotted in figure 3.2. It drops two orders of magnitude when the approximation is increased from first to second order. Based on the figure, a second order approximation is used for further results.

The computed mean drag is  $\mu_D = 76.34$  N with a standard deviation of  $\sigma_D = 7.212$  N,

### 3.1 Subsonic flow around a NACA0012 airfoil

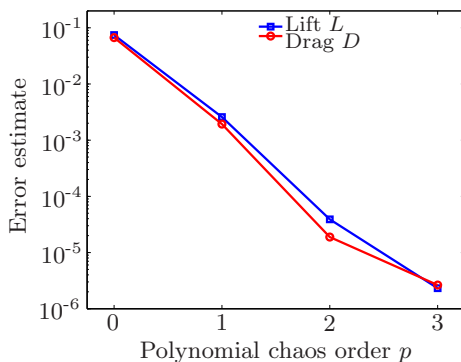


**Figure 3.2:** Convergence of the Probabilistic Collocation method for the lift and drag force with respect to the polynomial chaos order  $p$ .

**Table 3.1:** The uncertain Mach number and weights for the deterministic solves and the solutions for the drag and lift for the polynomial chaos orders  $p = 0$  to 4.

Polynomial chaos order $p$	Collocation point	Quadrature weight	Mach number	Drag [N]	Lift [N]
0	1	1.00000	0.30000	76.15972	3563.363
1	1	0.50000	0.28500	69.13470	3200.048
	2	0.50000	0.31500	83.54528	3949.263
2	1	0.16667	0.27402	64.21719	2948.015
	2	0.66667	0.30000	76.15972	3563.363
	3	0.16667	0.32598	89.18566	4246.479
3	1	0.04588	0.26498	60.31209	2749.275
	2	0.45412	0.28887	70.91320	3291.672
	3	0.45412	0.31113	81.60429	3847.493
	4	0.04588	0.33502	93.97566	4500.648
4	1	0.01126	0.25715	57.02602	2583.091
	2	0.22207	0.27967	66.72228	3076.164
	3	0.53334	0.30000	76.15972	3563.363
	4	0.22207	0.32033	86.26064	4092.068
	5	0.01126	0.34285	98.24158	4728.320

### Chapter 3: Flow applications of the Probabilistic Collocation method

this results in a coefficient of variation of 9.45%. The lift has a mean of  $\mu_L = 3575$  N, a standard deviation of  $\sigma_L = 375.2$  N and a coefficient of variation of 10.5%. As  $D, L \sim M^2$ , a second order expansion approximates this relation well. The probability density functions of the drag and lift are shown in figure 3.3. A Monte Carlo simulation using 10,000 Latin Hypercube samples is added as a reference solution. The figure shows a good correspondence between the Monte Carlo simulation and the Probabilistic Collocation approximation using only three deterministic solves.

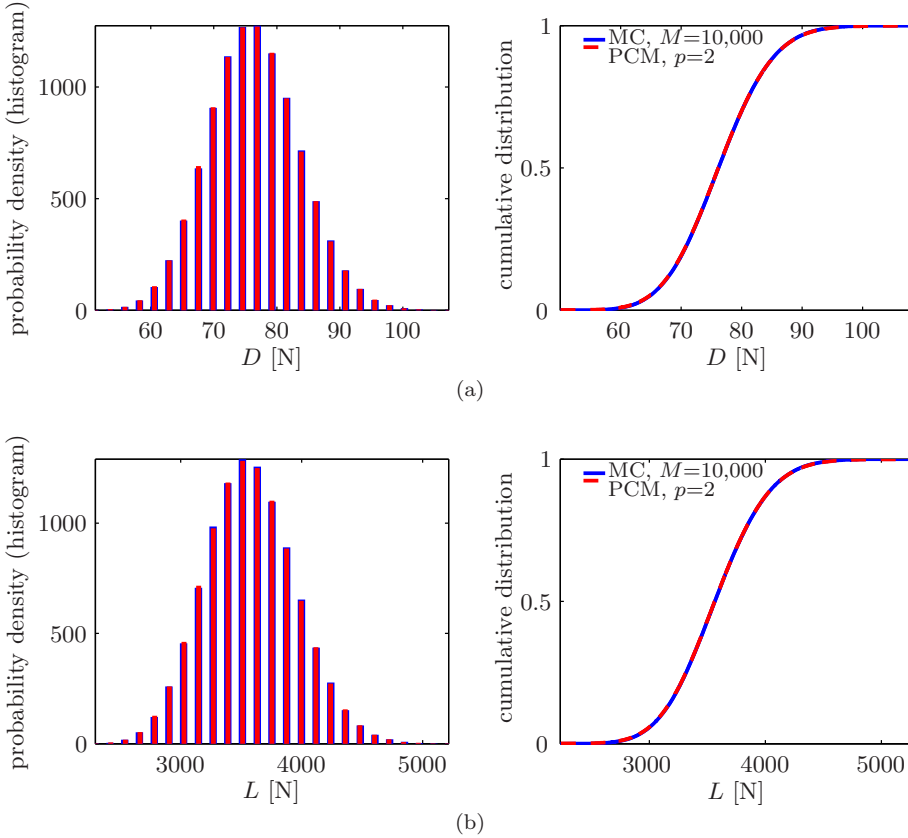


**Figure 3.3:** The probability density function (as a histogram) and the cumulative distribution function of the drag  $D$  (a) and the lift  $L$  (b) obtained from a second order Probabilistic Collocation computation and a Monte Carlo simulation using 10,000 Latin Hypercube samples.

Another way to visualize the results of a stochastic simulation is by observing the mean and variance of the pressure field around the airfoil. Figure 3.4 shows the pressure fields obtained from a second order Probabilistic Collocation computation. The mean pressure around the airfoil is shown in figure 3.4(a) and the variance of the



### 3.1 Subsonic flow around a NACA0012 airfoil

pressure field in 3.4(b). From the variance field it is clear that the input uncertainty results in the highest uncertainty in the static pressure near the leading edge of the airfoil's upper surface.

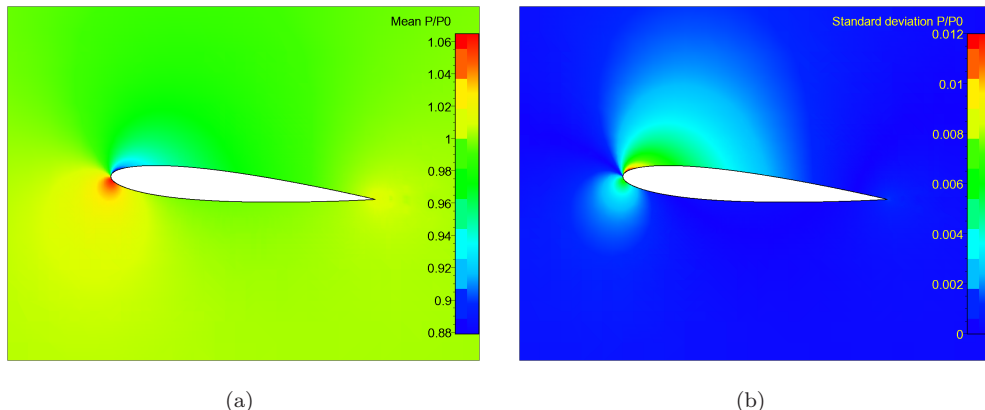


**Figure 3.4:** The mean (a) and the variance (b) pressure field obtained from a second order Probabilistic Collocation computation, with FINE™/Hexa as deterministic solver.

The pressure distribution or skin friction on the airfoil surface can be represented by uncertainty bar plots. Figure 3.5(a) shows the mean pressure distribution on the upper and lower surface with the uncertainty bars indicating the interval which contains 99% of all possible values. This interval is obtained from the distribution function of the pressure at each position on the airfoil. It can be seen in the figure that the uncertain free stream Mach number leads to the highest variation in pressure on the upper surface near the leading edge. The uncertainty bars for the skin friction along the airfoil surface are shown in figure 3.5(b). The skin friction shows more constant variations along the entire airfoil for an uncertain free stream Mach number.

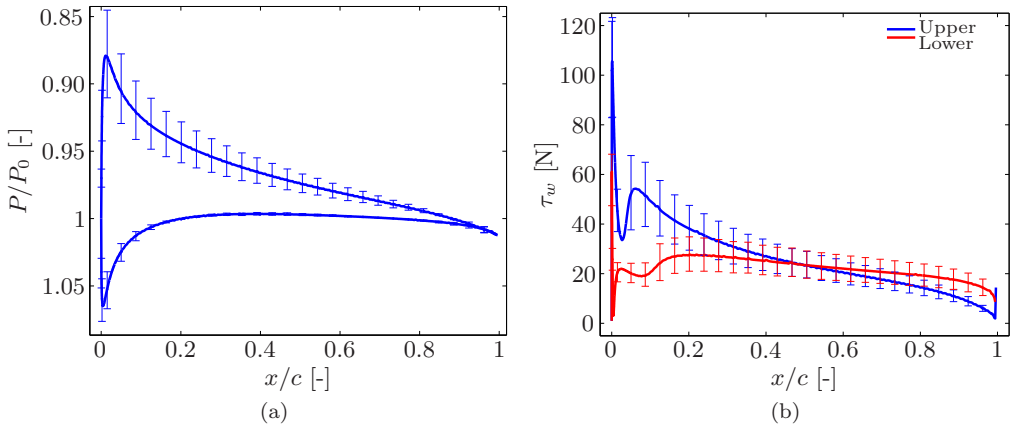


**Figure 3.5:** Pressure distribution (a) and skin friction distribution (b) on the upper and the lower surface of the NACA0012 airfoil. The mean is indicated by bold solid lines, the uncertainty bars show the interval which contains 99% of all possible values.

## 3.2 Transonic flow around a RAE2822 airfoil

The Probabilistic Collocation method is applied to transonic flow around a RAE2822 airfoil [Loeven and Bijl (2009a)]. Three sources of uncertainty are present, the free stream Mach number, the angle of attack and the relative thickness of the airfoil. First all uncertainties are propagated independently, to see the separate effects of the uncertainties. After that all three uncertainties are propagated simultaneously to allow for interaction between the uncertainties.

### 3.2.1 Deterministic test case description

The geometry and a close up of the computational grid are shown in figure 3.6(a). A grid convergence study has been performed (see table 3.2) to ensure that the deterministic results are grid independent. All computations are performed on the grid of 76,063 cells. About 800 cells are present on the surface of the airfoil with  $y^+ \leq 1$ . Furthermore, the computations are converged to a relative residual of  $10^{-10}$  to eliminate the iteration error. The coefficients are converged up to 7 digits in this case. The flow parameters are set according to Cook et al. (1979), i.e. the mean flow Mach number is  $M_\infty = 0.734$ , the angle of attack is  $\alpha = 2.79^\circ$ , and the Reynolds number is  $6.5 \times 10^6$ . The Mach number in the flow field around the airfoil is shown in figure 3.6(b).

**Table 3.2:** Grid convergence study for flow around the RAE2822 airfoil. Shown are the lift  $C_l$  and drag  $C_d$  coefficient rounded on 1 count ( $10^{-3}$  and  $10^{-4}$  respectively) for different grid sizes.

# grid cells	$C_l$ [-]	$C_d$ [-]
27,718	0.771	0.0194
37,675	0.771	0.0190
59,902	0.774	0.0187
<b>76,063</b>	<b>0.772</b>	<b>0.0187</b>
144,013	0.772	0.0187

### 3.2.2 Uncertain parameters

The uncertain parameters have normal distributions, as shown in figure 3.7. The free stream Mach number has a mean of  $\mu_M = 0.734$  and a standard deviation of  $\sigma_M = 0.005$ . The angle of attack has a mean and standard deviation of  $\mu_\alpha = 5^\circ$  and  $\sigma_\alpha = 0.1^\circ$ . For the relative thickness, the mean and standard deviation are  $\mu_t = 1$  and  $\sigma_t = 0.005$ . This results in coefficients of variation  $CV = \sigma/\mu$  of 0.68%, 3.58%, and 0.5% respectively.

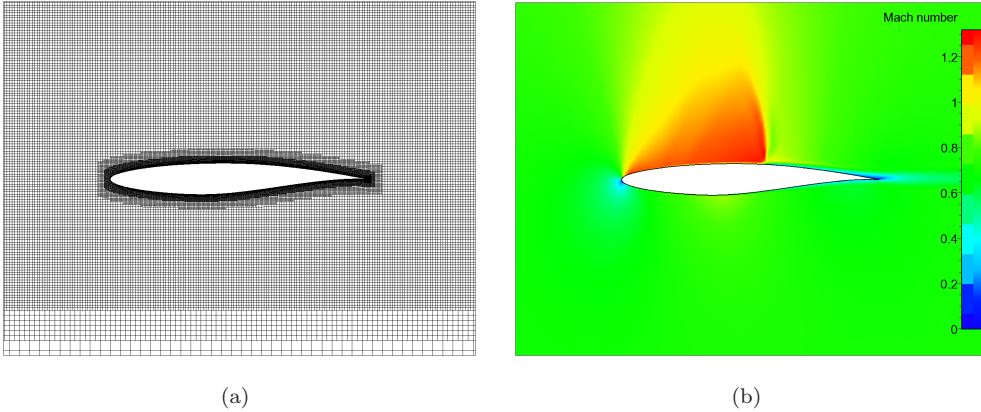


**Figure 3.6:** Computational grid near the airfoil (a) and the Mach number around the airfoil (b).

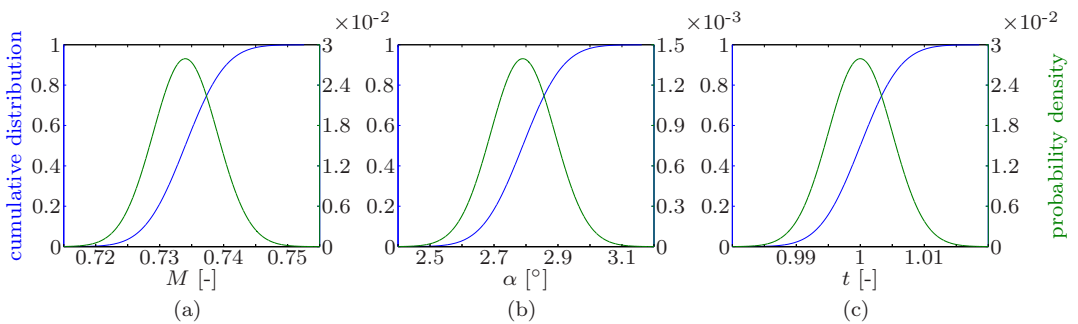


**Figure 3.7:** Probability distribution functions of the uncertain parameters.

### 3.2.3 Results Probabilistic Collocation method

In order to check the convergence of the Probabilistic Collocation method, computations are performed from  $p = 0$  to 3. The error is estimated using an approximation which is one order higher according equation (2.21). That is why the figures show the estimated error up to  $p = 2$ . The convergence is shown until the estimated error is below  $10^{-3}$ , for this test case a second order approximation was sufficient.

#### Uncertain Mach number

The convergence of Probabilistic Collocation method with respect to the polynomial order is shown in figure 3.8 for the lift and drag coefficient for an uncertain Mach number. The estimated error drops two orders of magnitude when the approximation is increased to second order. The approximation of  $p = 0$  corresponds with a deterministic computation with all parameters set to the mean value. Further results are for  $p = 2$ , which means 3 deterministic computations have to be performed.

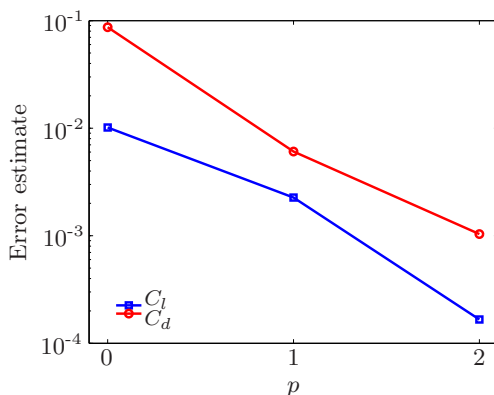


**Figure 3.8:** Convergence of the Probabilistic Collocation method for the lift coefficient  $C_l$  and drag coefficient  $C_d$  for an uncertain Mach number  $M$  with respect to the polynomial chaos order  $p$ .

The mean of the Mach number around the airfoil shows no significant difference with the deterministic Mach number (see figure 3.6(b)). Figure 3.9 shows the standard deviation of the Mach number around the airfoil. There is a large standard deviation present in the shock area. Also the wake shows an increased standard deviation. The maximum standard deviation is 0.18, which is in the order of 25% of the free stream Mach number. Clearly, this case is highly sensitive to variations of the free stream Mach number. The distribution of the free stream Mach number only showed a coefficient of variation of  $CV_M = 0.68\%$ .

Next, figure 3.10 shows the pressure coefficient distribution on the surface of the airfoil. Uncertainty bars indicate the 99% interval. The interval is obtained from the

computed cumulative distribution function of the pressure and includes 99% of all possible values that can occur. Also here, the largest uncertainty is present near the shock.

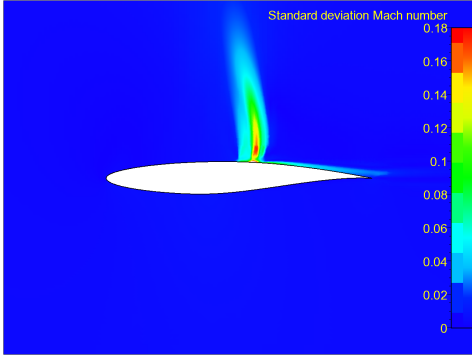


**Figure 3.9:** Standard deviation field of the Mach number  $\sigma_M$  resulting from an uncertain Mach number  $M$ .

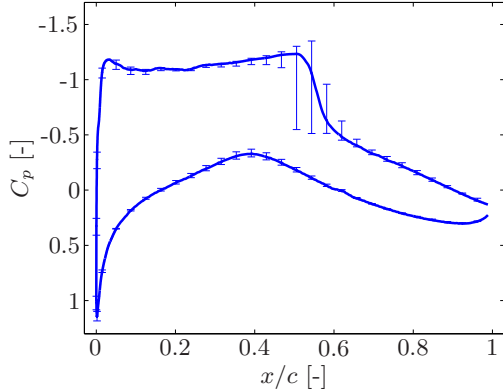


**Figure 3.10:** The pressure coefficient  $C_p$  on the surface of the airfoil with 99% uncertainty bars resulting from an uncertain Mach number  $M$ .

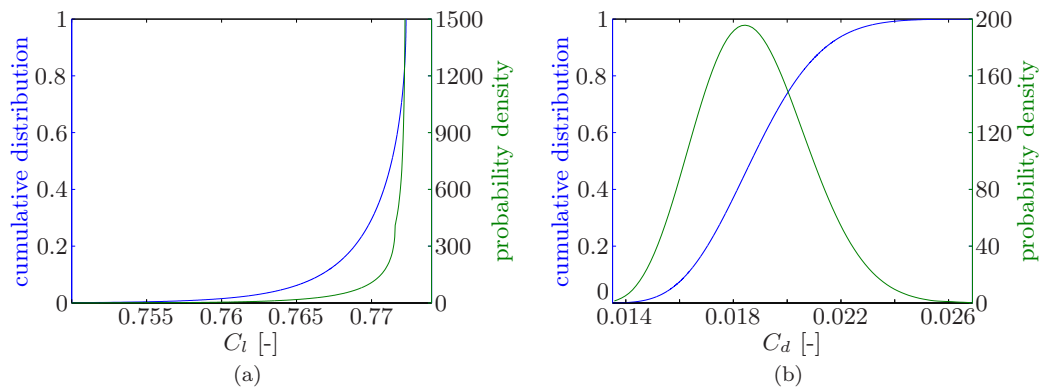
Other outputs of interest are the lift and drag coefficients. Figure 3.11 shows the probability distribution functions of both quantities. The lift (figure 3.11(a)) depends nonlinearly on the Mach number and shows a distribution which is bounded on the upper side. There is a maximum in the response for a certain Mach number. At a higher Mach number, the lift decreases again. The drag, shown in figure 3.11(b), has a positive skewness. Although the input variation of the Mach number is small ( $CV_M = 0.68\%$ ), the variation in the drag coefficient covers a range of 100 drag counts. The mean, standard deviation and the coefficient of variation are summarized at the end of this section in table 3.3. The lift shows a coefficient variation of 0.38%, whereas the drag has a coefficient of variation of 10.64%. For the chosen Mach number, the drag coefficient of the RAE2822 airfoil is highly sensitive to the free stream Mach number. A small uncertainty of 0.68% in the Mach number is amplified to a coefficient of variation of 10.64% for the drag coefficient.

### Uncertain angle of attack

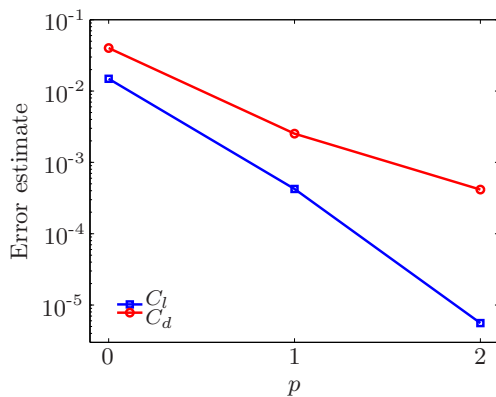
The convergence of the Probabilistic Collocation method with respect to the polynomial chaos order is shown in figure 3.12 for the lift and drag coefficient for an uncertain angle of attack. Again a drop of two to three orders of magnitude are observed between a polynomial order of  $p = 0$  to 2. Further results are for  $p = 2$ , which means 3 deterministic computations have to be performed.

Figure 3.13 shows the standard deviation of the Mach number around the airfoil.

### 3.2 Transonic flow around a RAE2822 airfoil



**Figure 3.11:** The probability density function (—) and the cumulative distribution function (—) of the lift coefficient  $C_l$  (a) and the drag coefficient  $C_d$  (b) resulting from an uncertain Mach number  $M$ .



**Figure 3.12:** Convergence of the Probabilistic Collocation method for the lift coefficient  $C_l$  and drag coefficient  $C_d$  for an uncertain angle of attack  $\alpha$  with respect to the polynomial chaos order  $p$ .

Again a peak of standard deviation is present in the shock area. The variation is about 6% of the free stream Mach number. In the case of an uncertain angle of attack, however, there is also a standard deviation present before the shock. This is more clear in figure 3.14, which shows the pressure coefficient distribution on the surface of the airfoil. Here relatively large uncertainty bars are present in the shock area and on the upper surface before the shock. The shock position moves less than for the case with an uncertain Mach number.

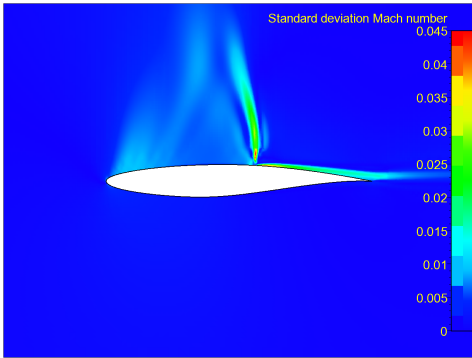


**Figure 3.13:** Standard deviation field of the Mach number  $\sigma_M$  resulting from an uncertain angle of attack  $\alpha$ .

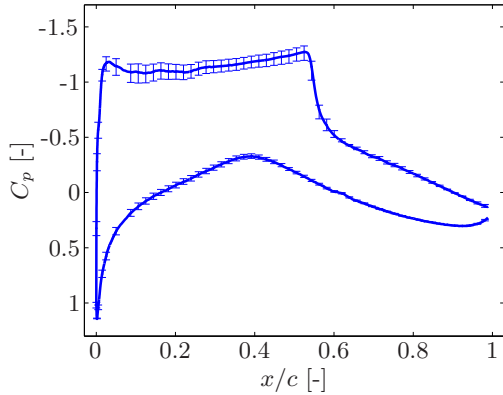


**Figure 3.14:** The pressure coefficient  $C_p$  on the surface of the airfoil with 99% uncertainty bars resulting from an uncertain angle of attack  $\alpha$ .

The lift and drag coefficient show a large variation due to the uncertain angle of attack. Table 3.3 shows coefficients of variation of  $CV_{C_l} = 2.10\%$  and  $CV_{C_d} = 5.62\%$  respectively, resulting from a coefficient of variation of  $\alpha$  of 3.58%. The probability distribution functions in figure 3.15 cover, therefore, a wide range. The shape of the distributions is similar to the truncated normal distribution of the uncertain angle of attack.

### Uncertain relative thickness

The convergence of the Probabilistic Collocation method with respect to the polynomial order are shown in figure 3.16 for the lift and drag coefficient for an uncertain relative thickness. The coefficient of variation of the relative thickness is only 0.5%. For this small variation, the response is nearly linear. This results in a quick drop of the estimated error for  $p = 1$ , and a small decrease of the error for higher orders. To allow second order effects, further results are for  $p = 2$ , which means 3 deterministic computations have to be performed.

The standard deviation of the Mach number is depicted in figure 3.17. The maximum value of the standard deviation is about 9.5% of the free stream Mach number.



### 3.2 Transonic flow around a RAE2822 airfoil

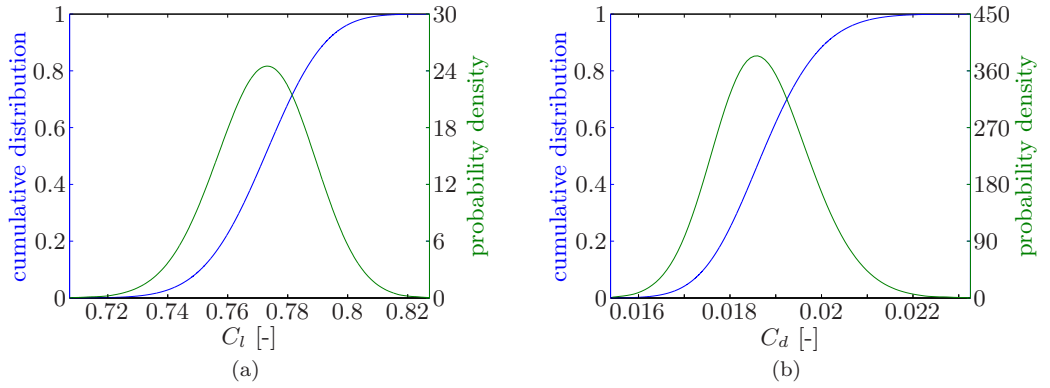


**Figure 3.15:** The probability density function (—) and the cumulative distribution function (—) of the lift coefficient  $C_l$  (a) and the drag coefficient  $C_d$  (b) resulting from an uncertain angle of attack  $\alpha$ .

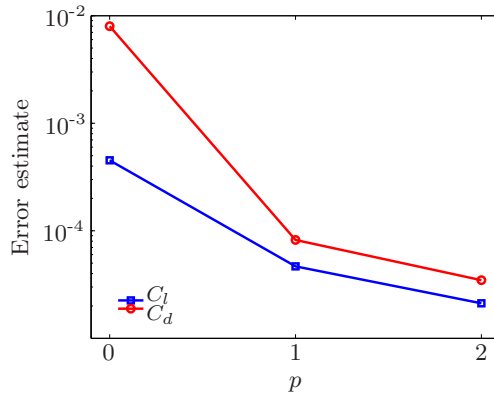


**Figure 3.16:** Convergence of the Probabilistic Collocation method for the lift coefficient  $C_l$  and drag coefficient  $C_d$  for an uncertain relative thickness  $t$  with respect to the polynomial chaos order  $p$ .

### Chapter 3: Flow applications of the Probabilistic Collocation method

Compared with the coefficient of variation of 0.5% for the relative thickness, it is a large amplification of uncertainty. The standard deviation is only concentrated near the shock, as can be seen in figure 3.18. The uncertainty bars of the pressure coefficient on the surface of the airfoil are very small, only near the shock some variation is present.

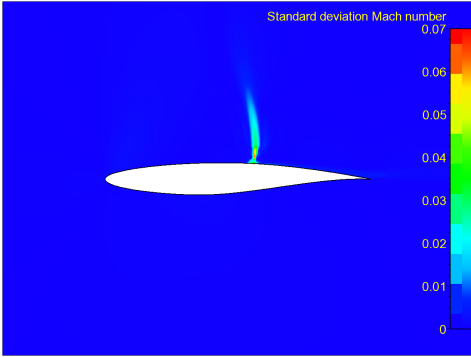


**Figure 3.17:** Standard deviation field of the Mach number  $\sigma_M$  resulting from an uncertain relative thickness  $t$ .

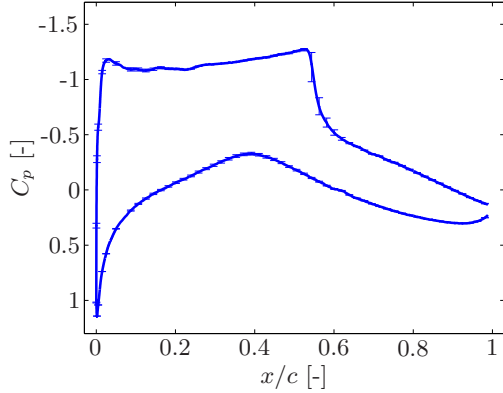


**Figure 3.18:** The pressure coefficient on the surface of the airfoil  $C_p$  with 99% uncertainty bars resulting from an uncertain relative thickness  $t$ .

The small variation can also be seen in the lift and drag coefficients. Table 3.3 shows a coefficient of variation of 0.06% and 1.13% respectively. Compared with the variation of the relative thickness of 0.5%, the variation of the drag coefficient is more than doubled. Figure 3.19 shows some skewness in the distributions, with a small range for the lift coefficient and a significant range for the drag coefficient.

#### Uncertain Mach number, angle of attack, and relative thickness

The convergence of the Probabilistic Collocation method with respect to the polynomial order are shown in figure 3.20 for the lift and drag coefficient. More than two orders decrease of the estimated error was observed for a second order approximation. Further results are for  $p = 2$ , which requires  $(2+1)^3 = 27$  deterministic computations.

The standard deviation of the Mach number around the airfoil is shown in figure 3.21, which is similar to the case of uncertain Mach number (figure 3.9). The uncertain Mach number is the dominating parameter for this output, the effect of the angle of attack and relative thickness are small. From the pressure coefficient on the surface of the airfoil in figure 3.22, a combination of the separate effects can be distinguished. Before the shock, large uncertainty bars are present. This is mainly due to the uncertain angle of attack, as can be seen in figure 3.14. In the shock area, the

### 3.2 Transonic flow around a RAE2822 airfoil

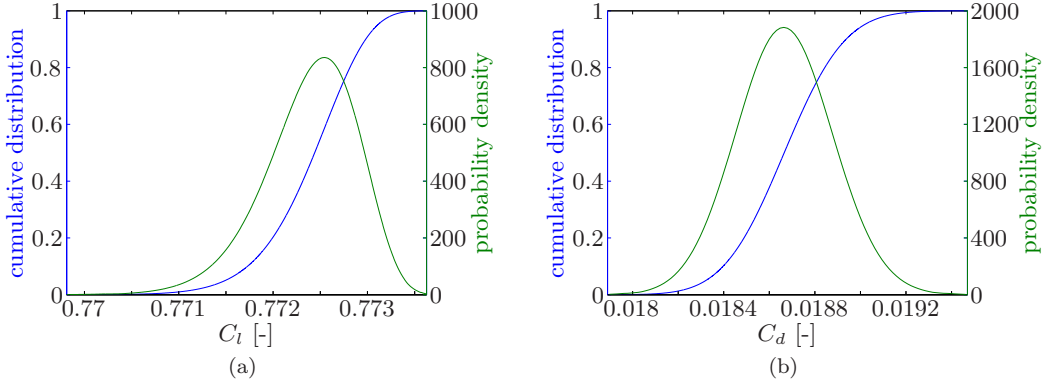


**Figure 3.19:** The probability density function (—) and the cumulative distribution function (—) of the lift coefficient  $C_l$  (a) and the drag coefficient  $C_d$  (b) resulting from an uncertain relative thickness  $t$ .

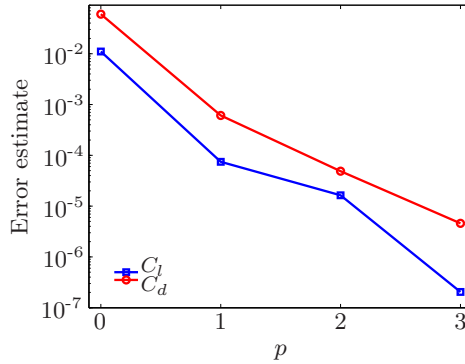


**Figure 3.20:** Convergence of the Probabilistic Collocation method for the lift and drag with respect to the polynomial chaos order  $p$  for an uncertain Mach number  $M$ , angle of attack  $\alpha$ , and relative thickness  $t$ .

uncertainty bars are similar to the case of the uncertain Mach number (figure 3.10). The effect of the relative thickness is not noticeably present.

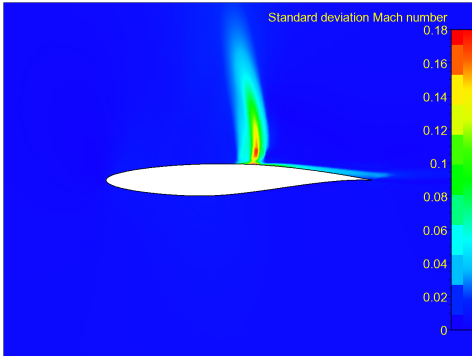


**Figure 3.21:** Standard deviation field of the Mach number  $\sigma_M$  resulting from an uncertain Mach number  $M$ , angle of attack  $\alpha$ , and relative thickness  $t$ .

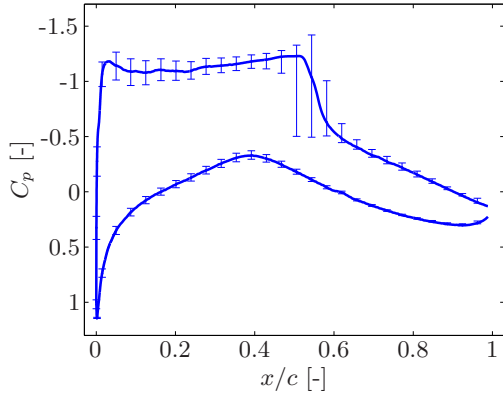


**Figure 3.22:** The pressure coefficient  $C_p$  on the surface of the airfoil with 99% uncertainty bars resulting from an uncertain Mach number  $M$ , angle of attack  $\alpha$ , and relative thickness  $t$ .

The probability distribution functions of the lift and drag coefficients are shown in figure 3.23. The lift coefficient (figure 3.23(a)) is most sensitive to the angle of attack. The probability distribution resulting from all three uncertainties closely resembles the distribution functions of the angle of attack shown in figure 3.15(a). For the drag coefficient (figure 3.23(b)), the Mach number is most important. This probability distribution resulting from all three uncertainties is close to the distribution functions of the Mach number shown in figure 3.11(a).

Table 3.3 summarizes the mean, standard deviation and coefficient of variation of  $C_l$  and  $C_d$ . All uncertain parameters have a negative impact on the performance of the RAE2822 airfoil. The mean drag increases and the mean lift decreases. Furthermore, the flow around the RAE2822 airfoil is highly sensitive to the uncertain parameters. The coefficients of variation of the parameters ranged from 0.5 to 3.58%, for all three uncertain parameter simultaneously this results in a coefficient of variation of 11.96% for  $C_d$ . The coefficient of variation of  $C_d$  is mainly determined by the uncertain  $M$ . For  $C_l$ , the uncertain  $\alpha$  contributes most to the coefficient of variation.

### 3.3 Summary

The Probabilistic Collocation method was applied successfully to two flow applications, subsonic and transonic flow around an airfoil. Since the method is non-intrusive, a commercial CFD solver could be employed.

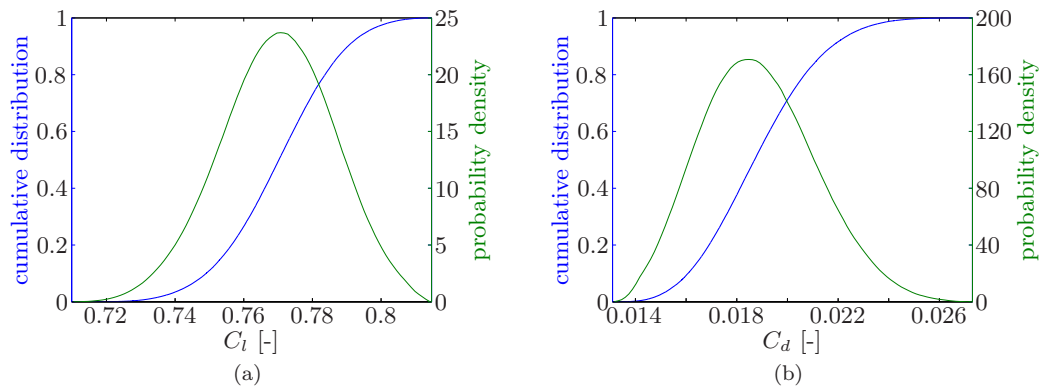


**Figure 3.23:** The probability density function (—) and the cumulative distribution function (—) of the lift coefficient  $C_l$  (a) and the drag coefficient  $C_d$  (b) resulting from an uncertain Mach number  $M$ , angle of attack  $\alpha$ , and relative thickness  $t$ .

**Table 3.3:** Summary of the mean, standard deviation and coefficient of variation of the lift  $C_l$  and drag  $C_d$  coefficients obtained from a second order Probabilistic Collocation approximation.

Uncertainty	$C_l$			$C_d$		
	$\mu$	$\sigma$	$CV$	$\mu$	$\sigma$	$CV$
$M$	0.7702	0.00309	0.40%	0.01877	0.002000	10.65%
$\alpha$	0.7720	0.01624	2.10%	0.01873	0.001048	5.59%
$t$	0.7724	0.00051	0.07%	0.01867	0.000211	1.13%
$M, \alpha, t$	0.7698	0.01652	2.15%	0.01883	0.002252	11.96%
deterministic	0.7724	-	-	0.01866	-	-

### ***Chapter 3: Flow applications of the Probabilistic Collocation method***

The first test case shows subsonic turbulent flow around the NACA0012 airfoil. The free stream Mach number was assumed to be uncertain with a coefficient of variation of 5%. A Monte Carlo simulation using 10,000 Latin Hypercube samples has been performed to validate the Probabilistic Collocation method. Good agreement has been found between the Monte Carlo simulation and a second order Probabilistic Collocation approximation, requiring three deterministic solves. Probability density functions are shown for the lift and drag forces. The coefficients of variation are 10.5% and 9.45% for the lift and drag respectively. This is an amplification of a factor 2 of the coefficient of variation of the uncertain free stream Mach number. The pressure and skin friction on the surface of the airfoil are shown as the mean with uncertainty bars indicating the interval that contains 99% of all possible values. The mean and standard deviation field of the static pressure showed that the flow is most sensitive to the uncertain freestream Mach number near the suction peak at the leading edge.

The second test case was transonic turbulent flow around a RAE2822 airfoil. Uncertainties were present in the free stream Mach number, angle of attack and relative thickness of the airfoil. The uncertainties were propagated first separately to see the effect of each parameter on the solution. Statistics of the lift and drag coefficient were shown, as well as mean and standard deviation of the Mach number in the flow field around the airfoil. Furthermore, the pressure coefficient on the surface of the airfoil was shown as the mean with uncertainty bars indicating the interval that cover 99% of all possible values. Finally, all three uncertainties were propagated simultaneously to include interactions between the parameters. The results show that the flow is most sensitive to uncertainties near the shock wave. The lift coefficient shows a coefficient of variation of 2.15% and the drag coefficient has a coefficient of variation of 11.96%. Especially the drag coefficient turns out to be sensitive, since the coefficients of variation were 0.68%, 3.58%, and 0.5% for the Mach number, angle of attack, and relative thickness respectively. A second order Probabilistic Collocation approximation was used to propagate the uncertain parameters. This required 3 computations for the separate cases and 27 for the simultaneous case.

---

# Modifications of the Probabilistic Collocation method

---

For test cases with a discontinuous response or time dependent test cases for which the response changes with time, the standard Probabilistic Collocation method needs some modification to efficiently propagate uncertainties. Two test cases are shown in this chapter to show the modifications of the Probabilistic Collocation method and the use of them for these test cases.

The first test case considers a stall flutter problem. The model consists of a rigid airfoil attached to a torsional spring. The required aerodynamic moment is obtained from the Onera dynamic stall model [Tran and Petot (1981)]. This case is time dependent and the dynamic stall model contains non-polynomial nonlinearities. Furthermore, the response of the system has a discontinuous second derivative. The application of the Probabilistic Collocation method to the stall flutter case and results can be found in the papers of Loeven, Sarkar, Witteveen and Bijl (2007) and Sarkar et al. (2009). In case of stall flutter, the output of interest is a bifurcation diagram. The goal for this test case is to construct a stochastic bifurcation diagram resulting from an uncertain structural equilibrium angle (through an external moment added to the model). This uncertainty may arise due to differences between the designed wing and the actual product, or due to an unknown deformation under loading. The non-polynomial nonlinearities in the model do not pose a problem to applying the Probabilistic Collocation method. The discontinuous derivative of the response, however, results in a

## Chapter 4: Modifications of the Probabilistic Collocation method

Probabilistic Collocation approximation that oscillates around the reference solution obtained from a Monte Carlo simulation. A multi-element formulation of the Probabilistic Collocation method [Loeven, Sarkar, Witteveen and Bijl (2007); Foo et al. (2008)] is used to accurately approximate the response near the bifurcation point.

The second test case in this chapter considers flow around a circular cylinder at low Reynolds number. The flow reaches a state of period vortex shedding. For the cylinder case, the lift and drag are periodic functions of time. If the standard Probabilistic Collocation method is applied to this test case, an increasing order of approximation has to be used if a constant accuracy is required. This is caused by the fact that the response becomes more nonlinear with time. This problem is solved by utilizing the periodic response of the system. The time series are parameterized by assuming a periodic motion [Witteveen et al. (2007*a,b*, 2008)]. The Probabilistic Collocation method is then applied to the time independent parameters that describe the periodic motion like: mean value, phase, amplitude and frequency. This approach results in a time independent error.

### 4.1 Multi-Element formulation applied to stall flutter

As will be shown later in this section, the response of the stall flutter model has a discontinuous derivative. This is caused by a switch in the model, which activates the stall model above a certain angle of attack. When the standard Probabilistic Collocation method is applied, the reconstructed solutions show oscillations around the reference solution obtained from a Monte Carlo simulation. In order to avoid oscillations a multi-element formulation of the Probabilistic Collocation method is proposed.

#### 4.1.1 Multi-Element Probabilistic Collocation

In case of the Multi-Element Probabilistic Collocation method, each random variable is expanded as [Loeven, Sarkar, Witteveen and Bijl (2007); Foo et al. (2008)]:

$$u(\mathbf{x}, t, \omega) = \sum_{i=1}^{N_e} \sum_{j=1}^{N_p} u_{ij}(\mathbf{x}, t) L_{ij}(\xi_i(\omega)), \quad (4.1)$$

where the solution  $u(\mathbf{x}, t, \omega)$ , a function of space  $\mathbf{x}$  and time  $t$  and the random event  $\omega \in \Omega$ . The expansion is written as a summation over the number of elements  $N_e$  and the number of collocation points in each element  $N_p$ . The complete probability space is given by  $(\Omega, \mathcal{F}, P)$ , with  $\Omega$  the set of outcomes,  $\mathcal{F} \subset 2^\Omega$  the  $\sigma$ -algebra of events and  $P: \mathcal{F} \rightarrow [0, 1]$  a probability measure. Furthermore,  $u_{ij}(\mathbf{x}, t)$  is the solution  $u(\mathbf{x}, t, \omega)$  at the collocation point  $\omega_{ij}$ , which is the collocation point  $j$  in element  $i$ ;  $L_{ij}$  is the Lagrange interpolating polynomial chaos corresponding to the collocation points  $\omega_{ij}$ ;  $\xi_i$  is the basis random variable in element  $i$ .



### 4.1 Multi-Element formulation applied to stall flutter

The procedure to obtain the collocation points and weights is the same as the standard Probabilistic Collocation method, explained in section 2.2. In each element the collocation points are computed based on the weighting function in the element  $w(\xi_i) = f_{\xi_i}(\xi_i)$ . The weighting function  $f_{\xi_i}(\xi_i)$  is set equal to the global weighting function  $f_{\xi}(\xi)$  inside the element  $i$  and is set to zero outside the element. Figure 4.1 shows a lognormal distribution, which is approximated using 4 elements of equal probability. The left figures show how the cumulative distribution function and the probability density function are separated into 4 elements. The right figures show the resulting weighting functions of each element, which are used to compute the collocation points and weights inside the elements.

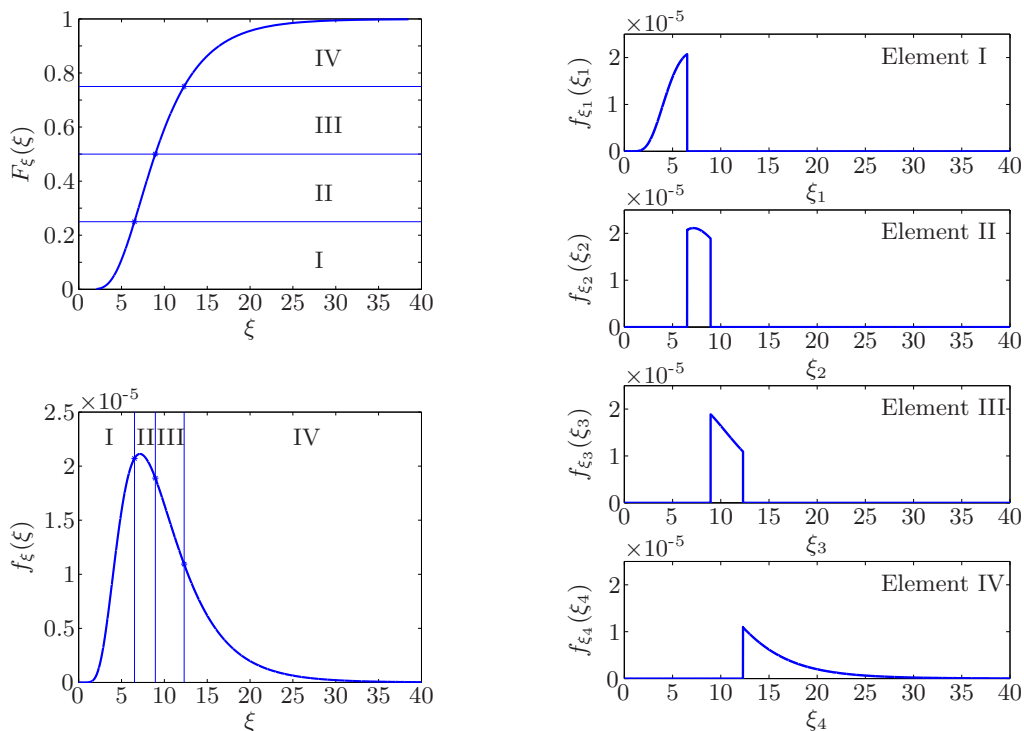


**Figure 4.1:** The cumulative distribution function and probability density function (left) of a lognormal basis with  $\mu=10$  and  $\sigma^2=25$ . On the right the weighting functions in each of the four elements.

#### 4.1.2 Deterministic stall flutter model

In this dynamic stall flutter problem, the aircraft wing or wind turbine blade is modeled as a two dimensional rigid airfoil. A NACA0012 airfoil is attached to a torsional spring and is subjected to the aerodynamic moment obtained from the Onera dynamic stall model [Tran and Petot (1981); Peters (1985); Dunn and Dugundji (1992)]. This

## Chapter 4: Modifications of the Probabilistic Collocation method

is standard practice in engineering aeroelastic problems. The structural model is shown in figure 4.2. The equation of motion for the single degree-of-freedom pitching airfoil is given below [Fung (1955)]:

$$I_\alpha \ddot{\alpha} + I_\alpha \omega_\alpha^2 \alpha + K_{nl1} \alpha^3 = M(t) + M_{ext1}. \quad (4.2)$$

Here,  $\ddot{\alpha}$  indicates a second order derivative with respect to time  $t$ ,  $I_\alpha$  is the wing mass moment of inertia;  $\alpha$  is the pitch angle,  $\omega_\alpha$  the natural frequency of the pitch elastic mode,  $K_{nl1}$  a nonlinear stiffness term accounting for concentrated structural nonlinearities in the torsional direction,  $M(t)$  is the time dependent aerodynamic moment and  $M_{ext1}$  a constant external torque applied to the airfoil. First the equations of motion are made non-dimensional to be able to investigate the effect of system parameters. The non-dimensional equation of motion of the single degree-of-freedom pitching oscillation is given by:

$$\alpha'' + \alpha \frac{1}{U^2} + K_{nl} \alpha^3 = \frac{1C_m}{\pi \mu r_\alpha^2} + M_{ext}, \quad (4.3)$$

where  $''$  denotes the second order derivative with respect to  $\tau = t\bar{V}/b$  the non-dimensional time, with  $\bar{V}$  the free stream velocity,  $b$  is the semi-chord of the blade,  $K_{nl}$  is the non-dimensional form of  $K_{nl1}$ ,  $r_\alpha = I_\alpha/mb^2$  the radius of gyration,  $\mu = m/\pi\rho b^2$  the mass ratio,  $U = \bar{V}/b\omega_\alpha$  the dimensionless free stream velocity,  $C_m$  the aerodynamic moment coefficient depending on  $\tau$  obtained from the dynamic stall model and  $M_{ext}$  is the non-dimensional form of  $M_{ext1}$ . The external torque  $M_{ext}$  is used to give the model a structural equilibrium angle [Price and Keleris (1996)].

The aerodynamic model is the Onera dynamic stall model [Dunn and Dugundji (1992); Peters (1985)] governed by the following set of differential equations

$$C_m = s_m \alpha' + k_{vm} \alpha'' + C_{m1} + C_{m2} \quad (4.4)$$

$$C'_{m1} + \lambda_m C_{m1} = \lambda_m (a_{om} \alpha + \sigma_m \alpha') + \alpha_m (a_{om} \alpha' + \sigma_m \alpha'') \quad (4.5)$$

$$C''_{m2} + 2d\omega C'_{m2} + w^2 (1 + d^2) C_{m2} = -w^2 (1 + d^2) (\Delta C_m | \alpha + e \Delta C'_m | \alpha), \quad (4.6)$$

where  $C_m$  is the aerodynamic moment. The aerodynamic moment is split into two parts: the inviscid circulatory part  $C_{m1}$  and the viscous part  $C_{m2}$ . The other coefficients  $s_m$ ,  $k_{vm}$ ,  $\lambda_m$ ,  $\alpha_m$ ,  $a_{om}$ ,  $\sigma_m$ ,  $d$ ,  $w$  and  $e$  are empirically determined coefficients found by applying parameter identification techniques on experimental data. The values for the coefficients for the NACA0012 airfoil have been obtained from Dunn and Dugundji (1992). The cubic structural stiffness  $K_{nl}$  is set to zero. The function  $\Delta C_m$  is a step function which activates a nonlinear function of  $\alpha$  above the static stall angle of  $12^\circ$  and is linear below the static stall angle.

The dimensionless free stream velocity  $U$  is used as bifurcation parameter for the analysis of this system. The external torque  $M_{ext}$  is set such that the system has an equilibrium pitch angle of  $4^\circ$ . The system is perturbed by an instantaneous pitch angle of  $10^\circ$ . A fourth order explicit Runge-Kutta scheme is used for the time integration.

## 4.1 Multi-Element formulation applied to stall flutter

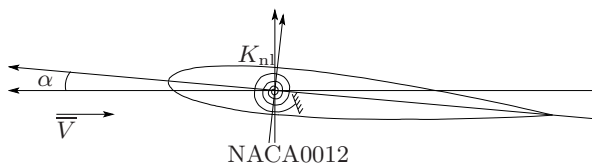


**Figure 4.2:** NACA0012 airfoil with a torsional spring.

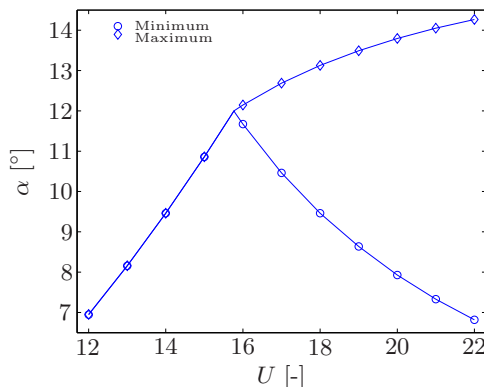


**Figure 4.3:** Deterministic bifurcation plot with the bifurcation point at  $U = 15.765$ .

After a transient part the system is in equilibrium. The deterministic bifurcation plot of the pitch angle for a range of  $U \in [12, 22]$  is shown in figure 4.3. The bifurcation diagram shows the minimum and maximum pitch angles of the time interval  $\tau = 750 - 800$ . This time interval covers at least one period of oscillation and is outside the transient part of the response. The bifurcation plot shows that the supercritical Hopf bifurcation is located at  $U_{\text{bif,det}} = 15.765$ . To the left of the bifurcation point,  $U \in [12, 15.765]$ , are the damped solutions, where the minimum and maximum pitch angles are equal. To the right,  $U \in [15.765, 22]$ , the solutions are period-one oscillations, represented by a different value of the minimum and maximum pitch angle.

Since the choice of the external torque  $M_{\text{ext}}$  has a strong effect on the bifurcation diagram it has to be chosen carefully. Price and Keleris (1996) used values of the order of  $10^{-4}$ . Here the mean  $\mu_{M_{\text{ext}}}$  is set to  $8.3 \times 10^{-4}$ , which corresponds to a structural equilibrium angle of  $4^\circ$ . A lognormal distribution is assumed with a coefficient of variation of  $CV_{M_{\text{ext}}} = 15\%$ .

### 4.1.3 Uncertainty quantification for the dynamic stall flutter problem

This section treats the uncertainty quantification of the dynamic stall flutter problem and leads to a stochastic bifurcation plot and the stochastic properties of the

## Chapter 4: Modifications of the Probabilistic Collocation method

bifurcation point.

The solution of the dynamic stall flutter problem is given as a bifurcation diagram, so the minimum and maximum pitch angles of the asymptotic state of the system are required. For the minimum pitch angle, expansion (4.1) becomes

$$\alpha_{\min}(\tau, \omega) = \sum_{i=1}^{N_e} \sum_{j=1}^{N_p} \alpha_{\min,ij}(\tau) L_{ij}(\xi_i(\omega)), \quad (4.7)$$

with

$$\alpha_{\min,ij} = \min(\alpha_{ij}(\tau)) \quad \text{for the time interval } \tau = [\tau_a, \tau_b], \quad (4.8)$$

where the time interval  $[\tau_a, \tau_b]$  is sufficiently large to contain at least one period of oscillation and is outside the transient part of the response. For the maximum a similar expression is used. Reconstruction of the stochastic properties of the minimum and maximum pitch angles (and thus the bifurcation diagram) is efficient and accurate due to the collocational approach.  $\alpha_{\min}$  and  $\alpha_{\max}$  are functionals of  $\alpha(\tau, \omega)$ . For the Galerkin Polynomial Chaos method the functionals have to be applied to the reconstructed solution  $\alpha(\tau, \omega)$ . Due to the long time integration, an increasing order of approximation needs to be used to maintain the required accuracy [Wan and Karniadakis (2006)]. Another drawback of the Galerkin Polynomial Chaos method for this dynamic stall flutter model is the presence of the nonlinear step function  $\Delta C_m$ . Since the (Multi-Element) Probabilistic Collocation method only requires the output of the model, no problems with the nonlinearity in the stall flutter problem occur [Sarkar et al. (2009)].

The response of the model can be divided into three categories, i.e. all damped solutions, all period-one oscillations and a bifurcated response. The Probabilistic Collocation method is used with one element for the first two response types and with two elements when the system has a bifurcated response. Each of them are discussed in detail below.

### Damped solutions, $U = 12$

The non-dimensional velocity  $U$  is set to 12, such that all responses are damped. For this range the equations are linear, since the pitch angle remains below the static stall angle of  $12^\circ$ . A third order Probabilistic Collocation approximation is used, requiring four deterministic solves. The mean of the pitch angle is  $\mu_\alpha = 6.95^\circ$  with a variance of  $\sigma_\alpha^2 = 3.31 \times 10^{-4}$ , this results in a coefficient of variation of the angle of attack of 15%. Figure 4.4(a) shows that the cumulative distribution function computed by the Probabilistic Collocation method corresponds to a Monte Carlo simulation using 100 uniformly sampled computations. The probability density function is shown in figure 4.4(b). Close agreement between the Monte Carlo simulation and the Probabilistic Collocation method is observed.

#### 4.1 Multi-Element formulation applied to stall flutter

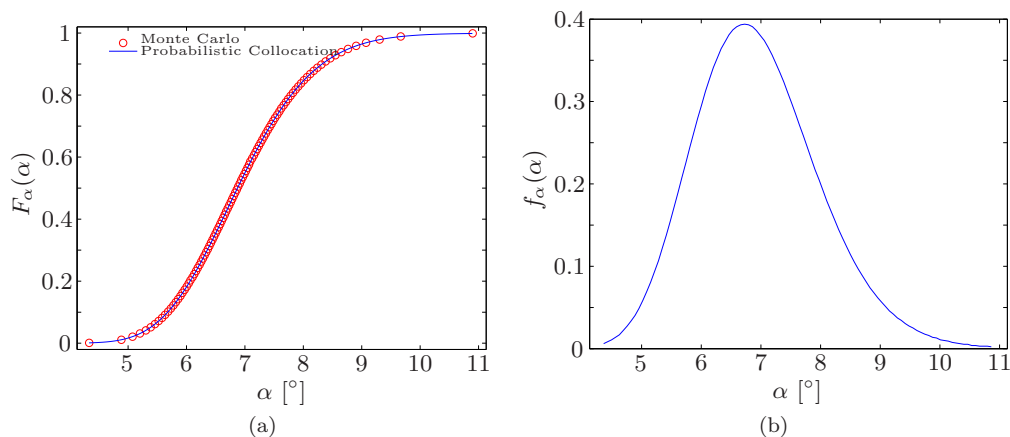


**Figure 4.4:** Distribution functions of the pitch angle  $\alpha$ , (a) the cumulative distribution function  $F_\alpha(\alpha)$  and (b) the probability density function  $f_\alpha(\alpha)$ , resulting from a lognormally distributed external torque  $M_{\text{ext}}$  with  $\mu_{M_{\text{ext}}} = 8.3 \times 10^{-4}$  and  $CV_{M_{\text{ext}}} = 15\%$  for  $U = 12$ .

#### Period-one oscillations, $U = 22$

The next case is a non-dimensional velocity of  $U = 22$ . All realizations result in a period-one oscillation. The system is in the nonlinear regime, since pitch angles above  $12^\circ$  occur, which activate the  $\Delta C_m$  function. Since no bifurcation is present in the response, a single element is sufficient for the Probabilistic Collocation method. The system is nonlinear now, which requires a higher order approximation. A third order approximation is used, so 4 deterministic solves are required. Figures 4.5(a) and 4.5(b) show the distribution functions of the minimum and maximum pitch angles during the oscillation. The mean of the minimum pitch angle is  $\mu_{\alpha, \text{min}} = 6.82^\circ$  with a variance of  $\sigma_\alpha^2 = 7.81 \times 10^{-4}$ , this results in a coefficient of variation of the minimum pitch angle of 23.5%. For the maximum pitch angle the mean is  $\mu_{\alpha, \text{max}} = 14.27^\circ$  with a variance of  $\sigma_\alpha^2 = 1.49 \times 10^{-4}$ , so a coefficient of variation of 4.9% for the maximum angle of attack is obtained. Since the input uncertainty has a coefficient of variation of 15%, it is increased for the minimum and decreased for the maximum pitch angle. The cumulative distribution function, shown in figure 4.5(a), matches the Monte Carlo results obtained from 100 uniformly sampled computations. Figure 4.5(b) shows the probability density function of the minimum and maximum pitch angle. Again a good agreement between the Monte Carlo simulation and the Probabilistic Collocation method is observed.

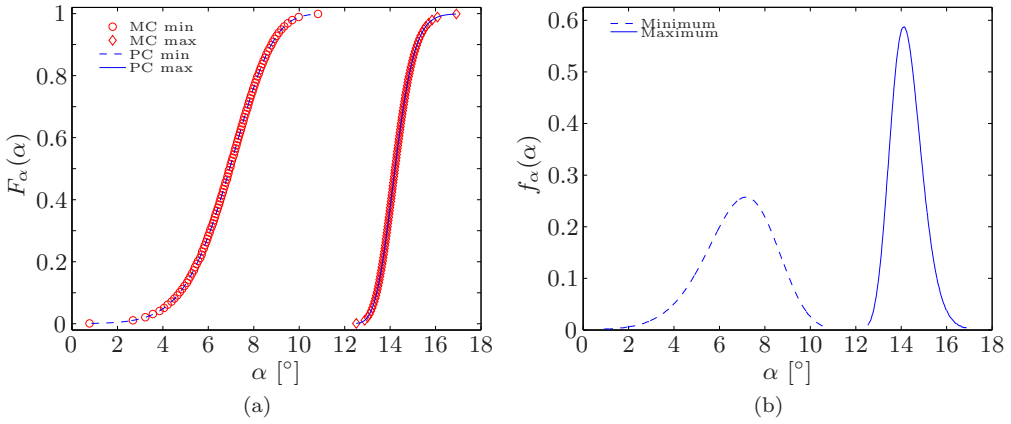


**Figure 4.5:** Distribution functions of the pitch angle  $\alpha$ , (a) the cumulative distribution function  $F_\alpha(\alpha)$  and (b) the probability density function  $f_\alpha(\alpha)$ , resulting from a lognormally distributed external torque  $M_{\text{ext}}$  with  $\mu_{M_{\text{ext}}} = 8.3 \times 10^{-4}$  and  $CV_{M_{\text{ext}}} = 15\%$  for  $U = 22$ .

### Damped solutions and period-one oscillations, $U = 16$

The third case, where  $U = 16$ , has a bifurcated response. The results of a single element computation are shown in figure 4.6. Due to the presence of the bifurcation the global polynomial approximation of the Probabilistic Collocation method oscillates around the response obtained from a Monte Carlo simulation using 100 uniformly sampled computations. For the maximum pitch angle the oscillations are not that severe, since the graph has just a small kink. For the minimum the discontinuous derivative in the bifurcation point results in a non-smooth solution, which cannot be approximated using polynomials. The difference between the Monte Carlo results and the Probabilistic Collocation approximation is more clear in figure 4.6(b). Both cumulative distribution functions deviate from the Monte Carlo results.

### Multi-Element Probabilistic Collocation with search samples

In order to compute cases with a bifurcated response, the number of elements is increased. This results in a piecewise polynomial approximation of the solution. To keep the algorithm as efficient as possible the least amount of elements is used. Two elements suffice for this case, since it was shown that the damped response and the period-one oscillations are approximated separately. One element is used for the approximation of the damped solutions and one for the period-one oscillations. This means that the two elements have to be separated by the bifurcation point. Since the location of the bifurcation point is in general not known in advance a search algorithm is used to find a coarse estimate of the bifurcation point.

## 4.1 Multi-Element formulation applied to stall flutter

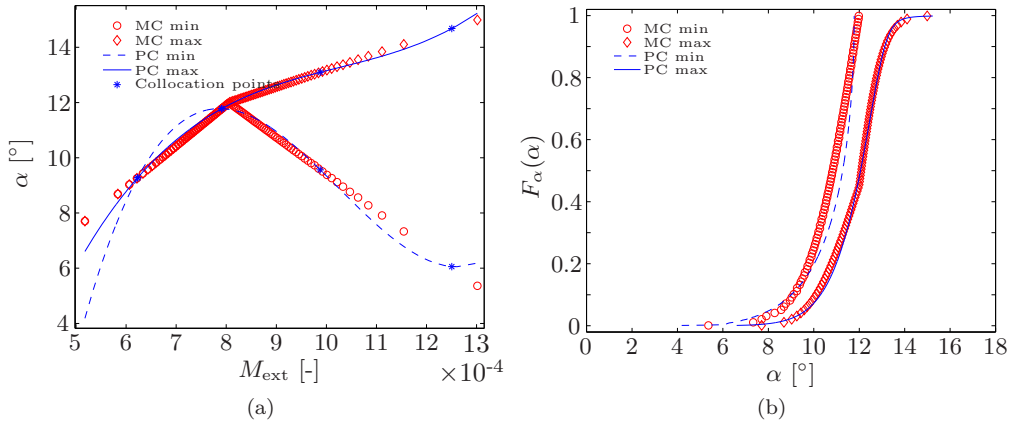


**Figure 4.6:** The approximated response (a) of the pitch angle using the Probabilistic Collocation method and the resulting cumulative distribution functions (b), resulting from a lognormally distributed external torque  $M_{\text{ext}}$  with  $\mu_{M_{\text{ext}}} = 8.3 \times 10^{-4}$  and  $CV_{M_{\text{ext}}} = 15\%$  for  $U = 16$ .

Another option is to use refinement of the elements [Foo et al. (2008)] to capture the bifurcation point. Refining an element, requires redistributing the collocation points. The collocation points that are already evaluated are not used anymore. For this test case, search samples are believed to be more efficient than a refinement strategy since the case is one dimensional.

Recently, the Adaptive Stochastic Finite Elements [Witteveen et al. (2009)] approach was developed. Since it is based on Newton-Cotes quadrature, the collocation points of the coarse approximation are also present in the refined approximation. This means that every evaluation of the model is used for the stochastic computation. However, no spectral convergence is obtained.

### Search samples

First two samples at  $\omega = 0.001$  and  $0.999$  were used to determine if the bifurcation is present. If there is a bifurcation, then a search algorithm is started. Figure 4.7(a) shows the search samples used for the case with  $U = 16$ . The search samples are numbered to show how the search is performed. The search algorithm subsequently halves the part of the parameter domain that contains the bifurcation. The third sample will be chosen in the middle of the parameter domain and so forth. The search is stopped when the amplitude of the period-one oscillation of the new point is below a threshold, here set to 0.2 degrees pitch angle. The value of 0.2 was empirically found to produce accurate results efficiently. Finally, one additional sample is added for more robustness and accuracy of estimating the bifurcation point. This extra

## Chapter 4: Modifications of the Probabilistic Collocation method

sample is located between the third sample, in the middle of the domain and the boundary sample which has the same type of response. The final sample, number 6, here is chosen halfway between sample 3 and 2, since they result both in a period-one oscillation.

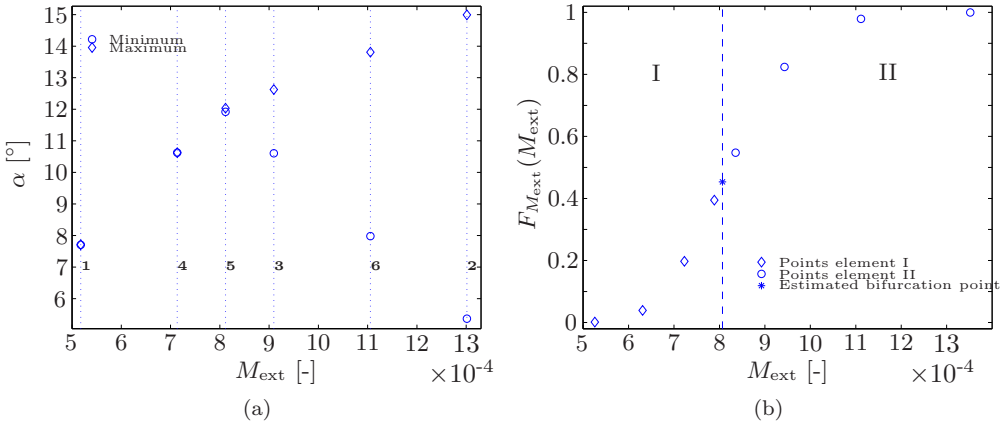


**Figure 4.7:** The figures show (a) the search samples in the response domain and (b) the collocation points of element I( $\circ$ ) and II( $\diamond$ ) based on the estimated bifurcation point( $*$ ).

### Bifurcated response with Multi-Element Probabilistic Collocation

Figure 4.8 shows the new results for the distribution functions for a non-dimensional velocity  $U$  of 16. Again a 3<sup>rd</sup> order approximation is obtained using two elements both of order 3. For this case a total of 14 samples is used, 6 search samples and 4 samples per element for a 3<sup>rd</sup> order approximation. So the increase in robustness of this approach is worth the effort, since 14 samples are sufficient to coincide with the Monte Carlo simulation using 100 uniformly sampled computations. The mean of the minimum pitch angle is  $\mu_{\alpha, \min} = 10.62^\circ$  with a variation of  $\sigma_{\alpha, \min}^2 = 3.38 \times 10^{-4}$ , and for the maximum  $\mu_{\alpha, \max} = 11.82^\circ$  and  $\sigma_{\alpha, \max}^2 = 4.14 \times 10^{-4}$ . Both have a coefficient of variation of 9.9%, so the input uncertainty is damped in the output.

### Bifurcation plot with uncertainty bars

The previous section shows that the framework of search samples in combination with the Probabilistic Collocation method (using one or two elements) produces accurate results for all three possible response types. Now the framework can be applied to the stall flutter model to construct the stochastic bifurcation plot. Figure 4.9 shows the bifurcation plot with uncertainty bars arising from an uncertain external torque  $M_{\text{ext}}$ .



#### 4.1 Multi-Element formulation applied to stall flutter

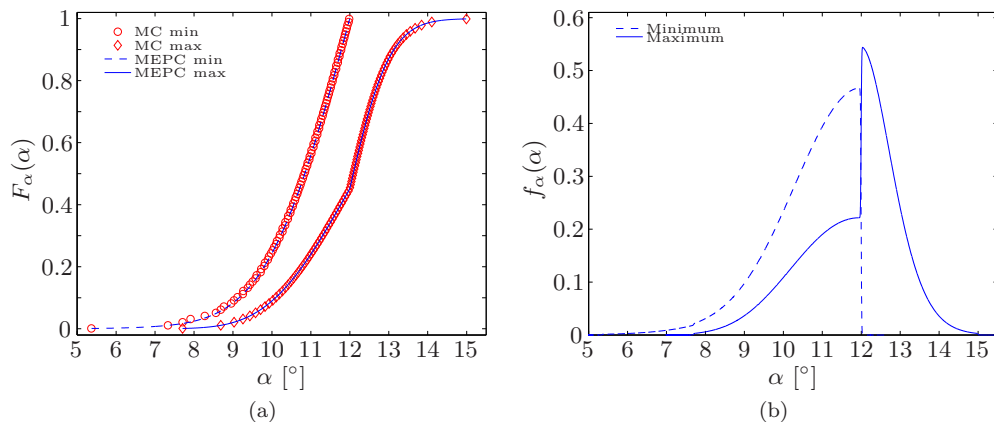


**Figure 4.8:** The distribution functions of the minimum and maximum angle of attack  $\alpha$ , (a) the cumulative distribution function  $F_\alpha(\alpha)$  and (b) the probability density function  $f_\alpha(\alpha)$ , resulting from a lognormally distributed external torque  $M_{\text{ext}}$  with  $\mu_{M_{\text{ext}}} = 8.3 \times 10^{-4}$  and  $CV_{M_{\text{ext}}} = 15\%$  for  $U = 16$ .

A total of 120 deterministic solves is used for the complete computation, including the search samples. The uncertainty bars show the intervals which contain 99.8% of all possible solutions, obtained from the distribution function of the minimum and maximum pitch angles. It can be seen that away from the region around the bifurcation point the mean is close to the deterministic computation. Since the bifurcation point has become a random variable, the mean shows no bifurcation point anymore. The graphs of the mean of the minimum and maximum pitch angle smoothly separate. The uncertainty bars, however, are very large indicating that the solution is sensitive to variations in the external torque. At velocities above the bifurcation point, the uncertainty bars of the minimum pitch angle covers an area which is larger than the mean value.

#### Stochastic properties of the bifurcation point

For engineers the bifurcation point and the influence of uncertainties on the bifurcation point is of great importance, since flutter can lead to failure of the structure. Due to the uncertain external torque the bifurcation point becomes a random variable as well. The mean is  $\mu_{U_{\text{bif}}} = 15.87$ , with a variance of  $\sigma_{U_{\text{bif}}}^2 = 1.37$  which results in a coefficient of variation of 7.4%. Figure 4.10 shows the cumulative distribution function and the probability density function of the bifurcation point. The deterministic value was  $U_{\text{bif}} = 15.765$ . Suppose 1% probability of flutter is acceptable, the bifurcation points becomes  $U_{\text{bif},1\%} = 13.34$ , which is 15.4% lower than the deterministic value. It is, therefore, of great importance to take uncertainty quantification into account in flutter computations.

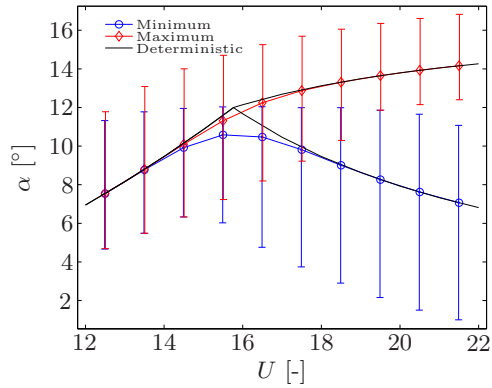


**Figure 4.9:** Stochastic bifurcation diagram with uncertain  $M_{\text{ext}}$ . Uncertainty bars show the interval that contains 99.8% of all possible values. The deterministic bifurcation diagram is shown by the solid black line.

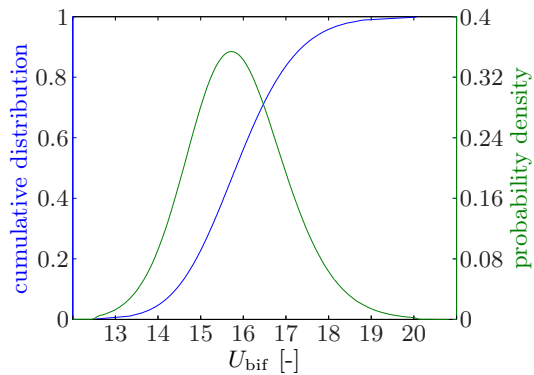


**Figure 4.10:** The probability density function (—) and the cumulative distribution function (—) of the bifurcation point  $U_{\text{bif}}$  resulting from an uncertain external torque  $M_{\text{ext}}$ .

## 4.2 Unsteady flow around a cylinder

This section demonstrates the application of the Probabilistic Collocation method to an unsteady flow problem. The case is a low Reynolds number flow around a cylinder. The incompressible laminar Navier-Stokes equations are solved using the OpenFOAM<sup>®</sup> incompressible solver on a structured grid. The mean Reynolds number is 150, which is well in the laminar regime. If the standard Probabilistic Collocation method would have been applied to this time dependent problem, the approximation will become less accurate after some time [Wan and Karniadakis (2006); Witteveen et al. (2008)]. The cylinder case results in a periodic solution. This is utilized by parameterizing the solution using 4 time-independent parameters to describe the period solution. This results in an efficient Probabilistic Collocation approximation with constant accuracy in time.

### 4.2.1 Probabilistic Collocation method for period-1 oscillations

As was seen in the stall flutter case, the Probabilistic Collocation method is successful in obtaining the statistics of output functionals. For periodic motions like vortex shedding behind a cylinder, a set of time-independent parameters can be defined which describe the unsteady behavior. Assuming the lift coefficient of the cylinder is governed by a cosine type period-1 oscillation, the lift coefficient can then be parameterized by:

$$C_l(t) = C_{l_0} + A_{C_l} \cos(2\pi f_{C_l} t + \Phi_{C_l}), \quad (4.9)$$

resulting in four parameters, i.e. the mean value  $C_{l_0}$ , the amplitude  $A_{C_l}$ , the frequency  $f_{C_l}$ , and the phase  $\Phi_{C_l}$ . These parameters will be the output functionals of interest from the deterministic solves for each collocation point. For the cylinder case a cosine type oscillation is assumed, but equation (4.9) can be generalized for any period shape (see [Witteveen et al. (2008)]).

In case of an uncertainty in the system, the lift coefficient becomes a random variable, of which the distribution changes in time. This means that the parameters in equation (4.9) become random variables as well. Equation (4.9) becomes:

$$C_l(t, \omega) = C_{l,0}(\omega) + A_{C_l}(\omega) \cos(2\pi f_{C_l}(\omega)t + \Phi_{C_l}(\omega)), \quad (4.10)$$

where  $\omega$  indicates a random event. The Probabilistic Collocation expansion (2.10) is applied to each parameter. For example the amplitude is expanded as

$$A_{C_l}(\omega) = \sum_{i=1}^{N_p} A_{C_{l,i}} L_i(\xi(\omega)), \quad (4.11)$$

where  $A_{C_{l,i}}$  is the amplitude of the lift coefficient and  $L_i$  is the Lagrange polynomial for collocation point  $i$ , and  $\xi(\omega)$  is the basis random variable, which is a linear combination of the uncertain parameter in the problem.

## Chapter 4: Modifications of the Probabilistic Collocation method

Summarizing, the procedure can be split into the following steps:

1. Determine the collocation points as done for the standard Probabilistic Collocation method (see chapter 2).
2. Run the deterministic solver for each collocation point.
3. Determine  $C_{l,0,i}$ ,  $A_{C_{l,i}}$ ,  $f_{C_{l,i}}$ , and  $\Phi_{C_{l,i}}$  from the lift coefficient time history for each collocation point.
4. Reconstruct the distribution functions  $C_{l,0}(\omega)$ ,  $A_{C_l}(\omega)$ ,  $f_{C_l}(\omega)$ , and  $\Phi_{C_l}(\omega)$  using equation (4.11).
5. Use the distributions from step 4 to reconstruct  $C_l(t, \omega)$  using equation (4.10).

Since this parameterization only holds for a periodic response, the transient behavior of the system is not captured well. The standard Probabilistic Collocation method, however, is able to capture the transient part, but breaks down at a later time. In order to reconstruct the entire history of the lift and drag coefficient, the approach of Witteveen et al. (2007b) is followed. First standard Probabilistic Collocation is applied until a periodic response is obtained. From that point in time the Probabilistic Collocation method for period-1 oscillations using equation (4.10) is used.

This approach has later been extended by Witteveen et al. (2007a) to be able to handle damped responses and multiperiod time series. Recently, a multi-frequency formulation using a wavelet decomposition was developed by Witteveen and Bijl (2009). More information on uncertainty propagation for unsteady problems can be found in the PhD thesis of Witteveen (2009).

### 4.2.2 Deterministic solution

The case is a cylinder in a laminar flow. Vortex shedding will occur, resulting in a periodically changing lift and drag with time. The total grid size is approximately 130,000 cells for which the layout is shown in figure 4.11(a). A zoom is shown in figure 4.11(b) where it can be seen that the grid is body conformal close to the cylinder.

The flow is set to a Reynolds number of  $Re=150$ . This flow regime is in the laminar parallel shedding range. The incompressible laminar Navier-Stokes equations are solved using the OpenFOAM<sup>®</sup> solver. An instantaneous deterministic vorticity plot with pressure contours at  $t=100$  is shown in figure 4.12. It shows the fully developed Von-Karman vortex street behind the cylinder.

The fully developed state of the flow is periodic vortex shedding. This results in a periodic response of the lift and drag coefficient. The periodic response is shown in figure 4.13(a) for the lift coefficient and in 4.13(b) for the drag coefficient, the corresponding  $C_d-C_l$  plot is given in figure 4.14. For the deterministic simulations a

## 4.2 Unsteady flow around a cylinder

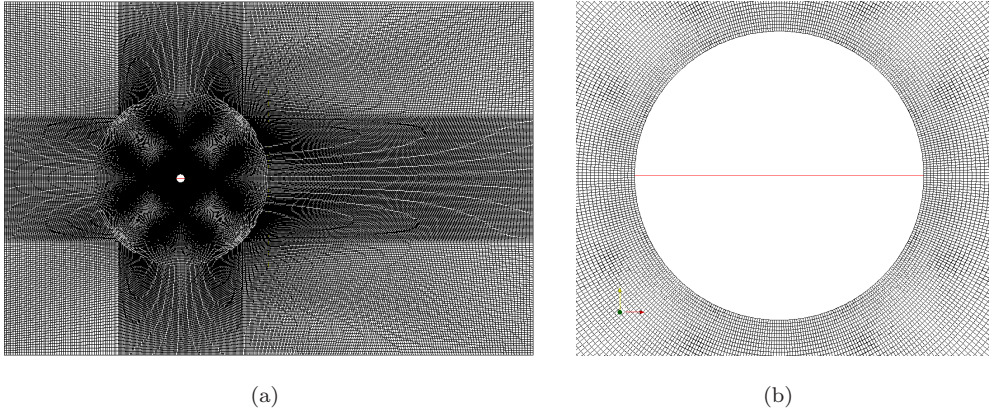


**Figure 4.11:** The total grid layout (a) and a zoom on the geometry (b).



**Figure 4.12:** Instantaneous deterministic vorticity plot at  $t=100$ .

## Chapter 4: Modifications of the Probabilistic Collocation method

periodic response is obtained after  $t=80$ . Some additional periods have been computed till  $t=100$ , as can be seen in figure 4.13.

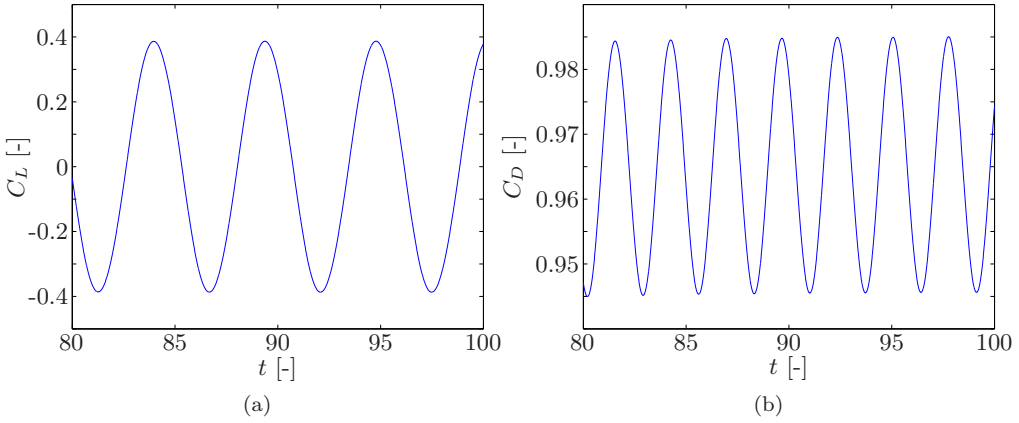


**Figure 4.13:** Period response (a) lift and (b) drag.

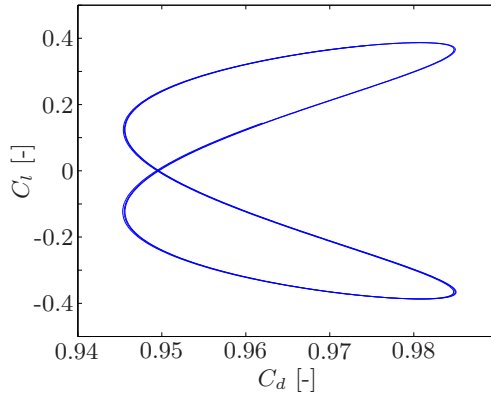


**Figure 4.14:**  $C_d$ - $C_l$  plot of the periodic motion.

The periodic response is characterized by the Strouhal number, given by:

$$Sr = \frac{f_{C_l} D}{U}, \quad (4.12)$$

where  $f_{C_l}$  the frequency of the lift coefficient  $C_l$ ,  $D$  the diameter of the cylinder, and  $U$  the free stream velocity. In the flow solver  $D$  and  $U$  are set to 1, so for this case the Strouhal number is equal to the frequency of the lift coefficient. For  $Re = 150$  (i.e.  $\nu = 1/Re = 6.667 \times 10^{-3}$ ) the Strouhal number is  $Sr = 0.18497$ , which corresponds well with literature [Williamson and Brown (1998)].

## 4.2 Unsteady flow around a cylinder

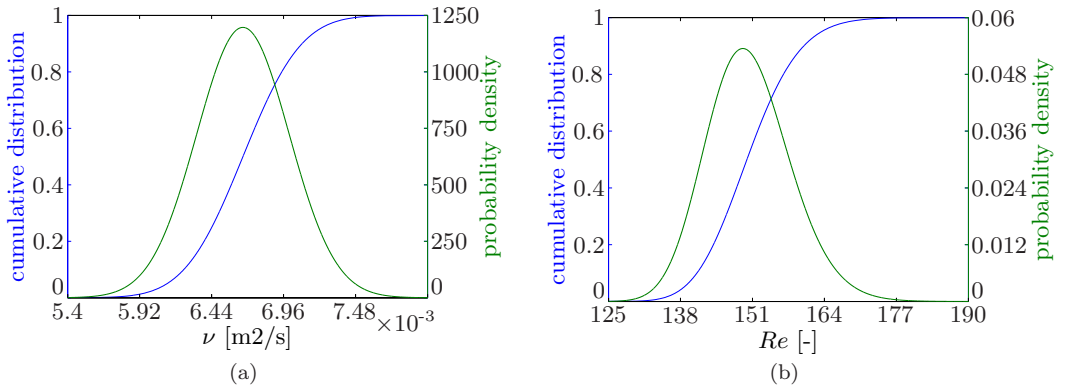


**Figure 4.15:** Input distribution of the (a) kinematic viscosity and (b) the resulting distribution of the Reynolds number

### 4.2.3 Stochastic analysis

The uncertain parameter chosen is the kinematic viscosity  $\nu$ . Hereby, the Reynolds number becomes uncertain, which affects the vortex shedding. A Gaussian input distribution is assumed with a coefficient of variation  $CV_\nu = \sigma_\nu/\mu_\nu$  of 5%. Figure 4.15(a) shows the (Gaussian) input distribution of the kinematic viscosity. The resulting distribution of the Reynolds number is shown in figure 4.15(b).

### 4.2.4 Stochastic results

The uncertain kinematic viscosity is propagated using the Probabilistic Collocation method of order  $p=2, 3, 4, 5$ , and 10. The low orders  $p = 2$  till 5 are to check convergence of the Probabilistic Collocation method, whereas the tenth order is computed to obtain a reference solution. The results show that, except for  $\Phi_{C_d}$  and  $C_{d,0}$ , the response is close to linear. However, for  $\Phi_{C_d}$  and  $C_{d,0}$  a fourth order approximation was required. No difference between the fourth and higher orders are observed. Therefore, a fourth order approximation is used for the computations. Figure 4.16 shows the 99% region of the  $C_d$ - $C_l$  graph for  $p=4$ . This means that with the given input distribution 99% of all possible results will be inside this region.

The time-independent parameters describing the period motion of the lift and drag coefficient are extracted for each collocation point from the interval  $t \in [80,100]$  (see figure 4.13). The mean Strouhal number is  $\mu_{Sr}=0.1850$  based on the input distribution for  $\mu$ , which is slightly higher than the deterministic value of 0.18497. The probability distribution of the Strouhal number is shown in figure 4.17(b). Other parameters that describe the periodic motion of  $C_l$  and  $C_d$  are given in figures 4.17 and 4.18, which are the amplitude  $A_{C_l}/A_{C_d}$ , the frequency  $f_{C_d}/f_{C_l}$ , the phase  $\Phi_{C_l}/\Phi_{C_d}$ , and the mean value  $C_{d,0}$ . The mean value of  $C_l$  is zero for all realizations. Except for  $\Phi_{C_d}$

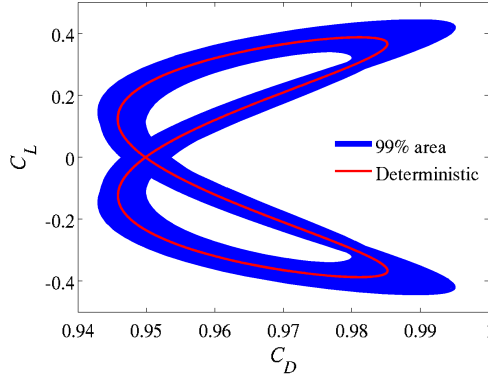


Figure 4.16: Stochastic results:  $C_d$ - $C_l$  graph with 99% interval.

and  $C_{d,0}$  all responses are almost linear, the distribution functions are close to the Gaussian distribution of  $\nu$ . The distribution functions of  $\Phi_{C_d}$  and  $C_{d,0}$  are not close to a Gaussian distribution anymore.

Table 4.1 shows the deterministic values, mean values, standard deviations, coefficients of variation and the amplification factors of each parameter. The uncertain kinematic viscosity has a coefficient of variation of 5%. Interesting to see is how the system amplifies or damps this input variation. As a measure the amplification factor  $\Psi$  is defined as:

$$\Psi = \frac{CV_{out}}{CV_{in}}. \quad (4.13)$$

Where in this case  $CV_{in} = CV_{\nu}$ . An amplification factor much smaller than 1 indicates that the output is not sensitive to variations in the input parameter, which is the case for the frequencies  $Sr$  and  $f_{C_d}$  and the mean value of the drag coefficient  $C_{d,0}$ . From table 4.1 it is clear that an uncertain  $\nu$  or  $Re$  mainly results in strong variations in the amplitude and phase of both  $C_l$  and  $C_d$ .

With the results from figure 4.17 and figure 4.18, the time series of the lift and drag coefficient can be reconstructed using equation (4.10). From the reconstructed distribution, the mean and standard deviation are obtained.

As shown in figure 4.13, the coefficients are periodic from  $t=80$ . The parameters describing the periodic motion are obtained from the time interval  $t \in [80,100]$ . The mean and standard deviation show a transient stochastic behavior and reach a limit state. To obtain the stochastic results until  $t=300$ , it is not necessary to run the deterministic simulations until that time. Since the parameters of the periodic response are already known, the results can easily be extrapolated by evaluation equation (4.9) till  $t=300$ . As can be seen in figures 4.19 and 4.20, all results reach a steady value when  $t$  increases.



## 4.2 Unsteady flow around a cylinder

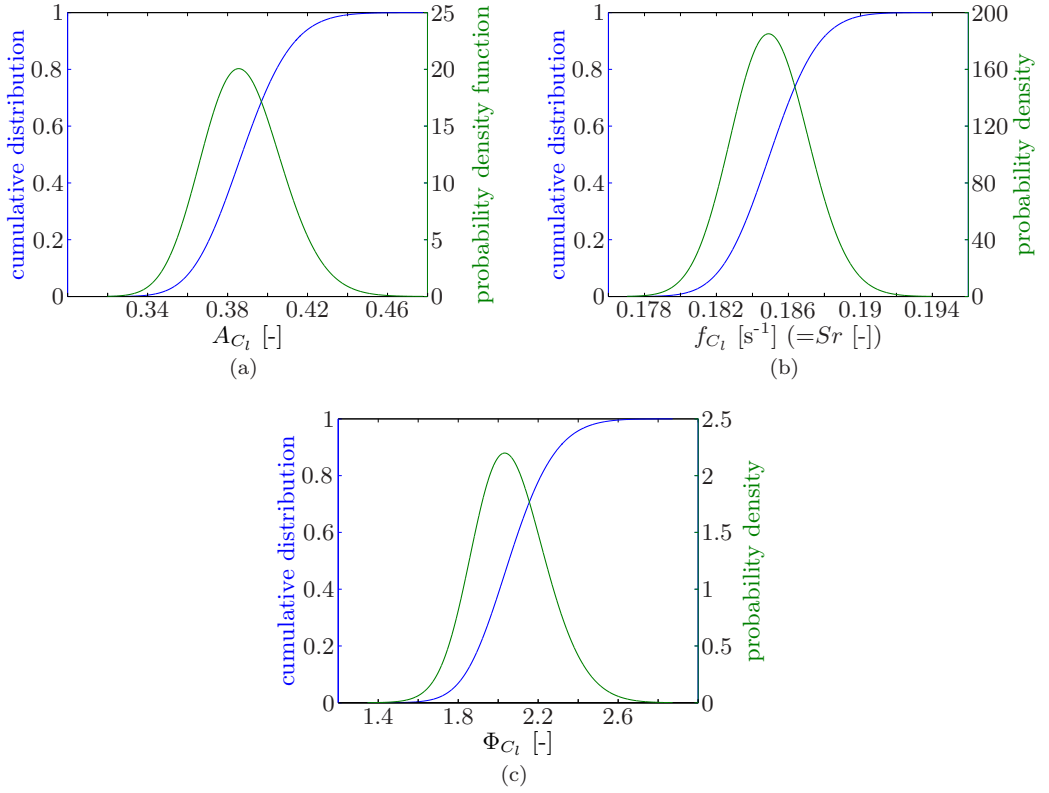


**Figure 4.17:** Parameters that describe the periodic motion of  $C_l$

**Table 4.1:** Mean  $\mu$ , standard deviation  $\sigma$ , coefficient of variation  $CV$  and amplification factor  $\Upsilon$  of functional outputs of  $C_l$  and  $C_d$ .

Quantity	Deterministic value	Mean $\mu$	Standard deviation $\sigma$	Coeff. of var. $CV$	Amp. fac. $\Upsilon$
$A_{C_l}$	0.3871	0.3878	0.02004	5.17%	1.034
$Sr$	0.1849	0.1850	0.00216	1.17%	0.234
$\Phi_{C_l}$	2.0533	2.0625	0.18567	9%	1.8
$A_{C_d}$	0.0198	0.0199	0.002114	10.6%	2.12
$f_{C_d}$	0.3697	0.3699	0.004397	1.19%	0.238
$\Phi_{C_d}$	3.5942	3.5008	0.43599	12.45%	2.49
$C_{d,0}$	0.9654	0.9657	0.0008271	0.0856%	0.0171

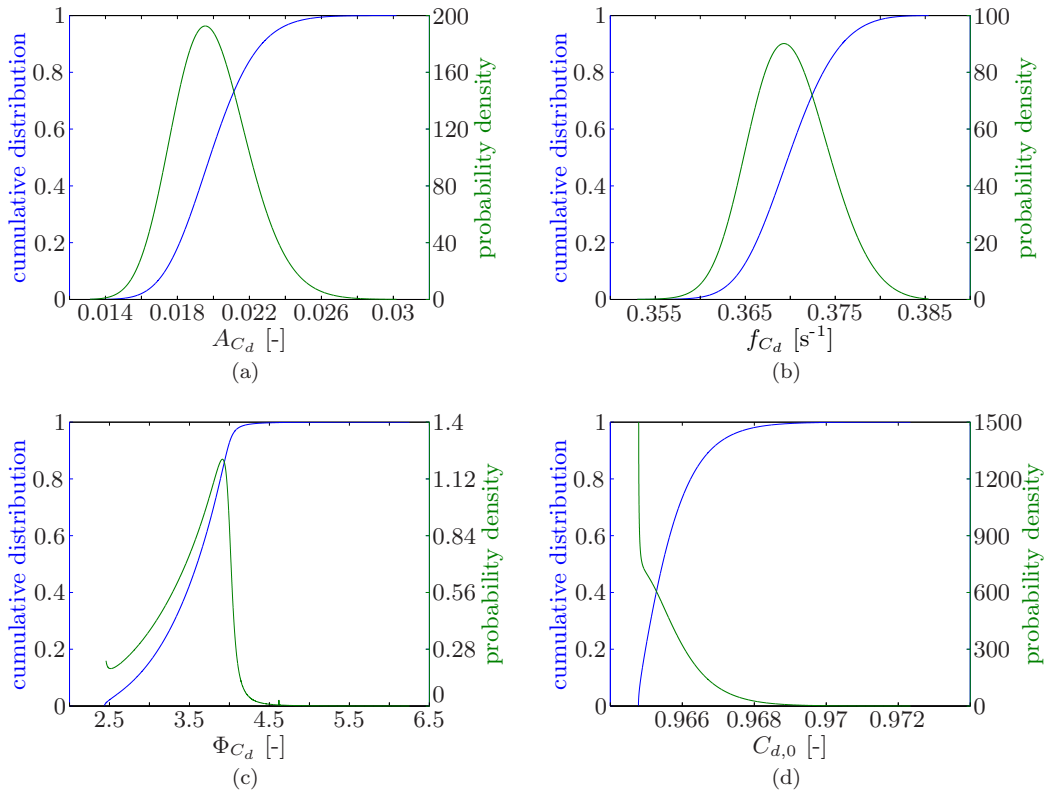


Figure 4.18: Parameters that describe the periodic motion of  $C_d$

In the figures two lines are shown. First the dashed red line indicates the standard Probabilistic Collocation results. For the transient part, the results are good. However, after a certain time, the standard Probabilistic Collocation approximation breaks down. Increasing the order delays this effect only slightly. The blue line shows the final solution, which consists of the standard Probabilistic Collocation approximation for the transient part and the Probabilistic Collocation for period-1 oscillations for the periodic part. This approach is similar as the approach of Witteveen et al. (2007b), where good agreement with Monte Carlo simulation is shown.

Figure 4.19 shows the time series for the mean and standard deviation of the lift coefficient. The mean damps out to a value of  $\mu_{C_l}=0$ , which is the same as the mean of the mean value  $\mu_{C_{l,0}}$ . The value of  $C_{l,0}$  is 0 for all collocation points. The standard deviation goes to a limit state of  $\sigma_{C_l}=0.2746$ .

The results for the drag coefficient are shown in figure 4.20. In the limit, the mean goes to  $\mu_{C_d}=0.9657$ , which is exactly the same as the mean of the mean value  $\mu_{C_{d,0}}$ . The response of the standard deviation of the drag coefficient (see figure 4.20(b)) is not behaving smoothly. The switch between the standard Probabilistic Collocation and the period-1 formulation is clearly visible. It has been checked that the time series for each collocation point reaches a periodic motion, so the period-1 Probabilistic Collocation formulation is valid here. The standard deviation reaches a value of  $\sigma_{C_d}=0.0142$ .

Apart from the mean and standard deviation, also the probability distribution reaches a limit state. The result is shown in figure 4.21. These histograms show a typical picture of a cosine response with a phase and frequency shift between the collocation points. Highest probabilities occur near the edges, while the mean has a low probability to occur.

### 4.3 Summary

For test cases with a discontinuous response or time dependent test cases for which the response changes with time, the standard Probabilistic Collocation method cannot readily be applied. With some minor modifications, it is possible to efficiently propagate uncertainties in such cases.

First a stall flutter problem was shown where the model contains a (nonpolynomial) nonlinearity. Furthermore, the output of interest is the minimum and maximum pitch angle of the airfoil in the limit state. Due to the nonlinearity in the model and this specific output of interest, the intrusive Galerkin Polynomial Chaos method cannot be applied efficiently to this test case. The response of the model was divided into three parts. The first part where all solutions are damped. The second part contains a bifurcation point. Some solutions are damped, while other show a limit cycle oscillation. An thirdly, the part were all solution result in a limit cycle oscillation. The Probabilistic Collocation method shows no problem with approximations in the first and third part. When the bifurcation is present, the approximation fails. For this

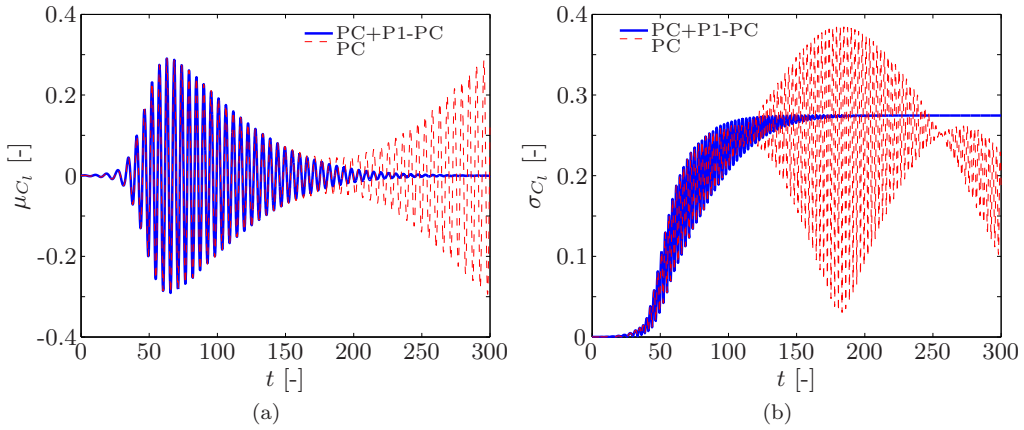


**Figure 4.19:** Time series of the mean  $\mu_{C_l}$  and the standard deviation  $\sigma_{C_l}$  of the lift coefficient. The blue line (—) indicates the final solution based on standard Probabilistic Collocation for the transient part and Probabilistic Collocation for period-1 oscillations for the periodic part. The dashed red line (- -) indicates the standard Probabilistic Collocation method. A fourth order approximation is used, requiring 5 deterministic solves.

case a multi-element formulation in combination with search samples was successfully applied. The result was a stochastic bifurcation plot, which showed the mean of the minimum and maximum pitch angle with uncertainty bars indication 99.8% of all possible values. Furthermore, the probability distribution of the bifurcation point was found.

The second test case was a low Reynolds number flow around a cylinder. The Reynolds number is assumed to be uncertain, to investigate the effect on the response of the lift and drag coefficient. In this case the response surface becomes more nonlinear in time. This is caused by a frequency difference in the solution due to the presence of the uncertain parameter. This requires an increasing polynomial chaos order to maintain the same accuracy. If the unsteady simulation results in a period-1 oscillation, the Probabilistic Collocation method should be applied to time independent parameters that describe the oscillatory response. These parameters are the amplitude, mean value, period and phase. The result is a time independent accuracy, so a constant polynomial chaos order can be used regardless of the simulation time. The period-1 Probabilistic Collocation approach was successfully applied to vortex shedding from a circular cylinder. It was shown that the frequency and mean value are insensitive to variation of the Reynolds number. On the other hand, the amplitude and the phase are highly sensitive to the Reynolds number, the input uncertainty of 5% was amplified to an output uncertainty in the order of 10%.

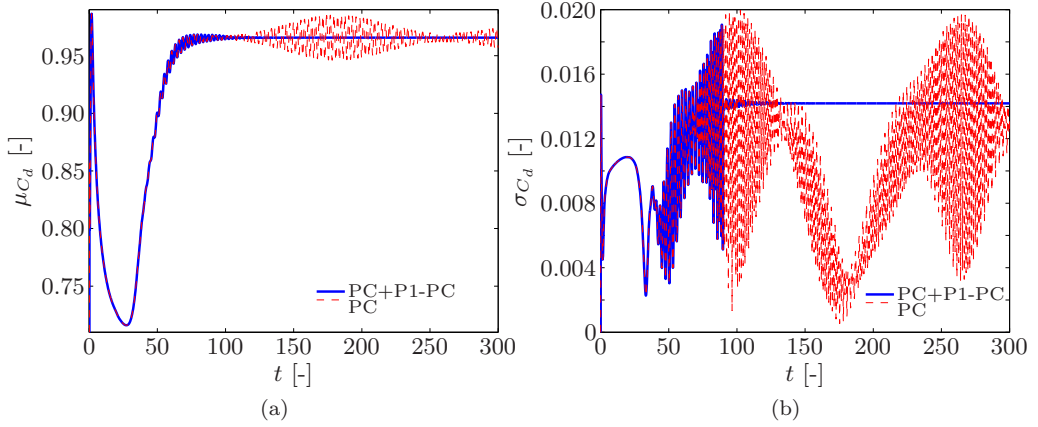


**Figure 4.20:** Time series of the mean  $\mu_{C_d}$  and the standard deviation  $\sigma_{C_d}$  of the drag coefficient. The blue line (—) indicates the final solution based on standard Probabilistic Collocation for the transient part and Probabilistic Collocation for period-1 oscillations for the periodic part. The dashed red line (---) indicates the standard Probabilistic Collocation method. A fourth order approximation is used, requiring 5 deterministic solves.

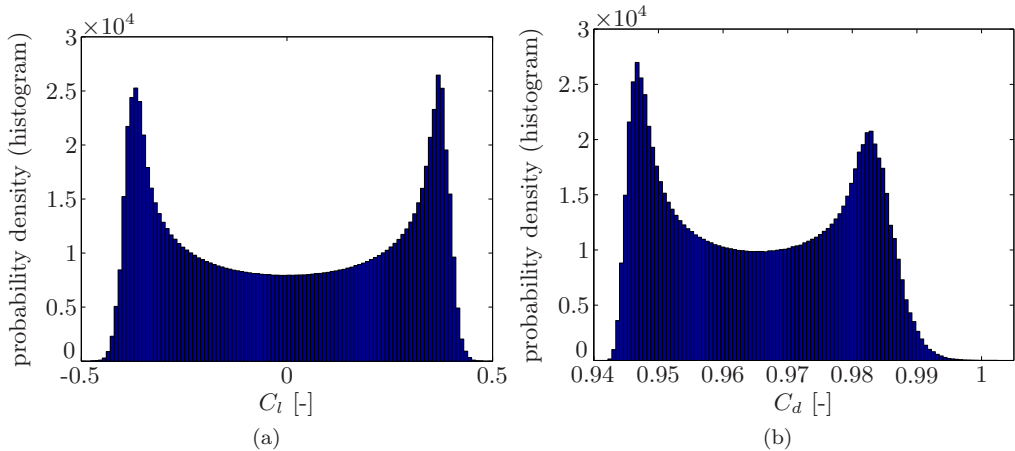


**Figure 4.21:** Limit state of the probability density functions (histograms) of the lift and drag coefficient at  $t=300$ .



---

# Geometric uncertainties

---

Geometric uncertainties are present in reality, for example due to production tolerances or unknown deformations during operation. The geometry of a well-designed airfoil might differ from the actually produced airfoil. Apart from that, the construction may deform under loading during operation or change due to for example icing. In this study the geometric uncertainty is written as a parametric uncertainty by parameterizing the geometry and assuming an uncertainty on the parameters. Geometric uncertainties directly influence the aerodynamic performance. Therefore, they are of great interest, especially for industry. Examples of the shape parameters of an airfoil are the relative thickness, maximum camber, or leading edge radius, depending on the parameterization.

The effect of geometric uncertainties on Computational Fluid Dynamics (CFD) has been investigated before using sensitivity analysis [Ilinca et al. (2006); Etienne et al. (2006)] and moment methods [Gumbert et al. (2002)]. Ilinca et al. (2006) treat shape sensitivities of unsteady laminar flow around a cylinder in ground proximity. Shape sensitivities are investigated by Etienne et al. (2006) for flexible plates in a flow domain. Gumbert et al. (2002) included first order moments in robust design optimization of a 3D flexible wing with uncertain wing geometry.

Instead of sensitivities or lower order approximations of the mean and variance, in this study the probability distribution function of the output of interest is computed. From the probability distribution more accurate intervals can be extracted, which contain for example 95% of all possible values that can occur. The Probabilistic

## Chapter 5: Geometric uncertainties

Collocation method [Babuška et al. (2007); Loeven, Witteveen and Bijl (2007a)] described in chapter 2 is used for uncertainty propagation.

The first test case is a 4-digit series NACA airfoil. For this airfoil series, the geometry is determined by three parameters. These are the maximum camber, maximum camber location and the thickness, all in percents of the chord. Each shape parameter is assumed to be uncertain separately to investigate the effect of the parameter on the solution. After that all parameters are considered uncertain simultaneously to study the combined effect. JavaFOIL [Hepperle (1996–2010)] is used as a deterministic solver, which uses low fidelity flow models. It consists of a potential flow solver combined with boundary layer analysis. It is quick to run, but lack the capability of computing and showing flow phenomena in the flow field.

The next step is to apply CFD, where a computational grid is constructed around the object. On this grid, the equations governing fluid motion are solved by the flow solver. When the geometry is uncertain, the geometry is different for every collocation point. This means that a new computational grid has to be constructed, which is a time consuming job. In this section the flow solver is adapted, such that grid deformation techniques [de Boer et al. (2007)] can be used to treat geometric uncertainties in an efficient way [Jakobsson and Amoignon (2007)].

Secondly, flow around a NACA0012 airfoil is considered with uncertain camber and relative thickness. A commercial CFD solver is used to perform several deterministic solves to obtain a Probabilistic Collocation approximation. Computations at subsonic flow ( $M = 0.3$ ) and at transonic flow ( $M = 0.8$ ) are accomplished. The pressure distribution on the surface of the airfoil with uncertainty bars is shown, as well as the probability distribution functions of the lift, drag and for the transonic case the shock location.

A problem in this approach is the determination of the probability density functions of the parameters. Here truncated normal distributions are used, since this seems a reasonable assumption for produced items. The mean has the highest probability and products outside the tolerance interval are rejected. This chapter is based on the results from Loeven and Bijl (2008a).

### 5.1 NACA5412 results using JavaFOIL

The geometry of an airfoil of the NACA 4-digit series is described by three parameters. The general form is NACA $XYZ$ , where  $XYZ$  represent the following shape parameters:  $X$  is the maximum camber,  $Y$  the maximum camber location and  $Z$  the thickness of the airfoil, all in percents of the chord. For example NACA5412 (see figure 5.1) is an airfoil with 5 percent maximum camber, located at 40 percent of the chord and the thickness is 12 percent of the chord.

The next sections show the effect of uncertainties on all three shape parameters separately and simultaneously. These uncertainties occur in reality when due to the





**Figure 5.1:** NACA5412 airfoil

production process the final product differs from the design. Two things have to be taken into account when this approach is followed. First the choice of input distribution of a shape parameter is not obvious. Here truncated normal distributions are used, since this seems a reasonable assumption for products. The mean has the highest probability and products outside the tolerance interval are rejected. The coefficient of variation is set to  $CV = 10\%$  and the distribution is truncated at  $\mu \pm 3\sigma$ . Secondly, there are different ways of parameterizing the shape of an airfoil. Furthermore, if multiple uncertain shape parameters are considered, they are not likely to be independent. All parameters together determine the actual shape, so an uncertain shape will affect all parameters. The effect of the way of parameterization is not investigated here.

The results of section 5.1 consist of a  $C_l$  and  $C_d$  for a range of angles of attack of -1 to 15 degrees. The lift coefficient is obtained using the panel method with stall and transition models [Eppler and Somers (1980); Eppler (1978)], implemented in JavaFOIL [Hepperle (1996–2010)]. Here the Eppler stall model combined with the  $e^N$  transition model [Drela and Giles (1986)] are used. It has been validated by Hepperle (1996–2010) that for this range of angles of attack the used panel method in combination with the stall and transition model accurately predicts the lift and drag of the airfoil.

The flow around the airfoil is set to a Reynolds number of  $3 \times 10^6$  at sea level. The uncertainty bars show the interval that contains 100% of all possible values, obtained from the cumulative distribution function. A second order approximation is used, meaning 3 deterministic solves for each parameter. The accuracy is checked by computing a fourth order approximation with 5 solves, which showed no significant improvement. Figure 5.2 shows that each parameter has a different effect on the lift coefficient.

### Uncertain maximum camber: NACA $X$ 412

The results for the uncertain maximum camber  $X$  are shown in figure 5.2(a). The mean is set to  $\mu_X = 5\%$  of the chord. With a coefficient of variation to  $CV_X = 10\%$ , the standard deviation is  $\sigma_X = 0.5\%$ . The uncertain camber shifts the  $C_l$ - $\alpha$  graph up and down for every collocation point. From figure 5.2(a) it can be seen that this results in equally sized uncertainty bars. The coefficient of variation of the lift coefficient decreases when the angle of attack is increased, see figure 5.3(a). The input coefficient of variation of 10% increases to 12% for low angles of attack and decreased to 3% near the maximum lift coefficient.

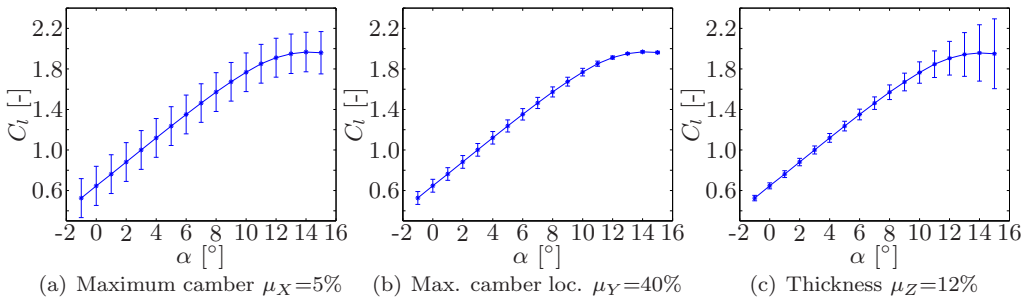


**Figure 5.2:** The lift coefficient of a NACA5412 airfoil for an uncertain (a) the maximum camber  $X$ , (b) maximum camber location  $Y$  and (c) thickness  $Z$ , assuming a truncated normal distribution with a coefficient of variation of 10%. The uncertainty bars show the 100% interval obtained from a second order Probabilistic Collocation computation (3 deterministic solves).

### Uncertain maximum camber location: NACA5Y12

Figure 5.2(b) shows the results for a maximum camber location with a mean of 40% of the chord with coefficient of variation of  $CV_Y=10\%$ . This yields a standard deviation of 4%. An uncertain maximum camber location  $Y$  has much lower influence on the  $C_l$ - $\alpha$  graph as the maximum camber. Figure 5.3(b) shows that for low angles of attack the coefficient of the variation is less than 5% compared to an input of 10%. Near the maximum lift coefficient, the coefficient of variation decreases to less than 0.5%. It can be concluded that the lift coefficient is not sensitive to variations in the maximum camber location of the airfoil.

### Uncertain maximum thickness: NACA54Z

Figure 5.2(c) shows the results for an uncertain thickness  $Z$  with an input coefficient of variation of  $CV_Z=10\%$ . The mean thickness is  $\mu_Z=12\%$  of the chord, the standard deviation is  $\sigma_Z=0.12\%$ . The coefficient of variation of the lift coefficient is about 1% for low angles of attack. When separation starts moving forward from the trailing edge the coefficient increases rapidly to 6% at an angle of attack of  $15^\circ$ , as can be seen in figure 5.3(c). The turbulent separation is influenced mostly by the thickness. On a thinner airfoil separation starts at a lower angle of attack than for a thicker airfoil. This leads to larger uncertainty bars at higher angles of attack. When looking at separation, one has to be careful. For JavaFOIL the stall and separation model work well for standard airfoils like the NACA 4-digit series.

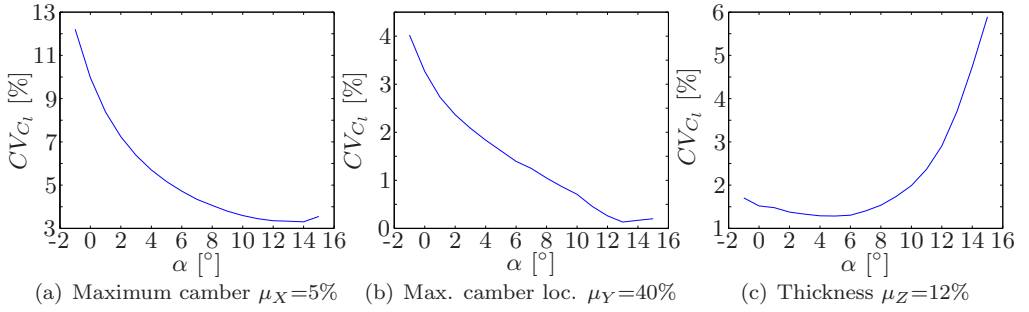


**Figure 5.3:** The coefficient of variation of the lift coefficient of a NACA5412 airfoil for an uncertain (a) the maximum camber  $X$ , (b) maximum camber location  $Y$  and (c) thickness  $Z$ , assuming a truncated normal distribution with a coefficient of variation of 10%.

### Complete geometry uncertain: NACA $XYZ$

The previous sections showed that each parameter has a different effect on the solution. Now all parameters are assumed to be uncertain simultaneously. For example strains in the material can lead to a different maximum camber, maximum camber location and thickness. Probably the parameters are correlated in reality. In the current work, independency of the parameters is assumed. However, nonlinear interaction of the uncertain parameters in the model are taken into account.

All parameters have a truncated Gaussian distribution with a coefficient of variation of  $CV_{XYZ}=10\%$ . The mean airfoil is the NACA5412 airfoil shown in figure 5.1. The input uncertainty is propagated using a second order probabilistic collocation approach, requiring 27 deterministic computations. Figure 5.4(a) and 5.4(b) show the lift and drag coefficient with respect to the angle of attack, including uncertainty bars which indicate the interval that contains all possible values. For  $C_d$  the mean is in the order of  $10^{-3}$  and the variance in the order of  $10^{-7}$  for low angles of attack. Due to numerical errors, oscillations of the polynomial approximation are visible in the 100% interval. This is most clear at  $\alpha$  is  $2^\circ$ . The drag polar is shown in figures 5.5(a). Figure 5.5(a) shows the 100% uncertainty bars from figures 5.4(a) and 5.4(b) in a drag polar. For the lift coefficient the bars are vertical and for the drag the uncertainty bars are horizontal. To clarify the figure, the bars are connected resulting in two areas, one originating from the drag coefficient and one from the lift coefficient. For low angles of attack ( $\leq 5^\circ$ ), inside the drag bucket, the uncertainty of the drag coefficient is most important. For angles of attack larger than  $5^\circ$  the lift coefficient's uncertainty bars determine the uncertainty region.

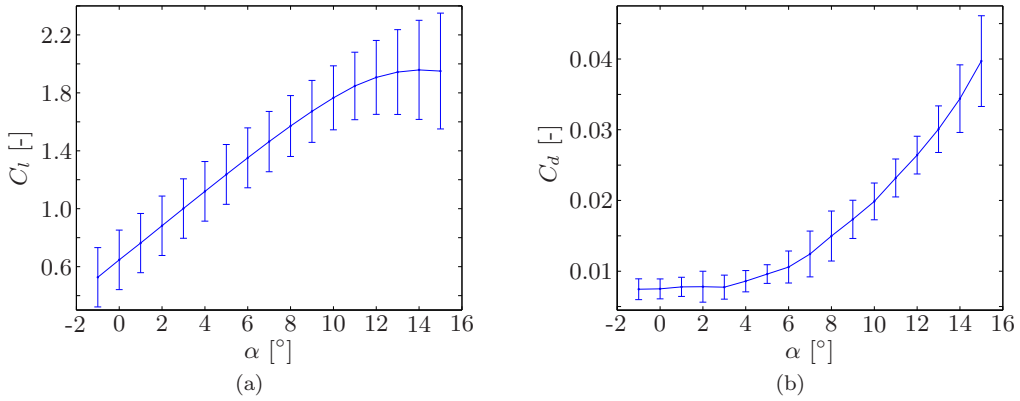


**Figure 5.4:** Characteristics of a NACA5412 airfoil with all three geometric parameters uncertain. Shown are the mean lift (a) and drag (b) coefficient with respect to the angle of attack, the uncertainty bars show the 100% interval obtained from a second order Probabilistic Collocation approximation (27 deterministic solves).

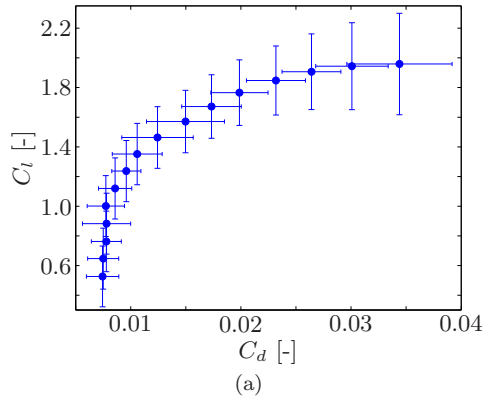


**Figure 5.5:** The mean drag polar for a NACA5412 with all three geometric parameters uncertain. The uncertainty bars show the 100% interval obtained from a second order Probabilistic Collocation approximation (27 deterministic solves).

## 5.2 Grid deformation for geometrical uncertainties

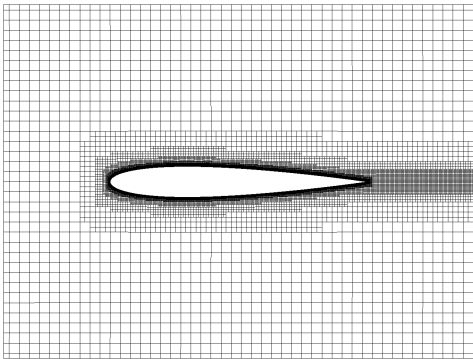
When taking geometrical uncertainties into account like relative thickness, the geometry changes for every collocation point. In CFD a computational grid is constructed around the object. The equations governing fluid flow are then solved on this grid by the flow solver. Creating a computational grid can be a time consuming job. In order to avoid the construction of a new grid for every collocation point, a grid deformation technique is employed. The grid is deformed using radial basis functions (RBF's) [de Boer et al. (2007); Jakobsson and Amoignon (2007)]. RBF's provide a robust grid deformation technique for unstructured grids, and do not require connectivity information. Here the thin plate spline RBF is used, which was shown to be robust and accurate with the highest computational efficiency [de Boer et al. (2007)]. Normally, the grid deformation routine is only available for unsteady simulations. The flow solver is adapted to be able to use grid deformation before the steady solver was started. Jakobsson and Amoignon (2007) used grid deformation in a similar way for aerodynamic shape optimization.

The grid deformation was tested for three relatively large geometrical deformations. In uncertainty quantification problems the deviations from the nominal conditions are in general in the order of a few percents up to 10 percent. If the CFD solver can produce acceptable results for the extreme test cases, it is assumed to work properly for uncertainty quantification. The baseline configuration is a NACA0012 airfoil, shown in figure 5.6(a). First the relative thickness is changed, such that the airfoil becomes a NACA0018 airfoil (see figure 5.6(b)). This means the thickness is multiplied by 1.5, which is a very large deviation from the nominal conditions in uncertainty quantification. The second case is shown in figure 5.6(c), here the angle of attack is change from  $0^\circ$  to  $5^\circ$ . And for the third case the camber of the airfoil is increased to 5 percent, depicted in figure 5.6(d).

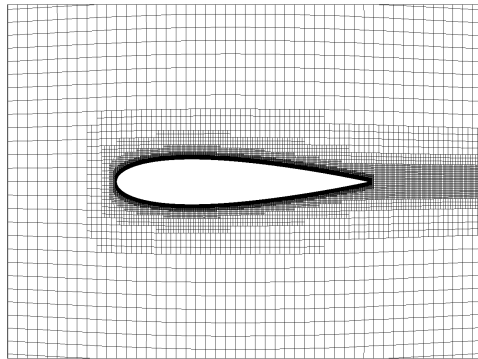
For all cases in figure 5.6, the deformed grids are of good quality. To validate the results, computations are performed using the deformed grids and the new geometry with a new grid. For all cases the lift and drag coefficients were within a few percent, so the procedure can safely be used for uncertainty quantification. Especially, since the geometrical uncertainties for the test cases of chapters 3, 5 and 8 are much smaller. The error due to grid deformation can be neglected for these test cases.

## 5.3 A NACA0012 airfoil with uncertain camber and thickness

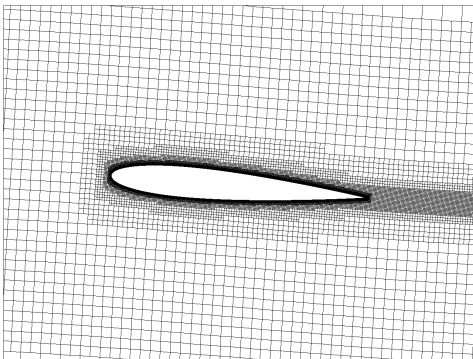
Two cases are presented for the NACA0012 airfoil with uncertain geometry. The first case is at a Mach number of  $M=0.3$ . Here the flow is modelled using the Reynolds-averaged Navier-Stokes equations and the Spalart-Allmaras turbulence model. The second case is transonic flow at  $M=0.8$ , where the flow is solved using the Euler equations.



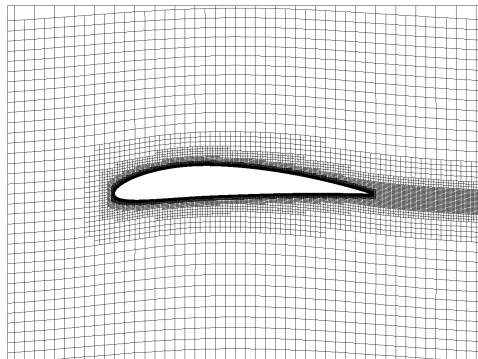
(a) Original grid NACA0012 airfoil.



(b) Deformed grid to a NACA0018 airfoil.



(c) Deformed grid to an angle of attack of  $5^\circ$ .



(d) Deformed grid to a camber of 5 percent.

**Figure 5.6:** The original grid layout near the airfoil (a) and the deformed grids for a 1.5 times thicker airfoil (b), an angle of attack of  $5^\circ$  (c) and a camber of 5 percent (d).

## 5.3 A NACA0012 airfoil with uncertain camber and thickness

### 5.3.1 Subsonic flow at $M=0.3$

The previous section showed that the camber and relative thickness have the largest effect on the lift and drag of an airfoil. In this section flow around a NACA0012 airfoil with uncertain camber and relative thickness is considered. The uncertainties are propagated using the Probabilistic Collocation method. The airfoil is under an angle of attack of  $5^\circ$  and the Reynolds number is equal to  $3 \times 10^6$ . The deterministic computations are performed using the FINE™/Hexa solver by Numeca International on a grid of 76,919 cells. Approximately 1600 cells cover the surface of the airfoil with  $y^+ \leq 1$ . The grid layout is shown in figure 5.7.

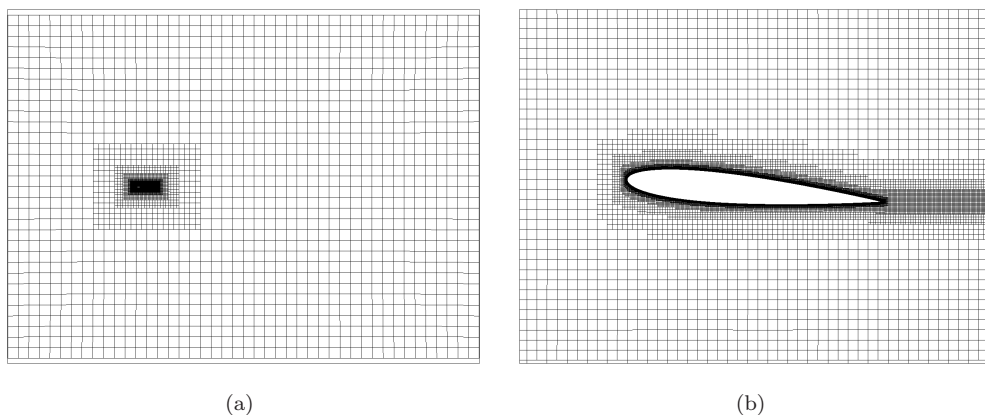


**Figure 5.7:** The computational grid layout (a) and a detailed view of the grid near the airfoil (b).

The flow is modeled by the Reynolds-averaged Navier-Stokes equations using the Spalart-Allmaras turbulence model. The air properties are at 0m ISA. The mean free stream Mach number is set to  $M=0.3$  and the free stream flow is fully turbulent. The pressure coefficient around the mean airfoil is shown in figure 5.8.

The uncertainties are the camber  $c$  and the relative thickness  $t$  of the airfoil, both are assumed to have a truncated normal distribution. The camber is truncated at  $[-1\%, +1\%]$ , the mean is  $\mu_c=0\%$  and the standard deviation is  $\sigma_c=0.4472\%$ . The relative thickness is truncated at  $[11\%, 13\%]$  with a mean of  $\mu_t=12\%$  and a standard deviation of  $\sigma_t=0.425\%$ . Both uncertain parameters are assumed to be independent and propagated through the system simultaneously. A second order Probabilistic Collocation approximation is used, which requires 9 deterministic solves.

Figure 5.9 shows the pressure coefficient at the surface of the airfoil. The mean is shown by the solid line, the uncertainty bars indicate the interval containing 95% of all possible values. The uncertainties in camber and relative thickness have a significant influence on the pressure near the leading edge and between 20 and 60 percent of the chord.

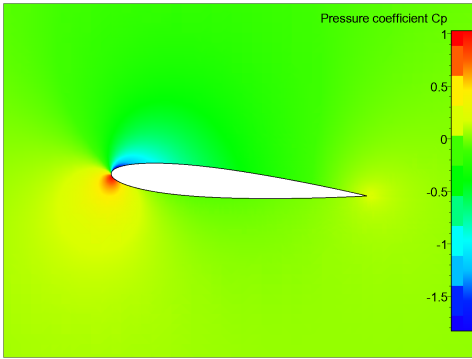


**Figure 5.8:** Pressure coefficient around the mean airfoil at  $M=0.3$ .

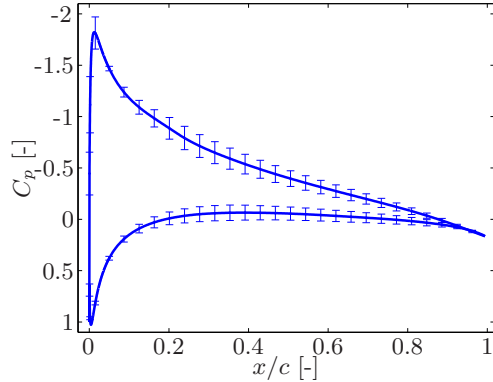


**Figure 5.9:** Pressure distribution at the surface of the airfoil. The mean is indicated with the solid line (—), the uncertainty bars show the area containing 95% of all possible values.

The probability distribution functions of the lift and drag coefficient are shown in figure 5.10(a) and 5.10(b). The deterministic coefficients (i.e. with both uncertainties set to the mean value) are  $C_l=0.5416$  and  $C_d=0.0127$ . From the uncertainties in the camber and relative thickness the mean values result in  $\mu_{C_l}=0.5405$  and  $\mu_{C_d}=0.0128$ , which are very close to the deterministic values. The standard deviations are  $\sigma_{C_l}=0.0479$  and  $\sigma_{C_d}=0.0002$ , resulting in coefficients of variation of  $CV_{C_l}=8.86\%$  and  $CV_{C_d}=1.8\%$ . The variation in the lift coefficient is much higher than the variation in drag coefficient based on the present uncertainties. The probability density functions show that the lift is propagated almost linearly, it is close to a truncated normal distribution. The drag coefficient, however, shows a highly skewed distribution. The area of the lift coefficient covers over 300 liftcounts. Although the area of the drag coefficient covers about 10 dragcounts, it is still a significant amount.

### 5.3.2 Transonic flow at $M=0.8$

The airfoil is under an angle of attack of  $5^\circ$  and again the relative thickness and camber are assumed to be uncertain. The deterministic computations are performed using the FINE™/Hexa solver by Numeca International on a grid of 45,402 cells. Approximately 1600 cells cover the surface of the airfoil. No viscous layers are inserted since the flow is modeled using the Euler equations. The close up of the grid layout is shown in figure 5.11. A refined box is used to resolve the shock. The mean free stream Mach number is  $M=0.8$ . The pressure coefficient is shown in figure 5.12, indicating a clear shock starting at the upper surface at  $x/c=0.7809$ . The uncertainties are the camber  $c$  and the relative thickness  $t$  of the airfoil, with the same parameters as the subsonic case.



### 5.3 A NACA0012 airfoil with uncertain camber and thickness

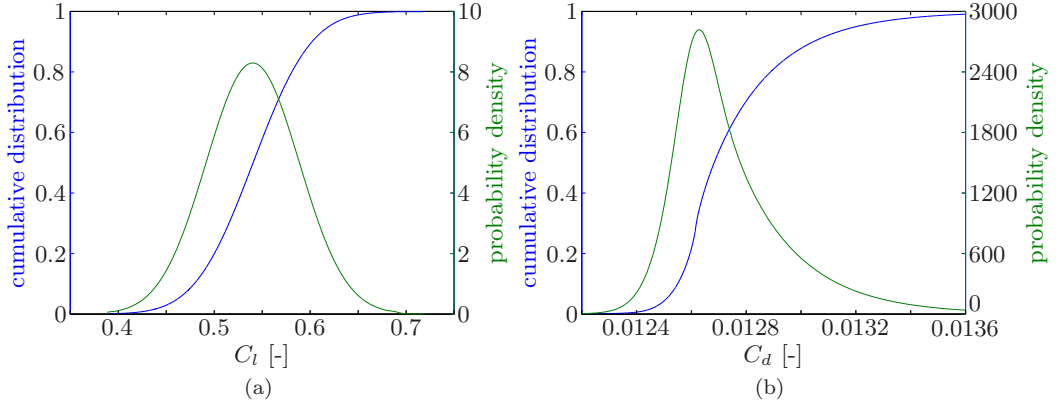


**Figure 5.10:** Probability distribution functions for  $C_l$  and  $C_d$  using a second order Probabilistic Collocation approximation.

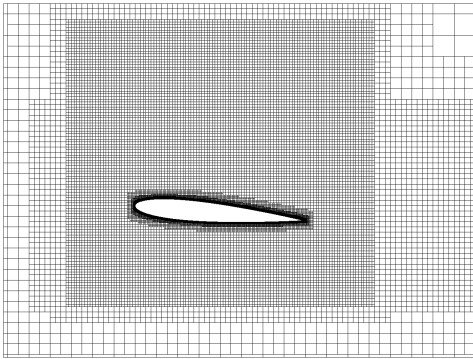


**Figure 5.11:** The computational grid layout near the airfoil.

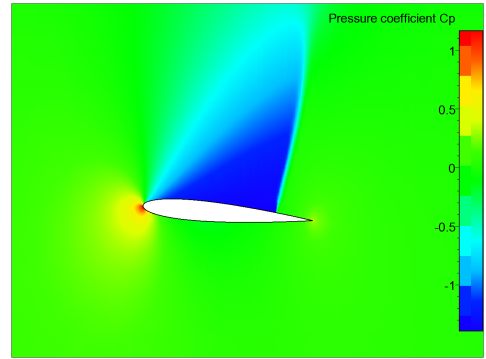


**Figure 5.12:** Pressure coefficient around the mean airfoil at  $M=0.8$ .

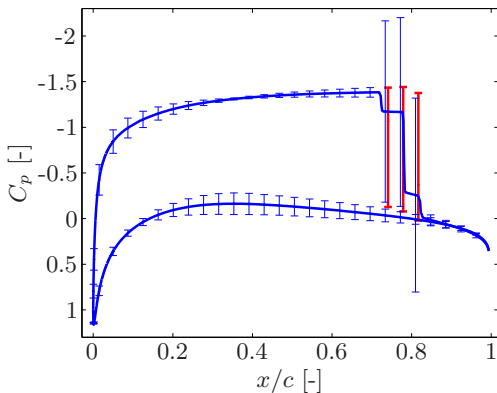


**Figure 5.13:** Pressure distribution at the surface of the airfoil. The mean is indicated with the solid blue line (—), the uncertainty bars show the region containing all possible values. The red bars (—) show the piecewise linear approximation near the shock location.

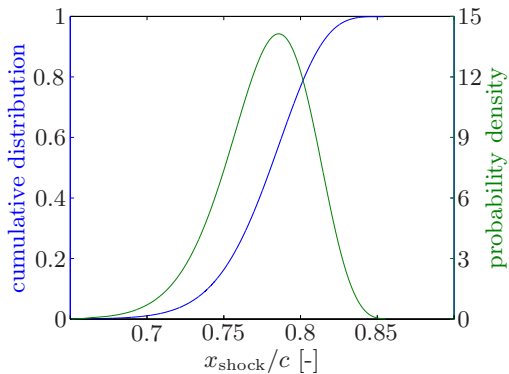


**Figure 5.14:** Probability distribution functions of the shock location using a second order Probabilistic Collocation approximation.

Figure 5.13 shows the pressure coefficient at the surface of the airfoil. The mean is shown by the solid line, whereas the uncertainty bars indicate the 95% interval. Due to the presence of the shock the response surface of the pressure coefficient contains a discontinuity. This causes the global polynomial approximation to oscillate and produce erroneous approximations, as can be observed by the large uncertainty bars near the shock location. To be able to accurately approximate the uncertainty bars around the shock, a Multi-Element Probabilistic Collocation approach [Loeven, Sarkar, Witteveen and Bijl (2007); Foo et al. (2008)] can be used (see chapter 4).

Another way of treating the discontinuity is to use the information that is already available from the collocation points. Namely, the shock location itself is an output functional which is easily approximated using the Probabilistic Collocation method. Based on the probability distribution of the shock position, the location where the Probabilistic Collocation expansion will result in an oscillatory approximation due to the discontinuity. Inside this part of the domain a piecewise linear approximation through the collocation points is used to approximate the response surface without erroneous results. The results of the piecewise linear approximation are shown in figure 5.13 by the red bars. The linear uncertainty bars show no over or undershoots outside the area around the shock. It is possible to obtain an accurate approximation of the mean and the uncertainty bars using a second order Probabilistic Collocation approximation requiring only 3 deterministic solves.

The probability distribution functions of the shock location are shown in figure 5.14. The deterministic shock location is at  $x_{\text{shock,det}}/c=0.7809$ . The mean shock loca-

tion based on the input uncertainties is  $\mu_{x_{\text{shock}}/c}=0.7779$  with a standard deviation of  $\sigma_{x_{\text{shock}}/c}=0.0288$  resulting in a coefficient of variation of  $CV_{x_{\text{shock}}/c}=3.7\%$ . This variation is significant, the area of possible shock locations covers over 15% of the chord (see figure 5.14).

## 5.4 Summary

Imperfections and wear are inherently present in real life, and can be treated as uncertainties in simulations. These uncertainties can have a significant effect on the performance and have, therefore, been investigated in this chapter. Other studies used sensitivity analysis and moment methods. This study uses the Probabilistic Collocation method, in order to propagate the probability density functions of the uncertain geometric parameters to the performance parameters of the model.

First a low fidelity flow model was used to assess the effect of uncertainties in three geometrical parameters on the performance of a NACA5412 airfoil. A coefficient of variation of 10% was assumed for the maximum camber, maximum camber location, and relative thickness, with a truncated normal distribution. The maximum camber affected the polar in the complete range from  $\alpha=0$  to  $15^\circ$ . The maximum camber location showed a small effect on the performance of the airfoil. The thickness mainly results in large standard deviations at higher angles of attack.

Secondly, a CFD test case was shown with two uncertain geometrical parameters (i.e. maximum camber and thickness) for subsonic and transonic flow around a NACA0012 airfoil. To efficiently propagate the uncertainties, a grid deformation technique was used to deform the grid of the case with the mean values for the uncertain geometric parameters to the grid required for each collocation point. For the subsonic case, the lift coefficient was shown to be most sensitive to the geometric variations. A coefficient of variation was obtained of 8,86% and 1.8% for the lift and drag coefficient, respectively. The transonic case results in a shock wave at the upper surface of the airfoil. The shock location showed a coefficient of variation of 3.7%. The standard Probabilistic Collocation approximation fails near the shock due to the discontinuity in the response. To be able to accurately approximate the uncertainty bars of the pressure, a linear approximation is used in the area where the discontinuity is present. This area was obtained from the probability density function of the shock location. The discontinuity was treated successfully in this way and required no additional deterministic solves.



---

# Uncertainty analysis of the $k$ - $\epsilon$ turbulence model parameters

---

In this chapter the effects of uncertainties in the  $k$ - $\epsilon$  turbulence model on the solution of a computational fluid dynamics simulation are investigated. The flows computed in this thesis are modelled using the Reynolds-averaged Navier-Stokes (RANS) equations with a turbulence model. The number of RANS equations is less than the number of variables, so additional equations are required. Here the Boussinesq hypothesis is employed, resulting in an eddy viscosity that has to be computed by a turbulence model. These eddy viscosity turbulence models often contain a set of parameters that can be tuned to specific problems. The default values for those parameters are obtained or tuned from theory, experiments or direct numerical simulations of simplified flows. After fixing these parameters, the model is applied to all kinds of flows. This introduces uncertainties in the simulations due to experimental uncertainties and the questionable applicability of the parameters to arbitrary flows.

The goal of this chapter is to quantify the effect of these uncertainties on the solution. First the probability distribution functions of the turbulence model parameters have to be determined from the original experiments or simulations on which the values are based upon. Next the uncertainties are propagated through the CFD solver using the Probabilistic Collocation method. The results are analyzed to determine which parameters affect the solution most and to see the difference between the deterministic results and the stochastic results. Further information can be found in

Platteeuw et al. (2008) and the master thesis of Platteeuw (2008). Turgeon et al. (2002, 2004) studied the sensitivity of the  $k$ - $\epsilon$  turbulence model parameters on several flow problems. The study of Turgeon et al. (2002, 2004) did not include probability density functions and the physical relations between coefficients.

A big challenge is to find physically based probability density functions for the the  $k$ - $\epsilon$  model parameters. Relations between parameters are maintained to assure physical validity of the model as much as possible. The standard values for the the  $k$ - $\epsilon$  model parameters are a compromise chosen to give the best performance for a range of flows.

Two test cases are computed to investigate the effect of the uncertainties in the model parameters on the solution. Firstly, the turbulent flat plate test case with a fully developed boundary layer is considered. Secondly, subsonic flow around a NACA0012 airfoil is investigated.

## 6.1 Turbulence modeling

A brief introduction to turbulence modeling is given in section 6.1.1. Section 6.1.2 shows the standard  $k$ - $\epsilon$  model, which is used in this chapter.

### 6.1.1 Incompressible Reynolds-averaged Navier Stokes equations

When the velocity of a fluid is much lower than the speed of sound ( $u/a \lesssim 0.3$ ), the flow can be modelled by the incompressible Navier-Stokes equations. This means the density is assumed to be constant. The equations without body forces, then become:

$$\frac{\partial u_i}{\partial x_i} = 0, \quad (6.1)$$

$$\frac{\partial u_i}{\partial t} + u_j \frac{\partial u_i}{\partial x_j} = \frac{1}{\rho} \frac{\partial \sigma_{ij}}{\partial x_j}, \quad (6.2)$$

with  $u$  the velocity,  $x$  the spatial coordinate,  $t$  time,  $\rho$  the density of the fluid and  $\sigma$  the stress tensor. The indices  $i$  and  $j$  can have value 1, 2, or 3, as they represent the  $x$ ,  $y$ , and  $z$  directions respectively. Here the Einstein convention is used, thus a repeated index means summation.

For a Newtonian fluid the stress tensor in the momentum equation (6.2) becomes:

$$\sigma_{ij} = -p\delta_{ij} + \mu \left( \frac{\partial u_i}{\partial x_j} + \frac{\partial u_j}{\partial x_i} \right), \quad (6.3)$$

where the isotropic part is the static pressure  $p$  and the non-isotropic term, the shear stress, is related to the velocity gradients. Substituting equation (6.3) in equation (6.2) results in the following momentum equation:

$$\frac{\partial u_i}{\partial t} + u_j \frac{\partial u_i}{\partial x_j} = \frac{1}{\rho} \frac{\partial}{\partial x_j} \left[ -p\delta_{ij} + \mu \left( \frac{\partial u_i}{\partial x_j} + \frac{\partial u_j}{\partial x_i} \right) \right]. \quad (6.4)$$

## 6.1 Turbulence modeling

Solving the Navier-Stokes equations (6.1) and (6.4) directly is not feasible for engineering flow problems. To resolve all the turbulent scales, a very small time step and fine spatial computational grid are required. The number of floating point operations scales with  $Re^3$ , limiting direct numerical simulations to low Reynolds numbers. To be able to model high Reynolds number flows, Reynolds averaging [Reynolds (1894); Davidson (2004)] is applied. The Reynolds-averaged Navier-Stokes equations are obtained by decomposing each instantaneous variable into an ensemble mean and turbulent fluctuation:

$$u_i = \overline{u_i} + u'_i. \quad (6.5)$$

Equation (6.5) is substituted into equations (6.1) and (6.4) and takes the ensemble average, the results are the incompressible Reynolds-averaged Navier-Stokes equations:

$$\frac{\partial \overline{u_i}}{\partial x_i} = 0, \quad (6.6)$$

$$\frac{\partial \overline{u_i}}{\partial t} + \overline{u_j} \frac{\partial \overline{u_i}}{\partial x_j} = \frac{1}{\rho} \frac{\partial}{\partial x_j} \left[ -\overline{p} \delta_{ij} + \mu \left( \frac{\partial \overline{u_i}}{\partial x_j} + \frac{\partial \overline{u_j}}{\partial x_i} \right) - \rho \overline{u'_i u'_j} \right]. \quad (6.7)$$

The equations are similar to the original Navier-Stokes equations. In the momentum equation, however, an extra term appeared, the so-called Reynolds-stresses  $\Sigma_{ij}$ :

$$\Sigma_{ij} = -\overline{\rho u'_i u'_j},$$

with  $\rho$  the fluid density and  $u'_i$  the velocity fluctuation in the  $i$ -direction. These correlation terms form the coupling between the mean flow and the turbulence. Because the number of unknowns is larger than the number of equations, extra relations are needed to solve the problem.

Additional equations for the Reynolds stresses can be derived, which results in the so-called Reynolds stress model. Here, the Boussinesq hypothesis is used, which states that the Reynolds stress can be decomposed in a similar way as the fluid stress (equation (6.3)), introducing a turbulent viscosity or eddy viscosity  $\mu_T$ :

$$\Sigma_{ij} = -\frac{1}{3} \overline{\rho u'^2} \delta_{ij} + \mu_T \left( \frac{\partial \overline{u_i}}{\partial x_j} + \frac{\partial \overline{u_j}}{\partial x_i} \right). \quad (6.8)$$

The Boussinesq hypothesis is based on the assumption that the turbulent length scale is much smaller than the length scale of the problem. In other words the turbulent stresses can be obtained from local flow properties, which is often not the case. As a consequence, empirical relations and tuning of the models are required to make them work for a large diversity of flow problems. Although a sound physical basis for this approach is lacking, the approach provides reasonable results in many applications. This mainly holds for flows around simple geometries. More on the Boussinesq hypothesis and its limitations can be found in the books of Wilcox (1993), Nieuwstadt (1998), Pope (2000) and Davidson (2004).

## Chapter 6: Uncertainty analysis of the $k$ - $\epsilon$ turbulence model parameters

Substituting equation (6.8) into the momentum equation results in the final Reynolds averaged Navier-Stokes equations for an incompressible, Newtonian fluid:

$$\frac{\partial \bar{u}_i}{\partial x_i} = 0, \quad (6.6)$$

$$\frac{\partial \bar{u}_i}{\partial t} + \bar{u}_j \frac{\partial \bar{u}_i}{\partial x_j} = \frac{1}{\rho} \frac{\partial}{\partial x_j} \left[ - \left( \bar{p} + \frac{1}{3} \rho \overline{u_k'^2} \right) \delta_{ij} + (\mu + \mu_T) \left( \frac{\partial \bar{u}_i}{\partial x_j} + \frac{\partial \bar{u}_j}{\partial x_i} \right) \right], \quad (6.9)$$

where the turbulent pressure term  $\frac{1}{3} \rho \overline{u_k'^2}$  is often neglected since it is normally very small compared to the static pressure. This means that for solving the mean flow, only additional relations are required to determine the eddy viscosity. Three levels of approximation can be distinguished when closing the system of equations.

First the *algebraic* or *zero-equation models*, where the eddy viscosity is directly computed from the hydrodynamic variables. As a consequence, zero-equation models may not be able to properly account for history effects on the turbulence, such as convection and diffusion of turbulent energy. Commonly used models are the Baldwin-Lomax model [Baldwin and Lomax (1978)] or the Cebeci-Smith model [Cebeci and Smith (1974)].

Secondly, there are *one-equation models*, where a transport equation is solved for a turbulent quantity. This can be the turbulent kinetic energy or a viscosity like variable. The one-equation models are easy to use and computationally cheap. The models cover only one transport equation, therefore, the models fail for some test cases. Since there is no turbulent decay, the spreading of a planar jet is heavily overpredicted. On the other hand are external wall bounded flows well solved by the Spalart-Allmaras model. Well known models are, among others, the Spalart-Allmaras model [Spalart and Allmaras (1992)] and the Baldwin-Barth model [Baldwin and Barth (1990)].

Thirdly, *two-equations models* include two extra transport equations to represent the turbulent properties of the flow. This allows to account for convection and diffusion of turbulent energy. One of the transported variables is the turbulent kinetic energy  $k$ . The second transported variable depends on the type of the two-equation model. Common choices are the turbulent dissipation  $\epsilon$ , or the specific dissipation  $\omega$ . The second variable can be thought of as the variable that determines the scale of the turbulence (length-scale or time-scale), whereas the first variable,  $k$ , determines the energy in the turbulence. Models like the  $k$ - $\epsilon$  model [Jones and Launder (1972); Launder and Sharma (1974)], the  $k$ - $\omega$  model [Wilcox (1993)], and the SST  $k$ - $\omega$  model [Menter (1994)] have become industry standard models and are used for most types of engineering problems.

From zero- to two-equation models, the models become more complex, better in modeling turbulence and computationally more expensive. All turbulence closure models use model coefficients which are tuned for simplified flow experiments and fundamental flow problems. It is then assumed that these coefficients, which are derived from a few experiments, are representative for a large range of flows. This means that there is a certain amount of uncertainty present in the input of the turbulence model, which can have an impact on the final solution.



### 6.1.2 The $k$ - $\epsilon$ model

In this chapter, uncertainty quantification is applied to the standard  $k$ - $\epsilon$  model of turbulence as proposed by Jones and Launder (1972) by considering the model parameters as random variables. This will provide insight into the effect of uncertainties in the model parameters on the solution. More on the probability distribution of the model parameters can be found in the next section.

The two transport equations, which are added to the Reynolds averaged Navier-Stokes equations are one for the turbulent kinetic energy  $k$  and one for the rate of turbulent dissipation  $\epsilon$ . A turbulent velocity scale is then given by  $v = \sqrt{k}$ , and a turbulent time scale as  $\tau = k/\epsilon$ . For an incompressible flow, the transport equations are [Nieuwstadt (1998)]:

$$\frac{\partial k}{\partial t} + \bar{u}_i \frac{\partial k}{\partial x_i} = P - \epsilon + \frac{\partial}{\partial x_j} \left[ \left( \nu + \frac{\nu_T}{\sigma_k} \right) \frac{\partial k}{\partial x_j} \right], \quad (6.10)$$

$$\frac{\partial \epsilon}{\partial t} + \bar{u}_i \frac{\partial \epsilon}{\partial x_i} = C_{1,\epsilon} \frac{P\epsilon}{k} - C_{2,\epsilon} \frac{\epsilon^2}{k} + \frac{\partial}{\partial x_j} \left[ \left( \nu + \frac{\nu_T}{\sigma_\epsilon} \right) \frac{\partial \epsilon}{\partial x_j} \right], \quad (6.11)$$

where the production term  $P$  is given by:

$$P = -\overline{u'_i u'_j} \frac{\partial \bar{u}_j}{\partial x_i}. \quad (6.12)$$

The turbulent kinematic viscosity  $\nu_T$  is then modeled as:

$$\nu_T = C_\mu \frac{k^2}{\epsilon}.$$

Up to this point five model constants are introduced:  $C_\mu$ ,  $\sigma_k$ ,  $\sigma_\epsilon$ ,  $C_{1,\epsilon}$ , and  $C_{2,\epsilon}$ . The most commonly used values are given by Launder and Sharma (1974):

$$C_\mu = 0.09, \quad \sigma_k = 1.0, \quad \sigma_\epsilon = 1.3, \quad C_{1,\epsilon} = 1.44, \quad C_{2,\epsilon} = 1.92.$$

The coefficients are determined by demanding that this turbulence model should satisfy experimental data for certain simple standard flow cases, see Nieuwstadt (1998), Pope (2000), and Davidson (2004).

Because the standard  $k$ - $\epsilon$  model is derived under the assumption of a high (local) turbulent Reynolds number, regions of low turbulent Reynolds number, such as close to the wall, are poorly modeled. In those regions the destruction-of-dissipation term is singular at the wall since  $\epsilon$  is finite and the turbulent kinetic energy  $k$  is zero. This leads to numerical problems in the first two terms of the right-hand-side of equation (6.11). Fixes to this problem include the use of damping functions or wall functions.

In this work, wall functions as proposed by Launder and Spalding (1974) are used which are based on the log-law equation:

$$u^+ = \frac{1}{\kappa} \ln y^+ + C, \quad (6.13)$$

## Chapter 6: Uncertainty analysis of the $k$ - $\epsilon$ turbulence model parameters

where  $\kappa$  is the von Kármán constant and  $C$  a parameter related to the wall roughness. The dimensionless inner variables  $y^+$  and  $u^+$  are defined as  $y^+ \equiv yu_\tau/\nu$  and  $u^+ \equiv u/u_\tau$ , with  $u_\tau$  the friction velocity. The friction velocity is defined as  $u^+ = \sqrt{\tau_w/\rho}$ , with  $\tau_w$  the wall shear stress. For smooth walls, generally one takes  $\kappa=0.4187$  and  $C=5.24$ . A consequence of employing wall functions near the wall is that the first cell should lie within the log-law region  $30 \lesssim y^+ \lesssim 300$ . A good value is close to the lower bound, so  $y^+ \approx 30$  [Fluent Inc. (2005)].

### 6.2 Probability distributions of the model parameters

In the previous section, 7 constants were obtained from the standard  $k$ - $\epsilon$  model in combination with wall functions. The turbulent inlet conditions for  $k$  and  $\epsilon$  can also be uncertain, but this chapter focuses on the model constants. For the uncertainty analysis, probability density functions of the model parameters are required. The probability density functions are fit through results from experiments and direct numerical simulations. The quality of the fit is measured using the Kolmogorov-Smirnov test [Stephens (1974)]. The distribution that fits the data best is used for further analysis. Details of the distributions below can be found in appendix A. To avoid problems with numerical stability and limiter interference, all distributions are taken on a finite interval. When a (semi)-infinite distribution is obtained like for example a normal distribution, it is truncated at  $F_{0.1\%}$  and  $F_{99.9\%}$ .

#### Model parameter $C_\mu$

This model constant is obtained from considering simple turbulent shear flow with  $S = \partial\bar{u}_1/\partial x_2 = \bar{u}/\partial y$  the only non-zero mean velocity gradient [Pope (2000)]. From the definition of the eddy viscosity and production of turbulent energy, one can write equation (6.12) as:

$$P = -\overline{u'_i u'_j} S = C_\mu \frac{k^2}{\epsilon} S^2.$$

Reworking towards  $C_\mu$  yields:

$$C_\mu = \frac{P}{\epsilon} \left( \frac{\epsilon}{Sk} \right)^2.$$

The value of 0.09 was obtained from a measurement on channel flow, which is a practical example of simple shear flow. The original data could not be found, so data is used from a direct numerical simulation of Iwamoto (2002) and Hoyas and Jimenez (2006). The flow database stretches over the Reynolds numbers  $Re_\tau=[110, 150, 180, 300, 400, 550, 650, 950, 2000]$  and serves as basis for an input distribution for  $C_\mu$ . The results of the direct numerical simulations are shown in figure 6.1.

The wall functions demand the first cell to be in the log-layer. Therefore, only measurement points which satisfy the criterion  $y^+ \geq 30$  are considered. The standard

## 6.2 Probability distributions of the model parameters

distribution that best matches this data set according to the Kolmogorov-Smirnov test is a logistic distribution  $\mathcal{L}(m, b)$  with parameters  $m=0.08355$  and  $b=0.01069$  (see appendix A for more information about the logistic distribution). The mean  $\mu_{C_\mu}=0.08355$  is about 8% lower than the deterministic value of 0.09. The standard deviation is  $\sigma_{C_\mu}=0.01939$ , so the coefficient of variation is 23.2%. The distribution is truncated at the extreme values of the experimental data set. The distribution is shown in figure 6.2.

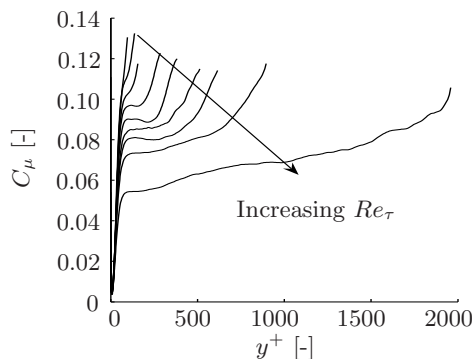


**Figure 6.1:**  $C_\mu$  extracted from the direct numerical simulations of Hoyas and Jimenez (2006).

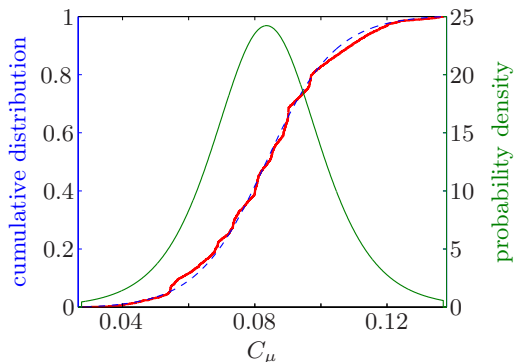


**Figure 6.2:** Probability distribution of  $C_\mu$ , with the experimental (—) and Logistic (--) cumulative distribution functions and the probability density function (—).

### Model parameter $C_{2,\epsilon}$

The value of  $C_{2,\epsilon}$  is determined by considering homogeneous turbulence [Pope (2000)], of which grid-generated turbulence is a practical example. For homogeneous turbulence the two transport equations (6.10) and (6.11) become:

$$\frac{dk}{dt} = P - \epsilon, \quad (6.14)$$

$$\frac{d\epsilon}{dt} = C_{1,\epsilon} \frac{P\epsilon}{k} - C_{2,\epsilon} \frac{\epsilon^2}{k}. \quad (6.15)$$

In the absence of mean velocity gradients, the production is zero and the turbulence decays. For this case, equations (6.14) and (6.15) have as solutions:

$$k(t) = k_0 \left( \frac{t}{t_0} \right)^{-n}, \quad \epsilon(t) = \epsilon_0 \left( \frac{t}{t_0} \right)^{-(n+1)},$$

## Chapter 6: Uncertainty analysis of the $k$ - $\epsilon$ turbulence model parameters

where  $k$  and  $\epsilon$  have the values  $k_0$  and  $\epsilon_0$  at the reference time  $t_0 = n \frac{k_0}{\epsilon_0}$ . The decay exponent  $n$  is:

$$n = \frac{1}{C_{2,\epsilon} - 1} \quad \Leftrightarrow \quad C_{2,\epsilon} = \frac{n + 1}{n}.$$

In Mohamed and LaRue (1990), the value for the decay exponent of turbulence is investigated. The experimental data is shown in figure 6.3. Since there is a limited set of data points, outliers can have a strong effect on the probability density function of  $C_{2,\epsilon}$ . Therefore, a box-and-whisker plot is used to identify and eliminate outliers. The boxplot is shown in figure 6.4. The red line in the middle of the box indicates the median of the data set. The edges of the box are the 25th and 75th percentiles, and the whiskers indicate the largest/smallest data point that is within 1.5 times the size of the box extending from both sides. The red crosses are outliers, which are removed from the dataset.

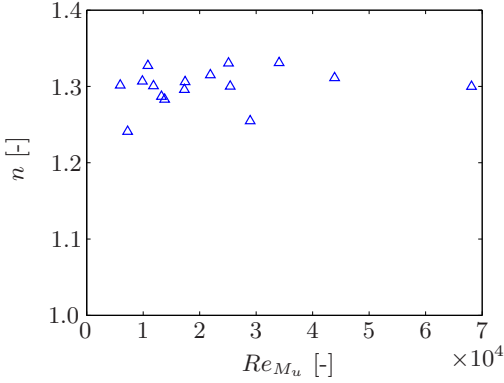


**Figure 6.3:** Variation of the decay rate exponent  $n$  with respect to the Reynolds number  $Re_{M_u}$  from the experimental data of Mohamed and LaRue (1990).

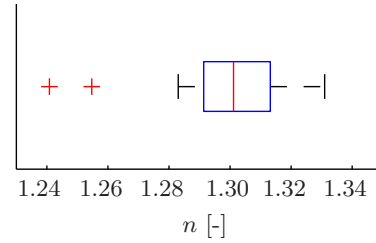


**Figure 6.4:** Box-and-whisker plot for the experimental data for  $C_{2,\epsilon}$ .

With this limited amount of data, it is impossible to determine a reliable distribution for  $C_{2,\epsilon}$ . Therefore, a truncated normal distribution is assumed. The best fit of the truncated normal distribution has a mean of  $\mu_{C_{2,\epsilon}} = 1.77$  and a standard deviation of  $\sigma_{C_{2,\epsilon}} = 0.008389$ , this means a coefficient of variation of 0.474%.

Pope (2000) states that experiments indicate a value of  $C_{2,\epsilon} \approx 1.76$ . With this value, however, good results are only obtained for decaying turbulence. For all other applications the results are bad. As a compromise  $C_{2,\epsilon} = 1.92$  is used in numerical simulations. Experience shows that it is a far better choice [Pope (2000)]. To take this into account, the probability density function is shifted such that the mean value corresponds to the common value 1.92, keeping the coefficient of variation equal to

## 6.2 Probability distributions of the model parameters

0.474%. So the final distribution parameters are  $\mathcal{N}(1.92, 8.325 \times 10^{-5})$ . The distribution is shown in figure 6.5.

### Model parameter $\sigma_k$

Parameter  $\sigma_k$  is determined by a computer optimization process [Hanjalic and Launder (1972)]. However, no data has been found to construct a distribution. Therefore, a truncated normal distribution is assumed (based on a normal distribution truncated on  $\mu \pm 3\sigma$ ) with mean equal to the commonly used deterministic value  $\mu_{\sigma_k} = 1$ . The standard deviation is defined such that the interval is within a 5% range with respect to the mean, thus  $\sigma_{\sigma_k} = 0.05/3$ . This is similar to the variation taken in the sensitivity study of Turgeon et al. (2002). The distribution is shown in figure 6.6.

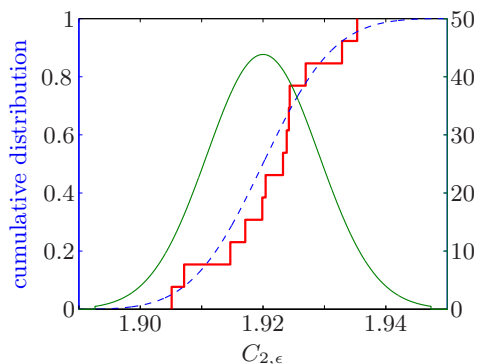


**Figure 6.5:** Probability distribution of  $C_{2,\epsilon}$ , with the shifted experimental (—) and Normal (- -) cumulative distribution functions and the probability density function (—).

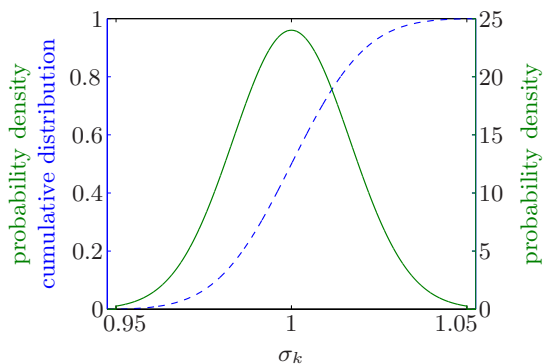


**Figure 6.6:** Probability distribution of  $\sigma_k$ , with the truncated Normal cumulative distribution function (- -) and the probability density function (—).

### Von Kármán constant $\kappa$

The distribution for the von Kármán constant is obtained from measured velocity profiles. Österlund et al. (2000) measured 70 velocity profiles and collected them in terms of  $u^+$  and  $y^+$  values. The following diagnostic function  $\Gamma$  is used to find  $\kappa$  from the velocity profiles:

$$\Gamma \equiv y^+ \frac{du^+}{dy^+} = \frac{1}{\kappa}, \quad (6.16)$$

which is obtained by differentiating equation (6.13) with respect to  $y^+$ . The probability density function for  $\kappa$  is based on these data as follows. The velocity gradient  $du^+/dy^+$  is evaluated in each measurement point and substituted into equation

(6.16), yielding a value for  $\kappa$ . The data are restricted to the values for  $\kappa$  in the range  $50 \leq y^+ \leq 100$ . For  $y^+ \leq 50$ , the location is not well within the log-layer and  $\kappa$  deviates significantly from the common value 0.42. For  $y^+ \geq 100$ , a decrease of  $\kappa$  from the common low Reynolds value 0.42 to the high Reynolds value 0.38 is observed, see also the work of Österlund et al. (2000). A box-and-whisker plot of the obtained dataset is used to remove several outliers, as can be seen in figure 6.7.

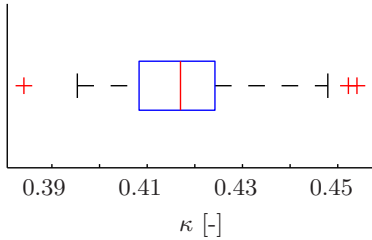


**Figure 6.7:** Box-and-whisker plot for the experimental data for  $\kappa$ .

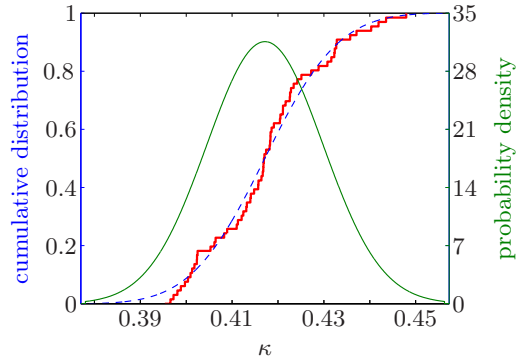


**Figure 6.8:** Probability distribution of  $\kappa$ , with the experimental (—) and truncated Normal (--) cumulative distribution functions and the probability density function (—).

The best fit to the final data set is a normal distribution with parameters  $\mathcal{N}(0.417, 1.57 \times 10^{-4})$ , the distribution is truncated at  $F_{0.1\%}$  and  $F_{99.9\%}$ . The mean is  $\mu_\kappa = 0.417$  and the standard deviation is  $\sigma_\kappa = 0.0125$ , this results in a coefficient of variation of 3%. The distribution is shown in figure 6.8.

## Wall function parameter $C$

The wall function parameter  $C$  is also obtained from the measured velocity profiles of Österlund et al. (2000). The values are computed by rewriting the log-law (equation 6.13):

$$C = u^+ - \frac{1}{\kappa} \ln y^+, \quad (6.17)$$

which is valid for the upper part of the low-law [Wilcox (1993)]. Therefore, the data is restricted for the upper part of the log-law, i.e.  $y^+ \geq 100$  and  $y/\delta \leq 0.2$ . The  $\kappa$  is taken equal to the mean value of the previous discussion, i.e.  $\kappa = 0.417$ . For each velocity profile, the values for  $C$  are averaged.

A shifted Weibull distribution is found to be the best fit with the following parameters: shape  $\alpha = 2.06$ , scale  $\beta = 0.415$ , and a shift to location  $\theta = 4.855$ . The distribution

## 6.2 Probability distributions of the model parameters

is truncated at  $F_{0.1\%}$  and  $F_{99.9\%}$ . This results in a mean of  $\mu_C = 5.22$ , a standard deviation of  $\sigma_C = 0.1867$  and a coefficient of variation of 3.6%. The distribution is shown in figure 6.9.

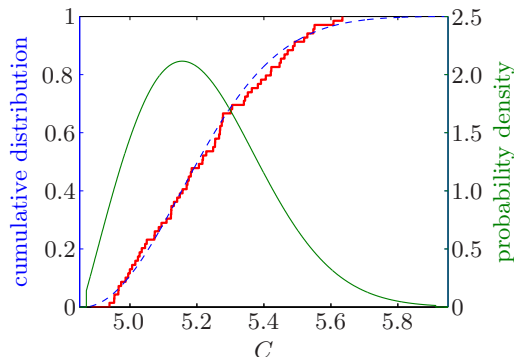


**Figure 6.9:** Probability distribution of  $C$ , with the experimental (—) and Weibull (--) cumulative distribution functions and the probability density function (—).

### Model parameter $C_{1,\epsilon}$

For parameter  $C_{1,\epsilon}$ , no probability density function is required, since it depends on  $C_{2,\epsilon}$ . Their relation is determined from homogeneous shear flow. As discussed in Pope (2000), the principal experimental observations are that the Reynolds stresses become self-similar, and that the non-dimensional parameters  $Sk/\epsilon$  and  $P/\epsilon$  become constant. Since the imposed mean shear rate  $S$  is constant, the constancy of  $Sk/\epsilon$  implies that the turbulence timescale  $\tau \equiv k/\epsilon$  is also fixed. From the two turbulent transport equations for homogeneous turbulence (6.14) and (6.15), we obtain:

$$\frac{d}{dt} \left( \frac{k}{\epsilon} \right) = \frac{d\tau}{dt} = (C_{2,\epsilon} - 1) - (C_{1,\epsilon} - 1) \left( \frac{P}{\epsilon} \right).$$

Evidently, the model predicts that  $\tau$  does not change with time for the particular value of  $P/\epsilon$ :

$$\left( \frac{P}{\epsilon} \right) \equiv \frac{C_{2,\epsilon} - 1}{C_{1,\epsilon} - 1}.$$

Substituting the commonly used values for the two coefficients of the standard deterministic  $k$ - $\epsilon$  model results in  $P/\epsilon \approx 2.09$ . In this study, the ratio  $P/\epsilon$  is fixed to 2.09 and it is adopted that the variable  $C_{1,\epsilon}$  is dependent on  $C_{2,\epsilon}$ :

$$C_{1,\epsilon} = \frac{1}{P/\epsilon} C_{2,\epsilon} + \frac{P/\epsilon - 1}{P/\epsilon}. \quad (6.18)$$

So the value for  $C_{1,\epsilon}$  is adjusted according equation (6.18) when  $C_{2,\epsilon}$  is uncertain.

### Model parameter $\sigma_\epsilon$

Parameter  $\sigma_\epsilon$  depends on the other model parameters, so like for  $C_{1,\epsilon}$  no probability density function is required. The parameter  $\sigma_\epsilon$  controls the diffusion rate of  $\epsilon$  and is determined by looking at wall flow and reproduction of the log layer [Nieuwstadt (1998); Pope (2000)].

Consider a fully developed high-Reynolds-number channel flow. In this case, the state variables only vary in a direction normal to the main flow, which is here denoted as the  $y$ -direction. The turbulent transport equations (6.10) and (6.11) then reduce to:

$$0 = \frac{d}{dy} \left[ \left( \nu + \frac{\nu_T}{\sigma_k} \right) \frac{dk}{dy} \right] + P - \epsilon, \quad (6.19)$$

$$0 = \frac{d}{dy} \left[ \left( \nu + \frac{\nu_T}{\sigma_\epsilon} \right) \frac{d\epsilon}{dy} \right] + C_{1,\epsilon} \frac{P\epsilon}{k} - C_{2,\epsilon} \frac{\epsilon^2}{k}. \quad (6.20)$$

In the log-law region, the production and dissipation balance (both are equal to  $u_\tau^2/(\kappa y)$ ) [Pope (2000)]. Hence in equation (6.19)  $P$  and  $\epsilon$  drop out, implying a uniform  $k$ . In equation (6.20), the equality of  $P$  and  $\epsilon$  leads to a net sink balanced by the diffusion of  $\epsilon$  away from the wall. Following Pope (2000), equation (6.20) is satisfied by :

$$\epsilon = \frac{C_\mu^{3/4} k^{3/2}}{\kappa y},$$

and the constants are related by:

$$\kappa^2 = \sigma_\epsilon C_\mu^{1/2} (C_{2,\epsilon} - C_{1,\epsilon}). \quad (6.21)$$

Equation (6.21) is rewritten to compute  $\sigma_\epsilon$ :

$$\sigma_\epsilon = \frac{\kappa^2}{C_\mu^{1/2} (C_{2,\epsilon} - C_{1,\epsilon})}. \quad (6.22)$$

Hence  $\sigma_\epsilon$  is dependent on  $\kappa$ ,  $C_\mu$ , and  $C_{2,\epsilon}$ , and is computed using equation 6.22 when one of these parameters is uncertain.

## 6.3 Turbulent flow over a flat plate

In this section uncertainty analysis of the  $k$ - $\epsilon$  model parameters is applied to the turbulent flat plate test case. Stochastic computational results are compared with deterministic computations and experiments. From the study of all uncertain parameters, it is concluded that  $C_\mu$ ,  $\kappa$ , and  $C$  are the most important parameters. For these parameters, the results are discussed in more detail in the final section.





near the beginning of the plate. The final grid is displayed in figure 6.11. The total simulation time is in the order of 15 minutes on an AMD Opteron 2800 MHz processor.

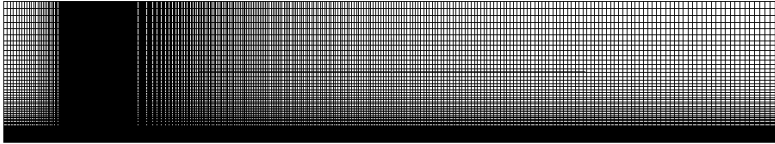


Figure 6.11: The computational grid containing 32,000 finite-volumes.

For the numerical computation, the open-source solver OpenFOAM<sup>®</sup> (2009) is used to solve the incompressible turbulent Reynolds-averaged Navier-Stokes equations using the SIMPLE algorithm. The schemes are set to first-order upwind for the transported turbulent quantities and to second-order central for the velocity field. The steady-state convergence criterion is to have a residual lower than  $10^{-7}$  for all state variables, which is attained within 1000 iterations (see figure 6.12).

Table 6.1: Properties of various grids for the grid convergence study of the turbulent flat plate test case.

Grid	# Cells	$C_d \times 10^{-3}$
1	3,976	2.9214
2	8,000	2.9343
3	15,792	2.9487
4	<b>32,000</b>	<b>2.9587</b>
5	63,958	2.9654
6	128,000	2.9701

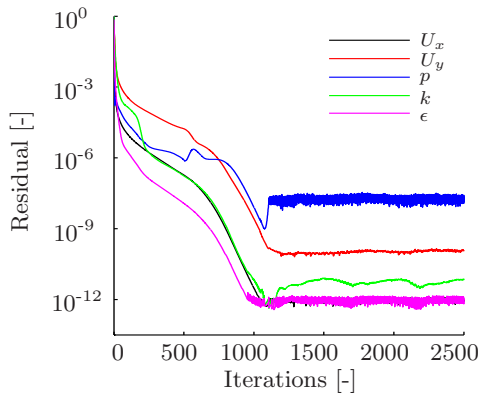


Figure 6.12: Convergence history of the residuals of the flow parameters with respect to the number of iterations.

The drag coefficient of the plate only consists of friction, so  $C_d$  is obtained by integrating the skin friction coefficient along the plate:

$$C_d = \frac{1}{L} \int_0^L C_f(x) dx, \quad (6.23)$$

with  $L$  the length of the plate. For the  $k$ - $\epsilon$  model, the drag coefficient becomes  $C_d = 0.0029587$ . White (2006) provides a relation between the drag coefficient and

### 6.3 Turbulent flow over a flat plate

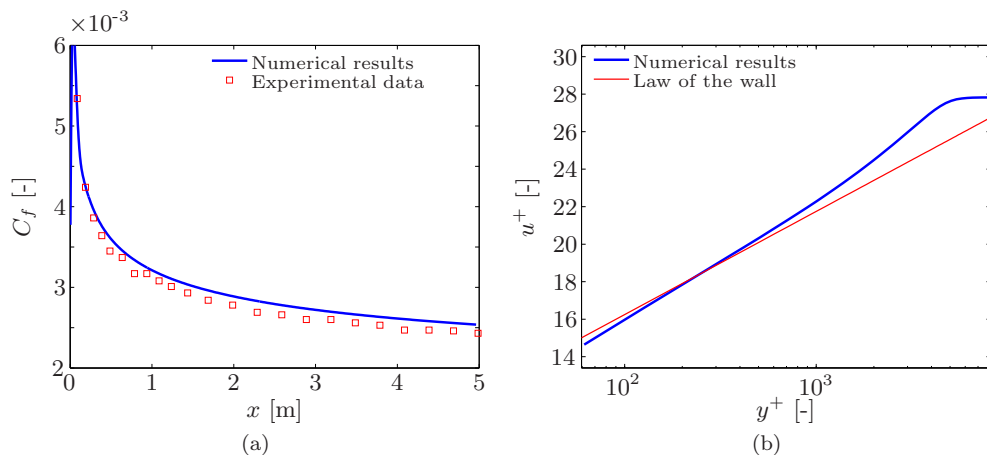


**Figure 6.13:** Numerical results compared with experiments and theory, with (a) the numerically computed skinfriction coefficient  $C_f$  compared with the experimental results of Wieghardt and Tillman (1951) and (b) the numerically computed boundary layer profile compared to the law of the wall (equation (6.13)).

the Reynolds number:

$$C_{d,\text{White}} \approx \frac{0.523}{\ln^2(0.06Re_L)}. \quad (6.24)$$

Substituting the values of the test case of this section, the estimated drag coefficient of White becomes  $C_{d,\text{White}} = 0.0029156$ , which is 1.5% lower than the  $k$ - $\epsilon$  results.

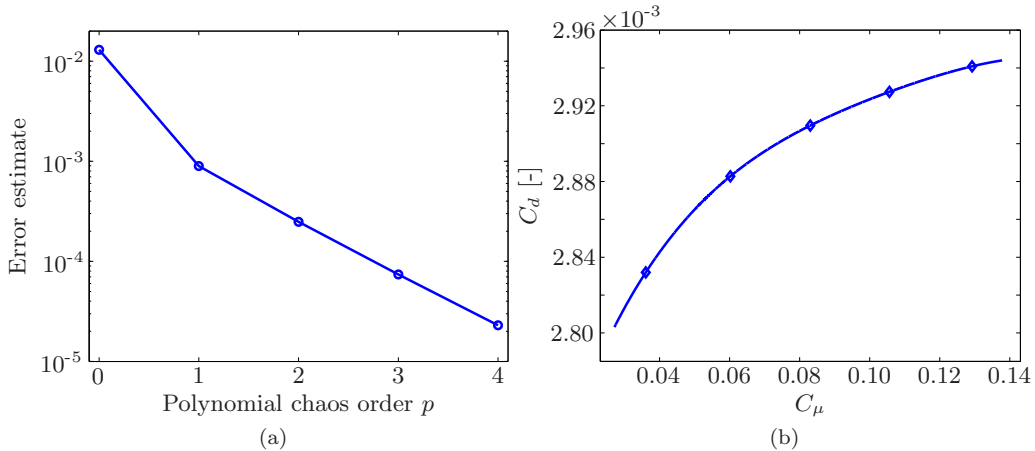
Figure 6.13 depicts the numerical results in the same graph with experimental data and the theoretical law of the wall. Figure 6.13(a) shows the skinfriction coefficient along the plate. The numerical simulations predict slightly higher values than the experimental data of Wieghardt and Tillman (1951). This effect has been mentioned by Wilcox (1993) as well. Nevertheless, all experimental data points are within 4% of the numerical predictions.

Figure 6.13(b) shows the law of the wall extracted at  $x = 4.8$  m. The red line is the theoretical relation of equation (6.13). The blue line indicates the numerical results with the defect layer visible for higher  $y^+$  values. Since wall functions are used, no numerical results are available for smaller  $y^+$  values.

#### 6.3.2 Comparing the different parameters

For every parameter the convergence of the Probabilistic Collocation method is monitored by estimating the error using an approximation of one order higher (see equation (2.21)). The error is evaluated for the drag coefficient. The convergence of the estimated error with respect to the polynomial chaos order is shown in figure 6.14(a).

The response surface of the drag coefficient (see figure 6.14(b)), is curved such that a second order polynomial cannot approximate this function well. A third order approximation still shows discrepancies at lower values for  $C_\mu$ , therefore, further results are obtained using a fourth order Probabilistic Collocation approximation, requiring 5 deterministic solves.



**Figure 6.14:** Results for an uncertain model parameter  $C_\mu$ , with (a) the convergence of the Probabilistic Collocation approximation with respect to the polynomial chaos order  $p$  and (b) the response surface of the drag coefficient  $C_d$  obtained with a fourth order Probabilistic Collocation approximation.

The convergence of the Probabilistic Collocation method for  $\kappa$  is shown in figure 6.15(a). For engineering applications a first or second order approximation is sufficiently accurate. A low order approximation suffices for the  $C_d$  result because the response surface is smooth and nearly linear, hence easy to approximate using polynomials (see figure 6.15(b)).

As the convergence of the Probabilistic Collocation method for all other parameters looks similar to the convergence for  $\kappa$ , a second order approximation is used. All figures containing the response surfaces of the drag coefficient with respect to each parameter are shown in figure C.1 in appendix C.

Table 6.2 shows the effect that all uncertain parameters have on the drag coefficient.. Most important is the coefficient of variation ( $CV = \sigma/\mu$ ) of the drag coefficient. The von Kármán constant  $\kappa$  results in the largest coefficient of variation of the drag coefficient. The parameters  $C$  and  $C_\mu$  have less influence on the drag coefficient, but are still worth taking into account. The parameters  $C_{2,\epsilon}$  and  $\sigma_k$  have a negligible effect on the drag coefficient.

Another interesting parameter is the ratio between the  $CV$  of the drag coefficient and the  $CV$  of the input parameter, here denoted as the amplification factor  $\Upsilon$ . The

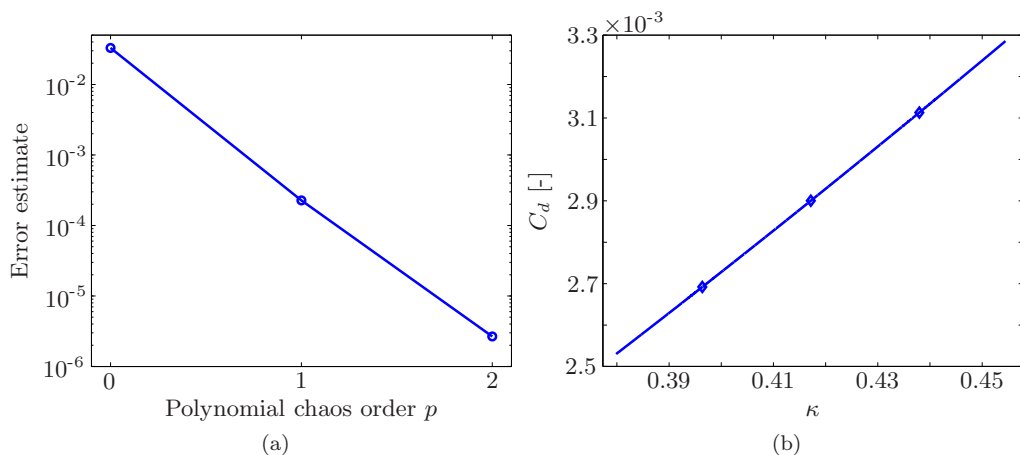


**Figure 6.15:** Results for an uncertain von Kármán constant  $\kappa$ , with (a) the convergence of the Probabilistic Collocation approximation with respect to the polynomial chaos order  $p$  and (b) the response surface of the drag coefficient  $C_d$  obtained with a second order Probabilistic Collocation approximation.

amplification factor is defined in equation (4.13), here this is  $\Upsilon = CV_{C_d}/CV_{\text{parameter}}$ .  $\Upsilon$  is an indication of the sensitivity of the drag coefficient with respect to the uncertain parameter. It tells how important it is to estimate the input distribution correctly. If the amplification factor is larger than 1, the  $CV$  of the input is amplified. This results in a larger  $CV$  of the drag coefficient than the input  $CV$ . If the amplification is much smaller than 1, the system is not sensitive to variation of the uncertain parameter.

The coefficient of variation of  $\kappa$  is by far dominant for  $C_d$  followed by the wall function parameter  $C$ . This could be anticipated since  $C_d$  is derived from the state variables in the cells closest to the wall, exactly where the wall functions are applied. Model parameter  $C_\mu$  has a low amplification factor, but due to the high input coefficient of variation, the impact on the drag coefficient is important to take into account. The remaining parameters have a considerably smaller effect with  $\sigma_k$  the least important. Turgeon et al. (2002) concluded from a sensitivity study that variations in  $\sigma_k$  have the least effect on  $C_d$ , which is in agreement with the current results.

All results for each uncertain parameter can be found in appendix C. The appendix shows the response surfaces in figure C.1, the statistics of the law of the wall and the skinfriction coefficient along the plate in figures C.2 and C.3 respectively. Furthermore, the probability distribution functions of the drag coefficient are depicted in figure C.4.

In order to demonstrate the effect of each parameter in the freestream, figure 6.16 shows profiles of the coefficients of variation of the velocity  $CV_U$  and the eddy viscosity  $CV_{\nu_T}$  near the end of the plate at  $x = 4.8\text{m}$ , where the boundary layer is fully

**Table 6.2:** Statistics of the drag coefficient  $C_d$  for each uncertain parameter. The mean  $\mu_{C_d}$  and the standard deviation  $\sigma_{C_d}$  are obtained from the Probabilistic Collocation method. The difference between the mean and the value of White (2006),  $C_{D,White} = 0.0029156$ , is listed. Also the coefficient of variation  $CV = \mu/\sigma$  and the amplification factor  $\Upsilon = CV_{C_d}/CV_{parameter}$  are shown.

Parameter	$\mu_{C_d}$ $\times 10^{-3}$	$\epsilon^{White}$ %	$\sigma_{C_d}$ $\times 10^{-4}$	$CV_{C_d}$ %	Amplification factor $\Upsilon$
$C_\mu$	2.9070	-0.293	0.1943	0.668	0.0288
$C_{2,\epsilon}$	2.9157	0.006	0.0061	0.021	0.0440
$\sigma_k$	2.9157	0.006	0.0007	0.003	0.0015
$\kappa$	2.9010	-0.499	1.2517	4.315	1.4365
$C$	2.9207	0.174	0.3362	1.151	0.3218

developed. It is confirmed that these profiles are qualitatively speaking identical for the last three meters of the plate, hence the discussion is representative for the part where the boundary layer is fully developed.

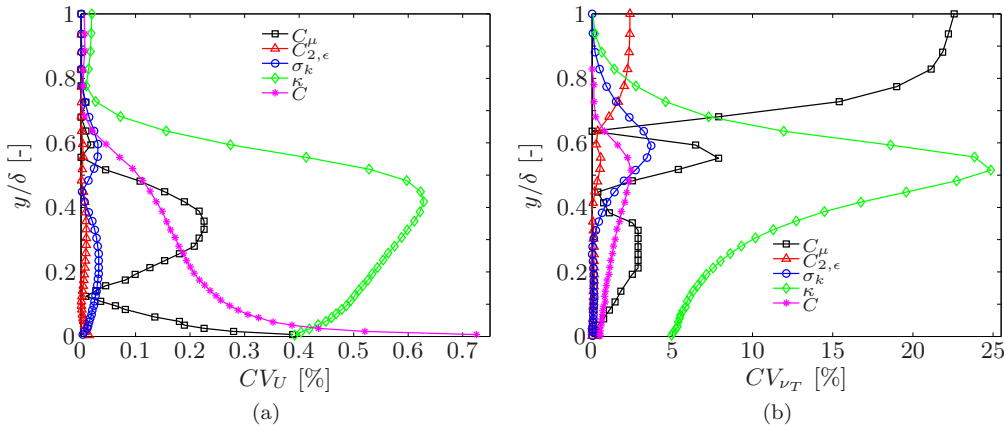


**Figure 6.16:** Boundary layer profiles for the coefficient of variation of (a) the velocity  $CV_U$  and (b) the eddy viscosity  $CV_{\nu_T}$  at a streamwise location of  $x = 4.8m$ .

Figure 6.16(a) shows that both wall function parameters  $\kappa$  and  $C$  and  $C_\mu$  are dominant for variations in  $U$ . At the cell closest to the wall, uncertainty is largest for parameter  $C$ .

Figure 6.16(b) shows the effect on the eddy viscosity. Parameter  $\kappa$  is dominant inside the boundary layer and near the wall. Parameters  $C_{2,\epsilon}$  and  $C_\mu$  have an effect on the eddy viscosity of the free stream as well. The uncertainty in  $C_{2,\epsilon}$  leads to a different decay in the free stream for each deterministic solve. Finally, recall that  $\nu_T = C_\mu k^2/\epsilon$ , hence the uncertainty in  $C_\mu$  is directly propagated to  $\nu_T$ . Despite the

### 6.3 Turbulent flow over a flat plate

non-zero variation in the free stream for these three variables, the effect on the mean velocity is negligible because the mean strain rate tensor is zero in the correspondent region. The uncertain  $\kappa$  results in the coefficient of variation of the eddy viscosity in the boundary layer of 25%, which is a huge amplification of the input variation of 3%.

Since the wall function parameters  $\kappa$ ,  $C$ , and  $C_\mu$  have a significant effect on the drag coefficient and the flow field, they are discussed in more detail below. A combined analysis where all parameters are simultaneously is not performed. Apart from  $\kappa$ , the amplification factors of the drag coefficient are much smaller than one and the standard deviation much smaller than one drag count.

#### Von Kármán constant $\kappa$

In this section, the parameter  $\kappa$  is discussed in more detail, since it has the largest influence on the drag coefficient  $C_d$ .

Figure 6.17 shows the results for the drag coefficient and the skinfriction coefficient along the plate. The statistics are obtained from a second order Probabilistic Collocation approximation. First, figure 6.17(a) shows the probability distribution functions of the drag coefficient. The almost linear response surface results in a distribution of  $C_d$  which is very close to a truncated normal distribution (similar to the distribution of  $\kappa$ ). The uncertainty interval stretches over nearly 8 drag counts.

In figure 6.17(b), the statistics of the friction coefficient along the plate are shown. In addition, the figure shows the experimental results of Wieghardt and Tillman (1951) and the deterministic  $k$ - $\epsilon$  results. The stochastic results are shown as the mean and the 100% uncertainty interval. A large spread is present in  $C_f$ , and all experimental values fall well within the uncertainty region. Interesting is the fact that the mean curve is closer to the experimental values than the deterministic  $k$ - $\epsilon$  solution.

#### Wall function parameter $C$

The second parameter that has a significant influence on the drag coefficient  $C_d$  is the wall function parameter  $C$ , which has a Weibull distribution. The convergence of the Probabilistic Collocation method for  $C$  is similar to the convergence for  $\kappa$ . A second order Probabilistic Collocation approximation is used for further results. Like for  $\kappa$ , the response surface is smooth and almost linear, see figure C.1(e) in appendix C.

Figure 6.18(a) shows the probability distributions functions of the drag coefficient resulting from uncertain  $C$ . The uncertainty interval stretches over approximately 2 drag counts. Since the response surface is almost linear, the probability density and cumulative distribution function are very close to a Weibull distribution.

The statistics for the skinfriction coefficient are given in figure 6.18(b). The uncertainty interval along the complete length of the plate covers all experimental values. Again, the mean curve is closer to experimental values than the standard  $k$ - $\epsilon$  result. For this case it is clear that the 100% interval obtained from the cumulative distribu-

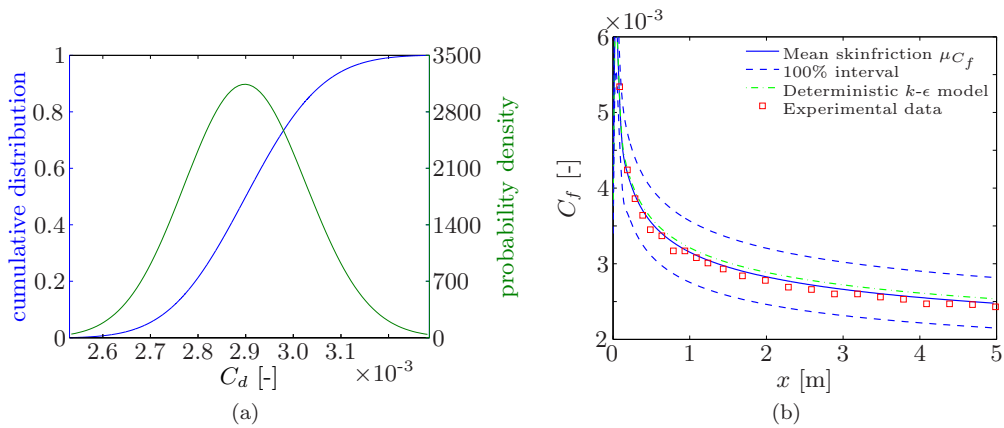


**Figure 6.17:** Results for an uncertain von Kármán constant  $\kappa$ , with (a) the probability density (–) and the cumulative distribution (–) function of the drag coefficient  $C_d$  and (b) skinfriction coefficient  $C_f$  along the plate, obtained with a second order Probabilistic Collocation approximation.

tion function provides valuable information. The uncertainty interval is asymmetric, with a larger spread below the mean. By plotting just  $\mu \pm \sigma$  this effect would be missed and the interval would be too large above the mean.

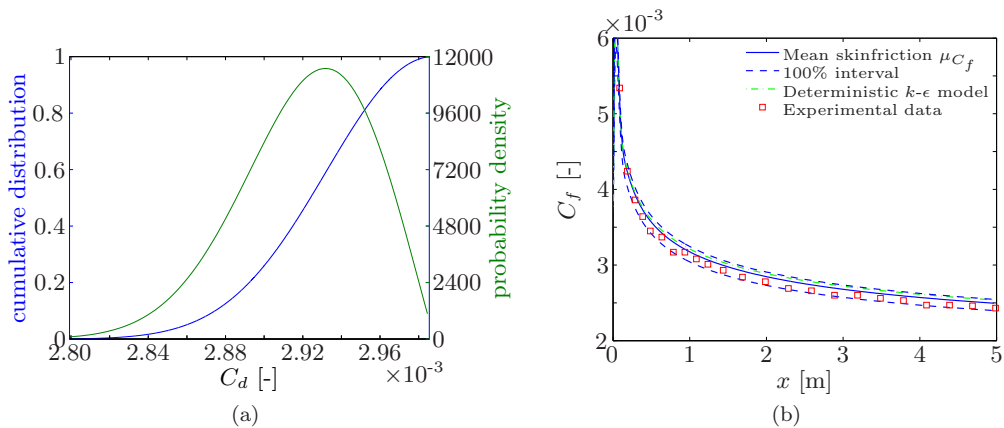


**Figure 6.18:** Results for an uncertain wall function parameter  $C$ , with (a) the probability density (–) and the cumulative distribution (–) function of the drag coefficient  $C_d$  and (b) skinfriction coefficient  $C_f$  along the plate, obtained with a second order Probabilistic Collocation approximation.



**Model parameter  $C_\mu$** 

Due to the large coefficient of variation of  $C_\mu$ , the effect on the drag coefficient is significant. Even though the drag coefficient is not very sensitive to changes in  $C_\mu$ .

Figure 6.19(a) shows the probability distributions functions of the drag coefficient resulting from uncertain  $C_\mu$ . The uncertainty interval stretches over approximately 1 drag count. Due to the nonlinear response surface, the distribution function is not close to the logistic distribution anymore.

The skinfriction coefficient is shown in figure 6.19(b). The figure shows the mean and 100% interval obtained from the Probabilistic Collocation approximation, the deterministic results and the experimental data of Wieghardt and Tillman (1951). The mean of  $C_\mu$  is lower than the deterministic value. For the flat plate case, the lower value results in a better approximation of the skinfriction coefficient. The mean skinfriction coefficient  $\mu_{C_f}$  is closer to the experimental data than the deterministic curve. All experimental data points are within the interval.

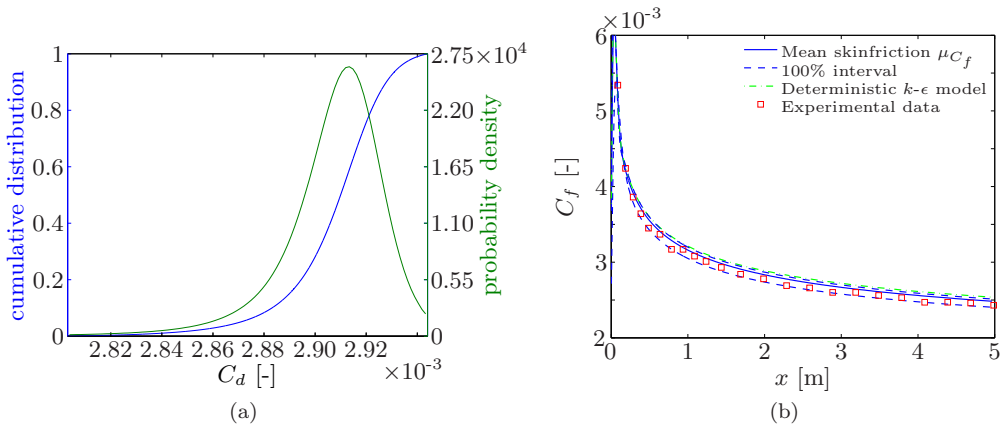


**Figure 6.19:** Results for an uncertain model parameter  $C_\mu$ , with (a) the probability density (–) and the cumulative distribution (–) function of the drag coefficient  $C_d$  and (b) skinfriction coefficient  $C_f$  along the plate, obtained with a fourth order Probabilistic Collocation approximation.

**6.4 Flow around a NACA0012 airfoil**

This section presents the influence of the uncertain  $k-\epsilon$  model parameters on flow around a NACA0012 airfoil. First, a general description of the deterministic test case is given. Secondly, the influence of all uncertain parameters is investigated. The final section shows the results for  $C_\mu$  and  $\kappa$  in more detail, since these parameters have the largest influence on the solution.

### 6.4.1 Deterministic test case description

The case settings are equal to those of Gregory and O’Reilly (1973) and Zingg (1991). The Mach number is set to  $M = 0.16$  and the Reynolds number is  $2.88 \times 10^6$ . The airfoil is put under an angle of attack of  $6^\circ$ .

The turbulence intensity at the test section was measured by Gregory and O’Reilly (1973) to be  $\mathcal{I} \approx 0.25\%$ . The boundary conditions for  $k$  and  $\epsilon$  are set such that the turbulence intensity at the airfoil matches the experimental turbulence intensity.

**Table 6.3:** Properties of various grids for the grid convergence study of the NACA0012 test case.

Grid	# Cells	$C_l$	$C_d$
1	30,792	0.63696	0.014793
2	32,600	0.63670	0.014734
3	39,129	0.63641	0.014754
4	53,203	0.63660	0.014628
5	88,036	0.63680	0.014452
<b>6</b>	<b>131,265</b>	<b>0.63756</b>	<b>0.014176</b>
7	188,988	0.63756	0.014181
8	330,272	0.63756	0.014179

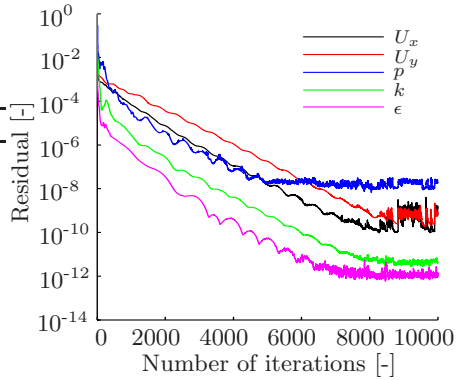


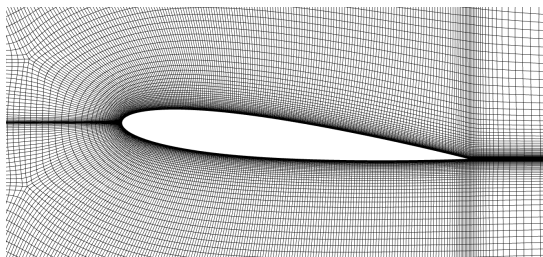
**Figure 6.20:** Typical convergence history for all state variables.

The solution is evaluated on a structured grid with C-topology created using GridPro. The computational grid is refined near and behind the airfoil to capture the boundary layer and the wake. OpenFOAM<sup>®</sup> (2009) is used to solve the incompressible Reynolds averaged Navier-Stokes equations numerically. The steady-state convergence criteria is set to an absolute residual lower than  $10^{-7}$  for all state variables. Figure 6.20 shows a convergence history for a typical solve. One sees that convergence is reached within 6,000 iterations, this takes about 6 hours on a single AMD Opteron 2220 processor for a grid of 131,265 cells.

A grid convergence study on 8 grids has been performed, all having the same settings for the boundary layer to assure the right  $y^+$  value. The lift and drag coefficient for all grids are listed in table 6.3. From grid 6 onwards, the absolute variation in the lift coefficient is below  $10^{-5}$ . The drag coefficient variation is less than a drag count. Compared to Zingg (1991), this variation is acceptable and grid 6 is chosen to be used for the simulations in the remainder of this section.

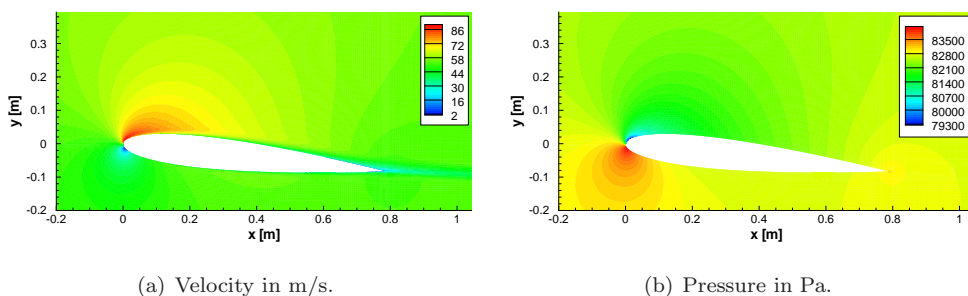
The variation in  $y^+$  of the cells adjacent to the airfoil is within the limits of the log-law region:  $20.36 \leq y^+ \leq 76.85$  and a mean value of 39.40. The final grid is depicted in figure 6.21.

Figure 6.22 shows the deterministic velocity and pressure field. Note that the incompressibility assumption still holds since the maximum Mach number is  $M_{\max} \approx$



**Figure 6.21:** Final C-grid with 131,265 cells used for flow around the NACA0012 airfoil.

$86/340 \approx 0.25$ , well below the generally taken incompressibility limit of  $M < 0.3$ . The pressure (see figure 6.22(b)) shows a high pressure at the stagnation point and a low pressure at the suction peak. In contrast with the turbulent flat plate test case, a pressure gradient is present along the airfoil.



**Figure 6.22:** Velocity and pressure fields obtained with the standard  $k-\epsilon$  model for the NACA0012 at  $6^\circ$  angle of attack.

The numerical solution is compared to a roughened airfoil, since the simulations involve fully turbulent flow. In Abbott and Doenhoff (1959), the section properties of a roughened NACA0012 profile are listed. In the experimental set-up, the leading-edge roughness consists of 0.011 inch carborundum grains applied over a surface length of  $0.08\bar{c}$  and on both sides of the model. For a  $6^\circ$  angle of attack, the lift coefficient is  $\sim 0.63$  and the drag coefficient  $\sim 0.0145$ . When compared to the values in table 6.3, the lift and drag coefficient are within 1% and 3%, respectively, of the experimental results.

The pressure coefficient is defined as  $C_p = (p - p_\infty) / (\frac{1}{2}\rho U_\infty^2)$ , where  $p$  is the pressure at which  $C_p$  is evaluated. In Gregory and O'Reilly (1973), the pressure coefficient is measured. Figure 6.23 shows the numerical and experimental results, where good agreement can be seen. It is concluded that the numerical simulation yields satisfactory results.

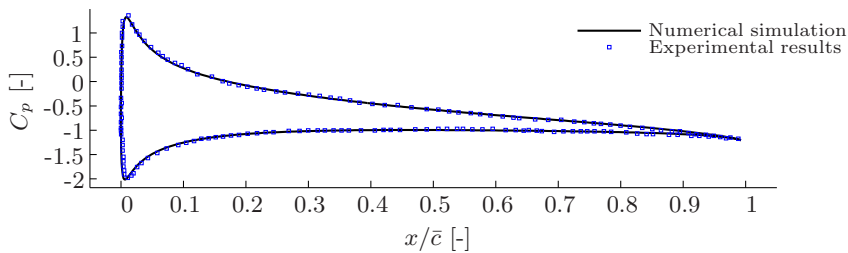


Figure 6.23: Comparison of numerical and experimental pressure coefficient along the airfoil at  $6^\circ$  angle of attack.

### 6.4.2 Influence of each individual parameter

In this section, the five uncertain parameters as given in section 6.2 will separately be assumed uncertain. Convergence of the Probabilistic Collocation method is monitored by evaluating the estimated error of the lift and drag coefficient using an approximation of one order higher (see equation (2.21)).

Figure 6.24 shows the convergence of the estimated error with respect to the polynomial chaos order. For  $C_\mu$  the response surface is curved as it is the case for the turbulent flat plate test case. The convergence is shown in figure 6.24(a). A fourth order approximation is used to propagate  $C_\mu$ . The responses of the other parameters are smooth, almost linear, so a second order approximation is sufficient (see e.g. the convergence for  $\kappa$  in figure 6.24(b)).

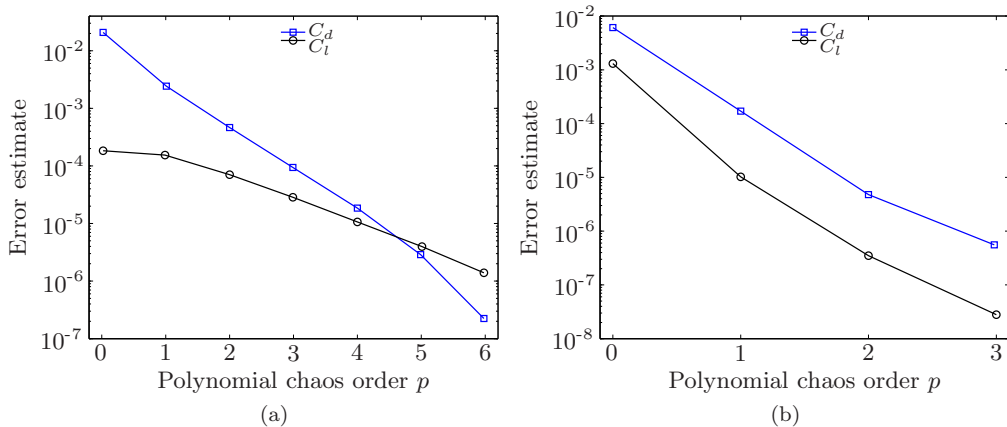


Figure 6.24: Convergence of the Probabilistic Collocation for the lift  $C_l$  and drag coefficient  $C_d$  with respect to the polynomial chaos order  $p$  for uncertain (a) model parameter  $C_\mu$  and (b) the von Kármán constant  $\kappa$ .

Table 6.4 summarizes the results for all uncertain parameters. Looking at the coeffi-

## 6.4 Flow around a NACA0012 airfoil

coefficients of variation of the lift and drag coefficient, it can be concluded that the effect of most uncertain parameters is small. Only  $C_\mu$  has a significant effect on the drag coefficient with a coefficient of variation of 2.967%. As for the flat plate, the solution is not sensitive to variation in model parameter  $C_\mu$ , but due to the large variation of  $C_\mu$  the lift and drag coefficients shows a significant variation. The second parameter that has some influence is  $\kappa$ , which results in the second largest coefficient of variation for the drag coefficient of 0.881%. For the lift coefficient,  $\kappa$  results in a small coefficient of variation of 0.188%, while all other parameters have a negligible effect. The largest amplification factor is, however, obtained for  $C_{2,\epsilon}$  for both  $C_l$  and  $C_d$ . Due to the small coefficient of variation of  $C_{2,\epsilon}$ , the influence on  $C_l$  and  $C_d$  is negligible.

The mean values of  $C_l$  and  $C_d$ , are lower than the deterministic values of 0.6376 and 0.01418 respectively. In addition, the mean values of  $C_l$  are slightly closer to the experimental value of 0.63, while the mean values of  $C_d$  are up to 3.6 counts further away from the experimental value of 0.0145. The conclusion of the sensitivity study of Turgeon et al. (2002) is confirmed: the solution is least influenced by variations in  $\sigma_k$ .

Below the results for  $C_\mu$  and  $\kappa$  are discussed in more detail. A more detailed discussion of the other parameters can be found in the master thesis of Platteeuw (2008). Combined effects by propagating all parameters simultaneously are not investigated here.

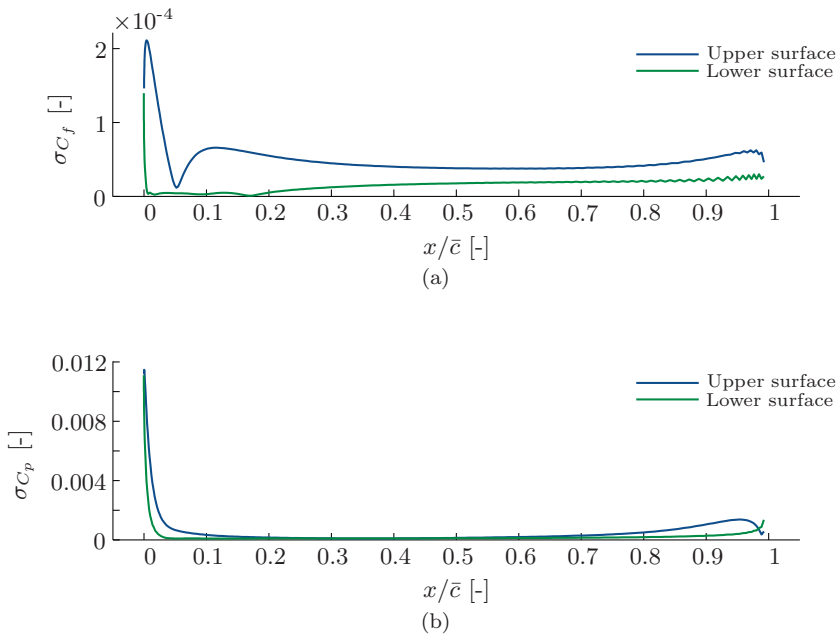
**Table 6.4:** Statistics of the lift coefficient  $C_l$  and drag coefficient  $C_d$  of the NACA0012 airfoil obtained from the Probabilistic Collocation method in combination with OpenFOAM<sup>®</sup> (2009).

Parameter	$C_l$			
	$\mu$	$\sigma \times 10^{-3}$	$CV$	$\Upsilon$
$C_\mu$	0.6371	0.3121	0.049	0.0021
$C_{2,\epsilon}$	0.6372	0.2725	0.043	0.0899
$\sigma_k$	0.6376	0.1194	0.019	0.0112
$\kappa$	0.6374	1.1980	0.188	0.0626
$C$	0.6374	0.5857	0.092	0.0256
Parameter	$C_d$			
	$\mu \times 10^{-2}$	$\sigma \times 10^{-4}$	$CV$	$\Upsilon$
$C_\mu$	1.382	4.1000	2.967	0.1279
$C_{2,\epsilon}$	1.399	0.2775	0.198	0.4174
$\sigma_k$	1.418	0.1034	0.073	0.0438
$\kappa$	1.398	1.2320	0.881	0.2934
$C$	1.417	0.3967	0.280	0.0783

Parameter  $C_\mu$

Figure 6.25 shows the standard deviation of the skinfriction and pressure coefficient along the surface of the airfoil. The largest standard deviation of  $C_f$  is located at the upper side of the airfoil, see figure 6.25(a). The irregular behavior at the trailing edge is numerical noise, also found in the mean  $C_f$  solution. The maximum value is found at the suction peak near the leading edge. Proceeding in streamwise direction along the upper surface, a dip centered at  $0.06\bar{c}$  is encountered. After that, the standard deviation for  $C_f$  is more or less constant. At the lower surface, the  $C_f$  uncertainty is increasing slightly towards the trailing edge.

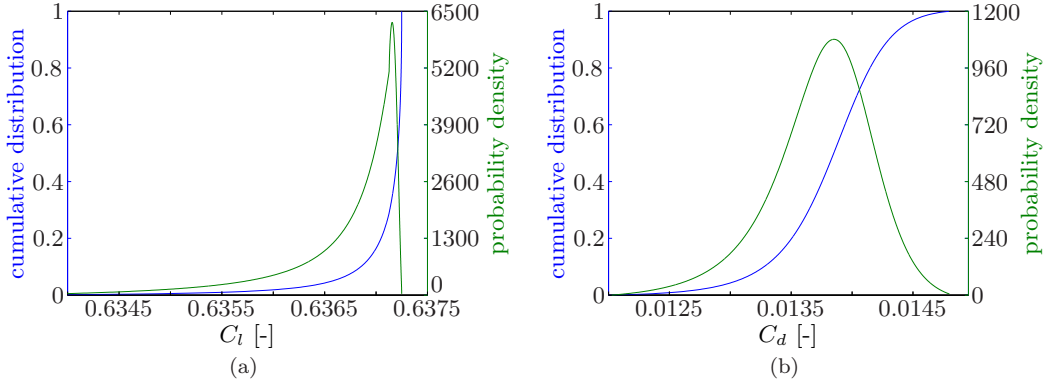
Figure 6.25(b) shows that the largest standard deviation of  $C_p$  is located near the suction peak. Considering the adverse pressure gradient region at the upper surface, one sees that the standard deviation in  $C_p$  is increasing near the aft of the airfoil. At the lower surface, the adverse pressure gradient region is more aft, and the standard deviation increases from  $x/\bar{c} > 0.8$ .



**Figure 6.25:** Standard deviation of (a) the skinfriction coefficient  $\sigma_{C_f}$  and (b) the pressure coefficient  $\sigma_{C_p}$  along the airfoil surface resulting from the uncertain parameter  $C_\mu$  obtained with a fourth order Probabilistic Collocation approximation.

Figure 6.26 shows the probability distribution functions of the lift and drag coefficient of the airfoil. As the response surface of  $C_l$  is curved, the shape of the distribution functions (see figure 6.26(a)) are, therefore, a non-linear transformation of the input

distribution. The distribution functions of  $C_l$  cover about 2 liftcounts and high values of  $C_l$  are most likely to occur. Figure 6.26(b) shows the distribution functions of  $C_d$ . The response surface is close to linear, therefore, the distribution of  $C_d$  is close to a logistic distribution (similar to  $C_\mu$ ). The probability distribution functions of  $C_d$  stretches over 23 drag counts.



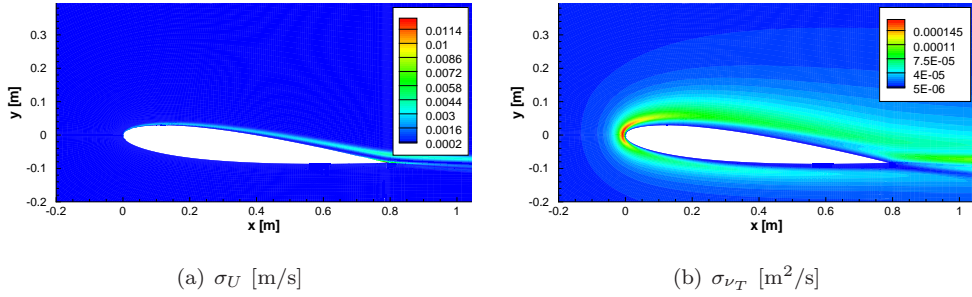
**Figure 6.26:** Probability distribution functions of (a)  $C_l$  and (b)  $C_d$  resulting from uncertain parameter  $C_\mu$ , obtained using a fourth order Probabilistic Collocation approximation.

Figure 6.27 depicts the standard deviation of the velocity and eddy viscosity in the flow field. In figure 6.27(a), the largest standard deviation is present in the upper part of the boundary layer, with a maximum near the trailing edge. In the wake, the standard deviation is decaying. For the eddy viscosity (see figure 6.27(b)), the standard deviation is mainly located at the upper boundary layer and the region above, with a maximum found near the leading edge. In the wake, the standard deviation is increasing downstream.

### Von Kármán constant $\kappa$

The standard deviation of the pressure and eddy viscosity resulting from an uncertain  $\kappa$  is very small. Integrating these quantities, however, shows a noticeable effect in the probability distributions of the lift and drag coefficient (see figure 6.28). Both responses are smooth and almost linear and cover almost 7 counts. Therefore, the distribution are close to a truncated normal distribution, similar to the distribution of  $\kappa$ .

Figure 6.29 displays the standard deviation field of the velocity and eddy viscosity. The largest standard deviation of  $U$  is found in the upper part of the boundary layer. The standard deviation of the velocity attains a peak in the wake originating from the upper surface. Behind the airfoil, the standard deviation of  $U$  is decaying. The



**Figure 6.27:** Standard deviation of (a) the velocity  $\sigma_U$  and (b) the eddy viscosity  $\sigma_{\nu_T}$  resulting from an uncertain parameter  $C_\mu$  obtained with a fourth order Probabilistic Collocation approximation.

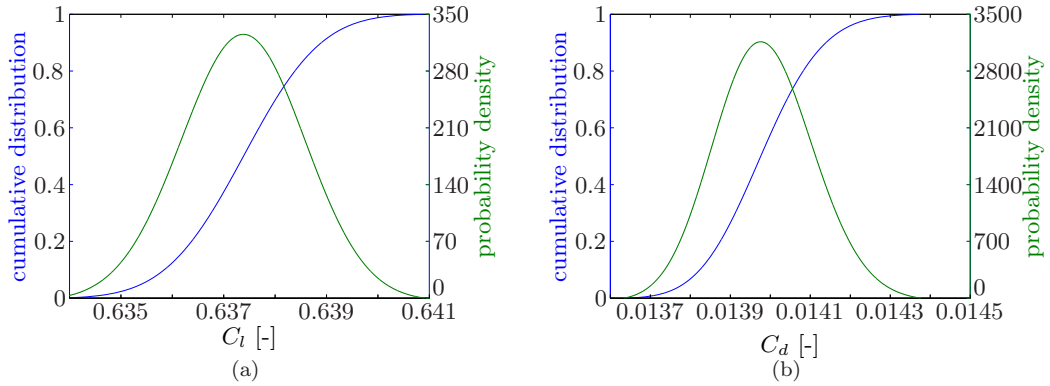


**Figure 6.28:** Probability distribution functions of (a)  $C_l$  and (b)  $C_d$  resulting from an uncertain von Kármán constant  $\kappa$ , obtained using a fourth order Probabilistic Collocation approximation.



standard deviation of  $\nu_T$  is largest inside the boundary layer and wake.

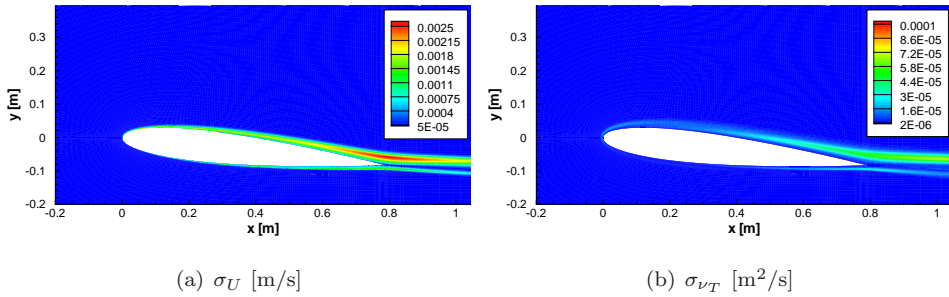


**Figure 6.29:** Standard deviation of (a) the velocity  $\sigma_U$  and (b) the eddy viscosity  $\sigma_{\nu_T}$  resulting from an uncertain von Kármán constant  $\kappa$  obtained with a second order Probabilistic Collocation approximation.

## 6.5 Summary

The  $k$ - $\epsilon$  turbulence model and the standard wall functions contain several parameters that are tuned to computed or measured simplified flow problems. Some parameters are related to each other to assure physical laws are maintained. Finally, 5 parameters were left over to be analysed as uncertainties in the model, i.e.  $C_\mu$ ,  $C_{2,\epsilon}$ ,  $\sigma_k$ ,  $\kappa$ , and  $C$ . Two test cases were performed. Firstly, a fully developed turbulent boundary layer on a flat plate and secondly, turbulent flow around a NACA0012 airfoil.

As a general conclusion, the effect of uncertainties in the parameters on the flow solution is case dependent. For both performed test cases, different effects were shown. In case of the turbulent flat plate, the wall function parameter  $\kappa$  was dominant with a coefficient of variation of 4.3% for the drag coefficient. Although the drag coefficient was not much affected,  $C$  and  $C_\mu$  had a significant contribution to the standard deviation of the skinfriction coefficient along the plate. The introduction of different flow topologies such as a stagnation point, a suction peak, and a wake lead to different conclusions about the relative importance of coefficients for the airfoil test case. Only  $C_\mu$  and  $\kappa$  resulted in maximum 0.2% and 3% coefficient of variation for the lift and drag coefficient respectively.



---

# Operational uncertainties for a transonic compressor rotor

---

The compressor is one of the most sensitive components of a gas turbine. The performance is sensitive to variability in geometry and operating conditions. Uncertainty analysis is, therefore, of great importance to assure robustness of the design. The goal of this chapter is to demonstrate the use of the Probabilistic Collocation method for a turbomachinery case. Furthermore, the effect of operational uncertainties on the performance of the rotor is investigated. Recently, uncertainty quantification has been applied to CFD computations in turbomachinery [Gopinathrao, Mabilat and Alizadeh (2009); Gopinathrao, Bagshaw, Mabilat and Alizadeh (2009); Loeven and Bijl (2010)]. A commonly used test case for turbomachinery is the NASA Rotor 37 test case [Reid and Moore (1978); Dunham (1998)].

In 1993, a large group of researchers computed the NASA Rotor 37 test case on invitation of the ASME Turbomachinery Committee using RANS codes [Wisler (1993)]. These were blind simulations, only the geometric data were provided. The contributors to the study of Dunham (1998) had access to the experimental data when the computations were performed. The comparison between the experiments and CFD computations showed quite some differences. For example the efficiency was almost always underpredicted, possibly due to the treatment of the tip clearance in the simulations. Furthermore, the shock wave is stronger and more upstream in the computations than in the experiments. Dunham (1998) states that the main con-

## *Chapter 7: Operational uncertainties for a transonic compressor rotor*

tribution to the differences lies in the assumption of steady flow and the choice of turbulence model.

Gopinathrao, Bagshaw, Mabilat and Alizadeh (2009) have successfully applied the Probabilistic Collocation method to NASA Rotor 37 using Fluent and investigated how the choice of probability distribution for the uncertain parameters affects the solution. In this chapter, a quasi-3D study is used to validate the applicability of the Probabilistic Collocation method to a turbomachinery test case against a Monte Carlo simulation. Furthermore, standard deviation plots of flow quantities are shown to reveal areas in the flow field that are sensitive to operational uncertainties.

The rotor of a gas turbine is subject to several sources of uncertainty. One of them is operational uncertainty. It is always present when the rotor is operated in an environment that is different from the design conditions. Two operational uncertainties are considered. First the static outlet pressure in the validation test case and secondly, the total pressure profile at the inlet of the rotor for the 3D simulation. Another source of uncertainty is geometrical imperfection. Due to manufacturing tolerances or wear, the actual geometry might be different from the designed geometry. Especially, the effect of the tip clearance is known to have a significant effect on the efficiency of the rotor [Chima (1998); Gerolymos and Vallet (1999); Beheshti et al. (2004)]. In this chapter operational uncertainties are considered.

The effect of uncertainties on NASA Rotor 37 is investigated using the Probabilistic Collocation method with the FINE™/Hexa solver of Numeca International as a deterministic flow solver. First a quasi-3D computation, which represents a slice at 50% blade height, is performed to validate the applicability of the Probabilistic Collocation to the NASA Rotor 37 test case. A Monte Carlo simulation of 10,000 Latin Hypercube samples has been performed to obtain a stochastic reference solution. The quasi-3D case contains all features that characterize the flow through the compressor rotor. One important feature is the bow shock in front of the leading edge of the blade. The shock wave impinges on the boundary layer on the next blade. The static outlet pressure is assumed to be uncertain and to have a symmetric beta probability distribution. A symmetric beta distribution has the property that the mean value is most probable to occur. Furthermore, it is limited to an interval, where the probability smoothly decreases to zero near the edges of the interval. The Probabilistic Collocation method shows with 5 deterministic solves good correspondence with the Monte Carlo simulation.

After validating the Probabilistic Collocation method, it is applied to a 3D simulation of the rotor. Uncertainties are present in the total pressure profile at the inlet of the rotor. A symmetric beta distribution is assumed, with the interval chosen such that the standard deviation is in the order of the accuracy of the experiments of Reid and Moore (1978). The effect on the efficiency, total pressure ratio, mass flow, and the compressor map are shown. Furthermore, the mean and standard deviation of the static pressure in the flow field are visualized to show areas in the flow field that are sensitive to the uncertainties in the total pressure profile at the inlet of the rotor.

## 7.1 Deterministic test case description

NASA Rotor 37 was originally designed and tested as part of a research program involving four related axial-flow compressor stages [Reid and Moore (1978)] typical for aircraft turbine engines. It is shown in figure 7.1(a). The rotor has 36 blades with an aspect ratio of 1.19. The designed efficiency is  $\eta_{\text{design}} = 0.877$  with a total pressure ratio of  $p_2/p_{1\text{design}} = 2.106$ . The measured peak efficiency by Reid and Moore (1978) was  $\eta_{\text{measured}} = 0.876$  with a total pressure ratio of  $p_2/p_{1\text{measured}} = 2.056$ . The maximum attained mass flow is  $\dot{m}_{\text{choke}} = 20.93$  kg/s [Dunham (1998)].

### 7.1.1 Computational settings

The flow through NASA Rotor 37 is simulated by the Reynolds averaged Navier-Stokes equations in combination with the Spalart-Allmaras turbulence model. The equations are solved on a computational grid, which is described in the next section. The boundary conditions are treated at the end of this section.

#### The computational model and grid

The computational model of the NASA Rotor 37 consists of one blade with periodic boundary conditions, as shown in figure 7.1(d). The model of the complete rotor, i.e. 36 repeated blades, is shown in front view in figure 7.1(b) and from the side in 7.1(c).

The blade geometry can be found in the work of Reid and Moore (1978). Appendix D shows sections of the blade near the hub, at midspan and near the tip. Between the blade and the shroud a small gap is present, known as the tip clearance. The tip clearance is 0.356 mm. It is important to model the tip clearance correctly, since it has a significant influence on the results. Extensive research has been performed to the effect of the tip clearance by Gerolymos and Vallet (1999) and Beheshti et al. (2004).

The influence of the 3D computational grid was investigated by Tartinville and Hirsch (2006). The grid that is used, contains approximately 600,000 cells. Parts of the grid are shown in figure 7.2. A top view of the surface grid on the hub is displayed in figure 7.2(a). Figure 7.2(b) shows a close view of the blade near the hub. It is assured that along the surface  $y^+ = 1-2$ , to comply with the Spalart-Allmaras turbulence model. Furthermore, the grid is refined near the tip to capture the flow phenomena around the tip clearance. 37 cells are present in the tip gap in radial direction.

#### Boundary conditions

The rotational speed of the rotor is 17188.7 rpm (1800 rad/s), leading to a tip-speed of 454 m/s (1500 ft/s). The hub and blade in the computational model are rotating,

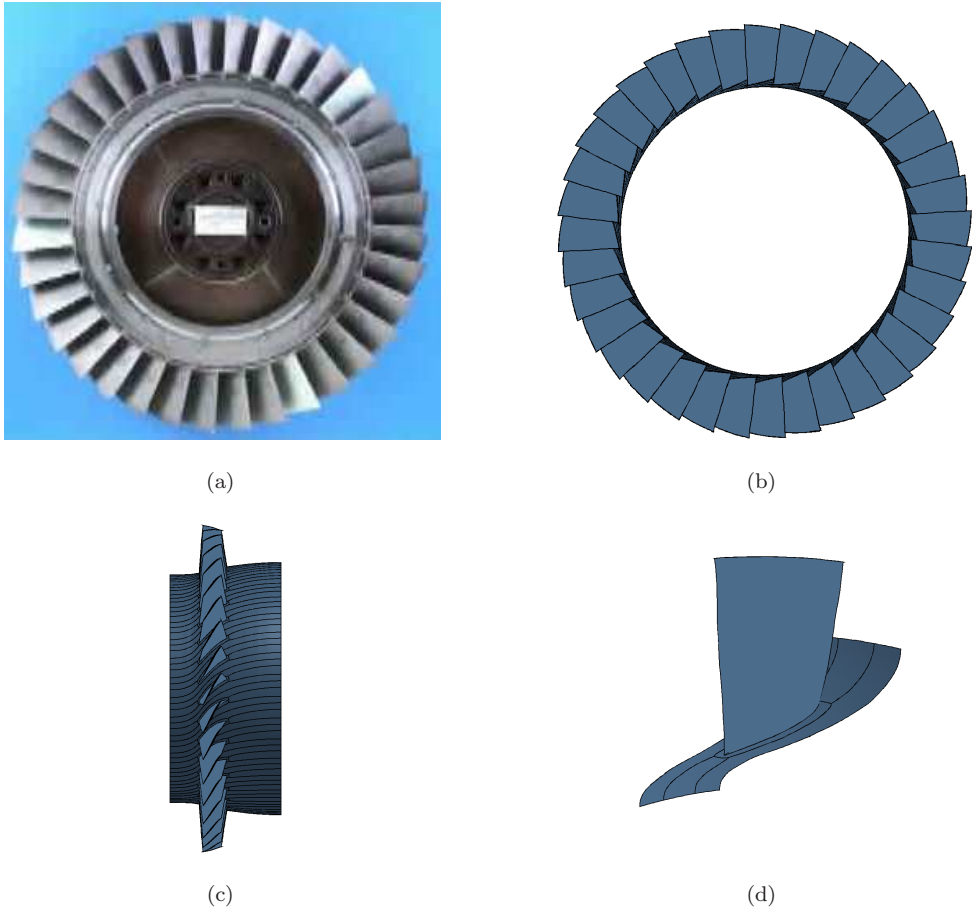


**Figure 7.1:** NASA Rotor 37, (a) real model front [Source: <http://www.grc.nasa.gov>] and (b) computational model front, (c) model side, (d) single blade.

## 7.1 Deterministic test case description

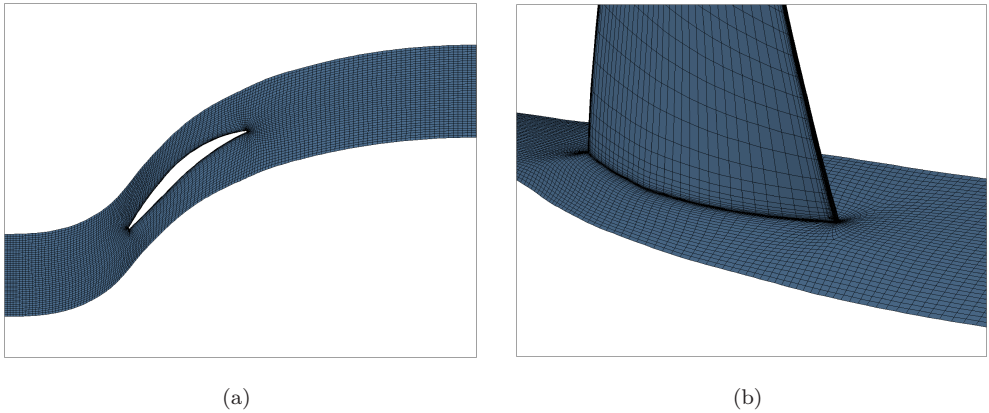


**Figure 7.2:** 3D computational grid for NASA Rotor 37, (a) a top view of the grid on the hub and (b) a close view of the blade near the hub.

while the shroud is kept fixed. At the inlet, a total pressure  $p_{t,\text{in}}$  and total temperature  $T_{t,\text{in}}$  profile are specified, which are experimentally determined and can be found in the work of Dunham (1998). The static outlet pressure is varied to change the mass flow and construct the compressor maps. At maximal efficiency, the static outlet pressure 1.175 bar.

### 7.1.2 Deterministic solution

The maximum adiabatic efficiency of the rotor is found to be  $\eta = 0.867$ . At the maximum efficiency, the mass flow is  $\dot{m} = 20.737$  kg/s and the total pressure ratio is  $p_2/p_1 = 2.077$ . The maximum mass flow is found to be  $\dot{m}_{\text{choke}} = 20.903$  kg/s. The results are summarized in table 7.1 together with the experimental values measured by Reid and Moore (1978). All values are within 1.03% of the measured data.

**Table 7.1:** Numerical simulation and experimental results [Reid and Moore (1978)] for NASA Rotor 37.

Quantity	Experimental	Numerical
Maximum adiabatic efficiency $\eta$ [-]	0.876	0.867 (-1.03%)
Pressure ratio at max. efficiency $p_2/p_1$ [-]	2.056	2.077 (+1.02%)
Massflow at max. efficiency $\dot{m}$ [kg/s]	20.74	20.737 (-0.014%)
Maximum mass flow $\dot{m}_{\text{choke}}$ [kg/s]	20.93	20.903 (-0.129%)

Figure 7.3 shows the compressor maps. The figure includes the numerical results and the experimental results from Reid and Moore (1978). A good agreement between the results is obtained. The only major difference between the numerical simulations

## Chapter 7: Operational uncertainties for a transonic compressor rotor

and the experiments is the rotor stall (the most left data point in figure 7.3). At stall the mass flow differs 0.8 kg/s ( $\approx 4\%$ ), which is a large difference. For the main goal, performing an uncertainty analysis for NASA Rotor 37, it is no problem.

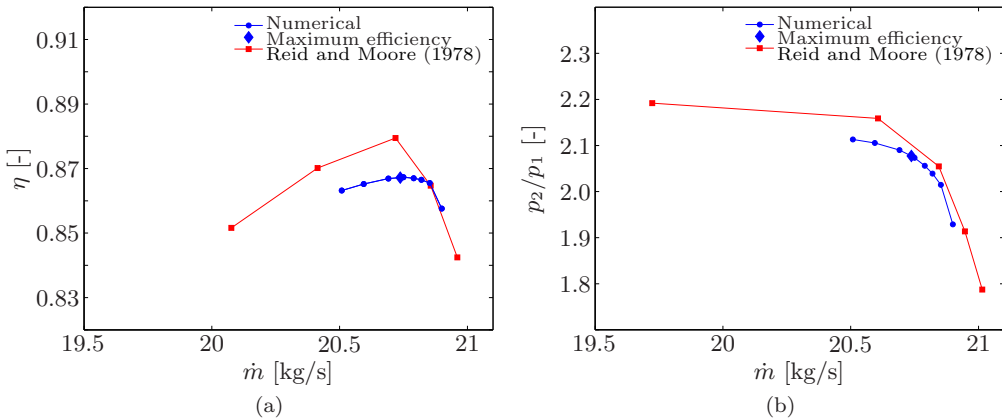


**Figure 7.3:** Compressor maps of NASA Rotor 37, with (a) the adiabatic efficiency  $\eta_{\text{adiabatic}}$  and (b) the total pressure ratio  $p_2/p_1$  against the mass flow  $\dot{m}$ . The figure shows the numerical results, the numerically determined maximum adiabatic efficiency and the experimental results from Reid and Moore (1978).

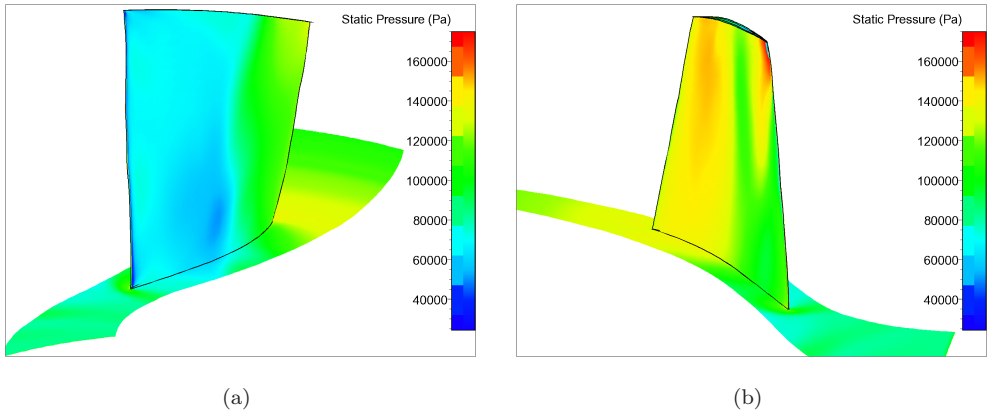
### Flow field

Figure 7.4 shows the static pressure on the surface of the hub and upper (a) and lower (b) side of the blade. Since the tip velocity is much higher than the root velocity, the shock angle and strength vary along the blade. The static pressure on both sides of the blade shows that the flow has a complex three dimensional structure.

To obtain a better understanding of the shock wave, flow properties on a slice at 50% blade height are shown in figure 7.5. The static pressure is depicted in figure 7.5(a), which clearly shows the shock wave. A bow shock is present at the leading edge of the blade. The shock wave impinges on the boundary layer on the suction side of the next blade. This causes flow separation, resulting in a low velocity area behind the shock. This is depicted in figure 7.5(b), which shows the relative Mach number. Figure 7.5(c) shows that the shock results in a sudden increase of eddy viscosity. This has a large influence on the drag of the blade.



## 7.2 Validation using a quasi-3D simulation



**Figure 7.4:** Static pressure on the surface of the hub at the (a) suction and (b) pressure side of the blade.

## 7.2 Validation using a quasi-3D simulation

To validate the Probabilistic Collocation method for NASA Rotor 37, a quasi-3D model is used. The flow contains the characteristics of transonic flow, e.g. a shock wave originating from the leading edge impinging the boundary layer of the next blade. The quasi-3D computation takes about 15 minutes computing time, which enables validation using a Monte Carlo simulation. Based on the Monte Carlo simulation it is concluded that the Probabilistic Collocation method is capable of efficiently propagating the uncertainties to obtain the statistics of the output of interest, like the efficiency of the rotor.

### Quasi-3D model

The quasi-3D model represents a slice at 50% of the blade height. A block structured grid of 5120 cells is used, as shown in figure 7.6(a). It is quasi-3D since it is curved (see figure 7.6(b)) such that 36 blades fill up a cylinder.

The deterministic static pressure and relative Mach number are shown in figure 7.7. Several flow passages are shown to make the shock structure more clear. The static pressure (see figure 7.7(a)) and relative Mach number (see figure 7.7(b)) compare very well with the true 3D results depicted in figure 7.5. The shock wave originates from the leading edge and causes a low speed region behind the shock on the suction side of the next blade.

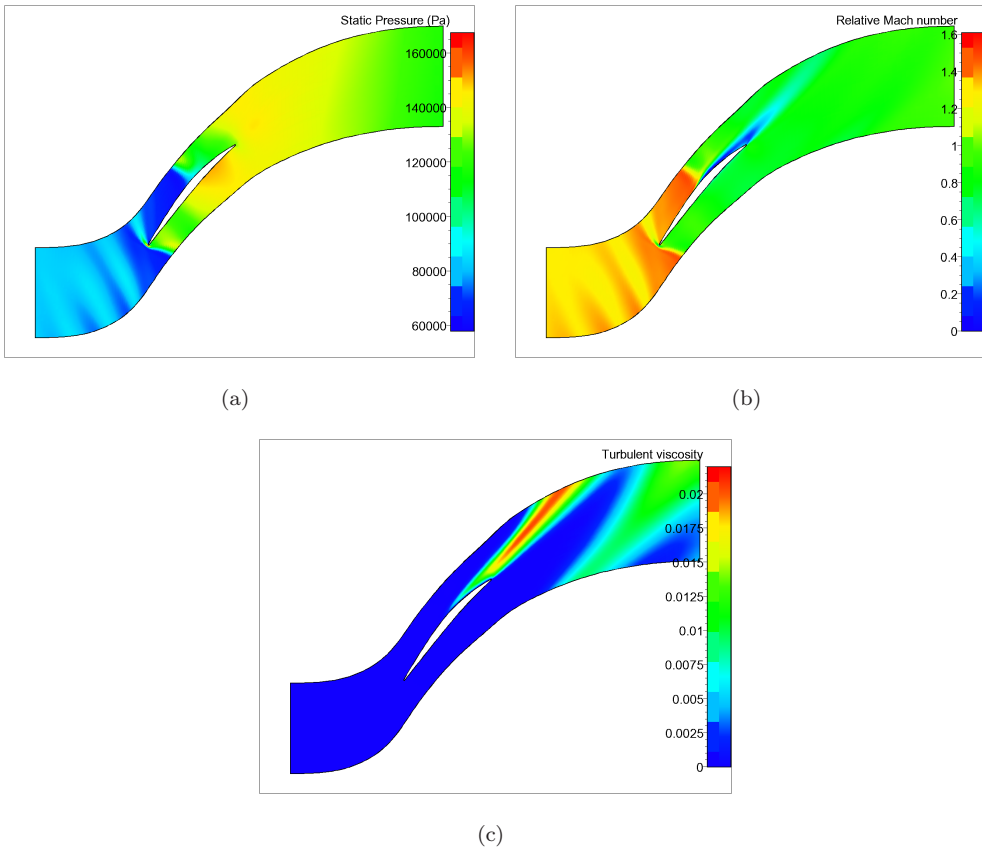


**Figure 7.5:** The static pressure (a), the relative Mach number (b) and the eddy viscosity (c) at 50% blade height.

## 7.2 Validation using a quasi-3D simulation

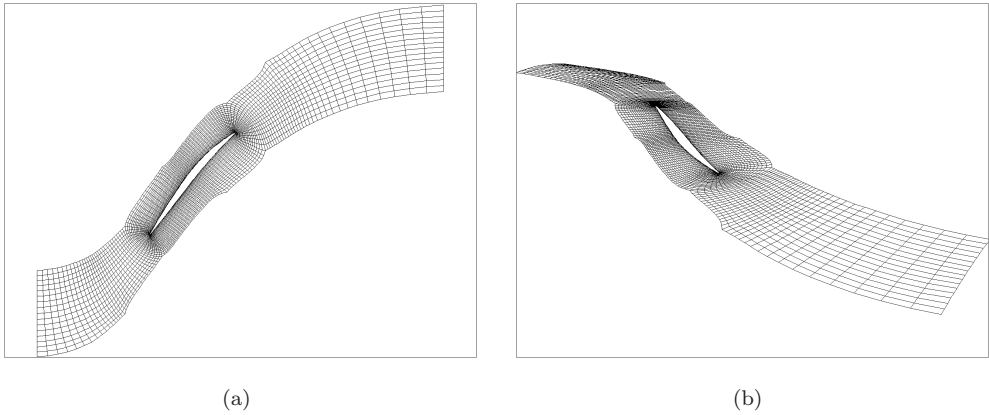


**Figure 7.6:** Quasi-3D computational grid shown in (a) a top view and (b) a 3D view.

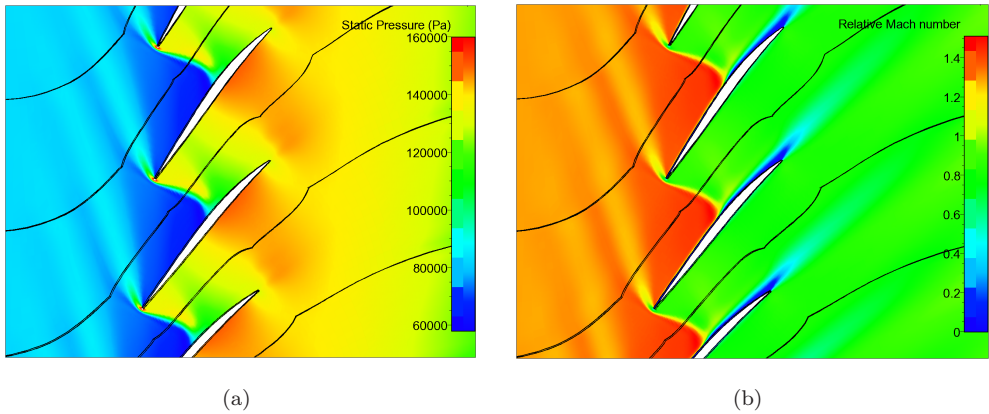


**Figure 7.7:** Quasi-3D flow field around the blades, with (a) the static pressure and (b) the relative Mach number.

### 7.2.1 Uncertain static pressure at the outlet

For the quasi-3D case, an uncertain static outlet pressure  $p_{\text{out}}$  is used for validation of the Probabilistic Collocation method. A symmetric beta distribution is used for  $p_{\text{out}}$ , with parameter settings  $\alpha = \beta = 4$ . This results in a distribution on the interval  $[a, b]$  with the maximum probability at the mean/median, i.e. the deterministic value in this case  $p_{\text{out}}=1.1$  bar. The interval is chosen to be  $\mu_{p_{\text{out}}} \pm 4\%$ . The distribution is shown in figure 7.8, more information on the beta distribution can be found in appendix A.

### Convergence of the Probabilistic Collocation method

The convergence of the estimated error of the adiabatic efficiency  $\eta$ , total pressure ratio  $p_2/p_1$ , and mass flow  $\dot{m}$  with respect to the polynomial order  $p$  are shown in figure 7.9. The error is estimated using the approximation of one order higher, according equation (2.21). For  $p=4$ , the estimated error has dropped over 2 orders of magnitude compared to  $p=1$ . Therefore, a fourth order Probabilistic Collocation approximation is used for further results in this section.

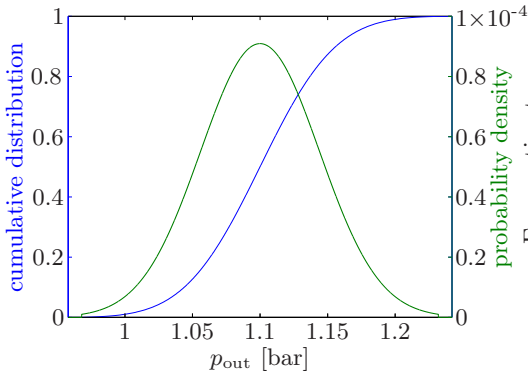


**Figure 7.8:** The probability density function (—) and the cumulative distribution function (—) of the static outlet pressure  $p_{\text{out}}$ .

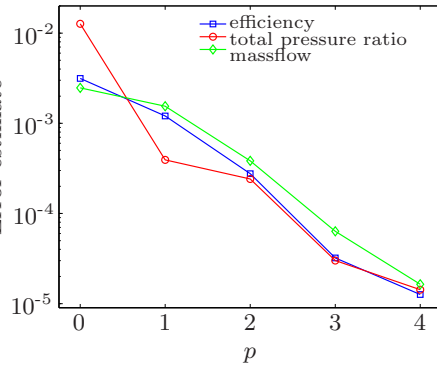


**Figure 7.9:** Convergence of the Probabilistic Collocation method for the adiabatic efficiency  $\eta$ , total pressure ratio  $p_2/p_1$ , and mass flow  $\dot{m}$  with respect to the polynomial chaos order  $p$ .

### 7.2.2 Stochastic results for the quasi-3D rotor

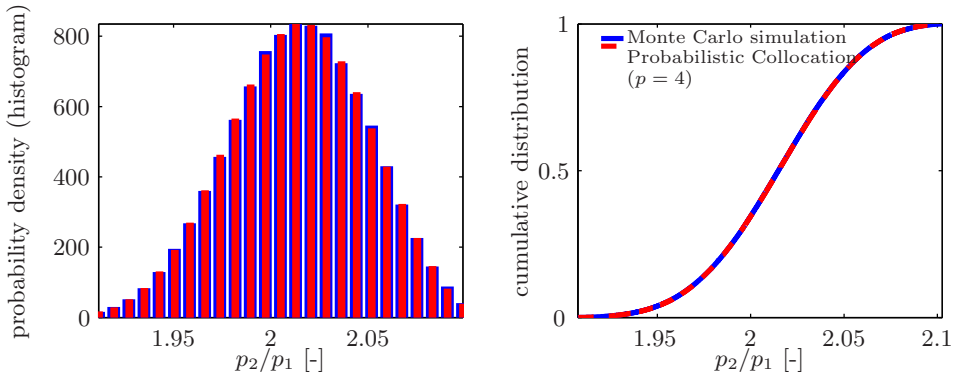
First the validation of the Probabilistic Collocation method with a Monte Carlo simulation is shown for an uncertain static outlet pressure  $p_{\text{out}}$ . This is done by comparing the distribution functions of  $\eta$ ,  $p_2/p_1$ , and  $\dot{m}$ , respectively. Secondly, the mean and

## 7.2 Validation using a quasi-3D simulation

standard deviation of the pressure and relative Mach number in the flow field are shown.

### Comparison with Monte Carlo simulation

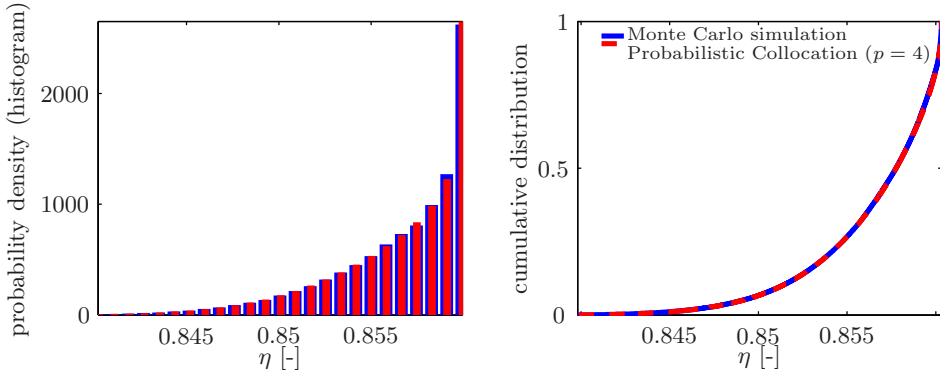
Figures 7.10-7.12 show the probability density function as a histogram and the cumulative distribution function of  $\eta$ ,  $p_2/p_1$ , and  $\dot{m}$ . For the Monte Carlo simulation 10,000 Latin Hypercube samples were used, whereas the Probabilistic Collocation approximation is constructed using 5 deterministic solves (fourth order). The total pressure ratio (figure 7.10) is almost linearly dependent on the uncertain  $p_{out}$ . Therefore, the distribution is close to a beta distribution, similar to the distribution of  $p_{out}$ . The efficiency and the mass flow, however, depend nonlinearly on the uncertain  $p_{out}$ , as can be seen in figures 7.11 and 7.12 respectively. Both quantities obtain a maximum for a certain  $p_{out}$ . This results in a distribution with the largest probability near the maximum value. The results show good correspondence between the Monte Carlo simulation and the Probabilistic Collocation results.



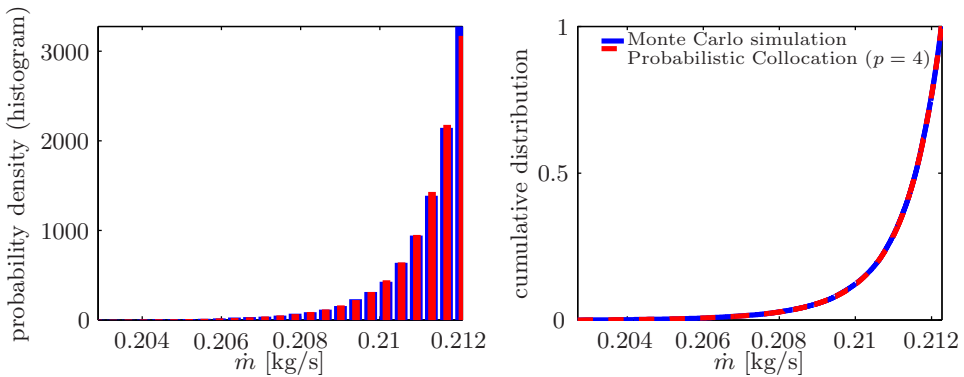
**Figure 7.10:** Probability density function (histogram) and cumulative distribution function of the total pressure ratio  $p_2/p_1$  obtained from Monte Carlo simulation (—) using 10,000 Latin Hypercube samples and a fourth order Probabilistic Collocation approximation (---) using 5 deterministic solves.

### Statistics of the flow field

Figure 7.13 shows the mean (a) and the standard deviation (b) of the static pressure field close to the blades. The mean is similar to the deterministic solution shown in figure 7.7(a). The standard deviation (figure 7.13(b)) shows that due to the uncertain static outlet pressure, largest standard deviation is present inside the shock wave due to a change in shock position. The largest standard deviation is 26,000 Pa, which corresponds to a local coefficient of variation in the order of 25%.

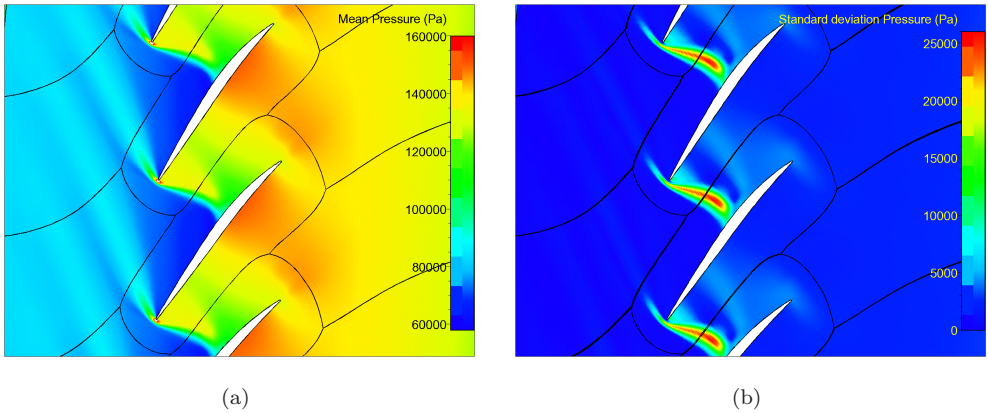


**Figure 7.11:** Probability density function (histogram) and cumulative distribution function of the adiabatic efficiency  $\eta$  obtained from Monte Carlo simulation (—) using 10,000 Latin Hypercube samples and a fourth order Probabilistic Collocation approximation (---) using 5 deterministic solves.



**Figure 7.12:** Probability density function (histogram) and cumulative distribution function of the mass flow  $\dot{m}$  obtained from Monte Carlo simulation (—) using 10,000 Latin Hypercube samples and a fourth order Probabilistic Collocation approximation (---) using 5 deterministic solves.

## 7.2 Validation using a quasi-3D simulation



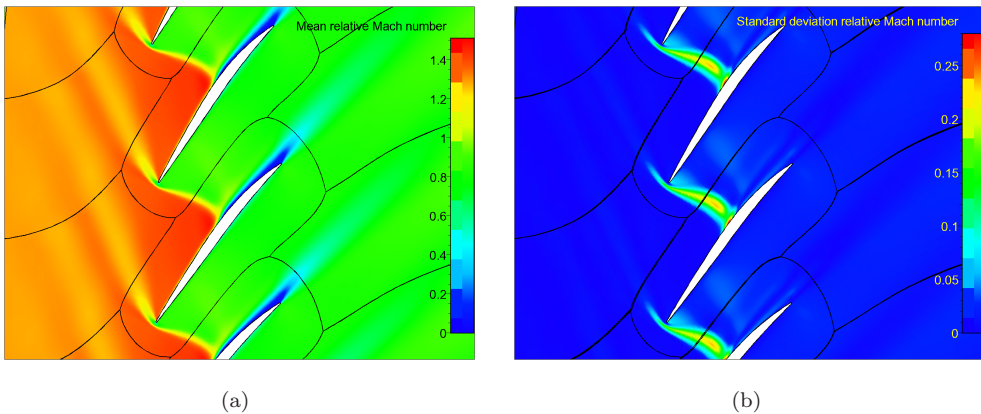
**Figure 7.13:** Quasi-3D static pressure fields around the rotor blades, with (a) the mean and (b) the standard deviation obtained from a fourth order Probabilistic Collocation approximation, based on an uncertain static outlet pressure.

Figure 7.14 depicts the mean and standard deviation of the relative Mach number, which shows a similar picture as the static pressure. Again a local coefficient of variation in the order of 25% is obtained near the shock wave. The difference is near the location where the shock wave interacts with the boundary layer on the suction side of the blade. Here the standard deviation has a peak of 0.26.

### 7.2.3 Conclusions of the validation

Based on the presented results, it can be concluded that the Probabilistic Collocation method is capable of propagating an uncertainty accurately and efficiently. Quantities of interest like adiabatic efficiency, total pressure ratio, and mass flow show good correspondence with a Monte Carlo simulation using 10,000 Latin hypercube samples using a fourth order Probabilistic Collocation approximation (requiring only 5 deterministic solves).

The flow fields show that the mean solutions are similar to the deterministic solution. The standard deviation indicates that the solutions are sensitive near the shock wave and the shock wave boundary layer interaction on the suction side of the blades. Local coefficients of variation in the order of 25% are observed while the coefficient of variation of the uncertain static outlet pressure was only 4%.



**Figure 7.14:** Quasi-3D relative Mach number fields around the rotor blades, with (a) the mean and (b) the standard deviation obtained from a fourth order Probabilistic Collocation approximation, based on an uncertain static outlet pressure.

## 7.3 NASA Rotor 37, 3D simulations

After the successful validation of the Probabilistic Collocation method using a quasi-2D setup, it is applied to the 3D simulations of NASA Rotor 37 at maximum efficiency.

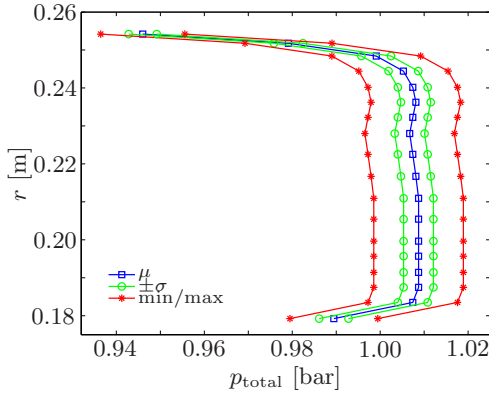
### 7.3.1 Uncertain total pressure profile at the inlet

The second source of uncertainty is the total pressure profile at the inlet of the rotor. According to Reid and Moore (1978), the uncertainty of the measurements of the profile is  $\pm 100$  Pa. Figure 7.15 shows the total pressure profile at the inlet, where the blue line indicates the mean/deterministic profile. The profile is assumed to vary  $\pm 1\%$  around the deterministic value, the minimum and maximum pressure profiles are indicated by the red lines in figure 7.15. This corresponds to a standard deviation of approximately  $\sigma_p \approx 300$  Pa, which is in the same order of the uncertainty of the measurement. The green lines in figure 7.15 show the profile one standard deviation away from the mean. Again a beta distribution is used with parameter  $\alpha = \beta = 4$ . This results in a symmetric distribution with the mean value as the most probable value (see Appendix A). The interval is fixed to  $\mu \pm 1\%$ , the coefficient of variation is  $CV_{p_{\text{total},\text{in}}} = 0.33\%$ .

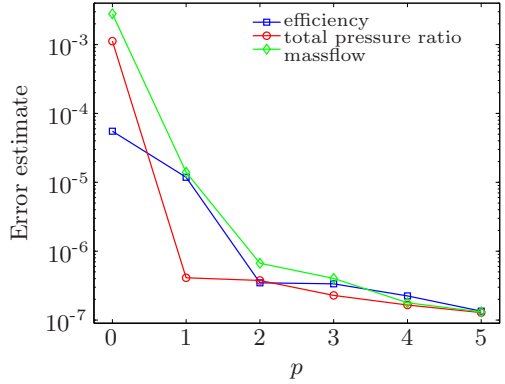
### 7.3.2 Stochastic results for the 3D simulations

Figure 7.16 shows the convergence of the Probabilistic Collocation method for the 3D simulations of NASA rotor 37 with uncertain total pressure profile at the inlet. The





**Figure 7.15:** Total pressure profile at the inlet of the rotor. Shown are the mean profile ( $\mu$ ),  $\pm$  one standard deviation ( $\pm\sigma$ ) and the boundaries of the interval of  $\pm 1\%$  (min/max).



**Figure 7.16:** Convergence of the Probabilistic Collocation method for the adiabatic efficiency  $\eta$ , total pressure ratio  $p_2/p_1$ , and mass flow  $\dot{m}$  with respect to the polynomial chaos order  $p$ .

convergence is shown for the adiabatic efficiency, total pressure ratio, and mass flow. Due to numerical noise, the stochastic approximation does not converge below approximately  $10^{-7}$ . A second order approximation results in a decrease of the estimated error of more than 2 orders of magnitude. The mean and variance are converged to 8 and 4 significant digits respectively. The probability distribution functions show no difference between the second and higher orders, therefore the second order is used in the remainder of this chapter.

Table 7.2 summarizes the statistics of  $\eta$ ,  $p_2/p_1$ , and  $\dot{m}$  at maximum efficiency. The table shows the mean, standard deviation, the coefficient of variation, and the amplification factor. The amplification factor was defined as  $\Upsilon = CV_{\text{solution}}/CV_{\text{unc. parameter}}$ , the ratio between the  $CV$  of the solution and the  $CV$  of the uncertain parameter. It is an indication of the sensitivity of the solution with respect to the uncertain parameter. The mean values of the solution are the same as the deterministically found values in table 7.1. The coefficients of variation are significantly different for each parameter. The adiabatic efficiency shows almost no variation, only 0.008% and is therefore not sensitive to variations in the total pressure profile at the inlet of the rotor. The amplification factor  $\Upsilon_\eta$  is 0.024, which indicates that the uncertainty in the total pressure profile is strongly damped for the efficiency. Secondly,  $p_2/p_1$  shows more variability with a  $CV_{p_2/p_1}$  of 0.158%. The coefficient of variation of the input uncertainty is, however, still damped since the amplification factor  $\Upsilon_{p_2/p_1} = 0.48$  is less than 1. The third parameter of interest,  $\dot{m}$ , shows a  $CV_{\dot{m}}$  of 0.386%, which corresponds with an  $\Upsilon_{\dot{m}}$  of 1.16. This means the uncertainty of the total pressure profile is amplified for the mass flow. The mass flow is the most sensitive to uncertainties in the total pressure profile at the inlet for this case. This observation agrees with results of Gopinathrao, Bagshaw, Mabilat and Alizadeh (2009).

Figure 7.17 shows the probability density and cumulative distribution function of  $\eta$ ,  $p_2/p_1$ , and  $\dot{m}$ . For the current case settings, the solution is not showing strong non-linear behavior for  $p_2/p_1$  and  $\dot{m}$ . The rotor is near maximum efficiency. This results in a nonlinear propagation of the uncertain total pressure profile to the adiabatic efficiency. The distribution of  $\eta$  shows the highest probability at the maximum value of  $\eta$ . The distributions of  $p_2/p_1$  and  $\dot{m}$  are close to the beta distribution with  $\alpha = \beta = 4$ , which was the type of distribution of the uncertain total pressure profile at the inlet. It can be seen that, although the standard deviations are small, the intervals of  $p_2/p_1$  and  $\dot{m}$  are worth to be taken into account. They cover a range of about  $6\sigma$ , which corresponds with 0.95% and 2.3% of the mean for  $p_2/p_1$  and  $\dot{m}$ , respectively.

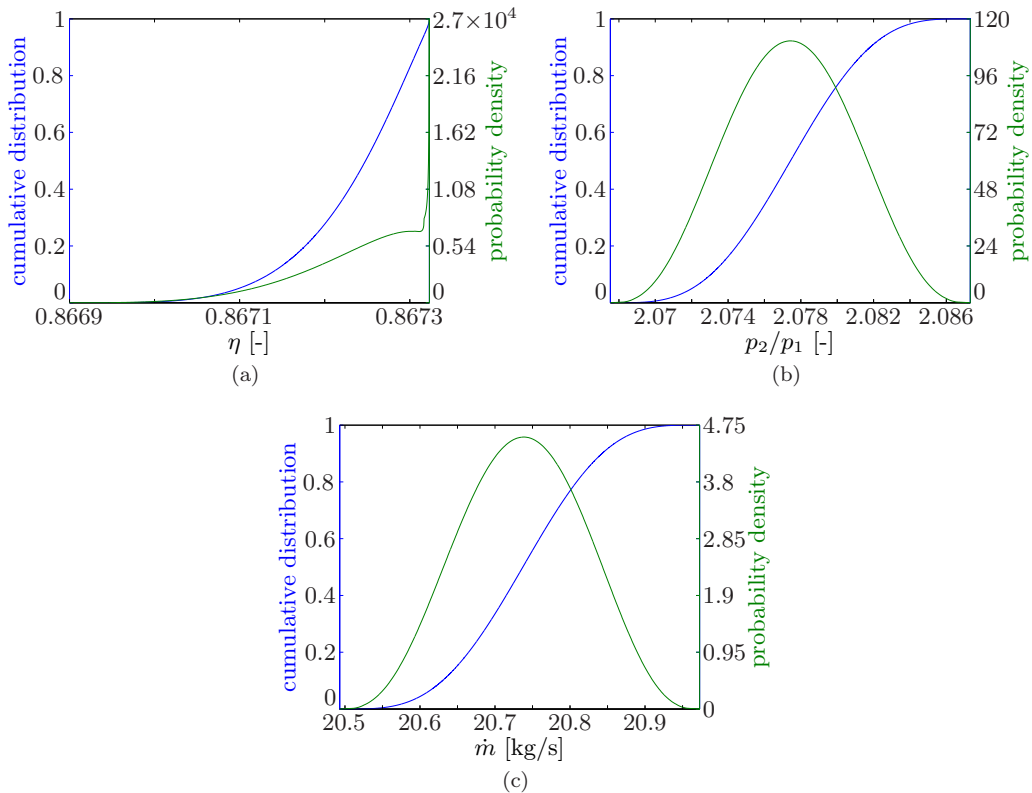


**Figure 7.17:** The probability density function (—) and the cumulative distribution function (—) of the adiabatic efficiency  $\eta$ , total pressure ratio  $p_2/p_1$  and the mass flow  $\dot{m}$ , obtained from a second order Probabilistic Collocation approximation for an uncertain total pressure profile at the inlet of the rotor.

Figure 7.18 shows the compressor maps for the mean values of  $\dot{m}$ ,  $\eta$  and  $p_2/p_1$  with uncertainty bars indicating  $\pm\sigma$ . Table 7.2 indicated that  $\dot{m}$  shows the largest CV. This can be seen in the compressor maps, since the uncertainty bars on  $\eta$  and  $p_2/p_1$

### 7.3 NASA Rotor 37, 3D simulations

**Table 7.2:** Statistics of the adiabatic efficiency  $\eta$ , total pressure ratio  $p_2/p_1$  and mass flow  $\dot{m}$  at maximum efficiency of NASA Rotor 37 obtained from a second order Probabilistic Collocation approximation for an uncertain total pressure profile at the inlet of the rotor.

Quantity	Mean $\mu$	Standard deviation $\sigma$	Coefficient of variation $CV$	Amplification factor $\Upsilon$
$\eta$	0.867	0.000069	0.008%	0.024
$p_2/p_1$	2.077	0.003293	0.158%	0.48
$\dot{m}$	20.737	0.08004	0.386%	1.16

are barely visible. The bars indicating the standard deviation of  $\dot{m}$  are significant. Clearly, it is important to take the uncertainty in the total pressure profile at the inlet into account when compressor maps are computed.

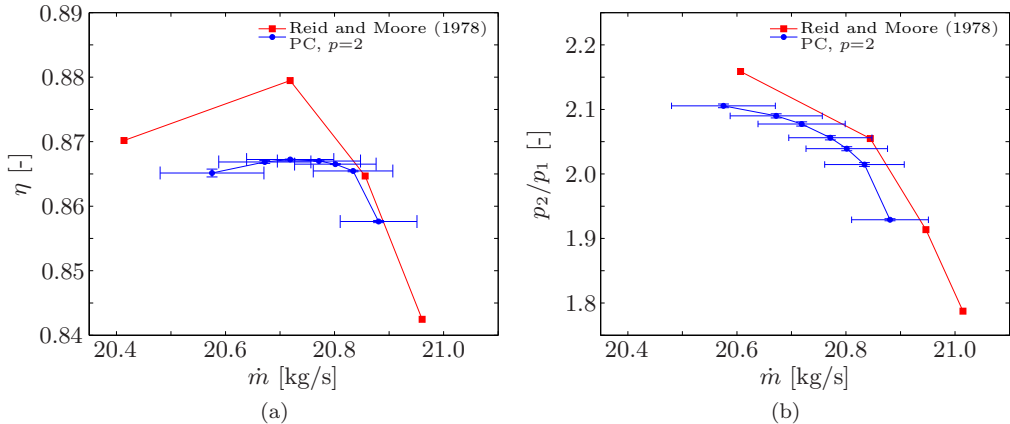


**Figure 7.18:** Compressor maps of NASA Rotor 37, with (a) the adiabatic efficiency  $\eta_{\text{adiabatic}}$  and (b) the total pressure ratio  $p_2/p_1$  against the mass flow  $\dot{m}$ . The figure shows the stochastic results as the mean  $\mu$  and uncertainty bars indicating  $\pm\sigma$ , and the experimental results from Reid and Moore (1978). Obtained from a second order Probabilistic Collocation approximation for an uncertain total pressure profile at the inlet of the rotor.

Figure 7.19 shows the mean and standard deviation of the static pressure in the flow field. Horizontal slices at 25%, 50% and 75% of the blade height are shown in figure 7.19(a) and vertical slices at different locations along the hub in figure 7.19(b) to obtain a picture of the three dimensional features of the flow. The mean static pressure field around the blade is similar to the deterministic simulation. The shock wave becomes stronger near the tip of the blade, due to the higher relative velocity. The largest variation is present in the shock region, as can be seen in figures 7.19(c) and 7.19(d).

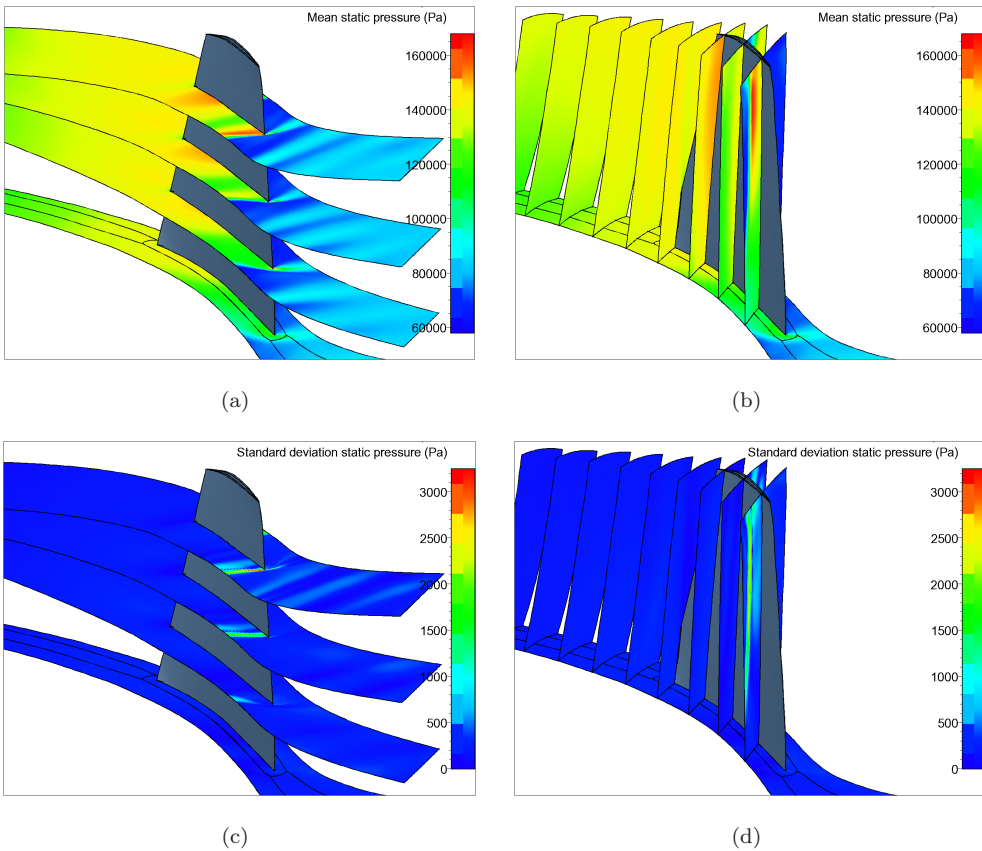


**Figure 7.19:** Static pressure fields, with the mean depicted in (a) and (b) and the standard deviation in (c) and (d). The horizontal slices are at 0%, 25%, 50%, and 75% of the blade height, obtained from a second order Probabilistic Collocation approximation for an uncertain total pressure profile at the inlet of the rotor.

## 7.4 Summary

Compressor rotors are components of a gas turbine that are highly sensitive to operational and geometrical uncertainties. The Probabilistic Collocation method was used to propagate operational uncertainties through simulations of NASA Rotor 37. Validation of the Probabilistic Collocation method with a Monte Carlo simulation using 10,000 Latin Hypercube samples demonstrated that the Probabilistic Collocation method can successfully be applied to a turbomachinery case. NASA Rotor 37 is a transonic axial flow compressor rotor. The flow is characterized by a bow shock in front of the leading edge. The shock wave impinges on the boundary layer of the next blade, causing separation and transition instantaneously.

The total pressure profile at the inlet of the rotor is assumed to be uncertain. A symmetric beta distribution was used for the pressure profile, with the standard deviation such that the uncertainty is in the same order of the measurement accuracy reported in literature. In the point of maximum efficiency, the mass flow was shown to be the most sensitive to the uncertainty, while the efficiency is least affected. The compressor maps are constructed as functions of the mass flow. It was shown to be important to take the uncertainty in the total pressure profile at the inlet into account. The mean static pressure field around the blade does not differ much from the deterministic simulation. The standard deviation of the static pressure showed that the largest variation is present near the shock wave and mainly in the region of the strongest shock, which is near the tip of the blade.



---

## Two-step approach for multiple uncertain parameters

---

A disadvantage of the standard Probabilistic Collocation method is the curse of dimensionality. For multiple uncertain parameters, even low order approximations cannot be computed within reasonable time. Table 8.1 summarizes the amount of deterministic simulations required for a certain polynomial chaos order and the number of uncertain parameters. Suppose 100 deterministic simulations are affordable, then a first order approximation is possible for 5 or 6 uncertain parameters. A first order approximation for 7 uncertain parameters requires 128 deterministic simulations. If the test case requires a second order propagation, 4 uncertain parameters is the maximum. A solution to this problem can be sparse grid approaches [Ganapathysubramanian and Zabaras (2007); Xiu and Hesthaven (2005)]. Advantages of sparse grid approaches are the fact that all uncertain parameters can be propagated efficiently and combined effects of the parameters are computed. However, some uncertain parameters may not affect the solution much, so taking them into account results in (unnecessary) additional computational effort. If this additional work hardly results in a better approximation of the statistics of the solution, these uncertain parameters can be treated as deterministic values.

This chapter provides details of the Probabilistic Collocation method in a two-step approach, it is based on results from Loeven et al. (2006*a*) and Loeven and Bijl (2008*b*, 2009*b*). The two-step approach starts by first performing a sensitivity analysis and

## Chapter 8: Two-step approach for multiple uncertain parameters

**Table 8.1:** The amount of work (i.e. the number of collocation points) of the standard Probabilistic Collocation method. The number of collocation points is given by  $N_p = (p + 1)^d$ , where  $p$  is the polynomial chaos order and  $d$  is the number of uncertain parameters.

Polynomial chaos order $p$	Number of uncertain parameters $d$						
	2	3	4	5	6	7	8
1	4	8	16	32	64	128	256
2	9	27	81	243	729	2,187	6,561
3	16	64	256	1,024	4,096	16,384	65,533
4	25	125	625	3,125	15,625	78,125	390,625

secondly propagating the statistics of the most important parameter(s) in the next step. For both steps the Probabilistic Collocation method is used, as described in chapter 2. The sensitivity analysis is based on the scaled sensitivity derivatives [Turgeon et al. (2003)]. The sensitivity derivatives are obtained from a first or second order Probabilistic Collocation approximation, depending on the distribution of the uncertain parameters. For each output of interest, the scaled sensitivity derivatives are compared, yielding the most important parameters. Next the probability distribution functions are propagated using higher order Probabilistic Collocation approximations. The two-step approach starts with a sensitivity analysis based on separate effects of the uncertain parameters, so interactions between parameters are not taken into account in this step. The second step is performed using a multi-dimensional Probabilistic Collocation expansion to include interactions between the parameters. By taking into account only the most important parameters, the number of deterministic computations is reduced significantly.

### 8.1 Sensitivity analysis using the Probabilistic Collocation method

Sensitivity analysis is used here as an efficient way of reducing the number of uncertain parameters. It is based on the scaled sensitivity derivatives [Turgeon et al. (2003)]. The sensitivity derivatives are used to identify the most important uncertain parameters in a particular physical system. A reduction of the amount of uncertain parameters results directly in less deterministic solves for uncertainty propagation (see table 8.1). This reduces the total computational time of the stochastic simulation considerably.

The sensitivity derivative is defined as the partial derivative of the solution  $u(\mathbf{x}, t, \omega)$  or any output of interest with respect to the uncertain parameter  $a(\omega)$ . The sensitivity derivatives are computed by differentiating a first or second order PC approximation. One can also use a finite difference approach, but then the size of the difference should be carefully chosen. A smaller difference leads to more accurate sensitivity deriva-



## 8.1 Sensitivity analysis using the Probabilistic Collocation method

tives. However, numerical noise of the deterministic CFD solver may produce wrong sensitivity derivatives. For symmetric distributions, like the normal distribution, the second collocation point with corresponding solution  $u_2(\mathbf{x}, t)$  is equal to the collocation point with mean settings. All uncertain parameters share this point, so it only has to be computed once. For this case two solves for each parameter are required to obtain the sensitivity derivative, with a total of  $2d + 1$  solves for the complete sensitivity analysis, with  $d$  the number of uncertain parameters. For asymmetric distributions  $3d$  deterministic solves would be required. Therefore, to save computational costs, a first order Probabilistic Collocation expansion is used for cases with asymmetric distributions, requiring  $2d$  solves. In this paper truncated normal distributions are used, which are symmetric. The approximation of the derivative is then obtained by first differentiating equation (2.10) for  $N_p = 3$  with respect to  $\xi(\omega)$ :

$$\begin{aligned} \left. \frac{\partial u}{\partial \xi} \right|_a &= u_{1,a}(\mathbf{x}, t) \left[ \frac{\xi(\omega_2) - \xi(\omega_3)}{(\xi(\omega_1) - \xi(\omega_2)) (\xi(\omega_1) - \xi(\omega_3))} \right] + \\ &u_{2,a}(\mathbf{x}, t) \left[ \frac{2\xi(\omega_2) - \xi(\omega_1) - \xi(\omega_3)}{(\xi(\omega_2) - \xi(\omega_1)) (\xi(\omega_2) - \xi(\omega_3))} \right] + \\ &u_{3,a}(\mathbf{x}, t) \left[ \frac{\xi(\omega_2) - \xi(\omega_1)}{(\xi(\omega_3) - \xi(\omega_1)) (\xi(\omega_3) - \xi(\omega_2))} \right], \end{aligned} \quad (8.1)$$

where  $u_{i,a}(x, t)$  indicates the  $i^{\text{th}}$  collocation point for uncertain parameter  $a(\omega)$ . The parameter  $a(\omega)$  is a linear combination of the random variable  $\xi(\omega)$ , so  $a(\omega) = A_a \xi(\omega) + B_a$ , with constants  $A_a$  and  $B_a$ . The sensitivity derivative of the solution with respect to parameter  $a(\omega)$  is given by

$$\frac{\partial u}{\partial a} = \left. \frac{\partial u}{\partial \xi} \right|_a \frac{\partial \xi}{\partial a} = \frac{1}{A_a} \left. \frac{\partial u}{\partial \xi} \right|_a. \quad (8.2)$$

When more parameters are involved in the problem the scaled sensitivity derivative with respect to each parameter is calculated. One has to take into account that this procedure provides the sensitivity information for each parameter separately, so no combined effects are taken into account in this step. Multiplying the sensitivity derivatives with the standard deviation  $\sigma_{a_i}$  of the parameters a good estimate of the effect of the uncertain parameter on the solution is obtained. Furthermore, the dimension of the scaled sensitivity derivatives is the same as the dimension of the solution. If the solution depends on  $N$  parameters, the most important parameter is

$$\max \left\{ \sigma_{a_1} \frac{\partial u}{\partial a_1}, \sigma_{a_2} \frac{\partial u}{\partial a_2}, \dots, \sigma_{a_d} \frac{\partial u}{\partial a_d} \right\}. \quad (8.3)$$

These scaled sensitivity derivatives are actually the estimation of the standard deviation using a first order perturbation method [Kleiber and Hien (1992), Borggaard et al. (2001)]. Once the most important parameters are obtained by equation (8.3), they are propagated simultaneously through the system to include interaction between the parameters.

## 8.2 Subsonic flow around a NACA0012 airfoil with 8 uncertain parameters

In this section the two-step framework is applied to steady flow around a NACA0012 airfoil with 8 uncertain parameters. A commercial deterministic CFD code is used to compute the deterministic solves for every collocation point. The deterministic case is flow around a NACA0012 airfoil at an angle of attack  $\alpha$  of  $5^\circ$  and a free stream velocity  $U$  of 100m/s ( $M=0.29$ ). The Reynolds number is equal to  $3 \times 10^6$ . The deterministic computations are performed using the FINE™/Hexa solver by Numeca International on a grid of approximately 100,000 cells. 1600 cells are present on the surface of the airfoil with  $y^+ \leq 1$ . A close-up of the grid layout is shown in figure 8.1(a). A grid convergence study was performed to make sure the deterministic solutions are grid independent. If the deterministic computations are not grid independent or numerically not sufficiently converged, the induced errors may be larger than the variations due to the uncertain parameter. For the grid convergence study grids of 50, 75, 100, 125, and 150 thousand cells were used. The grid of 100,000 cells showed no significant difference compared to the finer grids and was used for further computations. To assure sufficiently converged deterministic simulations, a Jacobian-free Newton-Krylov algorithm [Lucas et al. (2010)] is employed to efficiently converge to a residual of  $10^{-10}$ .

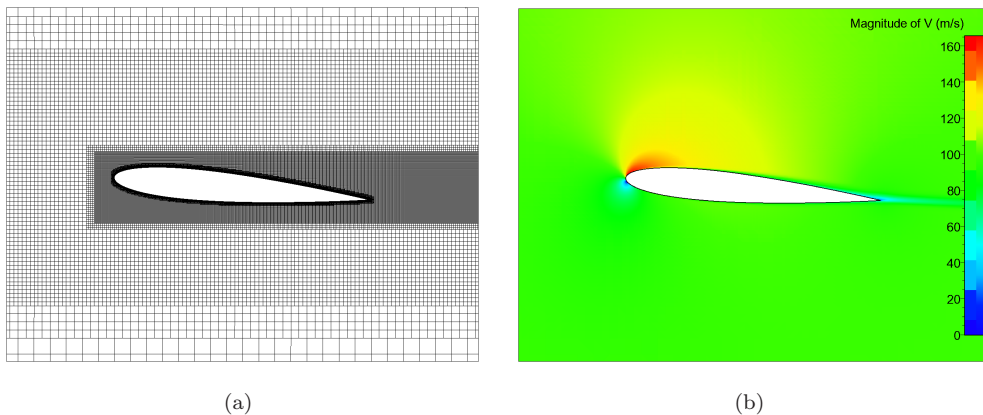


**Figure 8.1:** The mesh layout near the airfoil (a) and magnitude of velocity (b) of the mean conditions.

The flow is modeled by the Reynolds-averaged Navier-Stokes (RANS) equations using the Spalart-Allmaras turbulence model. Figure 8.1(b) shows the magnitude of velocity of the mean conditions. The mean air properties are at 0m ISA. The uncertainties are present in the free stream flow conditions, i.e. the velocity  $U$ , angle of attack  $\alpha$ , pressure  $p$ , temperature  $T$ , viscosity  $\nu$ , and turbulence intensity  $I$  and in the geometry by the thickness  $t$  and camber  $c$ . The free stream conditions are never constant in

## 8.2 Flow around a NACA0012 airfoil with 8 uncertain parameters

real flight due to atmospheric irregularities. The geometric uncertainties result from production tolerances in the fabrication process, as a result of which the actual airfoil slightly differs from the designed shape.

### Input distributions

All uncertain parameters are assumed to have a truncated normal distribution and are shown in figure 8.2; the specifications of the distributions are given in table 8.2. For this case all parameters are considered as dimensional quantities, as is often the case in engineering applications. Truncated normal distributions are used to avoid unphysical settings and too large variations. The variations in the geometry are chosen such that the parameters vary within a realistic interval. The parameters of the freestream are based on variations that can occur in flight, due to uncertain height and atmospheric conditions. The kinematic viscosity is varied to see the effect of the Reynolds number. For real life applications the input distributions should be measured to be able to find a realistic input distribution. One can think of measuring the shape of products after production or measuring air properties and freestream velocity and angle of attack during flight. Currently, these data are not available yet, so assumptions on the input distributions have to be made. For the truncated normal distributions it is important to use the orthogonalization procedure described in section 2.2. Only if the collocation points and weights are computed weighted with the probability density function of the uncertain parameters, spectral convergence is obtained. If one would use the Hermite polynomials (corresponding to a normal distribution), the support is infinite and collocation points will fall outside the truncation interval for higher orders of approximation.

**Table 8.2:** Distribution description of the uncertain parameters. All parameters have a truncated normal distributions, truncated on the  $\mu \pm 3\sigma$  interval.

Parameter	Mean $\mu$	Standard deviation $\sigma$	Minimal value	Maximal value	CV
$U$	100	5	85	115	5 %
$\alpha$	5	0.3333	4	6	6.67 %
$t$	12	0.3333	11	13	2.78 %
$c$	0	0.16667	-0.5	0.5	-
$p$	101325	1013.25	98285	104365	1 %
$T$	288.15	2.8815	279.5	296.8	1 %
$\nu$	$3.333 \times 10^{-5}$	$3.333 \times 10^{-7}$	$3.233 \times 10^{-5}$	$3.433 \times 10^{-5}$	1 %
$I$	0.1	0.005	0.085	0.115	5 %

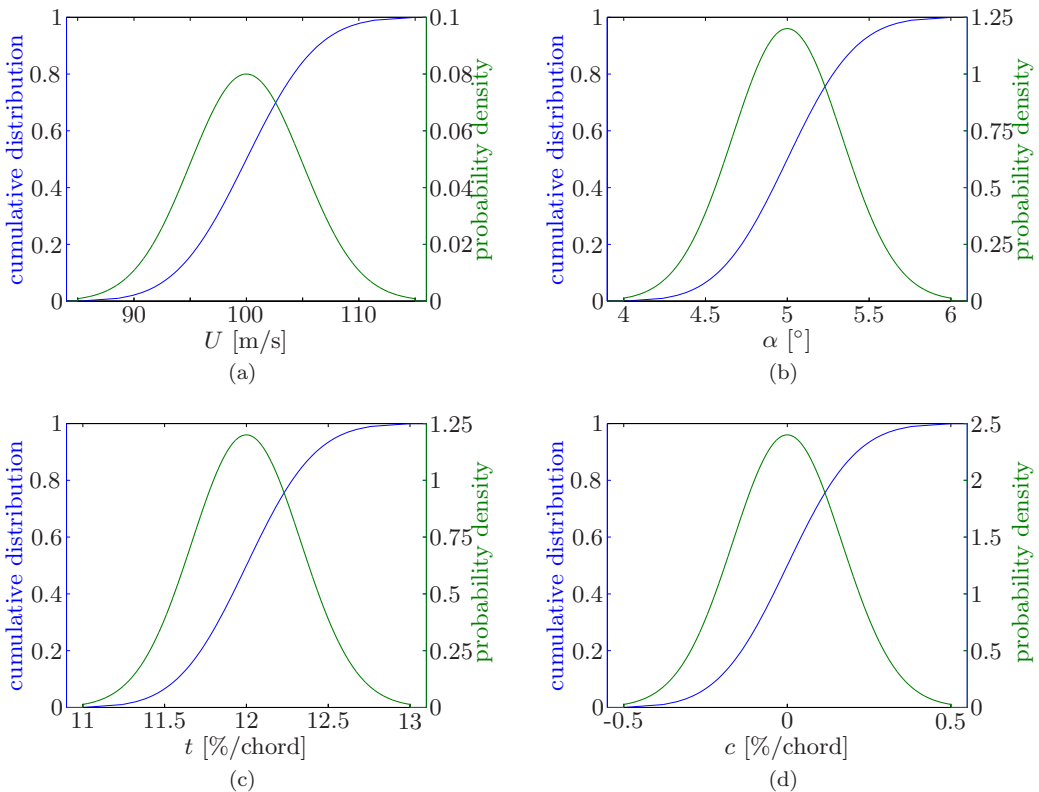
As was shown in table 8.1, 256 or 6561 deterministic computations are required in order to propagate the distributions of all eight parameters for a first or second order Probabilistic Collocation approximation respectively. The RANS computation of the NACA0012 airfoil on the grid of 100,000 cells runs in the order of 10 CPU

## Chapter 8: Two-step approach for multiple uncertain parameters

hours on an AMD Opteron 2800 MHz processor. A first or second order Probabilistic Collocation approximation is, therefore, not feasible for this problem for all parameters simultaneously. To be able to perform uncertainty quantification, the two-step approach is employed. The sensitivity analysis only requires 17 deterministic solves for all eight parameters. After that only the probability distributions of the most important parameters are propagated.

### 8.2.1 Step I: Identifying the most important parameter

In this section the lift and drag forces and coefficients are considered as the main output of interest. The scaled sensitivity derivatives (equation (8.3)) of the lift and drag forces are shown in figure 8.3. Figure 8.4 shows the scaled sensitivity derivatives for the lift and drag coefficients. The notation of the scaled sensitivities is for example  $L_{\tilde{U}} = \sigma_U \partial L / \partial U$  for the scaled sensitivity derivative of the lift force  $L$  with respect to the free stream velocity. Clearly, the conclusions depend on the output of interest.



(see figure caption on the next page)

## 8.2 Flow around a NACA0012 airfoil with 8 uncertain parameters

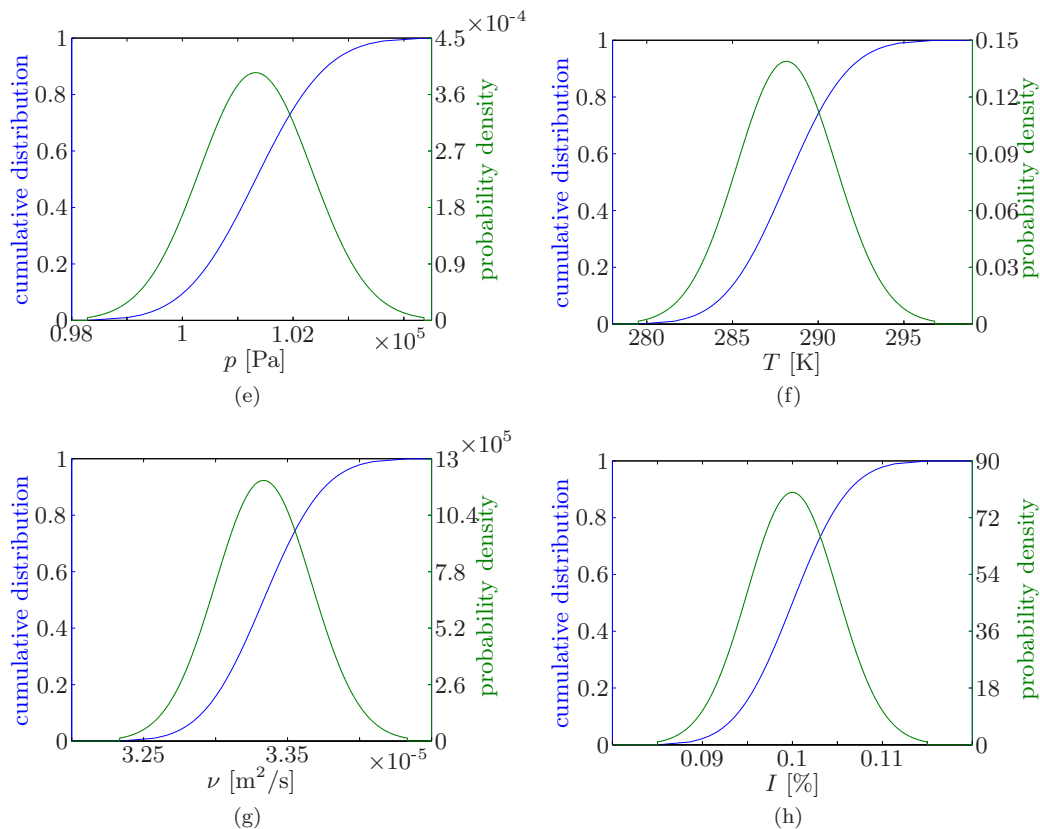
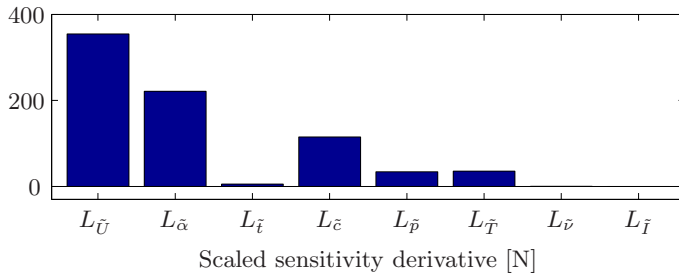


**Figure 8.2:** Uncertain input parameters (a) velocity, (b) angle of attack, (c) thickness, (d) camber, (e) pressure, (f) temperature, (g) viscosity, and (h) turbulence intensity; the cumulative distribution functions are shown by the blue line (—) and the probability density functions are indicated by the green line (—).

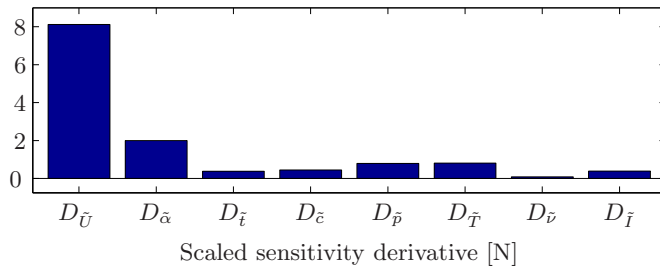
The sensitivity derivatives show the effects of the parameters separately. The user should, therefore, be careful when selecting the most important parameters, because combined effects are not taken into account in this step.

Since the forces depend on the dynamic pressure, the velocity is most dominant in this case. Also the angle of attack shows significant variation, as well as the camber for the lift force. For the coefficients, however, figure 8.4 shows that the expected coefficient of variation are differently distributed. The expected coefficient of variation of the lift coefficient is up to 7%, mainly due to an uncertain angle of attack and camber. The other parameters are not important for the lift coefficient. The maximum coefficient of variation of the drag coefficient is about 2.5%, due to uncertain angle of attack. All other parameters are shown to contribute less than 1% coefficient of variation in the drag coefficient. Based on these observations, further computations are performed for

uncertain velocity, angle of attack, and camber.



(a)



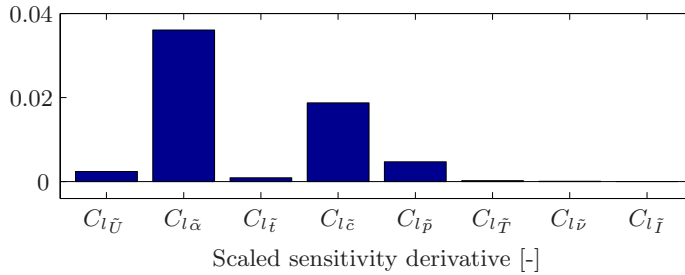
(b)

Figure 8.3: Scaled sensitivity derivatives of the lift  $L$  (a) and drag  $D$  (b) forces.

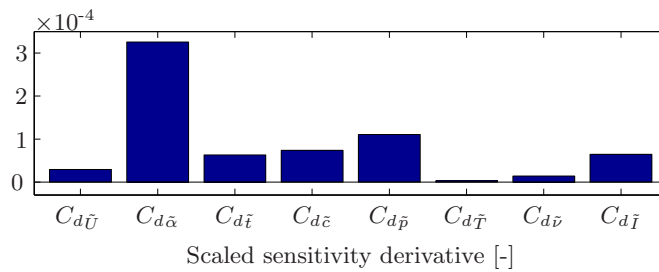
## 8.2.2 Step II: Propagating the probability distributions

The probability distribution functions of the most influential parameters: free stream velocity, angle of attack, and camber, are propagated using the Probabilistic Collocation method for  $p = 1, 2,$  and  $3,$  requiring 8, 27, and 64 deterministic computations respectively. The convergence of the Probabilistic Collocation method is checked by estimating the error using an approximation of one order higher, given by equation (2.21). The resulting convergence of the Probabilistic Collocation method for the lift and drag forces is shown in figure 8.5. In order to estimate the error of the third order approximation a fourth order computation was performed (requiring 125 deterministic solves). Figure 8.5, A estimated error drop of more than two orders of magnitude compared to the zeroth order is observed for a second order approximation. Since it is known that the forces depend quadratically on the free stream velocity, a second order approximation was expected to be appropriate here. Further results are, therefore, obtained from a second order Probabilistic Collocation approximation. So a total of 27 deterministic solves are required for the following results. Note that 7 computations were already performed for the sensitivity analysis in step I.

## 8.2 Flow around a NACA0012 airfoil with 8 uncertain parameters



(a)



(b)

**Figure 8.4:** Scaled sensitivity derivatives of the lift  $C_l$  (a) and drag  $C_d$  (b) coefficients.

The statistics of the lift and drag are summarized in table 8.3. The deterministic computations with the mean values for all uncertain parameter result in:  $L = 3395.763$  N,  $D = 79.41934$  N,  $C_l = 0.5544$ , and  $C_d = 0.012966$ . The difference between deterministic and mean values of the coefficients are less than one count (a lift count is defined as  $10^{-3}$ , and a drag count as  $10^{-4}$ ). This difference is negligible. On average the performance of the airfoil remains the same with the assumed uncertainties. The input uncertainties, however, result in possible variations of the output. A good indication for the variability of the output is the coefficient of variation ( $CV$ ), defined as  $CV = \sigma/\mu$ . The lift and drag force show a coefficient of variation of 12.59% and 10.39% respectively. The coefficient of variation of the lift and drag coefficients of 7.24% and 2.56% is smaller. These variations correspond very well with expected coefficients of variation based on the sensitivity analysis in section 8.2.1.

Figure 8.6 shows the distribution functions of the lift and drag forces, which look similar to the truncated normal input distribution. However, some skewness is introduced since  $L$  and  $D \sim U^2$ . The mean values are the most probable points and points away from the mean have less probability to occur. The distributions of the lift and drag coefficients are shown in figure 8.7, which show no skewness. The drag coefficient has a small variation. All possible values fall inside an interval of 24 dragcounts, whereas the interval of all possible values of the lift coefficients covers about 300 liftcounts,

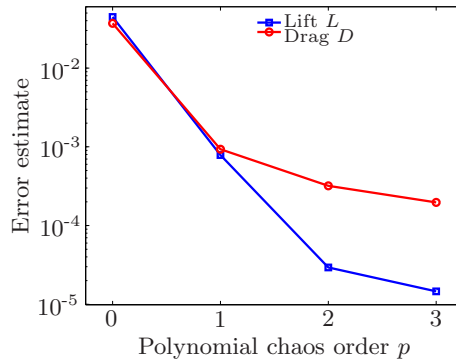


**Figure 8.5:** Convergence of the Probabilistic Collocation method for the lift  $L$  and drag  $D$  forces with respect to the polynomial chaos order  $p$ .

**Table 8.3:** Statistics of the solution resulting from uncertain free stream velocity  $U$ , angle of attack  $\alpha$  and airfoil camber  $c$  using a second order Probabilistic Collocation expansion.

Quantity	Mean $\mu$	Standard deviation $\sigma$	Minimal value	Maximal value	$CV$
Lift force $L$ [N]	3404.991	428.602	1923.069	5408.222	12.59%
Lift coefficient $C_l$	0.5543	0.0401	0.402108	0.7043135	7.24%
Drag force $D$ [N]	79.86150	8.29917	53.74992	113.9887	10.39%
Drag coefficient $C_d$	0.013004	0.000333	0.012019	0.014354	2.56%

which is large.

The variations in lift and drag are a direct consequence of variations in the pressure and skinfriction on the surface of the airfoil. Figure 8.8 shows the pressure distribution on the surface of the airfoil. The dashed lines indicate the interval which contain 100% of all possible outcomes. The shading presents the probability of the solution, dark blue means a high probability, white is no probability. Firstly, figure 8.8(a) shows the relative pressure  $P/P_0$ , where  $P_0$  is the free stream pressure. Secondly, figure 8.8(b) shows the pressure coefficient  $C_P = (P - P_0)/(\frac{1}{2}\rho U_0^2)$ , which is much less affected by the uncertain parameters. The figures show that a large contribution on the uncertainty bounds of the relative pressure is due to the dynamic pressure.

Figure 8.9(a) shows the skinfriction on the surface of the airfoil. The variation of the skinfriction is much less than the variation of the pressure. This results in less variation in drag compared to lift. The skinfriction coefficient  $C_f = \tau_w/(\frac{1}{2}\rho U_0^2)$  on the surface is shown in Figure 8.9(b), which turns out to be insensitive to the input uncertain parameters. As a result the drag coefficient shows a low coefficient of variation.



## 8.2 Flow around a NACA0012 airfoil with 8 uncertain parameters

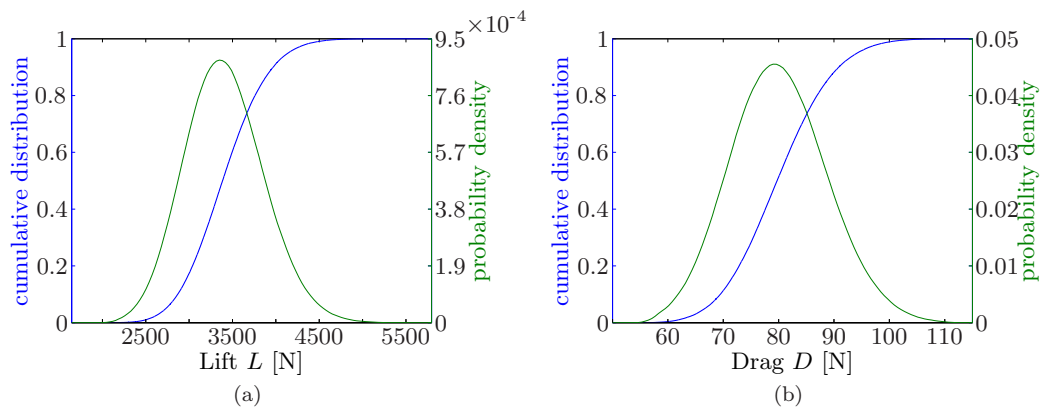


**Figure 8.6:** Distribution functions of the lift and drag forces resulting from uncertain  $U$ ,  $\alpha$ , and  $c$  using a second order Probabilistic Collocation approximation.

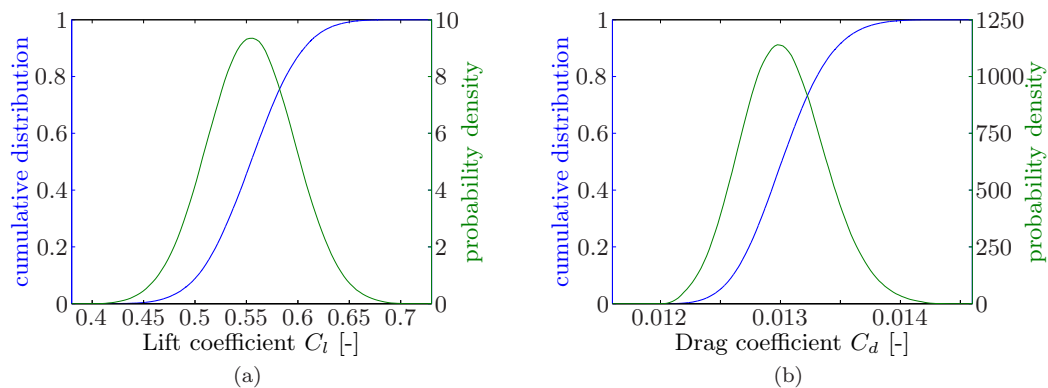
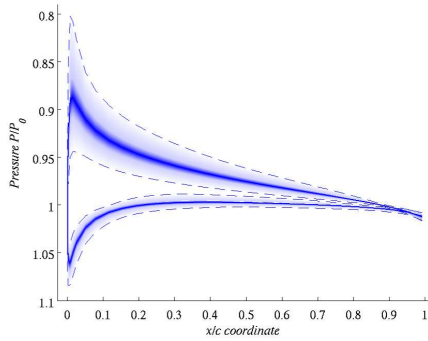
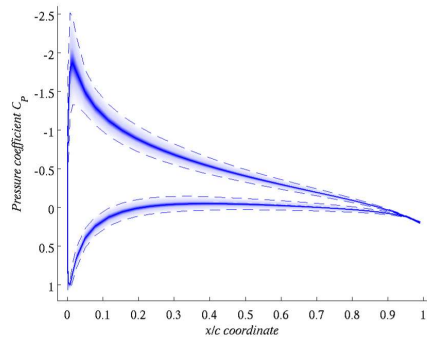


**Figure 8.7:** Distribution functions of the lift and drag coefficients resulting from uncertain  $U$ ,  $\alpha$ , and  $c$  using a second order Probabilistic Collocation approximation.

## Chapter 8: Two-step approach for multiple uncertain parameters

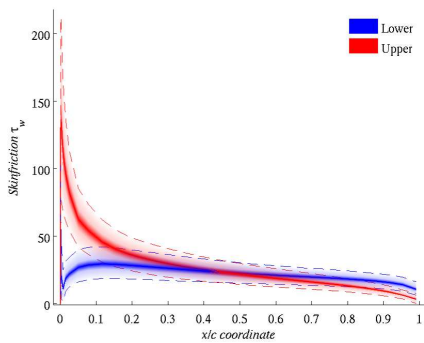


(a) Relative pressure  $P/P_0$  [-]

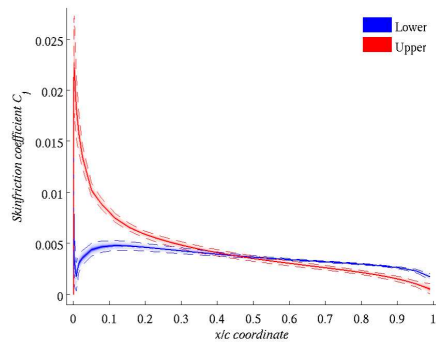


(b) Pressure coefficient  $C_P$  [-]

**Figure 8.8:** Relative pressure  $P/P_0$  and pressure coefficient  $C_P$  on the surface of the airfoil. The dashed lines (--) indicate the interval that covers all possible outcomes. The shaded area indicates the probability of the solution.



(a) Skinfriction  $\tau_w$  [N]



(b) Skinfriction coefficient  $C_f$  [-]

**Figure 8.9:** Skinfriction  $\tau_w$  and skinfriction coefficient  $C_f$  on the lower (--) and upper (--) surface of the airfoil. The dashed lines indicate the interval that covers all possible outcomes. The shaded area indicates the probability of the solution.

## 8.3 Summary

In this chapter a two-step approach was adopted to efficiently treat multiple uncertain parameters. The first step is a sensitivity analysis to find the most important parameters. This was done by a first or second order Probabilistic Collocation approximation, depending on the input distribution of the uncertain parameters. The sensitivity derivatives were scaled with the standard deviation of the uncertain parameters to get an estimation of the effect on the solution. No interactions between parameters are taken into account in this step. For the second step, a higher order Probabilistic Collocation approximation was used to propagate only the uncertainty of the most important parameters.

This approach was demonstrated on a flow simulation around a NACA0012 airfoil with 8 uncertain parameters. The sensitivity analysis required 17 computations and the second order propagation 27 of which 7 were already performed during the sensitivity analysis. The total amount of computations adds up to 37, which is an acceptable amount for the additional information that is obtained. If all 8 parameters would have been propagated simultaneously, a first or second order Probabilistic Collocation approximation requires 256 or 6561 deterministic simulations, respectively. Due to dependence on the dynamic pressure, and therefore quadratic dependence on the uncertain free stream velocity, the dimensional quantities showed a much larger variability than the dimensionless coefficients.



---

## A Probabilistic Radial Basis Function approach

---

In case of multiple uncertain parameters the amount of deterministic computations grows rapidly. For the Probabilistic Collocation method the number of points is equal to  $(p + 1)^d$ , with  $p$  the order of the approximation and  $d$  the number of uncertain parameters. As an alternative sparse grid approaches [Gerstner and Griebel (1998); Xiu and Hesthaven (2005); Ganapathysubramanian and Zabaras (2007)] can be used to increase the efficiency. Quadrature based methods, like the Probabilistic Collocation method, rely on a fixed number of collocation points and cannot give a result when one point is missing due to a deterministic solver that does not converge. For non-intrusive Polynomial Chaos methods the number of coefficients is  $M + 1 = (d + p)!/d!p!$ , see section B.2. Hosder et al. (2007) showed that for a robust non-intrusive Polynomial Chaos approximation the amount of sampling points should be twice the number of coefficients that needs to be determined, i.e.  $2 \times (M + 1)$ . All polynomial chaos based methods use a global polynomial approximation of the response surface.

A different approach was developed by Isukapalli et al. (1998). Their Stochastic Response Surface Method is based on a gradient assisted polynomial approximation of the stochastic response surface. Swiler et al. (2006) compared different response surface approaches. Next to polynomial regression, Kriging [Jones et al. (1998); Sacks et al. (1989)] and multivariate adaptive regression splines [Friedman (1991)]

## Chapter 9: A Probabilistic Radial Basis Function approach

have been investigated.

In this chapter the response surface is approximated using radial basis functions (RBFs) [Buhmann (2000)] through a limited number of support points. The Probabilistic Radial Basis Function (PRBF) approach for multiple uncertain parameters is explained in the work of Loeven, Witteveen and Bijl (2007*b*) and Loeven and Bijl (2008*c*). RBFs are used since they are known to be efficient interpolants in high dimensional spaces. The support points can be chosen by an arbitrary sampling strategy and, therefore, does not rely on quadrature rules. This is an advantage for CFD applications, since it might happen that one sample does not converge. Some quadrature rules fail if one point is missing. For the PRBF approach a new point can be chosen close to the point that did not converge until the deterministic solver converges. Here several combinations of different RBFs and sampling techniques are investigated. Recently, RBFs [Buhmann (2000); McDonald et al. (2007); Regis and Schoemaker (2007)] became more popular for response surface approximation in the field of optimization.

The PRBF approach is applied to three test cases. The first test case is the mass-spring problem, with uncertain spring stiffness and mass. A comparison of several commonly used RBFs and sampling techniques is made based on the convergence of the mean and variance with respect to the number of samples. The second test case is a turbulent Navier-Stokes simulation of flow around a NACA0012 airfoil with four uncertain parameters. The free stream Mach number and angle of attack are assumed to be uncertain, as well as the geometry of the airfoil. The NACA0012 airfoil is parameterized by the maximum camber and the relative thickness, both treated as an uncertainty. Thirdly, the PRBF approach is demonstrated for the RAE2822 test case described in section 3.2. A Monte Carlo simulation using 10,000 Latin Hypercube samples is performed to make a comparison between the Probabilistic Radial Basis Function, Probabilistic Collocation and Monte Carlo results.

## 9.1 Probabilistic Radial Basis Function Approach

This section introduces the Probabilistic Radial Basis Function approach and some commonly used RBFs. Furthermore, the sampling techniques used to obtain the support points for the RBFs are discussed.

### 9.1.1 Radial Basis Functions in a probabilistic framework

Consider a problem with  $d$  uncertain parameters  $a_1(\omega)$ ,  $a_2(\omega)$ ,  $\dots$ ,  $a_d(\omega)$ . The randomness of the parameters is indicated by  $\omega \in \Omega$ , which is a random event from the set of outcomes  $\Omega$ . The probability space is given by  $(\Omega, \mathcal{F}, P)$ , with  $\mathcal{F} \subset 2^\Omega$  the  $\sigma$ -algebra of events and  $P$  a probability measure. The parameter space is a  $d$ -dimensional probability space  $\mathbf{a}(\omega) = \{a_1(\omega), a_2(\omega), \dots, a_d(\omega)\}$ . The response surface

## 9.1 Probabilistic Radial Basis Function Approach

$u(\mathbf{a}(\omega))$  is approximated by:

$$u(\mathbf{a}(\omega)) \approx \sum_{i=1}^N \gamma_i \phi(\mathbf{r}_i(\omega)) = \sum_{i=1}^N \gamma_i \phi(\|\mathbf{a}(\omega) - \mathbf{a}(\omega_i)\|), \quad (9.1)$$

where  $N$  is the number of support points or centers  $\mathbf{a}(\omega_i)$ , and  $\phi$  is the RBF, defined as a function of the radius from the support point. Each support point corresponds to a set of parameter values  $\mathbf{a}(\omega_i) = \{a_1(\omega_i), a_2(\omega_i), \dots, a_d(\omega_i)\}$ . The radius to the support point  $\mathbf{a}(\omega_i)$  is:

$$\mathbf{r}_i(\omega) = \|\mathbf{a}(\omega) - \mathbf{a}(\omega_i)\|, \quad (9.2)$$

where  $\|\cdot\|$  is the Euclidian norm. The support points are obtained by sampling, which is treated in section 9.1.3. By sampling in  $\Omega$ , the approximation is weighted. For each sample  $\omega_i$ , the corresponding parameter values  $\mathbf{a}(\omega_i)$  are computed using the cumulative distribution functions of the uncertain parameters. The weighted approximation results in more samples in areas of high probability. For each support point, the problem is solved deterministically with the determined parameter settings. Therefore, at the support points  $a_i$  the solution  $f_i$  is known:

$$u(\mathbf{a}(\omega_i)) = f_i, \quad i = 1, \dots, N, \quad (9.3)$$

The coefficients  $\gamma_i$  are obtained by solving the system:

$$M\boldsymbol{\gamma} = \mathbf{f}, \quad (9.4)$$

which is obtained from equations (9.1) and (9.3). The vector  $\boldsymbol{\gamma}$  contains all coefficients  $\boldsymbol{\gamma} = (\gamma_1, \gamma_2, \dots, \gamma_N)^T$ , the vector  $\mathbf{f}$  consists of all solutions  $\mathbf{f} = (f_1, f_2, \dots, f_N)^T$ , and  $M$  is the interpolation matrix with  $M_{ij} = \phi(\|\mathbf{a}(\omega_i) - \mathbf{a}(\omega_j)\|)$ .

In this study globally supported RBFs are used, which means that each RBF influences the entire domain. The functions that are used are:

- Gaussian (G):  $\phi(\mathbf{r}) = e^{-(c\mathbf{r})^2}$ , positive definite
- Thin plate spline (TPS):  $\phi(\mathbf{r}) = \mathbf{r}^2 \log(\mathbf{r})$ , second order conditionally positive definite
- Multiquadric biharmonic (MQB):  $\phi(\mathbf{r}) = \sqrt{c^2 + \mathbf{r}^2}$ , positive definite
- Inverse multiquadric biharmonic (IMQB):  $\phi(\mathbf{r}) = \frac{1}{\sqrt{c^2 + \mathbf{r}^2}}$ , positive definite

The one-dimensional RBFs are shown in figure 9.1, for a shape parameter of  $c = 1$ . Note that the TPS does not have a shape parameter.

If the interpolation matrix  $M$  is positive definite, the RBF is also called positive definite. When an RBF is not positive definite a polynomial is added to the right

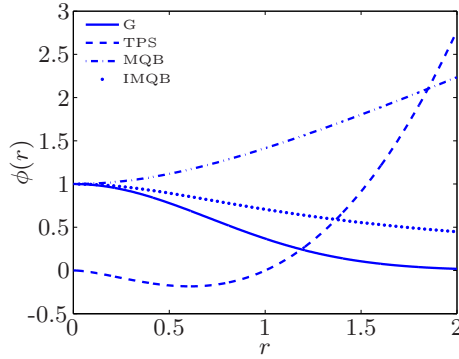


**Figure 9.1:** The Gaussian (—), thin plate spline (---), multiquadric biharmonic (— · —), and the inverse multiquadric biharmonic (···) RBFs, with shape parameter  $c = 1$ .

hand side of equation 9.1 to make the interpolation uniquely solvable:

$$u(\mathbf{a}(\omega)) \approx \sum_{i=1}^N \gamma_i \phi(\|\mathbf{a}(\omega) - \mathbf{a}(\omega_i)\|) + p(\mathbf{a}(\omega)). \tag{9.5}$$

For example, the thin plate spline RBF is second order conditionally positive definite. A  $k^{\text{th}}$  order conditionally positive definite requires the addition of a polynomial of order  $k - 1$ . Therefore, the thin plate spline RBF requires an additional linear polynomial. For three uncertain parameters ( $d=3$ ) this is equal to:

$$p(\mathbf{a}(\omega)) = \beta_0 + \beta_1 a_1(\omega) + \beta_2 a_2(\omega) + \beta_3 a_3(\omega). \tag{9.6}$$

The system that has to be solved to obtain the coefficients is:

$$\begin{bmatrix} M & P \\ P^T & 0 \end{bmatrix} \begin{bmatrix} \boldsymbol{\gamma} \\ \boldsymbol{\beta} \end{bmatrix} = \begin{bmatrix} \mathbf{f} \\ \end{bmatrix}, \tag{9.7}$$

with  $P_i = [1 \ a_1(\omega_i) \ a_2(\omega_i) \ a_3(\omega_i)]$  and  $i = 1, \dots, N$  is the  $i$ -th row of  $P$  for the three dimensional case.

### 9.1.2 Error estimation

The error of the RBF is approximated by removing one sample from the sample set and predicting the solution at that point using the remaining samples [Rippa (1999)]. This done for every sample and all errors are put into an error vector.

In the PRBF approach, a data set of  $N$  samples  $\{\mathbf{a}_i\}$  is available with known solutions  $\{f_i\}$  and the RBF approximation in equation (9.1):

$$u(\mathbf{a}) \approx \sum_{i=1}^N \gamma_i \phi(\mathbf{r}_i) = \sum_{i=1}^N \gamma_i \phi(\|\mathbf{a} - \mathbf{a}_i\|), \tag{9.1}$$



## 9.1 Probabilistic Radial Basis Function Approach

where  $\phi$  is the radial basis function and  $\gamma_i$  are the corresponding coefficients, the random event  $\omega$  is omitted in the notation for convenience.

Now a subset  $V^{(k)}$  is taken, which is the RBF approximation without sample  $k$ . The solution at sample  $k$  is approximated using the other samples by:

$$u^{(k)}(\mathbf{a}_k) \approx \sum_{\substack{i=1 \\ i \neq k}}^N \bar{\gamma}_i \phi(\mathbf{r}_i) = \sum_{\substack{i=1 \\ i \neq k}}^N \bar{\gamma}_i \phi(\|\mathbf{a}_k - \mathbf{a}_i\|). \quad (9.8)$$

Note that for every  $k$ , a new set of coefficients  $\bar{\gamma}_i$  is computed. Equation (9.8) is applied for  $k = 1, \dots, N$  and all errors are put into an error vector  $\mathbf{E}$ , with elements:

$$E_k = f_k - u^{(k)}(\mathbf{x}_k), \quad k = 1, \dots, N, \quad (9.9)$$

where  $f_k$  is the known solution at sample point  $k$ . A norm of  $\mathbf{E}$  is taken to obtain an error estimate of the approximation. Three vector norms have been explored by Rippa (1999):

$$L_1\text{-norm:} \quad |\mathbf{E}|_1 = \sum_{i=1}^N |E_i|, \quad (9.10)$$

$$L_2\text{-norm:} \quad |\mathbf{E}|_2 = \sqrt{\sum_{i=1}^N E_i^2}, \quad (9.11)$$

$$L_\infty\text{-norm:} \quad |\mathbf{E}|_\infty = \max_i |E_i|. \quad (9.12)$$

Rippa (1999) showed that the  $L_1$  norm of the vector  $\mathbf{E}$  resembles the RMS error of the RBF approximation best.

### Optimizing the shape parameter $c$

Three of the RBFs considered on page 147 contain a shape parameter  $c$ . The choice of the value for  $c$  determines whether the function results in a more local or global approximation near the support points. If the approximation becomes too local due to the choice for  $c$ , the error becomes very large. On the other hand, if  $c$  is chosen such that the approximation becomes too global, the system of equations (equation (9.4) or (9.7)) becomes badly conditioned. So there exists an optimal value for  $c$ . Improvements of 3 orders of magnitude of the error are observed between the optimal  $c$  and  $c = 1$  (see figure 9.2).

Rippa (1999) shows that the  $L_1$  norm of the vector  $\mathbf{E}$  resembles the RMS error of the approximated surface and shows good results for optimizing  $c$ . Tests show indeed that minimizing the  $L_1$ -norm produces slightly better values for  $c$  than the  $L_2$ -norm. The  $L_\infty$ -norm is not a good choice since it only takes the maximum into account. Often this results in a value for  $c$ , which yields a worse approximation than

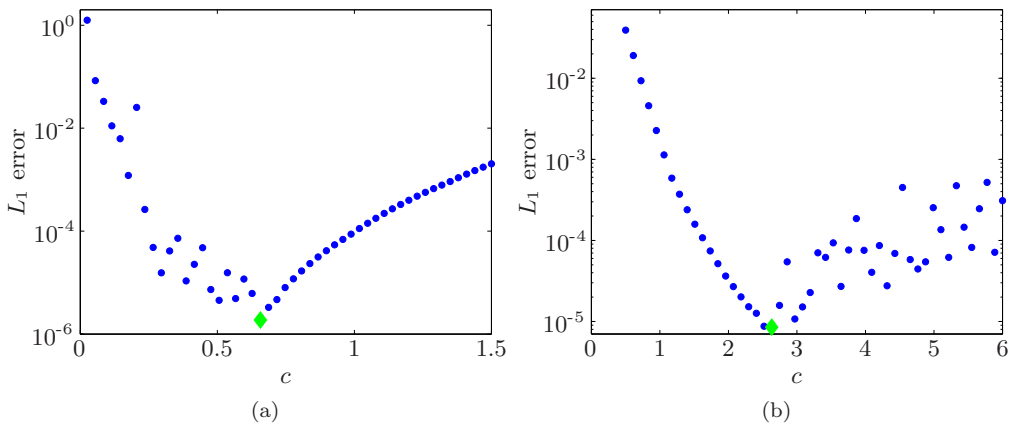


**Figure 9.2:**  $L_1$  error for a range of values for the shape parameter  $c$  for the Gaussian RBF (a) and the multiquadric biharmonic RBF (b).

the approximation with the non-optimized value for  $c$ . Using the  $L_1$ -norm shows improvement of the approximation in the entire domain.

Figure 9.2 shows typical graphs of the  $L_1$ -norm with respect to  $c$ . Figure 9.2(a) depicts the error norm for the Gaussian RBF. Here a smaller  $c$  leads to a more global approximation, since the tails of the Gaussian basis function are wider than the tails for a large  $c$ . Eventually this leads to an ill conditioned system of equations. For the multiquadric biharmonic RBF (see figure 9.2(b)) it is the opposite. A smaller  $c$  results in more local approximations and for larger  $c$  values the system becomes ill conditioned. The part of the graph where the system is ill conditioned is recognized by the large changes in error with only small variations in  $c$ . A brute force optimization is used. This means taking a range of  $c$  values in a large interval and selecting the  $c$  with the lowest  $L_1$  error. For single parameter cases, a brute force approach is feasible..

### 9.1.3 Sampling of the support points

The following sampling techniques are considered [Swiler et al. (2006); Du et al. (1999); Diwekar and Kalagnanam (1997); Metropolis and Ulam (1949)]:

- Random sampling:  $N$  samples are taken randomly in  $\Omega$ ;
- Latin Hypercube sampling (LHS):  $N$  samples are taken randomly in  $N$  volumes in  $\Omega$  of equal probability;

## 9.2 Evaluation of the radial basis functions and sampling techniques

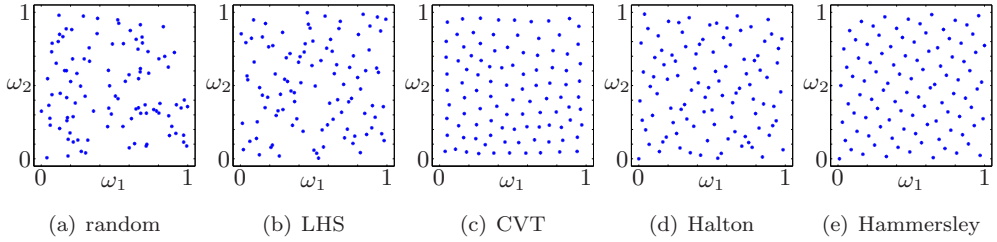


**Figure 9.3:** Sampling techniques, 100 points for two random variables.

- Centroidal Voronoi tessellation (CVT): The probability space is divided into  $N$  volumes in  $\Omega$  of equal probability. The  $N$  centroids of the volume are the samples;
- Halton sampling: the  $N$  samples are the first  $N$  values of the Halton sequence;
- Hammersley sampling: the  $N$  samples are the first  $N$  values of the Hammersley sequence.

Figure 9.3 shows 100 samples for two random variables using the mentioned sampling techniques. It can be seen that the deterministic sampling techniques provide a more homogeneous coverage than the random sampling and Latin Hypercube sampling. The sampling of the support points is done in the domain  $\Omega \in [0, 1]^d$ , where  $d$  is the number of uncertain parameters. The corresponding parameter values for each support point  $\mathbf{a}(\omega_i) = \{a_1(\omega_i), a_2(\omega_i), \dots, a_d(\omega_i)\}$  are obtained by the probability distribution functions of the uncertain parameters.

## 9.2 Evaluation of the radial basis functions and sampling techniques

The PRBF approach using different combinations of RBFs and sampling techniques is discussed in the next sections for the mass-spring problem with two uncertain parameters. The goal is to identify the most suitable sampling strategy and radial basis function to be used for uncertainty quantification. A comparison between the PRBF approach and the Probabilistic Collocation method is shown up to five uncertain parameters for two analytic test functions.

### 9.2.1 Mass-spring problem

The mass-spring configuration indicated by figure 9.4(a) is used to investigate the convergence of the RBFs and sampling methods. Consider a mass  $m$  mounted on a spring of length  $L$  in equilibrium with stiffness  $k$ . The base movement is prescribed by the function  $x_{\text{base}}(t)$ . The governing equations and initial conditions for this system are:

$$m\ddot{x} + kx = kx_{\text{base}} \quad t > 0 \quad (9.13)$$

$$x(0) = x_0 \quad (9.14)$$

$$\dot{x}(0) = 0, \quad (9.15)$$

where  $x_0$  is the initial position of the mass. It is assumed that the base is harmonically excited by  $x_{\text{base}}(t) = A \sin(\omega t)$ , with  $A = 0.1$  m and  $\omega = 0.5$  s<sup>-1</sup>. For this excitation the analytical solution is given by:

$$x(t) = x_0 \cos(\omega_n t) - \frac{\omega_n \omega A}{\omega_n^2 - \omega^2} \sin(\omega_n t) + \frac{\omega_n^2 A}{\omega_n^2 - \omega^2} \sin(\omega t), \quad (9.16)$$

in which  $\omega_n = \sqrt{\frac{k}{m}}$  is the natural frequency of the system. Figure 9.4(b) shows three deterministic solutions for  $\omega_n = 0.9, 1$ , and  $1.1$  s<sup>-1</sup>. It can be seen that a variation in  $\omega_n$  leads to significant variations of the mass position  $x$ . The mass  $m$  and spring stiffness  $k$  are assumed to be a uniformly distribution uncertain parameter, with mean  $\mu_k = 1$  N/m and  $\mu_m = 1$  kg and both with a coefficient of variation of  $CV = \sigma/\mu = 0.1$ .

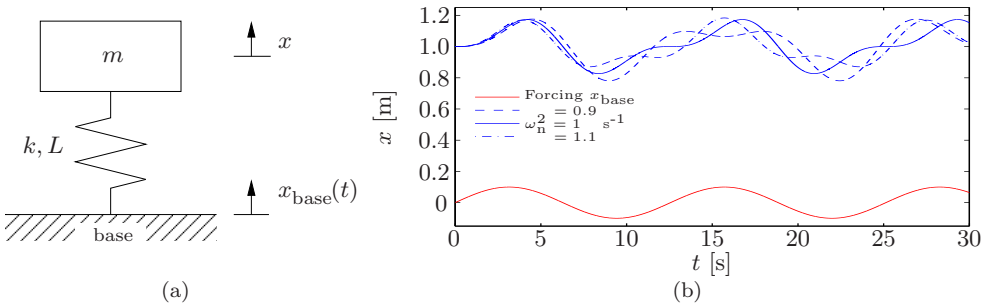
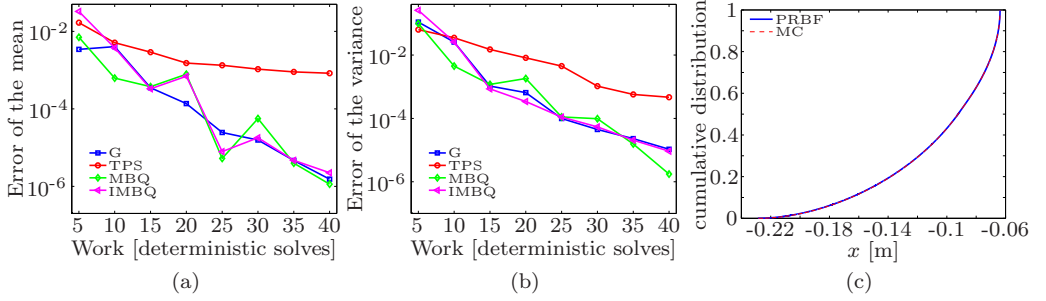


**Figure 9.4:** The mass-spring test problem with (a) the configuration and (b) deterministic solutions for values of  $\omega_n^2 = 0.9, 1$  and  $1.1$  s<sup>-1</sup>.

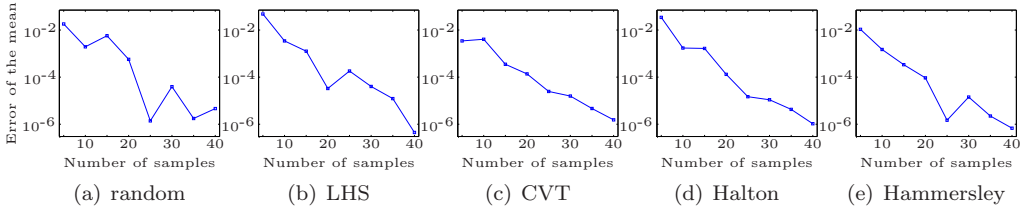
### Comparison of radial basis functions

Figure 9.5(a) and 9.5(b) show the convergence of the relative error of the mean and variance of the mass position at  $t = 10$  s for uniformly distributed  $m$  and  $k$  using

## 9.2 Evaluation of the radial basis functions and sampling techniques



**Figure 9.5:** Error convergence of the different RBFs with optimized shape parameter for the mean (a) and variance (b) of the mass position at  $t=10$  s resulting from uncertain mass  $m$  and spring stiffness  $k$  using CVT sampling and (c) the cumulative distribution function of the mass position  $x$  at  $t=10$  s obtained using the PRBF approach (—) using 16 CVT support points with the Gaussian RBF with optimized shape parameter  $c$  and Monte Carlo simulation (---) with 1,000,000 random samples.



**Figure 9.6:** Error convergence of the mean of the mass position at  $t = 10$  s resulting from uncertain mass  $m$  and spring stiffness  $k$  using the Gaussian RBF with optimized shape parameter  $c$  using random (a), Latin Hypercube (b), centroidal Voronoi tessellation (c), Halton (d) and Hammersley (e) sampling.

CVT sampling. The relative error of the mean and variance are defined as

$$\epsilon_{\mu} = \left| \frac{\mu_x(t) - \mu_{x_{\text{reference}}}(t)}{\mu_{x_{\text{reference}}}(t)} \right|, \quad \epsilon_{\sigma^2} = \left| \frac{\sigma_x^2(t) - \sigma_{x_{\text{reference}}}^2(t)}{\sigma_{x_{\text{reference}}}^2(t)} \right|, \quad (9.17)$$

with the reference solution  $x_{\text{reference}}(t)$  obtained from a Monte Carlo simulation using 1,000,000 random samples. The only RBF that performs worse than the others is the thin plate spline (TPS). The Gaussian RBF shows the smoothest decrease of the error compared to the (inverse) multiquadric biharmonic RBFs. The cumulative distribution function of the mass position  $x$  at  $t = 10$  s is given in figure 9.5(c). The distribution function is obtained using 16 CVT samples and the Gaussian RBF with optimized shape parameter  $c$ , the result shows good correspondence with the Monte Carlo simulation using 1,000,000 random samples.

## **Comparison of sampling techniques**

The sampling techniques are judged on:

- the convergence of the mean and variance of the solution;
- the uniformity of the distribution of the support points in probability space  $\Omega$ ;
- the ability to add extra support points for a higher accuracy.

### **Convergence of the mean and variance**

The effect of the sampling of the support points on the convergence of the mean is shown in figure 9.6. The Gaussian RBF is used for the response surface approximation. No significant difference exists between the sampling techniques, the error convergence of the variance shows similar results. This corresponds with observation of Swiler et al. (2006). Only the CVT and Halton sampling show a smooth decrease of the error.

### **Uniformity of the support points**

A uniform distribution of the samples in probability space is important for the stability of the RBFs. When two samples are close to each other, the resulting system of equations for the coefficients of the RBFs becomes nearly singular. Figure 9.3 shows the distribution of 100 samples in a two-dimensional parameter space. The most homogeneous distribution of the samples in probability space is obtained by the CVT sampling, also in higher dimensions. Also the Halton and Hammersley sampling result in a uniformly covered space. This depends, however, on the number of stochastic dimensions and the number of samples. Random sampling result in a less homogeneous distribution. Also the Latin Hypercube sampling, although less severe, can result in samples that are close to each other.

### **Ability to add a support point**

Two of the investigated sampling methods have the ability to add support points, namely random and Halton sampling. The other three sampling methods, Hammersley sampling, Latin Hypercube and centroidal Voronoi tessellations, recompute the sampling grid when more samples are required. This means that either earlier computed results cannot be reused or that the uniform distribution of the samples in probability space is not maintained.

## 9.2 Evaluation of the radial basis functions and sampling techniques

### Halton sampling for support point sampling and Gaussian RBF for response surface reconstruction

There was no significant difference between the convergence of the different sampling techniques, so no conclusion could be drawn based on this. The Halton sampling is chosen, based on the property that samples can be added when the accuracy is expected to be not sufficient. In this way, the convergence of the PRBF approach can be tracked by monitoring the change in mean and variance when a sample is added. The solution of the added sample can be predicted based on the RBF approximation of the previously computed samples. The difference between the prediction and the computed solution is an indication for the accuracy of the response surface approximation. Clustering of samples occurs in high dimensions [Robinson and Atcity (1999)] when the Halton sequence is used. To avoid this, for example a leaped Halton sequence can be used. Based on the performed computations, the Gaussian RBF is preferred for further use. The RBF shows the smoothest convergence and is least affected by stability problems when solving for the coefficients  $\gamma$ .

### 9.2.2 Comparison between the PRBF approach and Probabilistic Collocation up to 5 uncertain parameters

In order to compare the Probabilistic Radial Basis Function approach with the Probabilistic Collocation method an analytic test function is used. The function is the oscillatory Genz function [Genz (1984); Schürer (2003)]:

$$f(\mathbf{x}) = \cos\left(2\pi\beta_1 + \sum_{i=1}^d \alpha_i x_i\right), \quad \|\alpha\|_1 = \frac{110}{20\sqrt{d^3}}, \quad (9.18)$$

where  $\mathbf{x}$  is the  $d$ -dimensional surface spanned by vector  $x_i$ . Note that here the difficulty  $\|\alpha\|_1$  is a factor 20 smaller than the original Genz function. This is done to obtain a response that is more representative to CFD cases. The variables  $x_i$  are assumed to be uncertain with a uniform distribution on  $[0,1]$ . The output of interest are the mean and variance of  $f$ .

Table 9.1 shows the number of function evaluations required to obtain the mean and variance with an accuracy of  $10^{-3}$ . The table is constructed from the convergence plots in appendix E. For 3 uncertain parameters, the PRBF approach shows an improvement compared to the Probabilistic Collocation method. For 5 uncertain parameters, the Probabilistic Collocation method is not even feasible for CFD applications anymore, assuming that about 100 deterministic solves are affordable. When the convergence for the Probabilistic Collocation method is plotted against polynomial order, spectral convergence is observed. Due to the curse of dimensionality, the number of collocation points increases rapidly. The PRBF approach requires only a small number of additional support points with increasing dimension.

**Table 9.1:** Number of function evaluations to approximate the mean and variance with an accuracy below  $10^{-3}$ .

Stochastic dimension	PC		PRBF	
	mean $\mu_f$	variance $\sigma_f^2$	mean $\mu_f$	variance $\sigma_f^2$
2	9	16	10	15
3	27	64	20	35
4	81	256	30	60
5	243	1024	40	105

### 9.3 Flow around a NACA0012 airfoil with 4 uncertain parameters

In order to demonstrate the PRBF approach for a more realistic test problem, it is applied to steady flow around a NACA0012 airfoil with uncertain Mach number, angle of attack, thickness and maximum camber using a commercial deterministic CFD code. The deterministic case is at an angle of attack of  $5^\circ$  and a free stream Mach number of  $M=0.3$ . The Reynolds number is equal to  $3 \times 10^6$ . The deterministic computations are performed using the FINE™/Hexa solver by Numeca International on a grid of approximately 76,919 cells. Approximately 1600 cells cover the surface of the airfoil with  $y^+ \leq 1$ . The grid layout is shown in figure 9.7. The deterministic settings are the same as for the test case in section 5.3.1.

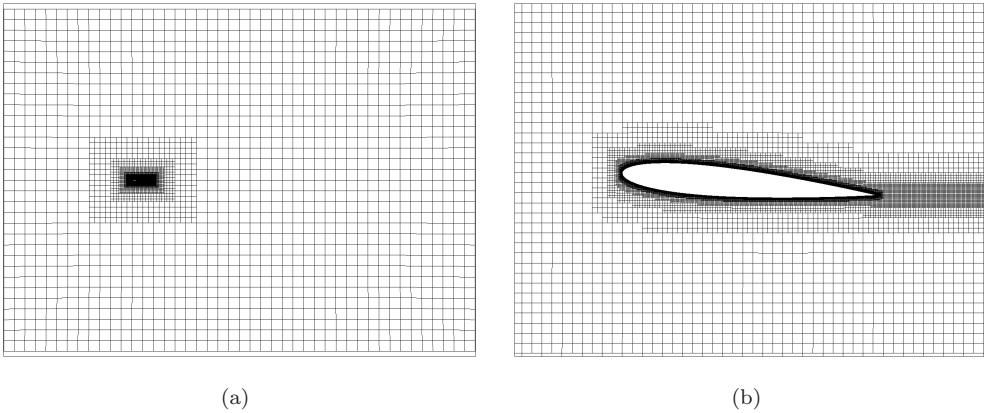


**Figure 9.7:** The computational mesh layout (a) and a detailed view of the airfoil (b).

The flow is modeled by the Reynolds-averaged Navier-Stokes equations using the Spalart-Allmaras turbulence model. The air properties are at 0 m ISA. The uncertainties are present in the free stream flow conditions, i.e. the Mach number and angle of attack, and the geometry. All parameters are assumed to have a truncated



## 9.4 Transonic flow around a RAE2822 airfoil with 3 uncertain parameters

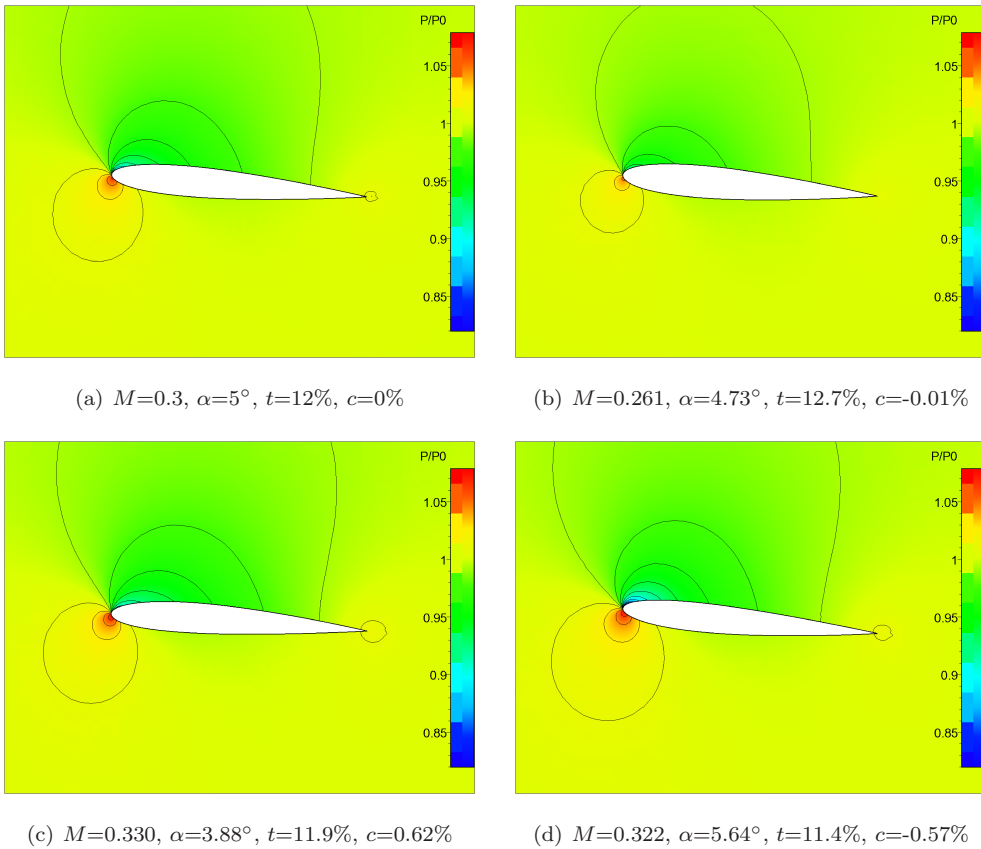
Gaussian distribution. The geometry of the airfoil is parametrized according to the NACA 4-digit airfoil series parameterization. Uncertain are the thickness and maximum camber. The free stream Mach number has a mean  $\mu_M=0.3$  and a standard deviation  $\sigma_M=0.03$ , on the interval  $[0.23, 0.37]$ . The mean angle of attack is  $\mu_\alpha=5^\circ$  with a standard deviation  $\sigma_\alpha=0.50^\circ$ , in the interval  $[3.84^\circ, 6.16^\circ]$ . The geometric parameters that represent the uncertainty are the thickness of the airfoil in percents of the chord with mean  $\mu_t=12\%$ , a standard deviation  $\sigma_t=0.425\%$  and truncated to the interval  $[11.02\%, 12.98\%]$  and the maximum camber in percents of the chord, which has mean  $\mu_c=0\%$ , standard deviation  $\sigma_c=0.4472\%$  and is truncated in the interval  $[-1.04\%, 1.04\%]$ . The uncertainty is propagated using the Probabilistic Radial Basis Function approach, with 35 support points obtained from Halton sampling. The flow solver is run deterministically for every support point. Figure 9.8(a) shows the pressure field with isolines of the mean conditions. Figures 9.8(b) till 9.8(d) show the pressure fields with isolines of three samples.

Figure 9.9(a) shows the convergence of the lift-over-drag ratio with respect to the number of samples for different values of the shape parameter  $c$  using the Gaussian RBF. The shape parameter determines the width of the Gaussian function. A large  $c$  results in more localized RBFs, as a small  $c$  provides a more global RBF. Figure 9.9(b) shows how the optimal  $c$  changes with the number of available support points. The figure shows that with this low number of samples a more global RBF results in a better approximation of the mean  $L/D$ . The mean  $L/D$  converges to 42.17, which is 1% lower than the deterministic value of 42.59. The standard deviation becomes  $\sigma_{L/D} = 4.051$ , which results in a coefficient of variation of  $CV_{L/D} = (\mu/\sigma)_{L/D} = 9.6\%$ .

The pressure on the airfoil surface is presented in figure 9.10. The mean pressure is shown with uncertainty bars indicating the area of plus and minus one standard deviation. It can be seen that the uncertain parameters result in the largest variation in the pressure on the upper part of the airfoil, mainly near the leading edge.

## 9.4 Transonic flow around a RAE2822 airfoil with 3 uncertain parameters

In this section, transonic flow around a RAE2822 airfoil is considered. The test case is the same as discussed in section 3.2. The Probabilistic Radial Basis Function approach is applied to the same test case. The results are compared with the Probabilistic Collocation results and a Monte Carlo simulation using 10,000 Latin Hypercube samples.



**Figure 9.8:** Pressure field and isolines (same scale) of the mean conditions (a) and for three samples (b), (c), and (d).

### 9.4 Transonic flow around a RAE2822 airfoil with 3 uncertain parameters

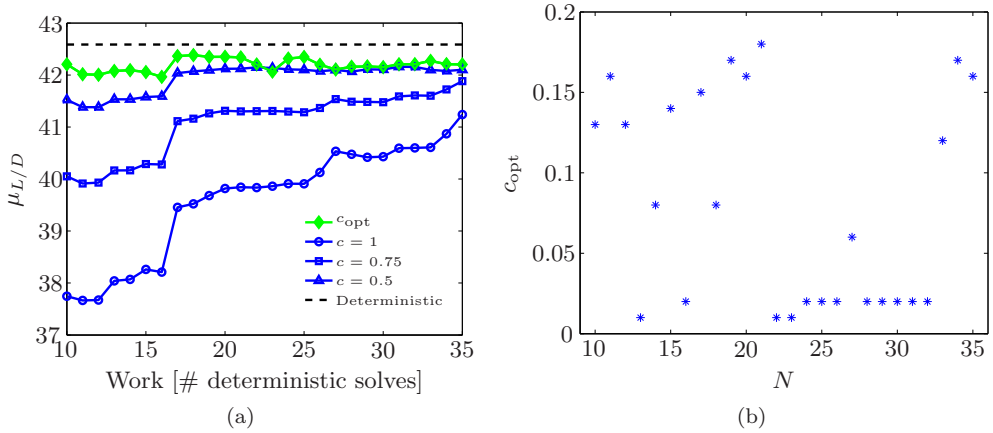


**Figure 9.9:** The convergence of the mean lift-over-drag ratio with respect to the number of samples for varying shape parameter  $c$  using the Gaussian RBF (a), the green line with diamonds ( $\blacklozenge$ ) indicates the  $L/D$  for the optimal shape parameter  $c_{opt}$  (b). The deterministic value is indicated by the dashed red line (--).

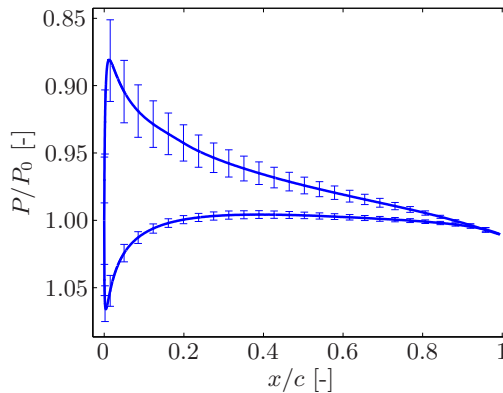


**Figure 9.10:** The mean pressure (—) along the surface of the airfoil with the bars indicating the standard deviation of the pressure, obtained using the Gaussian RBF with optimized shape parameter.

### 9.4.1 Test case settings

The flow parameters are set according to Cook et al. (1979), i.e. the mean flow Mach number is  $M_\infty = 0.734$ , the angle of attack is  $\alpha = 2.79^\circ$ , and the Reynolds number is  $6.5 \times 10^6$ . The computations are performed on a grid of 76,063 cells. About 800 cells are present on the surface of the airfoil with  $y^+ \leq 1$ . The computations are converged to a relative residual of  $10^{-10}$  to eliminate the iteration error.

Three uncertain parameters are considered simultaneously, which are the free stream Mach number, the angle of attack and the relative thickness. The uncertain parameters have normal distributions, as shown in figure 3.7. The free stream Mach number has a mean of  $\mu_M=0.734$  and a standard deviation of  $\sigma_M=0.005$ . The angle of attack has a mean and standard deviation of  $\mu_\alpha=2.79^\circ$  and  $\sigma_\alpha=0.1^\circ$ . For the relative thickness, the mean and standard deviation are  $\mu_t=1$  and  $\sigma_t=0.005$ . This results in coefficients of variation  $CV = \sigma/\mu$  of 0.68%, 3.58%, and 0.5% respectively.

### 9.4.2 Results of the Probabilistic Radial Basis Function approach

Table 9.2 shows the mean and standard deviation of the lift and drag coefficient. The results of the PRBF approach are well within 1 count ( $10^{-3}$  and  $10^{-4}$  respectively). With only 10 support points, the PRBF approach yields accurate results. Although the Probabilistic Collocation method shows spectral convergence and matches the Monte Carlo results with a low order approximation, the number of collocation points has to be 8, 27, 64, or more. This shows the benefit of the free choice of the support points in the PRBF approach. The numbers of table 9.2 are shown in figure E.2 in appendix E. The figures show that the PRBF results quickly are within 1% or 1 count from the mean and standard deviation.

**Table 9.2:** Results of the Probabilistic Radial Basis Function approach, the Probabilistic Collocation method and a Monte Carlo simulation using 10,000 Latin Hypercube samples.

Number of support pts	$C_l$		$C_d$	
	mean $\mu$	std $\sigma$	mean $\mu$	std $\sigma$
5	0.7701	0.01814	0.01869	0.002305
10	0.7694	0.01635	0.01880	0.002257
15	0.7697	0.01656	0.01881	0.002247
20	0.7695	0.01643	0.01882	0.002265
30	0.7699	0.01651	0.01883	0.002263
40	0.7695	0.01652	0.01882	0.002235
50	0.7698	0.01657	0.01883	0.002245
PC p=2 (27 pts.)	0.7698	0.01652	0.01883	0.002252
MC 10,000 LHS	0.7698	0.01652	0.01883	0.002254

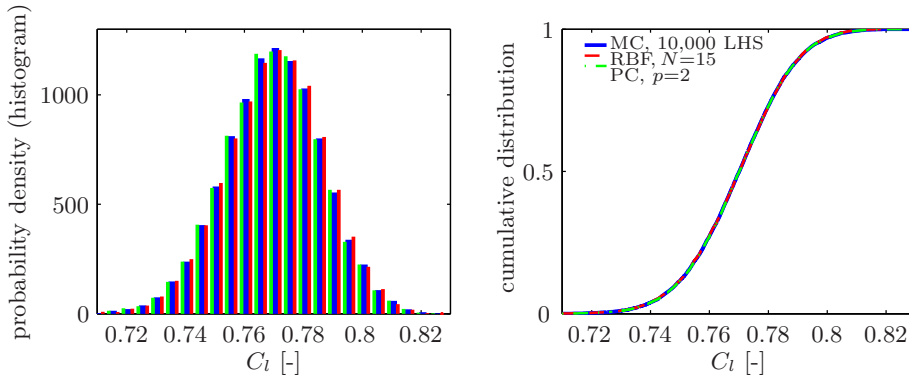


**Figure 9.11:** Probability density function (histogram) and cumulative distribution function of the lift coefficient  $C_l$  of the RAE2822 airfoil with uncertain free stream Mach number, angle of attack, and relative thickness. The figures shows the result of a Monte Carlo simulation using 10,000 Latin Hypercube samples, a Probabilistic Radial Basis Function approximation using 15 support points and a second order Probabilistic Collocation approximation using 27 deterministic solves.

Figures 9.11 and 9.12 show the probability density function as a histogram and the cumulative distribution function of  $C_l$  and  $C_d$ . The figures include the results from the Probabilistic Radial Basis Function approach using 15 support points, the Probabilistic Collocation method using a second order approximation and a Monte Carlo simulation with 10,000 Latin Hypercube samples. The Probabilistic Collocation results are discussed in more detail in section 3.2. Both distributions are close to a normal distribution, which was the distribution of the uncertain input parameters. The probability density function of  $C_d$  (figure 9.12) shows some skewness. A close agreement between all methods is observed, where the PRBF uses the least amount of CFD simulations.

## 9.5 Summary

The Probabilistic Radial Basis Function approach was shown to be a good uncertainty quantification method for cases with multiple uncertain parameters. Although the method does not show spectral convergence, the error of the mean and variance quickly decreases till acceptable levels (0.1-1%) with a low amount of support points.

Five different sampling strategies have been evaluated, i.e. random, Latin Hypercube, centroidal Voronoi tessellation, Halton, and Hammersley sampling. The convergence of the PRBF was not affected, so the choice of sampling strategy was made based on other properties. Halton sampling was used for further computations, since it allows the addition of new support points when a higher accuracy is required without disregarding the previously performed simulations.

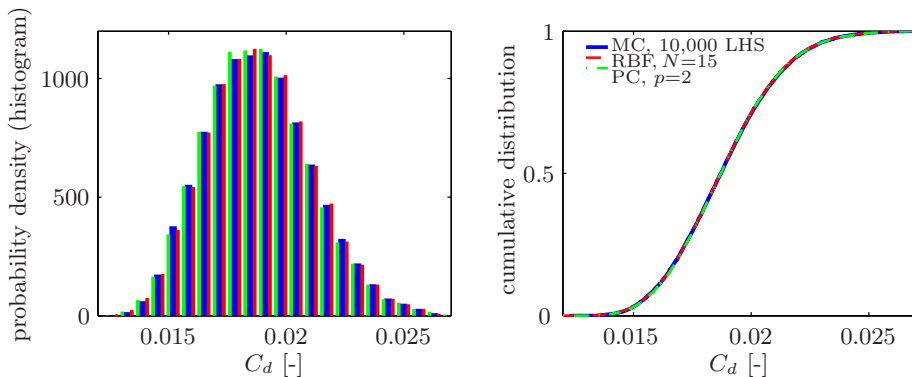


**Figure 9.12:** Probability density function (histogram) and cumulative distribution function of the drag coefficient  $C_d$  of the RAE2822 airfoil with uncertain free stream Mach number, angle of attack, and relative thickness. The figures shows the result of a Monte Carlo simulation using 10,000 Latin Hypercube samples, a Probabilistic Radial Basis Function approximation using 15 support points and a second order Probabilistic Collocation approximation using 27 deterministic solves.

Four RBFs have been used, i.e. the Gaussian, thin plate spline, multiquadric biharmonic, and the inverse multiquadric biharmonic RBFs. The thin plate spline performed worse than the other three. The Gaussian RBF is used for the reconstruction of the weighted response surface based on the smooth convergence and the RBF showed no stability problems when solving for the coefficients. The shape parameter is optimized to adapt the RBF optimally to the available support points and response.

The flow test cases demonstrate that the PRBF approach yields satisfactory results using only 10-35 support points. A big advantages for CFD applications is the ability to freely choose the support points, it does not rely on quadrature rules. If the flow solver does not convergence, one can choose a new point in the neighborhood and still maintain the ability to approximate the response correctly. Furthermore, the number of support points can be chosen according the available computational resources and required accuracy. A Monte Carlo simulation using 10,000 Latin Hypercube samples was performed for the flow around a RAE2822 airfoil with 3 uncertain parameters. Close agreement with the PRBF approach was shown, using only 15 support points.

# CHAPTER 10

---

## Conclusions

---

The conclusions are divided into two parts. First some general conclusions regarding the objectives of this thesis are presented. Secondly, conclusions on each chapter are drawn.

### 10.1 General conclusions

The main objective of this research was to obtain efficient approaches for uncertainty quantification in computational fluid dynamics (CFD) simulations, where the focus is on practical application of the method to a wide range of test cases.

Based on the results in this thesis, it can be concluded that the use of the Probabilistic Collocation method, and adapted versions, are capable of efficiently propagating uncertainties in CFD simulations. The development of the Probabilistic Radial Basis Function approach provided an efficient alternative for cases with multiple uncertain parameters.

Based on the experience with the test cases, it can be concluded that there is not a single method that is most efficient for all possible cases. However, by using the knowledge from the case, it is still possible to efficiently propagate uncertainties.

## **Chapter 10: Conclusions**

### **Efficient uncertainty propagation**

In the search for an efficient uncertainty propagation method, the Probabilistic Collocation method was developed. The Probabilistic Collocation method shows spectral convergence with respect to the order of approximation for many test cases. However, there are cases where the method fails or becomes too computationally intensive. These are cases where the response contains discontinuities, strong gradients or becomes more nonlinear in time (which can happen in unsteady simulations). For these cases the global polynomial approximation of the response is not capable to capture the features that are present. Modifications of the Probabilistic Collocation method are able to solve some of the issues. For example a multi-element formulation can adapt to discontinuities and a time-independent parameterization is able to maintain a constant accuracy in time.

### **Geometric uncertainties**

When geometric uncertainties, that affect the shape of the model, are present in a CFD simulation, a new grid has to be constructed for every collocation point in the Probabilistic Collocation method. A grid deformation routine was used to efficiently compute a new computational grid for every collocation point. Since the deviations from the base line configuration (mean) are in general small, the grid deformation does not reduce the mesh quality significantly. Test cases show that geometrical uncertainties have a significant influence on the performance, and should, therefore, be taken into account in simulations.

### **Multiple uncertain parameters**

When multiple uncertain parameters are present, the Probabilistic Collocation method suffers from the curse of dimensionality. The number of collocation points that is required, even for low orders of approximation increases exponentially with the number of uncertain parameters. For CFD simulations, this implies that if one is able to perform in the order of 100 deterministic computations, maximal 6 uncertain parameter can be propagated linearly.

In order to efficiently propagate multiple uncertainties, two approaches have been followed. First a Two-Step approach, where the uncertain parameters are first screened using a sensitivity analysis. In the second step, the probability density functions of the most important uncertain parameters are propagated using the Probabilistic Collocation method.

The second approach was the Probabilistic Radial Basis Function approach, where radial basis function were used to approximate the high-dimensional surface. For some cases, screening might still result in many uncertain parameters that are equally important. Radial basis functions are known for their good interpolation properties in high-dimensional spaces. The test cases showed that for 3 or more uncertain



parameters, the Probabilistic Radial Basis Function approach is a good alternative approach for the Probabilistic Collocation method.

## 10.2 Conclusions based on each chapter

### The Probabilistic Collocation method (chapter 2)

The Probabilistic Collocation method was developed, based on the polynomial chaos framework. It shows spectral convergence with respect to the polynomial chaos order for arbitrarily distributed uncertain parameters. The Probabilistic Collocation method is non-intrusive, enabling the use of existing (commercial) CFD solvers. A big advantage with respect to the intrusive Galerkin Polynomial Chaos method is the fact that propagation through nonlinear models do not result in an increase of computational effort. Furthermore, the uncertainty is trivially propagated to functionals of the solution like integral quantities. This was made clear in the performed test cases, where the output of interest was for example the lift and drag of an airfoil, the minimum and maximum pitch angle or the efficiency of a compressor rotor.

A comparison of the Probabilistic Collocation method with some existing methods for one uncertain parameter demonstrated the spectral convergence with respect to the polynomial chaos order. It was shown that the Probabilistic Collocation method was more efficient (more accurate with respect to the amount of computational work) than the intrusive Galerkin Polynomial Chaos method, the Non-Intrusive Polynomial Chaos method, and the Stochastic Collocation (MH) method for arbitrarily distributed uncertain parameters.

### Flow applications of the Probabilistic Collocation method (chapter 3)

The Probabilistic Collocation method was applied successfully to two flow applications. Since the method is non-intrusive, a commercial CFD solver could be employed. Subsonic and transonic flow around an airfoil have been considered.

The first test case is a simulation of subsonic turbulent flow around a NACA0012 airfoil where the free stream Mach number was assumed to be uncertain with a coefficient of variation of 5%. A Monte Carlo simulation using 10,000 Latin Hypercube samples has been performed to validate the Probabilistic Collocation method. Good agreement has been found between the Monte Carlo simulation and a second order Probabilistic Collocation approximation, requiring three deterministic solves. The coefficients of variation of the lift and drag are 10.5% and 9.45% respectively. This is an amplification of a factor 2 of the coefficient of variation of the uncertain free stream Mach number. The mean and standard deviation field of the static pressure showed that the flow is most sensitive to the uncertain freestream Mach number near the suction peak at the leading edge.

The second test case was transonic turbulent flow around a RAE2822 airfoil. Uncer-

## **Chapter 10: Conclusions**

tainties were present in the free stream Mach number, angle of attack and relative thickness of the airfoil. The uncertainties were propagated first separately to see the effect of each parameter on the solution. After that, all three uncertainties are propagated simultaneously to include interactions between the parameters. The results show that the flow is most sensitive to uncertainties near the shock wave. Especially the drag coefficient turns out to be sensitive, since the coefficients of variation of the uncertain parameters were significantly amplified. A second order Probabilistic Collocation approximation was used to propagate the uncertain parameters. This required 3 computations for the separate cases and 27 for the simultaneous case.

### **Modifications of the Probabilistic Collocation method (chapter 4)**

For test cases with a discontinuous response or time dependent test cases for which the response changes with time, the standard Probabilistic Collocation method cannot readily be applied. With some modifications, it is possible to efficiently propagate uncertainties in such cases.

First a stall flutter model was shown where the model contains a nonlinearity in the form of a step function. Furthermore, the output of interest is the minimum and maximum pitch angle of the airfoil in the limit state. For both reasons the intrusive Galerkin Polynomial Chaos method cannot be applied efficiently to this test case. The response of the model can contain a bifurcation point. In that case, some solutions are damped, while other show a limit cycle oscillation. When the bifurcation is present, the standard Probabilistic Collocation approximation fails. For this case a multi-element formulation in combination with search samples was successfully applied to uncertainty analysis of the stall flutter model. The result was a stochastic bifurcation plot, which showed the mean of the minimum and maximum pitch angle with uncertainty bars indication 99.8% of all possible values. Furthermore, the probability distribution of the bifurcation point was computed.

The second test case was a low Reynolds number flow around a static cylinder. The Reynolds number is assumed to be uncertain, to investigate the effect on the response of the lift and drag coefficient. In this case the response surface becomes more non-linear in time. This is caused by a frequency difference in the solution due to the presence of the uncertain parameter. This requires an increasing polynomial chaos order to maintain the same accuracy. The Probabilistic Collocation method was applied to time independent parameters that describe the oscillatory response. These parameters are the amplitude, mean value, period and phase. The result is a time independent accuracy, so a constant polynomial chaos order can be used regardless of the simulation time. The period-1 Probabilistic Collocation approach was successfully applied to vortex shedding from a circular cylinder. It was shown that the frequency and mean value are not sensitive to variation of the Reynolds number. On the other hand, the amplitude and the phase are highly sensitive to the Reynolds number, the input uncertainty of 5% was amplified to an output uncertainty in the order of 10%.

### Geometric uncertainties (chapter 5)

Imperfections and wear are inherently present in real life, and can be treated as uncertainties in simulations. These uncertainties can have a significant effect on the performance and have, therefore, been investigated in this chapter. In order to propagate the probability density functions of the uncertain geometric parameters to the performance parameters of the model, the Probabilistic Collocation method was used.

First a low fidelity flow model was used to assess the effect of uncertainties in three geometrical parameters on the performance of a NACA5412 airfoil. A coefficient of variation of 10% was assumed for the maximum camber, maximum camber location, and relative thickness, with a truncated normal distribution. The maximum camber affected the polar in the complete range from  $\alpha=0$  to  $15^\circ$ . The maximum camber location showed no effect on the performance of the airfoil. The thickness mainly results in large standard deviations at higher angles of attack.

Secondly, a CFD test case was shown with two uncertain geometrical parameters (i.e. maximum camber and thickness) for subsonic and transonic flow around a NACA0012 airfoil. To efficiently propagate the uncertainties, a grid deformation technique is used to deform the grid of the case with the mean values of the geometric parameters to the grid required for each collocation point. For the subsonic case, the lift coefficient was shown to be most sensitive to the geometric variations. The transonic case results in a shock wave at the upper surface of the airfoil. The standard Probabilistic Collocation approximation fails near the shock due to the discontinuity in the response. To be able to accurately approximate the uncertainty bars of the pressure, a linear approximation is used in the area where the discontinuity is present. This area was obtained from the probability density function of the shock location. The discontinuity was treated successfully in this way and required no additional deterministic solves.

### Uncertainty analysis of turbulence model parameters (chapter 6)

The  $k$ - $\epsilon$  turbulence model and the standard wall functions contain several parameters that are tuned to computed or measured simplified flow problems. Some parameters are related to each other to assure physical laws are maintained. Finally, 5 parameters were analyzed as uncertainties in the model, i.e.  $C_\mu$ ,  $C_{2,\epsilon}$ ,  $\sigma_k$ ,  $\kappa$ , and  $C$ . Two test cases have been performed, first a fully developed turbulent boundary layer on a flat plate and turbulent flow around a NACA0012 airfoil.

As a general conclusion, the effect of uncertainties in the parameters on the flow solution is case dependent. For both performed test cases, different effects were shown. In case of the turbulent flat plate, the wall function parameter  $\kappa$  was dominant with a coefficient of variation of 4.3% for the drag coefficient. Although the drag coefficient was not much affected,  $C$  and  $C_\mu$  had a significant contribution to the standard deviation of the skinfriction coefficient along the plate. The introduction of different flow topologies such as a stagnation point, a suction peak, and a wake lead to different

## **Chapter 10: Conclusions**

conclusions about the relative importance of coefficients for the airfoil test case. Only  $C_\mu$  and  $\kappa$  resulted in maximum 0.2% and 3% coefficient of variation for the lift and drag coefficient respectively.

### **Analysis of operational uncertainties for a transonic axial flow compressor (chapter 7)**

Compressor rotors are components of a gasturbine that are highly sensitive to operational and geometrical uncertainties. The Probabilistic Collocation method was used to propagate operational uncertainties through simulations of NASA Rotor 37. Validation of the Probabilistic Collocation method with a Monte Carlo simulation using 10,000 Latin Hypercube samples demonstrated that the Probabilistic Collocation method can successfully be applied to a turbomachinery case.

The total pressure profile at the inlet of the rotor is assumed to be uncertain. A symmetric beta distribution was used for the pressure profile, with the standard deviation such that the uncertainty is in the same order of the measurement accuracy reported in literature. The mass flow was shown to be the most sensitive to the uncertainty, while the efficiency is least affected. The compressor maps are constructed as functions of the mass flow. It was shown to be important to take the uncertainty in the total pressure profile at the inlet into account. The standard deviation of the static pressure in the flow field around the blade showed that the largest variation is present near the shock wave and mainly in the region of the strongest shock, which is near the tip of the blade.

### **Two-Step approach for multiple uncertain parameters (chapter 8)**

To reduce the number of deterministic computations in case of multiple uncertain parameters, a two-step approach was employed. The first step is a sensitivity analysis to find the most important parameters. This was done by a first or second order Probabilistic Collocation approximation, depending on the input distribution of the uncertain parameters. The sensitivity derivatives were scaled with the standard deviation of the uncertain parameters to get an estimation of the effect on the solution. No interactions between parameter are taken into account in this step. For the second step, a higher order Probabilistic Collocation approximation was used to propagate only the uncertainty of the most important parameters.

This approach was demonstrated on a flow simulation around a NACA0012 airfoil with 8 uncertain parameters. The sensitivity analysis required 17 computations and the second order propagation 27 of which 7 were already performed during the sensitivity analysis. The total amount of computations adds up to 37, which is an acceptable amount for the additional information that is obtained. If all 8 parameters would have been propagated simultaneously, a first or second order Probabilistic Collocation approximation requires 256 or 6561 respectively. Due to dependence on the dynamic pressure, and therefore quadratic dependence on the uncertain free stream velocity,

the dimensional quantities showed a much larger variability than the dimensionless coefficients.

### **A Probabilistic Radial Basis Function approach (chapter 9)**

If a sensitivity analysis still results in many uncertain parameters, one has to propagate all of them simultaneously. The Probabilistic Radial Basis Function (PRBF) approach was shown to be a good uncertainty quantification method for cases with multiple uncertain parameters. Although the method does not show spectral convergence, the error of the mean and variance quickly decreases till acceptable levels (0.1-1%) with a low amount of support points.

Five different sampling strategies have been evaluated, i.e. random, Latin Hypercube, centroidal Voronoi tessellation, Halton, and Hammersley sampling. The convergence of the PRBF was not affected, so the choice of sampling strategy was made based on other properties. Halton sampling was used for further computations, since it allows the addition of new support points when a higher accuracy is required without disregarding the previously performed simulations.

Four radial basis functions (RBFs) have been used, i.e. the Gaussian, thin plate spline, multiquadric biharmonic, and the inverse multiquadric biharmonic RBFs. The thin plate spline performed worse than the other three. The Gaussian RBF is used for the reconstruction of the weighted response surface based on the smooth convergence and the RBF showed no stability problems when solving for the coefficients. The shape parameter is optimized to adapt the RBF optimally to the available support points and response.

The flow test cases demonstrate that the PRBF approach yields satisfactory results using only 10-35 support points. A big advantage for CFD applications is the ability to freely choose the support points, the PRBF approach does not rely on quadrature rules. If the flow solver does not convergence, one can choose a new point in the neighborhood and still maintain the ability to approximate the response correctly. A Monte Carlo simulation using 10,000 Latin Hypercube samples was performed for the flow around a RAE2822 airfoil with 3 uncertain parameters. Close agreement with the PRBF approach was shown, using only 15 support points.



---

## Recommendations

---

This chapter presents recommendations based on the chapters of this thesis and the observations and experiences of the performed work. Many has been done on efficient uncertainty quantification in computational fluid dynamics (CFD). The development of the presented approaches and performed test cases gained a lot of insight in uncertainty propagation and the application to CFD simulations. Some recommendations directly relate to a chapter of the thesis, others provide ideas for future research and new applications.

### **Efficient uncertainty propagation**

The Probabilistic Collocation method is based on Gauss quadrature. Other quadrature schemes may provide a good alternative for certain test cases. One can think of sparse grid schemes or nested quadrature rules. Nested quadrature like Clenshaw-Curtis or Gauss-Kronrod quadrature, have the advantage that a higher order approximation reuses previously computed solutions. It should be investigated how they can be used in a polynomial chaos framework, such that the convergence properties are independent of the probability distribution of the uncertain parameters.

Furthermore, computational time can be saved by setting up the complete uncertainty propagation cycle efficiently. This includes managing the performed deterministic computations in such a way that computations that have to be performed due to an increase of approximation order or due the additions of new support points can use

## **Chapter 11: Recommendations**

the result of a computation with similar settings as an initial condition. Savings of computational time over 50% have been observed.

### **Uncertainty analysis of turbulence model parameters**

Turbulence models often work very well for a range of test cases and fail for others. Therefore, to obtain a better picture of the effect of uncertainties in the turbulence model parameters, more test cases should be performed. A good place to start are commonly used test cases like a shear layer, an expanding jet, a bump in a channel, etc.

Next to the  $k$ - $\epsilon$  turbulence model, it would be interesting to see the effect of uncertainties of the parameters of other turbulence models, like the SST  $k$ - $\omega$  model or the Spalart-Allmaras model. Finding suitable probability distributions for the parameters might be a difficult task.

### **Analysis of operational uncertainties for a transonic axial flow compressor**

For NASA Rotor 37 operational uncertainties have been investigated in this thesis. A significant influence on the performance was found. However, geometrical uncertainties will be another source of uncertainty that might have a significant influence on the performance. For example the tip clearance and surface roughness are known to affect the performance of the rotor [Chima (1998); Gerolymos and Vallet (1999); Beheshti et al. (2004)].

### **Two-Step approach for multiple uncertain parameters**

The two-step approach as presented in this thesis used the Probabilistic Collocation method to compute sensitivity derivatives for each uncertain parameter separately. It was assumed that the parameters are independent and have no interactions. Whether this assumption is valid or not and the effect on the choice of important parameters should be investigated in more detail. Another approach to take into account interactions between parameters is the Elementary Effects method [Morris (1991); Campolongo et al. (2007); Saltelli et al. (2008)].

### **A Probabilistic Radial Basis Function approach**

The Probabilistic Radial Basis Function approach was shown to be promising method for efficient uncertainty propagation for cases with multiple uncertain parameters. To increase the robustness of the radial basis function approximation, a filtering technique can be applied. This is common practice in deterministic simulations where radial basis functions are used to approximate discontinuous functions or functions with strong gradients.



## **Robustness of uncertainty propagation methods**

Many uncertainty propagation methods assume that the deterministic solutions (at a collocation point or support point) are exact. In practice, there is numerical noise on the solution for example due to insufficient convergence of the iterative solver or insufficient grid quality. Noise on the deterministic solves can cause the Probabilistic Collocation approximation to fail. Especially if this noise has the same order of magnitude as the effect of the uncertainty. This can be handled by incorporating some regression methodology to make the method more robust. This comes at the cost of efficiency, but for practical problems it might be worth the effort.

## **Accuracy of the stochastic simulation**

A stochastic simulation starts from the same errors as the deterministic simulations, like iteration and discretization error. But on top of that comes the uncertainty propagation error. It does not make sense to propagate uncertainties at a very high order of approximation when the deterministic solver is erroneous. Both the error of the deterministic solver and the uncertainty propagation error should be synchronized.

## **Robust design optimization**

The uncertainty propagation methods used in this thesis provide a good approximation of the global probability distribution of the solution. The mean and variance are accurately determined. The next step will be to combine uncertainty propagation with optimization to obtain a robust optimization method, i.e. optimize the mean and minimize the variance. Both approaches utilize the response surface, so an efficient response surface approximation benefits both the optimization and the uncertainty propagation.

## **Test suite for uncertainty propagation methods**

It has become clear that for uncertainty quantification there is no single method that performs best in all cases. Just as is the case in optimization. A valuable addition to the current work is to compare the existing methods on analytic test functions representing different possible responses. These tests should be done from 1 to many uncertain parameters, where many can be defined based on a study of representative test cases. A matrix similar to the work of Schürer (2003) should be constructed. The matrix of Schürer (2003) shows for several test functions, which numerical integration method performs best for a certain dimension. The test functions for the evaluation of integration methods, however, do not represent the response surfaces observed in the test cases performed in this thesis. For uncertainty propagation methods a suite containing test functions should be constructed that represent response surfaces commonly faced in practical problems.



---

## Commonly used probability distributions

---

This appendix provides the probability density functions, cumulative distribution functions, and relations for the mean and variance of some commonly used probability distributions.

### Normal distribution

A Normal distribution is specified by two parameters: the mean  $\mu$  and the variance  $\sigma^2$ . The probability density function  $f_x(x)$  is given by:

$$f_x(x) = \frac{1}{\sigma\sqrt{2\pi}} \exp\left(\frac{-(x-\mu)^2}{2\sigma^2}\right), \quad x \in \mathbb{R}.$$

The cumulative distribution function  $F_x(x)$  is:

$$F_x(x) = \frac{1}{2} \left(1 + \operatorname{erf}\left(\frac{x-\mu}{\sigma\sqrt{2}}\right)\right), \quad x \in \mathbb{R}.$$

## Appendix A: Commonly used probability distributions

### Truncated Normal distribution

A Truncated Normal distribution is a Normal distribution  $N(\mu, \sigma^2)$ , which is truncated on  $[a, b]$ ,  $\phi(x)$  is the probability density function and  $\Phi(x)$  is the cumulative distribution function of the standard Normal distribution  $N(0, 1)$ . The probability density function  $f_x(x)$  of the Truncated Normal distribution on  $[a, b]$  is given by:

$$f_x(x) = \begin{cases} 0 & x < a \\ \frac{\frac{1}{\sigma}\phi\left(\frac{x-\mu}{\sigma}\right)}{\Phi\left(\frac{b-\mu}{\sigma}\right) - \Phi\left(\frac{a-\mu}{\sigma}\right)} & a \leq x \leq b \\ 0 & x > b \end{cases} .$$

The cumulative distribution function  $F_x(x)$  is:

$$F_x(x) = \begin{cases} 0 & x < a \\ \frac{\frac{1}{\sigma}\phi\left(\frac{x-\mu}{\sigma}\right)}{\Phi\left(\frac{b-\mu}{\sigma}\right) - \Phi\left(\frac{a-\mu}{\sigma}\right)} & a \leq x \leq b \\ 0 & x > b \end{cases} .$$

The mean  $\mu_T$  and variance  $\sigma_T^2$  are:

$$\mu_T = \mu + \frac{\frac{a-\mu}{\sigma}\phi\left(\frac{a-\mu}{\sigma}\right) - \frac{b-\mu}{\sigma}\phi\left(\frac{b-\mu}{\sigma}\right)}{\Phi\left(\frac{b-\mu}{\sigma}\right) - \Phi\left(\frac{a-\mu}{\sigma}\right)}\sigma,$$

$$\sigma_T^2 = \sigma^2 \left[ 1 + \frac{\frac{a-\mu}{\sigma}\phi\left(\frac{a-\mu}{\sigma}\right) - \frac{b-\mu}{\sigma}\phi\left(\frac{b-\mu}{\sigma}\right)}{\Phi\left(\frac{b-\mu}{\sigma}\right) - \Phi\left(\frac{a-\mu}{\sigma}\right)} - \left( \frac{\phi\left(\frac{a-\mu}{\sigma}\right) - \phi\left(\frac{b-\mu}{\sigma}\right)}{\Phi\left(\frac{b-\mu}{\sigma}\right) - \Phi\left(\frac{a-\mu}{\sigma}\right)} \right)^2 \right].$$

### Log Normal distribution

The Log Normal distribution is specified by two parameters  $M$  and  $S$ . The probability density function  $f_x(x)$  is given by:

$$f_x(x) = \frac{1}{S\sqrt{2\pi}x} \exp\left(\frac{-(\ln(x) - M)^2}{2S^2}\right), \quad x \in \mathbb{R}^+.$$

The cumulative distribution function  $F_x(x)$  is:

$$F_x(x) = \frac{1}{2} \left( 1 + \operatorname{erf}\left(\frac{\ln(x) - M}{S\sqrt{2}}\right) \right), \quad x \in \mathbb{R}^+.$$

The mean and variance are:

$$\mu = \exp(M + S^2/2),$$

$$\sigma^2 = \exp(S^2 + 2M) (\exp(S^2) - 1).$$

## Uniform distribution

The Uniform distribution has a constant probability density on the interval  $[a,b]$ . The probability density function  $f_x(x)$  is given by:

$$f_x(x) = \begin{cases} 0 & x < a \\ (b-a)^{-1} & a \leq x \leq b \\ 0 & x > b \end{cases} .$$

The cumulative distribution function  $F_x(x)$  is given by:

$$F_x(x) = \begin{cases} 0 & x < a \\ (x-a)(b-a)^{-1} & a \leq x \leq b \\ 1 & x > b \end{cases} .$$

The mean and variance are:

$$\mu = \frac{1}{2}(a+b),$$
$$\sigma^2 = \frac{1}{12}(b-a)^2.$$

## Beta distribution

The Beta distribution defined on  $[0,1]$  is specified by two parameters  $\alpha$  and  $\beta$ . The Beta distribution can be translated to the arbitrary interval  $[a,b]$ . The probability density function  $f_x(x)$  is given by:

$$f_x(x) = \frac{(1-x)^{\beta-1} x^{\alpha-1}}{B(\alpha, \beta)},$$
$$= \frac{\Gamma(\alpha + \beta)}{\Gamma(\alpha)\Gamma(\beta)} (1-x)^{\beta-1} x^{\alpha-1}, \quad x \in [0, 1],$$

where  $B$  is the beta function and  $\Gamma$  is the gamma function. The cumulative distribution function  $F_x(x)$  is:

$$F_x(x) = \frac{B_x(\alpha, \beta)}{B(\alpha, \beta)} = I_x(\alpha, \beta), \quad x \in [0, 1],$$

where  $B_x$  is the incomplete beta function and  $I_x$  is the regularized incomplete beta function. The mean and variance are:

$$\mu = \frac{\alpha}{\alpha + \beta}$$
$$\sigma^2 = \frac{\alpha\beta}{(\alpha + \beta)^2 (\alpha + \beta + 1)}$$

## Appendix A: Commonly used probability distributions

### Logistic distribution

The Logistic distribution is specified by two parameters  $m$  and  $b$ . The probability density function  $f_x(x)$  is given by:

$$f_x(x) = \frac{\exp^{-(x-m)/b}}{b (1 + \exp^{-(x-m)/b})^2}, \quad x \in \mathbb{R}.$$

The cumulative distribution function  $F_x(x)$  is:

$$F_x(x) = \frac{1}{1 + \exp^{-(x-m)/b}}, \quad x \in \mathbb{R}.$$

The mean and variance are:

$$\begin{aligned} \mu &= m, \\ \sigma^2 &= \frac{1}{3}\pi^2 b^2. \end{aligned}$$

### Weibull distribution

The Weibull distribution is specified by two parameters  $\alpha$  and  $\beta$ . The probability density function  $f_x(x)$  is given by:

$$f_x(x) = \alpha\beta^{-\alpha}x^{\alpha-1} \exp(-(x/\beta)^\alpha), \quad x \in \mathbb{R}^+.$$

The cumulative distribution function  $F_x(x)$  is:

$$F_x(x) = 1 - \exp(-(x/\beta)^\alpha), \quad x \in \mathbb{R}^+.$$

The mean and variance are:

$$\begin{aligned} \mu &= \beta\Gamma(1 + \alpha^{-1}) \\ \sigma^2 &= \beta^2 [\Gamma(1 + 2\alpha^{-1}) - \Gamma^2(1 + \alpha^{-1})], \end{aligned}$$

where  $\Gamma$  is the Gamma function.

---

## Uncertainty propagation methods

---

This appendix shows the implementation of the Polynomial Chaos methods for the piston problem. The governing deterministic equations can be found in section 2.3. Here the implementation for an uncertain spring stiffness  $k$  is shown for the Galerkin Polynomial Chaos method [Ghanem and Spanos (1991); Xiu and Karniadakis (2002); Witteveen and Bijl (2006*a*)], the Non-Intrusive Polynomial Chaos method (Hosder et al. (2006); Walters (2003); Reagan et al. (2003)), the Probabilistic Collocation method [Babuška et al. (2007); Loeven, Witteveen and Bijl (2007*a*)], the Probabilistic Collocation (Tatang) method [Tatang et al. (1997)] and the Stochastic Collocation (Mathelin) method [Mathelin and Hussaini (2003)].

### B.1 Galerkin Polynomial Chaos method

The theory of the Galerkin Polynomial Chaos method is described in section 2.2.1. The polynomial chaos expansion for the uncertain parameter  $k$  is given by:

$$k(\omega) = \sum_{j=0}^M k_j \Psi_j(\xi(\omega)), \quad (\text{B.1})$$

where  $\Psi_j$  are chosen to be the polynomials that are orthogonal with respect to the probability density function of  $k$ ;  $M + 1$  is the number of polynomial coefficients.

## Appendix B: Uncertainty propagation methods

Since only one uncertain parameter is considered ( $n = 1$ ),  $M + 1$  is equal to  $p + 1$  the highest order polynomial. In case of a normal distribution, the cumulative distribution function is:

$$F_k(k) = \frac{1}{2} \left( 1 + \operatorname{erf} \left( \frac{k - \mu_k}{\sigma_k \sqrt{2}} \right) \right). \quad (\text{B.2})$$

Rewriting this yield for  $k(\omega)$  and  $\xi(\omega)$ :

$$k(\omega) = \sqrt{2} \sigma_k \operatorname{erf}^{-1} (2\omega - 1) + \mu_k, \quad (\text{B.3})$$

$$\xi(\omega) = \sqrt{2} \operatorname{erf}^{-1} (2\omega - 1). \quad (\text{B.4})$$

The expansion coefficients  $k_j$  in (B.1) are obtained by applying a Galerkin projection on each polynomial basis  $\Psi_i$ . This yields for the coefficients:

$$\begin{aligned} k_j &= \mu_k & j &= 0, \\ &= \zeta \mu_k & j &= 1, \\ &= 0 & j &> 1. \end{aligned}$$

Now all terms in the governing equations (2.31) that depend on  $k$  have to be expanded in the polynomials  $\Psi$  as well. The following expansions are substituted into (2.31):

$$\begin{aligned} \rho(\mathbf{x}, t, \omega) &= \sum_{i=0}^M \rho_i(\mathbf{x}, t) \Psi_i(\xi(\omega)), & \rho u(\mathbf{x}, t, \omega) &= \sum_{i=0}^M \rho u_i(\mathbf{x}, t) \Psi_i(\xi(\omega)), \\ q(t, \omega) &= \sum_{i=0}^M q_i(t) \Psi_i(\xi(\omega)), & \dot{q}(t, \omega) &= \sum_{i=0}^M \dot{q}_i(t) \Psi_i(\xi(\omega)). \end{aligned}$$

Substituting this into (2.28) and (2.30) and applying a Galerkin projection on  $\{\Psi_l\}$  results in the following set of coupled equations:

$$\frac{d\rho_{il}}{dt} = \frac{1}{2\Delta x} (\rho u_{i-1l} - \rho u_{i+1l}), \quad (\text{B.5})$$

$$\frac{d\rho u_{il}}{dt} = \frac{1}{2\Delta x} (\rho_{i-1l} - \rho_{i+1l}), \quad i = 1, \dots, N, \quad (\text{B.6})$$

for  $l = 0, \dots, M$ , with the properties for the ghost cells at the boundaries:

$$\begin{bmatrix} \rho_{0l} \\ \rho u_{0l} \end{bmatrix} = \begin{bmatrix} \rho_{1l} \\ -\rho u_{1l} \end{bmatrix} \quad \text{and} \quad \begin{bmatrix} \rho_{N+1l} \\ \rho u_{N+1l} \end{bmatrix} = \begin{bmatrix} \rho_{Nl} \\ 2\dot{q}_l - \rho u_{Nl} \end{bmatrix}. \quad (\text{B.7})$$

Doing the same for the structure yields:

$$\frac{dq_l}{dt} = \dot{q}_l, \quad (\text{B.8})$$

$$\frac{d\dot{q}_l}{dt} = \frac{-1}{m(\Psi_l^2)} \sum_{i=0}^M q_i (k_0 e_{i0l} + k_1 e_{i1l}) + \frac{\rho_{Nl}}{m}, \quad (\text{B.9})$$



## B.2 Non-Intrusive Polynomial Chaos/Spectral Projection

with  $e_{i0l} = (\Psi_i, \Psi_l)$  and  $e_{i1l} = (\xi(\omega), \Psi_i, \Psi_l)$  for  $l = 0, \dots, M$ , here  $(\cdot, \cdot)$  denotes the inner product defined in equation (2.6). From these equations it is clear that the coupling between the equations is only present in (B.9). Putting all equations together results in a large coupled system which has the size  $(M + 1)^2$  times the deterministic problem. The system is written as:

$$\frac{d\mathbf{x}}{dt} = A_{\text{GPC}}\mathbf{x}, \quad (\text{B.10})$$

where the system matrix  $A_{\text{GPC}}$  has a sparse block form, which can efficiently be solved using the Block-Gauss-Seidel algorithm (see Loeven (2005)).

## B.2 Non-Intrusive Polynomial Chaos/Spectral Projection

The idea of these non-intrusive approaches (Hosder et al. (2006); Walters (2003); Reagan et al. (2003)) is to estimate the coefficients of the polynomial chaos expansion based on a low number of deterministic solves. The Non-Intrusive Polynomial Chaos developed by Hosder et al. (2006); Walters (2003) takes for a polynomial chaos of order  $M$  a set of  $M + 1$  vectors  $\xi_i$  for  $i = 0, 1, 2, \dots, M$  in the random space. For one normally distributed parameter ( $n = 1$ ) the vector of a 4<sup>th</sup> order approximation is given by  $\xi = \{0, 1, -1, 2, -2\}$ . The Non-Intrusive Spectral Projection of Reagan et al. (2003) uses Latin Hypercube sampling to estimate the coefficients  $\bar{u}_i(\mathbf{x}, t)$ . For each of these samples the deterministic code is run. The polynomial coefficients of expansion (2.2) are obtained by solving the following linear system:

$$\begin{pmatrix} \Psi_0(\xi_0) & \Psi_1(\xi_0) & \dots & \Psi_M(\xi_0) \\ \Psi_0(\xi_1) & \Psi_1(\xi_1) & \dots & \Psi_M(\xi_1) \\ \vdots & \vdots & \ddots & \vdots \\ \Psi_0(\xi_M) & \Psi_1(\xi_M) & \dots & \Psi_M(\xi_M) \end{pmatrix} \begin{pmatrix} \bar{u}_0(\mathbf{x}, t) \\ \bar{u}_1(\mathbf{x}, t) \\ \vdots \\ \bar{u}_M(\mathbf{x}, t) \end{pmatrix} = \begin{pmatrix} u(\mathbf{x}, t, \xi_0) \\ u(\mathbf{x}, t, \xi_1) \\ \vdots \\ u(\mathbf{x}, t, \xi_M) \end{pmatrix}. \quad (\text{B.11})$$

The intrusive Galerkin approach results in the exact polynomial coefficients  $u_i(\mathbf{x}, t)$ , while the non-intrusive approach yields approximations of the polynomial coefficients  $u_i(\mathbf{x}, t)$ . The stochastic solution  $u(\mathbf{x}, t, \omega)$  is reconstructed using equation (2.2). The mean  $\mu_u$  and the variance  $\sigma_u^2$  of the solution are determined using:

$$\mu_u = u_0, \quad (\text{B.12})$$

$$\sigma_u^2 = \sum_{i=1}^M u_i(\mathbf{x}, t)^2 (\Psi_i^2). \quad (\text{B.13})$$

These expressions follow from the definition of the mean and variance.

For the piston problem with uncertain  $k$ , this means that for  $k$  expansion (B.1) is used. The piston problem is solved deterministically for the values of  $k$  that correspond with  $\xi = \{0, 1, -1, 2, -2\}$ . The polynomial chaos coefficients of the solution are

## Appendix B: Uncertainty propagation methods

obtained by solving equation (B.11). Later, Hosder et al. (2007) found that taking  $2 \times (M + 1)$  Latin Hypercube samples results in a better approximation of the polynomial chaos coefficients with less sensitivity to the samples. System (B.11) becomes overdetermined and is solved using a least squares approach.

### B.3 Probabilistic Collocation

The theory of the Probabilistic Collocation method is explained in section 2.2.2. The uncertain spring stiffness  $k$  is expanded as:

$$k(\omega) = \sum_{i=1}^{N_p} k_i h_i(\omega).$$

The coefficients  $k_i$  are calculated by mapping the collocation points  $\omega_i$  from the stochastic space into the parameter space by the cumulative distribution function of  $k$ . The collocation points  $\omega$  are computed based on the probability density function of  $k$ . The dependent parameters in the piston problem are expanded as follows:

$$\begin{aligned} \rho(\omega) &= \sum_{i=1}^{N_p} \rho_i h_i(\omega), & \rho u(\omega) &= \sum_{i=1}^{N_p} \rho u_i h_i(\omega), \\ q(\omega) &= \sum_{i=1}^{N_p} q_i h_i(\omega), & \dot{q}(\omega) &= \sum_{i=1}^{N_p} \dot{q}_i h_i(\omega). \end{aligned}$$

Substituting this in (2.28) and (2.30) and applying the quadrature rule to approximate the Galerkin projection on each basis  $\{h_l\}$ , results in the following set of equations:

$$\frac{d\rho_{il}}{dt} = \frac{1}{2\Delta x} (\rho u_{i-1l} - \rho u_{i+1l}), \quad (\text{B.14})$$

$$\frac{d\rho u_{il}}{dt} = \frac{1}{2\Delta x} (\rho_{i-1l} - \rho_{i+1l}), \quad i = 1, \dots, N, \quad (\text{B.15})$$

with the properties for the ghost cells at the boundaries:

$$\begin{bmatrix} \rho_{0l} \\ \rho u_{0l} \end{bmatrix} = \begin{bmatrix} \rho_{1l} \\ -\rho u_{1l} \end{bmatrix} \quad \text{and} \quad \begin{bmatrix} \rho_{N+1l} \\ \rho u_{N+1l} \end{bmatrix} = \begin{bmatrix} \rho_{Nl} \\ 2\dot{q}_l - \rho u_{Nl} \end{bmatrix}. \quad (\text{B.16})$$

and the structure:

$$\frac{dq_l}{dt} = \dot{q}_l, \quad (\text{B.17})$$

$$\frac{d\dot{q}_l}{dt} = \frac{-k_l}{m} q_l + \frac{\rho_{Nl}}{m}, \quad (\text{B.18})$$

## B.4 Probabilistic Collocation (T)

for  $l = 1, \dots, N_p$ . As can be seen, this set of equations is exactly the set of deterministic equations:

$$\frac{d\mathbf{x}_i}{dt} = A_i \mathbf{x}_i \quad \text{for } i = 1, \dots, N_p, \quad (\text{B.19})$$

in which:

$$\mathbf{x}_i = \begin{bmatrix} x_{fi} \\ x_{si} \end{bmatrix} \quad \text{and} \quad A_i = \begin{bmatrix} A_{fi} & A_{fsi} \\ A_{sfi} & A_{ssi} \end{bmatrix},$$

where  $x_{fi}$  contains the fluid properties  $\rho_i$  and  $\rho u_i$  and  $x_{si}$  the position  $q_i$  and velocity  $\dot{q}_i$  of the piston corresponding to collocation point  $\omega_i$ .

As can be seen this set of equations is fully decoupled and therefore trivially parallelizable. The deterministic piston problem is solved for every  $k_i$ , this results in  $N_p$  values for the piston position  $q_i$ . Through these points the Lagrange interpolating polynomial chaoses of order  $N_p - 1$  are constructed.

## B.4 Probabilistic Collocation (T)

This section explains the Probabilistic Collocation method of Tatang et al. (1997), indicated by (T). Consider the general model equation (2.1):

$$\mathcal{L}(\mathbf{x}, t, \omega; u(\mathbf{x}, t, \omega)) = S(\mathbf{x}, t, \omega), \quad (\text{B.20})$$

where the random event  $\omega$  is introduced through an uncertain parameter  $a(\omega)$ , which can be present in the operator  $\mathcal{L}$ , the source term  $S$  or the initial or boundary conditions. For convenience of notation, the space and time dependence have been omitted from here on. The Probabilistic Collocation (T) method starts from the polynomial chaos expansion (2.2) of the solution  $u$  for one uncertain parameter:

$$\hat{u} \approx \sum_{i=0}^M u_i(\Psi_i(\xi(\omega))), \quad (\text{B.21})$$

where  $\hat{u}$  indicates that the expansion is an approximation of  $u$ . Note that  $\xi(\omega)$  is a linear transformation of the uncertain parameter  $a(\omega)$ , so the model (B.20) can be written as:

$$u = f(\xi(\omega)), \quad (\text{B.22})$$

where  $f$  represents the response surface of  $u$  with respect to  $\xi$ . A residual of the model is defined as:

$$R(u_i, \xi(\omega)) = \hat{u}(\xi(\omega)) - u(\xi(\omega)). \quad (\text{B.23})$$

## Appendix B: Uncertainty propagation methods

The coefficients  $u_i$  can be determined by requiring that the residual and each polynomial  $\Psi_i$  are orthogonal to each other:

$$\int_{\xi} R(\{u_i\}, \xi(\omega)) \Psi_i(\xi(\omega)) d\xi = 0 \quad i = 0, \dots, M. \quad (\text{B.24})$$

This integral can be approximated using Gaussian quadrature, which results in:

$$R(u_i, \xi(\omega_j)) = 0 \quad i = 0, \dots, M, \quad (\text{B.25})$$

where  $\omega_j$  are the collocation points. Combining equation (B.25) with equation (B.23) yields after filling in the expansion (B.21) the same set of equation as the Non-Intrusive Polynomial Chaos method (B.11).

The mean and variance are computed using equations (2.8) and (2.9).

$$\mu_u = u_0, \quad (\text{B.26})$$

$$\sigma_u^2 = \sum_{i=1}^M u_i^2 (\Psi_i^2). \quad (\text{B.27})$$

The difference between the Non-Intrusive Polynomial Chaos method and the Probabilistic Collocation (T) method is the choice of collocation or sampling points. Tatang et al. (1997) uses collocation points that are equal to the Gauss quadrature points weighted with the probability density function of the uncertain parameter, like is done in the Probabilistic Collocation method explained in chapter 2.

For one uncertain parameter the results of the Probabilistic Collocation (T) method are exactly the same as for the Probabilistic Collocation method as used in this thesis. For multiple uncertain parameter it is unclear from the work of Tatang et al. (1997) how the collocation points are chosen. They present results for multiple uncertain parameters, where the number of collocation points is given by (2.3), i.e.  $M + 1 = (d + p)!/d!p!$ , where  $M + 1$  is the number of polynomial chaos coefficients,  $d$  the number of uncertain parameters, and  $p$  the polynomial chaos order. When constructing quadrature rules for multiple uncertain parameters, typically a tensor product is used. This results in  $N_p = (p + 1)^d$  collocation points, which results in much more points.

## B.5 Stochastic Collocation (MH)

A different spectral approach is the Stochastic Collocation (MH) method, developed by Mathelin and Hussaini (2003). In the Stochastic Collocation (MH) method for each collocation point the problem is solved deterministically. The Stochastic collocation (MH) method is here explained for the general differential equation.

In case of the Stochastic Collocation method the distribution function of the random variable is projected from  $[0, 1]$  on the domain  $[-1, 1]$ , which is called the  $\alpha$  domain,

by the linear transformation

$$F_u(u) = 2F_u(u) - 1, \quad (\text{B.28})$$

where  $F_u(u)$  is the projected distribution function on the  $\alpha$  domain  $[-1, 1]$  and  $F_u(u)$  the distribution function on  $[0, 1]$ . The solution in the  $\alpha$  domain is  $u(\mathbf{x}, t, \alpha)$ . The  $\alpha$  domain is a stochastic space which is defined according to a standard domain of orthogonal polynomials  $[-1, 1]$ . From the  $\alpha$  domain  $N_p$  collocation points  $\alpha_i$  are taken. The method proposed by Mathelin and Hussaini (2003) uses  $N_p$  Gauss-Legendre quadrature points and Lagrange interpolating polynomials of order  $N_p - 1$  for the function approximation. The solution  $u(\mathbf{x}, t, \alpha)$  is approximated by the following expansion

$$u(\mathbf{x}, t, \alpha) \approx \sum_{i=1}^{N_p} u_i(\mathbf{x}, t) h_i(\alpha), \quad (\text{B.29})$$

with  $u_i(\mathbf{x}, t)$  the values of  $u(\mathbf{x}, t, \alpha)$  at the collocation points  $\alpha_i$  and  $h_i(\alpha)$  interpolating polynomials of degree  $N_p - 1$ , with  $h_i(\alpha_j) = \delta_{ij}$ . Transformation (B.28) is applied to the general differential equation, after which expansion (B.29) is substituted. A Galerkin projection on each basis  $\{h_l\}$  is applied to make the error orthogonal to the functional space spanned by  $\{h_i\}$ :

$$\left( \mathcal{L}(a(\omega)) \sum_{i=1}^{N_p} u_i(\mathbf{x}, t) h_i, h_l \right) = (S, h_l), \quad l = 1, \dots, N_p. \quad (\text{B.30})$$

The Galerkin projection (B.30) is approximated using Gauss-Legendre quadrature. For a general inner product  $\langle f(\alpha), g(\alpha) \rangle$  of two functions  $f(\alpha)$  and  $g(\alpha)$  Gauss-Legendre quadrature results in:

$$\begin{aligned} \langle f(\alpha), g(\alpha) \rangle &= \sum_{i=1}^{N_p} \sum_{j=1}^{N_p} \sum_{l=1}^{N_p} f_i g_j h_i(\alpha_k) h_j(\alpha_k) w_k, \\ &= \sum_{i=1}^{N_p} \sum_{j=1}^{N_p} \sum_{k=1}^{N_p} f_i g_j \delta_{ik} \delta_{jk} w_k, \\ &= \sum_{k=1}^{N_p} f_k g_k w_k, \end{aligned} \quad (\text{B.31})$$

where  $w_k$  are the quadrature weights corresponding to the collocation points  $\alpha_k$ . The resulting set of equations is fully decoupled. The mean  $\mu_u$  and the variance  $\sigma_u^2$  of the stochastic solution can be determined using:

$$\mu_u = \sum_{i=1}^{N_p} \frac{1}{2} u_i(\mathbf{x}, t) w_i, \quad (\text{B.32})$$

$$\sigma_u^2 = \sum_{i=1}^{N_p} \frac{1}{2} (u_i(\mathbf{x}, t))^2 w_i - \left( \sum_{i=1}^{N_p} \frac{1}{2} u_i(\mathbf{x}, t) w_i \right)^2, \quad (\text{B.33})$$

## Appendix B: Uncertainty propagation methods

where  $w_i$  are the weights corresponding to the collocation points  $\alpha_i$ . These relations are derived from the definition of the mean and variance. The most important difference of the Stochastic Collocation (MH) method with the other collocation methods is the transformation to the artificial space  $\alpha$ . The polynomial expansion exists in the  $\alpha$  space and is, therefore, not a polynomial chaos expansion.

### Stochastic Collocation (MH) for the piston problem

The uncertain spring stiffness  $k$  is expanded as:

$$k(\alpha) = \sum_{i=1}^{N_p} k_i h_i(\alpha).$$

The coefficients  $k_i$  are calculated by mapping the Gauss-Legendre collocation points onto the physical domain of  $k$  using the inverse of the projected distribution function (B.28). The dependent parameters in the piston problem are expanded as follows:

$$\begin{aligned} \rho(\alpha) &= \sum_{i=1}^{N_p} \rho_i h_i(\alpha), & \rho u(\alpha) &= \sum_{i=1}^{N_p} \rho u_i h_i(\alpha), \\ q(\alpha) &= \sum_{i=1}^{N_p} q_i h_i(\alpha), & \dot{q}(\alpha) &= \sum_{i=1}^{N_p} \dot{q}_i h_i(\alpha). \end{aligned}$$

Substituting this in (2.28) and (2.30) and applying the quadrature rule to approximate the Galerkin projection on each basis  $\{h_l\}$ , results in the same set of equations as the Probabilistic Collocation method (equations (B.14)–(B.19)) only now for each collocation point  $\alpha_l$ .

The deterministic piston problem is solved for every  $k_i$ , this results in  $N_p$  values for the piston position  $q_i$ . Through these points Lagrange interpolating polynomials of order  $N_p - 1$  are constructed and by using the expansion of  $q(\alpha)$  the projected distribution function  $\mathcal{F}_q(q)$  is reconstructed. After mapping it back to the physical domain by (B.28) this results in the cumulative distribution function  $F_q(q)$ .

## APPENDIX C

---

# Figures turbulent flate plate

---

This appendix provides the results for uncertainty quantification of the  $k - \epsilon$  model parameter applied to the turbulent flat plate test case (see section 6.3).

Appendix C: Figures turbulent flate plate

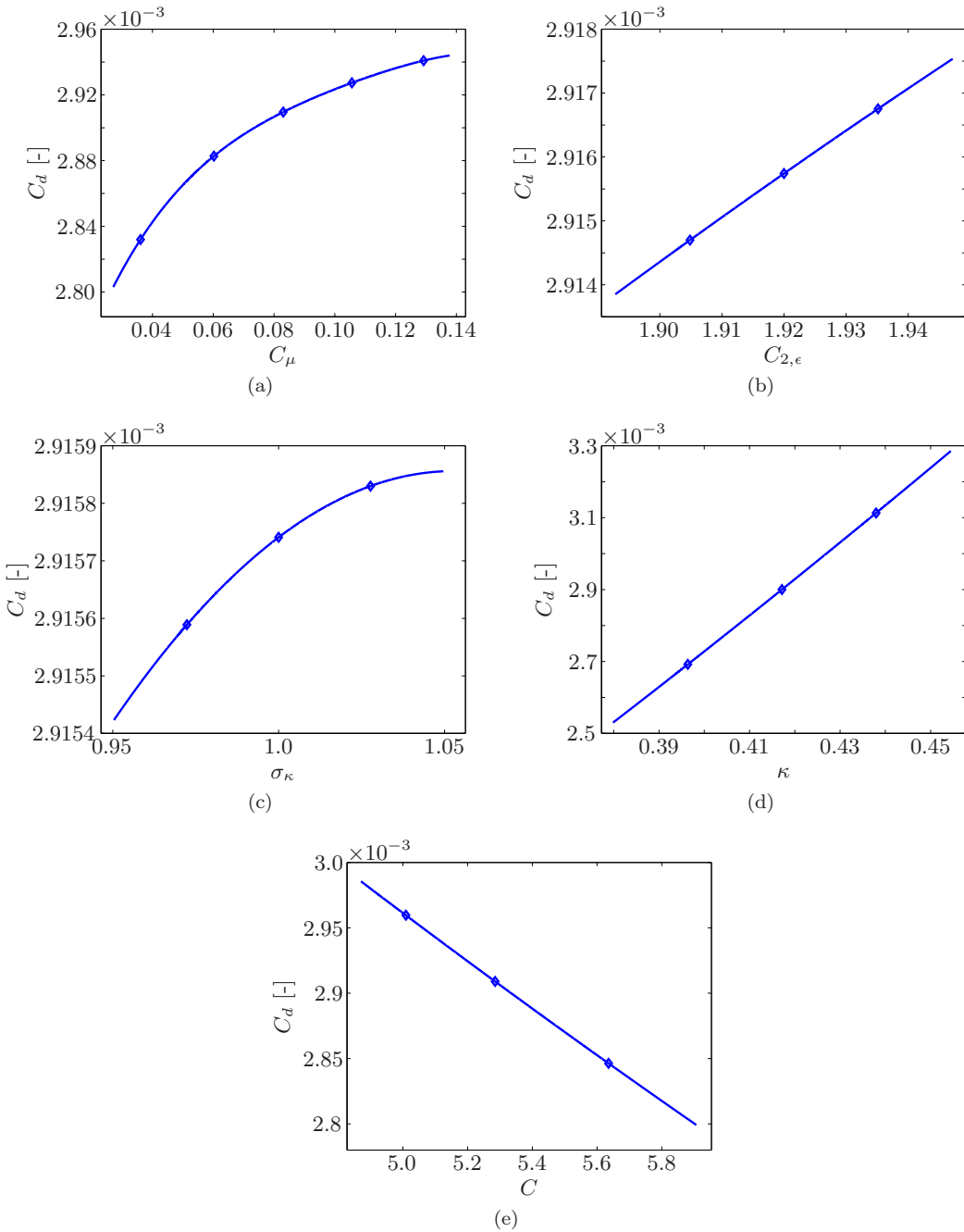
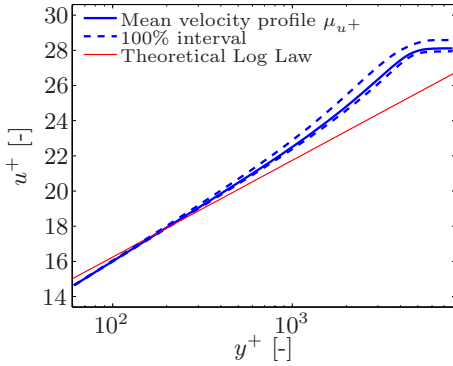
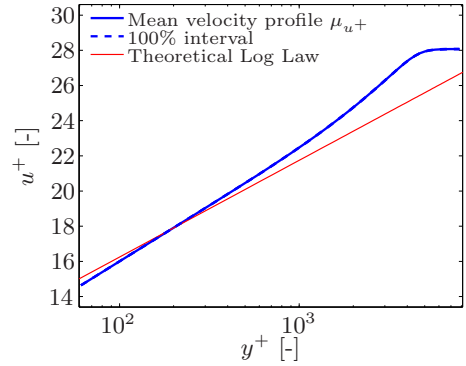


**Figure C.1:** Response surfaces of  $C_d$  with respect to the uncertain parameter. The solid blue line (—) shows the approximated response surface and the blue diamonds (◇) show the collocation points for the final approximation.

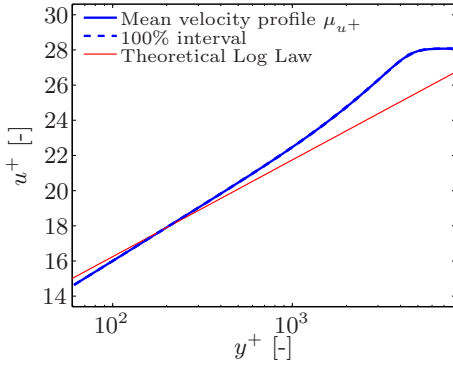




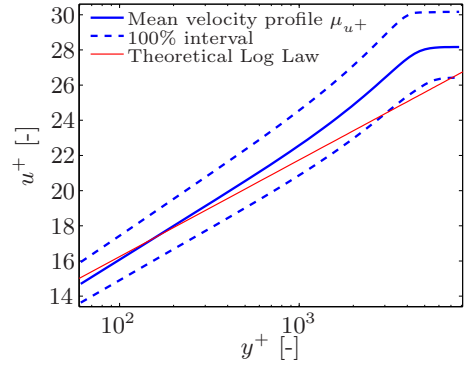
(a) Uncertain  $C_\mu$



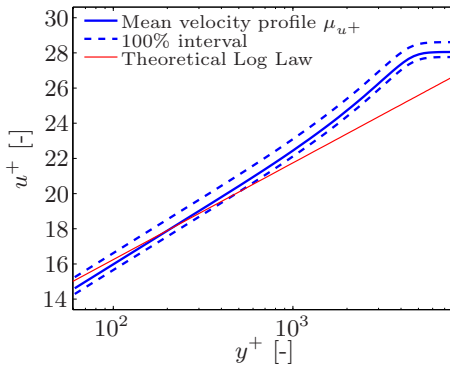
(b) Uncertain  $C_{2,\epsilon}$



(c) Uncertain  $\sigma_k$



(d) Uncertain  $\kappa$



(e) Uncertain  $C$

**Figure C.2:** The figures show the mean of the velocity profile  $u^+$  against the wall coordinate  $y^+$  by the solid blue line (—), the interval containing 100% of all possible values by the blue dashed line (---) and the theoretical log law by the red line (—).

### Appendix C: Figures turbulent flate plate

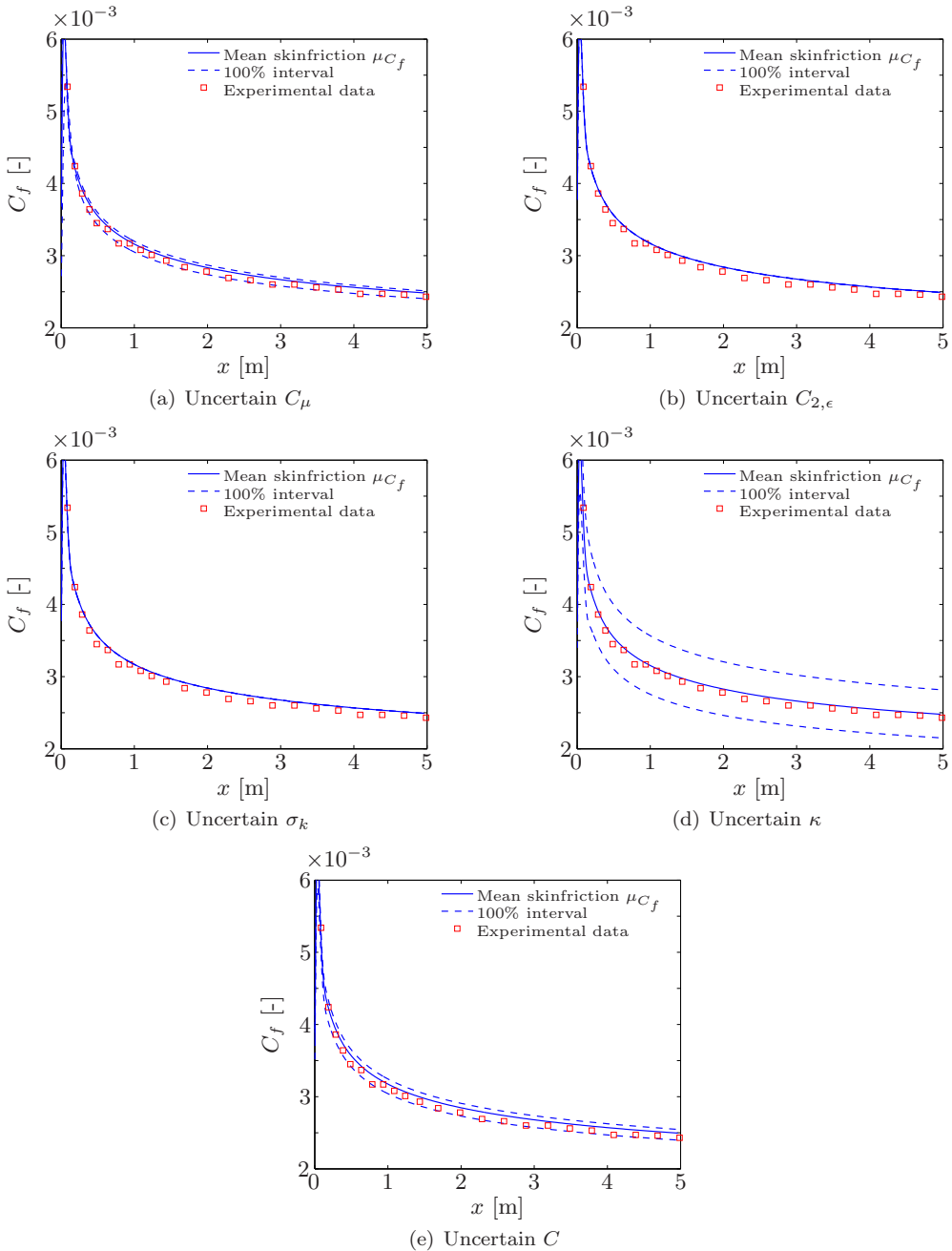


**Figure C.3:** The figures show the mean of the skinfriction  $C_f$  by the solid blue line (—), the interval containing 100% of all possible values by the blue dashed line (--) and the experimental data of Wiegardt and Tillman (1951) by the red squares ( $\square$ ).

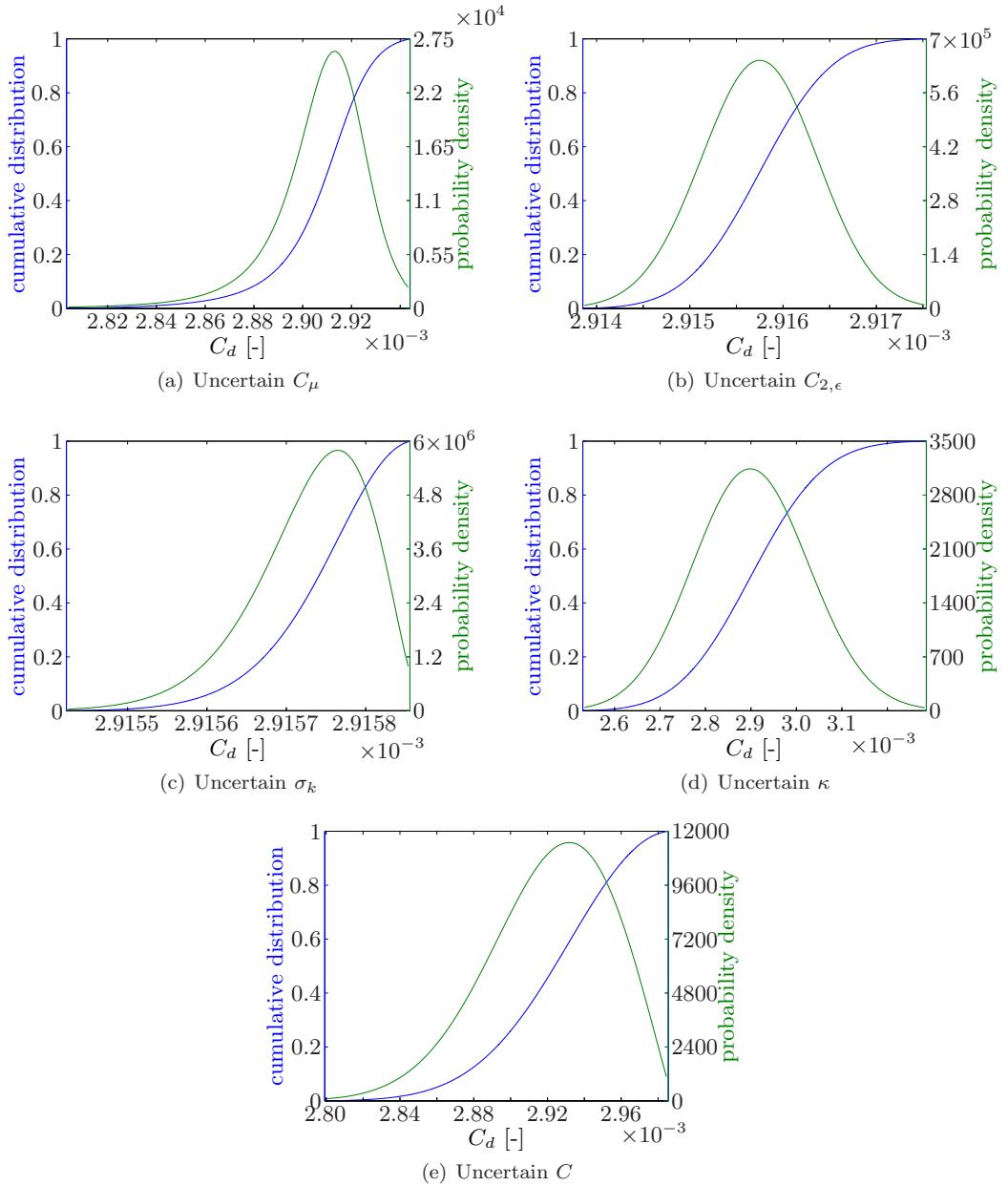


**Figure C.4:** Distribution functions of  $C_d$  for each uncertain parameter. The blue line (—) shows the cumulative distribution function and the green line (—) shows the probability density function.



---

## NASA Rotor 37 blade sections

---

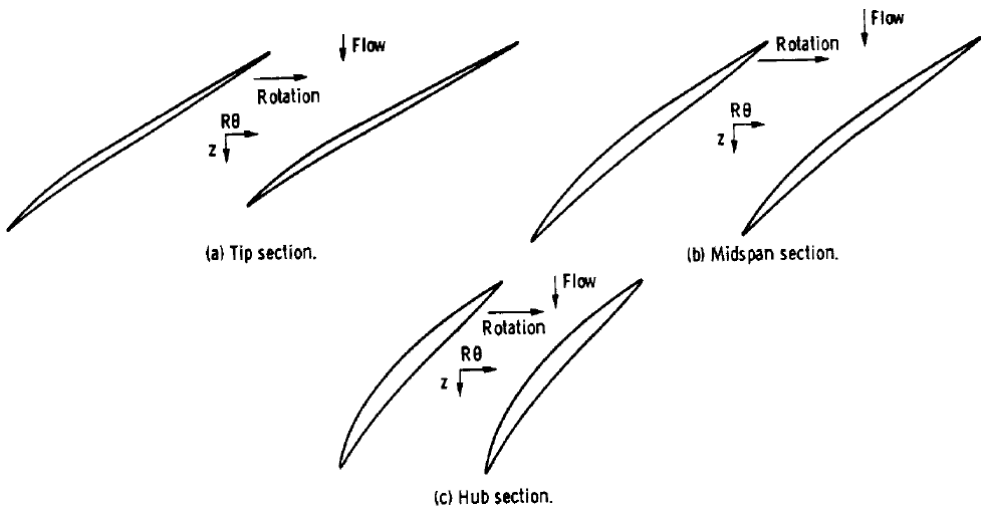


**Figure D.1:** Sections of the NASA Rotor 37 blade at different positions, taken from Reid and Moore (1978).



---

## Convergence plots PRBF and PC

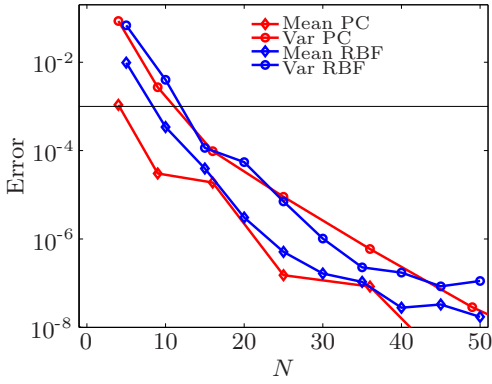
---

This appendix shows figures which are used to illustrate results in chapter 9.

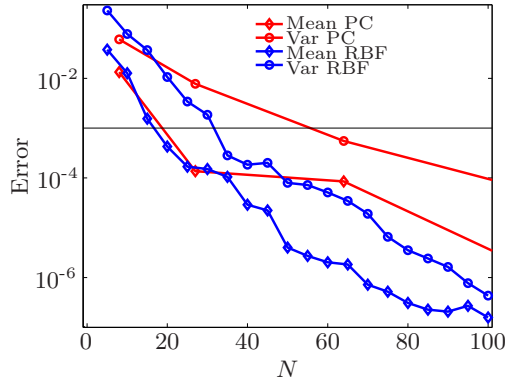
Figure E.1 is used to obtain the values of table 9.1 in section 9.2.2. The figure shows the convergence of the mean and variance for a modified version of Genz function 1 for the Probabilistic Radial Basis Function approach and the Probabilistic Collocation method. The black line shows the relative error of  $10^{-3}$  (0.1%).

Figure E.2 shows the mean and standard deviation of the lift and drag coefficient of the RAE2822 airfoil with uncertain Mach number, angle of attack and relative thickness. The test case is treated in section 9.4. The black line indicates the mean/standard deviation obtained from a Monte Carlo simulation using 10,000 Latin Hypercube samples. The red and green lines indicate the difference with the mean/standard deviation of 1 count and 1 percent respectively.

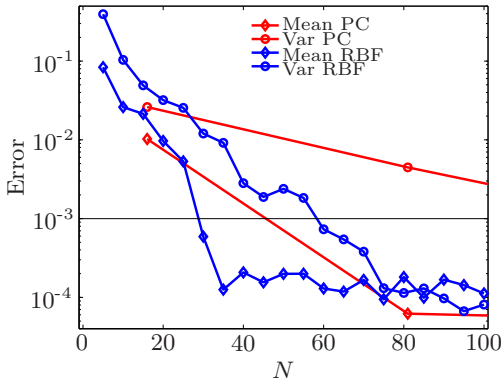
## Appendix E: Convergence plots PRBF and PC



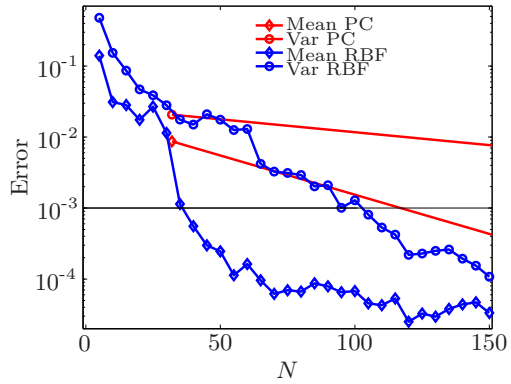
(a)  $d = 2$



(b)  $d = 3$



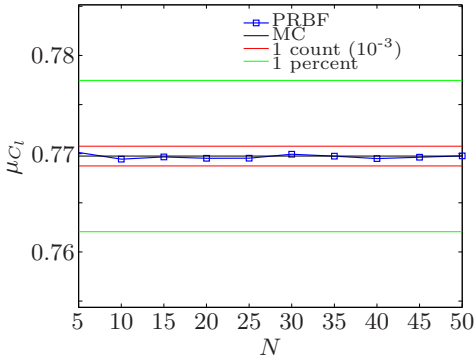
(c)  $d = 4$



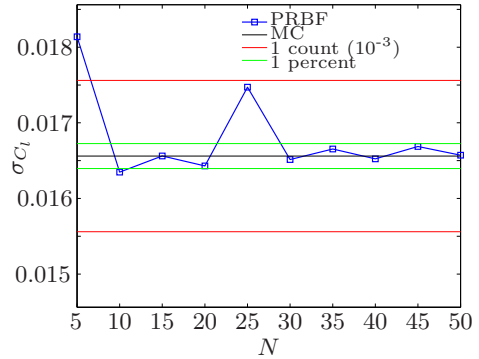
(d)  $d = 5$

**Figure E.1:** Convergence of the mean and variance of a modified version of Genz function 1 with respect to the number of deterministic solves for the Probabilistic Radial Basis Function approach and the Probabilistic Collocation method for increasing stochastic dimension (i.e. the number of uncertain parameters).

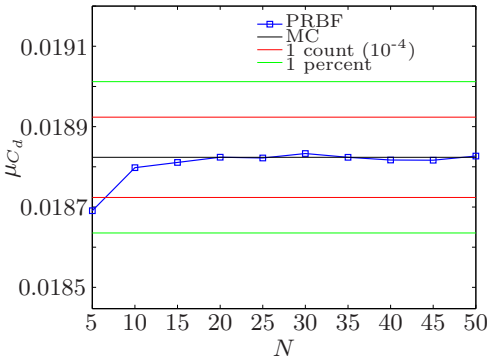




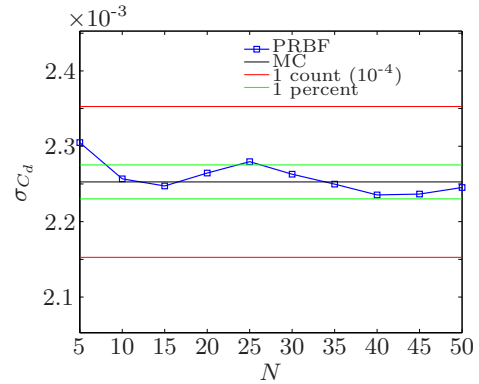
(a)



(b)



(c)



(d)

**Figure E.2:** Mean and standard deviation of the lift and drag coefficient of the RAE2822 airfoil with uncertain Mach number, angle of attack, and relative thickness. The black line indicates the mean/standard deviation obtained from a Monte Carlo simulation using 10,000 Latin Hypercube samples. The red and green lines indicate the difference with the mean/standard deviation of 1 count and 1 percent respectively.



---

## References

---

- Abbott, I.H. and Doenhoff, A.E. Von (1959), *Theory of wing sections*, Dover publications, Inc.
- Babuška, I., Nobile, F. and Tempone, R. (2007), ‘A stochastic collocation method for elliptic partial differential equations with random input data’, *SIAM Journal of Numerical Analysis* **45**(3), 1005–1034.
- Baldwin, B. and Barth, T. (1990), A one-equation turbulence transport model for high-Reynolds number wall-bounded flows, Technical Report NASA–TM–102847, NASA Ames Research Center.
- Baldwin, B.S. and Lomax, H. (1978), Thin-layer approximation and algebraic model for separated turbulent flows, *in* ‘Proceedings of the 16th AIAA Aerospace Sciences Meeting and Exhibit’, AIAA 1978–257, Huntsville (AL), United States.
- Beheshti, B.H., Teixeira, J.A., Ivey, P.C., Ghorbanian, K. and Farhanieh, B. (2004), ‘Parametric study of tip clearance – casing treatment on performance and stability of a transonic axial compressor’, *Journal of Turbomachinery* **126**, 527–535.
- Borggaard, J., Pelletier, D. and Turgeon, E. (2001), ‘Parametric uncertainty analysis for thermal fluid calculations’, *Nonlinear analysis* **47**, 4533–4543.
- Buhmann, M. D. (2000), ‘Radial basis functions’, *Acta Numerica* pp. 1–38. Cambridge University Press.
- Campolongo, F., Cariboni, J. and Saltelli, A. (2007), ‘An effective screening design for sensitivity analysis of large models’, *Environmental Modelling & Software* **22**(10), 1509–1518.

## References

- Cebeci, T. and Smith, A.M.O. (1974), ‘Analysis of turbulent boundary layers’, *Series in Applied Mathematics and Mechanics* **15**.
- Chima, R.V. (1998), ‘Calculation of tip clearance effects in a transonic compressor rotor’, *Journal of Turbomachinery* **120**(1), 131–140.
- Cook, P. H., McDonald, M. A. and Firmin, M. C. P. (1979), Experimental data base for computer program assessment – aerofoil rae 2822 , pressure distributions, and boundary layer and wake measurements, Technical Report AR–138, AGARD.
- Cullen, A.C. and Frey, H.C. (1999), *Probabilistic Techniques in Exposure Assessment: A Handbook for dealing with variability and uncertainty in models and inputs*, Plenum Press, New York.
- Davidson, P.A. (2004), *Turbulence - An introduction for scientists and engineers*, first edn, Oxford University Press.
- de Boer, A., van der Schoot, M. S. and Bijl, H. (2007), ‘Mesh deformation based on radial basis function interpolation’, *Computers and Structures* **85**(11-14), 784–795.
- Debusschere, B.J., Najm, H.N., Pébay, P.P., Knio, O.M., Ghanem, R.G. and Maître, O.P. Le (2001), ‘Numerical challenges in the use of polynomial chaos representations for stochastic processes’, *SIAM, J. Sci. Comput.* **26**(2), 698–719.
- Dinescu, C., Smirnov, S., Hirsch, Ch. and Lacor, C. (2010), ‘Assessment of intrusive and non-intrusive non-deterministic cfd methodologies based on polynomial chaos expansions’, *International Journal of Engineering Systems Modelling and Simulation* **2**, 87–98.
- Diwekar, U.M. and Kalagnanam, J.R. (1997), ‘An efficient sampling technique for optimization under uncertainty’, *AICHE Journal* **43**(2), 440–447.
- Drela, M. and Giles, M. B. (1986), Viscous-inviscid analysis of transonic and low Reynolds number airfoils, Technical Report 86–1786–CP, AIAA.
- Du, Q., Faber, V. and Gunzburger, M. (1999), ‘Centroidal voronoi tessellations: Applications and algorithms’, *SIAM Review* **41**(4), 637–676.
- Dunham, J. (1998), CFD validation for propulsion system components, Technical Report AR–355, AGARD.
- Dunn, P. and Dugundji, J. (1992), ‘Nonlinear stall flutter and divergence analysis of cantilevered graphite/epoxy wings’, *AIAA Journal* **30**(1), 153–162.
- Eppler, R. (1978), ‘Turbulent airfoils for general aviation’, *Journal of Aircraft* **15**(2).
- Eppler, R. and Somers, D. (1980), A computer program for the design and analysis of low-speed airfoils, Technical Report 80210, NASA TM.

- Etienne, S., Hay, A., Garon, A. and Pelletier, D. (2006), Shape sensitivity analysis of fluid-structure interaction problems, in 'Proceedings of the 36th AIAA Fluid Dynamics Conference and Exhibit', AIAA paper 2006-3217, San Francisco(CA), United States.
- Ferson, S., Oberkampf, W.L. and Ginzburg, L. (2008), 'Model validation and predictive capability for the thermal challenge problem', *Comput. Method. Appl. Mech. Engrg.* **197**, 2408-2430.
- Fluent Inc. (2005), *Fluent 6.2 User's Guide*.
- Foo, J., Wan, X. and Karniadakis, G. E. (2008), 'The multi-element probabilistic collocation method (ME-PCM): Error analysis and applications', *Journal of Computational Physics* **227**(22), 9572-9595.
- Friedman, J.H. (1991), 'Multivariate adaptive regression splines', *The Annals of Statistics* **19**(1), 1-67.
- Fung, Y. C. (1955), *An Introduction to the Theory of Aeroelasticity*, John Wiley & Sons, Inc., New York.
- Ganapathysubramanian, B. and Zabaras, N. (2007), 'Sparse grid collocation schemes for stochastic natural convection problems', *Journal of Computational Physics* **225**, 652-685.
- Gander, M. J. and Karp, A. H. (2001), 'Stable computation of high order gauss quadrature rules using discretization for measures in radiation transfer', *Journal of Quantitative Spectroscopy Radiative Transfer* **68**, 213-223.
- Gautschi, W. (2005), 'Orthogonal polynomials (in Matlab)', *Journal of Computational and Applied Mathematics* **178**, 215-234.
- Genz, A. (1984), 'Testing multidimensional integration routines', *Tools, Methods and Languages for Scientific Engineering Computation* pp. 81-94.
- Gerolymos, G.A. and Vallet, I. (1999), 'Tip-clearance and secondary flows in a transonic compressor rotor', *Journal of Turbomachinery* **121**, 751-762.
- Gerstner, T. and Griebel, M. (1998), 'Numerical integration using sparse grids', *Numerical Algorithms* **18**, 209-232.
- Ghanem, R. G. (1999), 'Ingredients for a general purpose stochastic finite elements implementation', *Comp. Meth. Appl. Mech. Engrg.* **168**, 19-34.
- Ghanem, R. G. and Spanos, P. D. (1991), *Stochastic Finite Elements: A Spectral Approach*, Dover.
- Ghanem, R.G., Doostan, A. and Red-Horse, J. (2008), 'A probabilistic construction of model validation', *Comput. Method. Appl. Mech. Engrg.* **197**, 2585-2595.

## References

- Godfrey, A. G. and Cliff, E. M. (2001), Sensitivity equations for turbulent flows, *in* 'Proceedings of the 39<sup>th</sup> AIAA Aerospace Sciences Meeting and Exhibit', AIAA Paper 2001-1060.
- Golub, G.H. and Welsch, J.H. (1969), 'Calculation of gauss quadrature rules', *Mathematics of Computation* **23**(106), 221-230.
- Gopinathrao, N.P., Bagshaw, D., Mabilat, C. and Alizadeh, S. (2009), Non-deterministic CFD simulation of a transonic compressor rotor, *in* 'Proceedings of ASME Turbo Expo 2009: Power for Land, Sea and Air', GT2009-60122, Orlando (FL), United States.
- Gopinathrao, N.P., Mabilat, C. and Alizadeh, S. (2009), Non-deterministic thermo-fluid analysis of a compressor rotor-stator cavity, *in* 'Proceedings of the 50th AIAA/ASME/ASCE/AHS/ASC Structures, Structural Dynamics and Materials Conference', AIAA paper 2009-2278, Schaumburg(IL), United States.
- Gragg, W.B. and Harrod, W.J. (1984), 'The numerically stable reconstruction of jacobi matrices from spectral data', *Numer. Math.* **44**, 317-335.
- Gregory, N. and O'Reilly, C.L. (1973), Low-speed aerodynamic characteristics of NACA 0012 aerofoil section, including the effects of upper-surface roughness simulating hoar frost, Technical Report 3726, Ministry of Defence, Aerodynamics Division N.P.L.
- Gumbert, C.R., Newman, P.A. and Hou, G.J.-W. (2002), Effect of random geometric uncertainty on the computational desing of a 3-D flexible wing, *in* 'Proceedings of the 20th AIAA Applied Aerodynamics Conference', AIAA paper 2002-2806, St. Louis.
- Hanjalic, K. and Launder, B.E. (1972), 'A Reynolds stress model of turbulence and its application to thin shear flows', *Journal of Fluid Mechanics* **52**, 609-638.
- Hepperle, M. (1996-2010), 'JavaFOIL'. <http://www.mh-aerotools.de/>.
- Hirsch, Ch. and Dinescu, C. (2007), NODESIM-CFD: A European project on non-deterministic simulations for CFD-based design methodologies, *in* 'NATO RTO-AVT-147 Symposium on Computational Uncertainty in Military Vehicle Design'.
- Hosder, S., Walters, R.W. and Balch, M. (2007), Efficient sampling for non-intrusive polynomial chaos applications with multiple uncertain input variables, *in* 'Proceedings of the 48th AIAA/ASME/ASCE/AHS/ASC Structures, Structural Dynamics and Materials Conference', AIAA Paper 2007-1939, Honolulu(HI), United States.
- Hosder, S., Walters, R.W. and Perez, R. (2006), A non-intrusive polynomial chaos method for uncertainty propagation in CFD simulations, *in* 'Proceedings of the 44th AIAA Aerospace Sciences Meeting and Exhibit', AIAA paper 2006-891, Reno(NV), United States.

- Hoyas, S. and Jimenez, J. (2006), ‘Scaling of velocity fluctuations in turbulent channels up to  $Re_\tau = 2000$ ’, *Phys. of Fluids* **18**(011702).
- Ilinca, F., Hay, A. and Pelletier, D. (2006), Shape sensitivity analysis of unsteady laminar flow past a cylinder in ground proximity, in ‘Proceedings of the 36th AIAA Fluid Dynamics Conference and Exhibit’, AIAA paper 2006-3880, San Francisco(CA), United States.
- Isukapalli, S.S., Roy, A. and Georgopoulos, P.G. (1998), ‘Stochastic response surface methods (SRSMs) for uncertainty propagation: Application to environmental and biological systems’, *Risk Analysis* **18**(3), 351–363.
- Iwamoto, K. (2002), Database of fully developed channel flow, Technical Report ILR-0201, THTLAB, Dept. of Mech. Eng., The Univ. of Tokyo.
- Jakobsson, S. and Amoignon, O. (2007), ‘Mesh deformation using radial basis functions for gradient-based aerodynamic shape optimization’, *Computers & Fluids* **36**, 1119–1136.
- Jones, D.R., Schonlau, M. and Welsch, W.J. (1998), ‘Efficient global optimization of expensive black-box functions’, *Journal of Global Optimization* **13**, 455–492.
- Jones, W. P. and Launder, B. E. (1972), ‘The prediction of laminarization with a two-equation model of turbulence’, *International Journal of Heat and Mass transfer* **15**(2), 301–304.
- Kearfott, R. B. (1996), ‘Interval computations: Introduction, uses and resources’, *Euromath Bulletin* **2**(1), 95–112.
- Kelvin, L. (1901), ‘Nineteenth century clouds over the dynamical theory of heat and light’, *Phil. Mag.* **2**, 1–40.
- Kleiber, M. and Hien, T. D. (1992), *The Stochastic Finite Element Method*, Wiley.
- Lacor, C. and Smirnov, S. (2007), Uncertainty propagation in the solution of compressible navier-stokes equations using polynomial chaos decomposition, in ‘Proceedings of NATO RTO-AVT-147 symposium on Computational Uncertainty’, Athens, Greece.
- Lacor, C. and Smirnov, S. (2008), Non-deterministic compressible navier-stokes simulations using polynomial chaos, in ‘Proceedings of the 5th European Congress on Computational Methods in Applied Sciences and Engineering, ECCOMAS’, Venice, Italy.
- Launder, B.E. and Sharma, B.I. (1974), ‘Application of the energy-dissipation model of turbulence to the calculation of flow near a spinning disc’, *Lett. Heat Mass Transf.* **1**, 131–138.
- Launder, B.E. and Spalding, D.B. (1974), ‘The numerical computation of turbulent flows’, *Comput. Methods Appl. Mech. Eng.* **3**(2), 269–289.

## References

- Loeven, A., Witteveen, J. and Bijl, H. (2006a), Efficient uncertainty quantification using a two-step approach with chaos collocation, *in* 'Proceedings of the ECCOMAS CFD Conference', Egmond aan Zee, The Netherlands.
- Loeven, G.J.A. (2005), Efficient uncertainty quantification in computational fluid-structure interaction: overview and comparison, Master's thesis, Delft University of Technology.
- Loeven, G.J.A. and Bijl, H. (2008a), Airfoil analysis with uncertain geometry using the probabilistic collocation method, *in* 'Proceedings of the 49th AIAA/ASME/ASCE/AHS/ASC Structures, Structural Dynamics and Materials Conference', AIAA paper 2008-2070, Schaumburg(IL), United States.
- Loeven, G.J.A. and Bijl, H. (2008b), 'Probabilistic collocation used in a two-step approach for efficient uncertainty quantification in computational fluid dynamics', *CMES Computer Modeling in Engineering & Sciences* **36**(3), 193-212.
- Loeven, G.J.A. and Bijl, H. (2008c), Radial basis functions applied to uncertainty propagation in CFD, *in* 'Proceedings of the 5th European Congress on Computational Methods in Applied Sciences and Engineering, ECCOMAS', Venice, Italy.
- Loeven, G.J.A. and Bijl, H. (2009a), Application of the probabilistic collocation method to transonic turbulent flow around a RAE2822 airfoil, *in* 'NODESIM-CFD Workshop on Quantification of CFD Uncertainties', Brussels, Belgium.
- Loeven, G.J.A. and Bijl, H. (2009b), An efficient framework for uncertainty quantification in computational fluid dynamics using probabilistic collocation, *in* 'Proceedings of the 50th AIAA/ASME/ASCE/AHS/ASC Structures, Structural Dynamics and Materials Conference', AIAA paper 2009-2275, Palm Springs(CA), United States.
- Loeven, G.J.A. and Bijl, H. (2010), The application of the probabilistic collocation method to a transonic axial flow compressor, *in* 'Proceedings of the 51th AIAA/ASME/ASCE/AHS/ASC Structures, Structural Dynamics and Materials Conference', AIAA paper 2010-2923, Orlando(FL), United States.
- Loeven, G.J.A., Sarkar, S., Witteveen, J.A.S. and Bijl, H. (2007), Dynamic stall flutter analysis with uncertainties using multi-element probabilistic collocation, *in* 'Proceedings of the 48th AIAA/ASME/ASCE/AHS/ASC Structures, Structural Dynamics and Materials Conference', AIAA paper 2007-1964, Honolulu(HI), United States.
- Loeven, G.J.A., Witteveen, J.A.S. and Bijl, H. (2006b), Efficient uncertainty quantification in computational fluid-structure interaction, *in* 'Proceedings of the 47th AIAA/ASME/ASCE/AHS/ASC Structures, Structural Dynamics and Materials Conference', AIAA paper 2006-1634, Newport(RI), United States.
- Loeven, G.J.A., Witteveen, J.A.S. and Bijl, H. (2007a), Probabilistic collocation: an efficient non-intrusive approach for arbitrarily distributed parametric uncertainties,



- in ‘Proceedings of the 45th AIAA Aerospace Sciences Meeting and Exhibit’, AIAA paper 2007–317, Reno(NV), United States.
- Loeven, G.J.A., Witteveen, J.A.S. and Bijl, H. (2007*b*), A probabilistic radial basis function approach for uncertainty quantification, in ‘Proceedings of NATO RTO-AVT-147 symposium on Computational Uncertainty’, Athens, Greece.
- Lucas, P., Bijl, H. and van Zuijlen, A.H. (2010), ‘Efficient unsteady high reynolds number flow computations on unstructured grids’, *Computers & Fluids* **39**, 271–282.
- Mathelin, L. and Hussaini, M.Y. (2003), A stochastic collocation algorithm for uncertainty analysis, Technical Report NASA–CR–2003-212153, NASA Langley Research Center.
- Mathelin, L., Hussaini, M.Y. and Zang, T.A. (2005), ‘Stochastic approaches to uncertainty quantification in CFD simulations’, *Numerical Algorithms* **38**, 209–236.
- McDonald, D. B., Grantham, W. J., Tabor, W. L. and Murphy, M. J. (2007), ‘Global and local optimization using radial basis function response surface models’, *Applied Mathematical Modelling* **31**, 2095–2110.
- Menter, F.R. (1994), ‘Two-equation eddy-viscosity turbulence model for engineering applications’, *AIAA Journal* **32**(8), 269–280.
- Metropolis, N. and Ulam, S. (1949), ‘The Monte Carlo method’, *Journal of the American Statistical Association* **44**(247), 335–341.
- Moens, D. and Vandepitte, D. (2002), ‘Fuzzy finite element method for frequency response function analysis of uncertain structures’, *AIAA Journal* **40**(1), 126–136.
- Mohamed, M.S. and LaRue, J.C. (1990), ‘The decay power law in grid-generated turbulence’, *J. Fluid Mech.* **219**, 195–214.
- Moore, R.E. and Yang, C.T. (1959), Interval analysis I, Technical Report LMSD-285875, Lockheed aircraft corporation.
- Morris, M.D. (1991), ‘Factorial sampling plans for preliminary computational experiments’, *Technometrics* **33**(2), 161–174.
- Nieuwstadt, F.T.M. (1998), *Turbulentie - Inleiding in de theorie en toepassingen van turbulente stromingen*, Epsilon Uitgaven.
- NUMECA International (2006), *User Manual - FINE™/Turbo v7*, 5, Avenue Franklin Roosevelt, 1050 Brussels, Belgium.
- Oberkampf, W.L., DeLand, S.M., Rutherford, B.M., Diegert, K.V. and Alvin, K.F. (2000), Estimation of total uncertainty in modeling and simulation, Technical Report SAND2000–0824, Sandia National Laboratories.

## References

- Oberkampf, W.L. and Ferson, S. (2007), Model validation under both aleatory and epistemic uncertainty, in 'Proceedings of NATO RTO-AVT-147 symposium on Computational Uncertainty', Athens, Greece.
- OpenFOAM<sup>®</sup> (2009), *OpenFOAM<sup>®</sup> v1.6 User Guide, the Open Source CFD toolbox*, Boston(MA), United States. <http://www.openfoam.org>.
- Österlund, J.M., Johansson, A.V., Nagib, H.M. and Hites, M.H. (2000), 'A note on the overlap region in turbulent boundary layers', *Physics of Fluids* **12**(1), 1–4.
- Peters, D.A. (1985), 'Towards a unified lift model for use in rotor blade stability analysis', *Journal of American Helicopter Society* **30**, 32–42.
- Platteeuw, P.D.A. (2008), Application of the probabilistic collocation method to uncertainty quantification in turbulence models; investigation of the  $k - \epsilon$  model of turbulence, Master's thesis, Delft University of Technology.
- Platteeuw, P.D.A., Loeven, G.J.A. and Bijl, H. (2008), Uncertainty quantification applied to the  $k - \epsilon$  model of turbulence using the probabilistic collocation method, in 'Proceedings of the 49th AIAA/ASME/ASCE/AHS/ASC Structures, Structural Dynamics and Materials Conference', AIAA paper 2008-2150, Schaumburg(IL), United States.
- Pope, S.B. (2000), *Turbulent Flows*, first edn, Cambridge University Press.
- Price, S. J. and Keleris, J. P. (1996), 'Non-linear dynamics of an airfoil forced to oscillate in dynamic stall', *Journal of Sound and Vibration* **194**(2), 265–283.
- Reagan, M. T., Najm, H. N., Ghanem, R. G. and Knio, O. M. (2003), 'Uncertainty quantification in reacting-flow simulations through non-intrusive spectral projection', *Combustion and Flame* **132**, 545–555.
- Regis, R. G. and Schoemaker, C. A. (2007), 'A stochastic radial basis function method for the global optimization of expensive functions', *INFORMS Journal on Computing* pp. 1–14.
- Reid, L. and Moore, R. D. (1978), Design and overall performance of four highly loaded, high-speed inlet stages for an advanced high-pressure-ratio core compressor, Technical Report NASA-TP-1337, NASA Lewis Research Center.
- Reynolds, O. (1894), 'On the dynamical theory of incompressible viscous fluids and the determination of the criterion', *Philosophical Transactions of the Royal Society of London. A* **186**, 123–164.
- Rippa, S. (1999), 'An algorithm for selecting a good value for the parameter  $c$  in radial basis function interpolation', *Advances in Computational Mathematics* **11**, 193–210.
- Robinson, D. and Atcitty, C. (1999), Comparison of quasi- and pseudo-monte carlo sampling for reliability and uncertainty analysis, in 'Proceedings of the AIAA Probabilistic Methods Conference', AIAA paper 1999-1589, St. Louis (MO), United States, pp. 2942–2949.

- Sacks, J., Schiller, S.B. and Welch, W.J. (1989), ‘Designs for computer experiments’, *Technometrics* **31**(1), 41–47.
- Saltelli, A., Ratto, M., Andres, T., Campolongo, F., Cariboni, J., Gatelli, D., Saisana, M. and Tarantola, S. (2008), *Global Sensitivity Analysis, The Primer*, John Wiley & Sons, Ltd.
- Sarkar, S., Witteveen, J. A. S., Loeven, A. and Bijl, H. (2009), ‘Effect of uncertainty on the bifurcation behavior of pitching airfoil stall flutter’, *Journal of Fluids and Structures* **25**(2), 304–320.
- Schürer, R. (2003), ‘A comparison between (quasi-)monte carlo and cubature rule based methods for solving high-dimensional integration problems’, *Mathematics and Computers in Simulation* **62**, 509–517.
- Spalart, P.R. and Allmaras, S.R. (1992), A one-equation turbulence model for aerodynamic flows, in ‘Proceedings of the 30th AIAA Aerospace Sciences Meeting and Exhibit’, AIAA paper 1992-439, Reno (NV), United States.
- Stephens, M. A. (1974), ‘Edf statistics for goodness of fit and some comparisons’, *Journal of the American Statistical Association* **69**(347), 730–737.
- Swiler, L. P., Slepoy, R. and Giunta, A. A. (2006), Evaluation of sampling methods in constructing response surface approximations, in ‘Proceedings of the 47<sup>th</sup> AIAA/ASME/ASCE/AHS/ASC Structures, Structural Dynamics, and Materials Conference’, AIAA Paper 2006-1827, Newport(RI), United States.
- Tartinville, B. and Hirsch, Ch. (2006), ‘Rotor 37’, *Notes in Numerical Fluid Mechanics and Multidisciplinary Design* **94**, 183–202. FLOMANIA – A European Initiative on Flow Physics Modelling.
- Tatang, M. A., Pan, W., Primm, R. G. and McRae, G. J. (1997), ‘An efficient method for parametric uncertainty analysis of numerical geophysical models’, *Journal of geophysical research* **102**(D18), 21925–21932.
- Tran, C. T. and Petot, T. (1981), ‘Semi-empirical model for the dynamic stall of airfoils in view of the application to the calculation of responses of a helicopter blade in forward flight’, *Vertica* **5**, 35–53.
- Turgeon, E., Pelletier, D. and Borggaard, J. (2003), ‘Applications of continuous sensitivity equations to flows with temperature-dependent properties’, *Numerical Heat Transfer* **44**, 611–624.
- Turgeon, E., Pelletier, D. and Borggaard, J. (2004), ‘A general continuous sensitivity equation formulation for the  $k - \epsilon$  model of turbulence’, *Int. J. Comput. Fluid D.* **18**(1), 29–46.
- Turgeon, E., Pelletier, D., Etienne, S. and Borggaard, J. (2002), Sensitivity and uncertainty analysis for turbulent flows, in ‘Proceedings of the 40th AIAA Aerospace Sciences Meeting and Exhibit’, AIAA paper 2002-0985, Reno(NV), United States.

## References

- van Zuijlen, A.H. and Bijl, H. (2004), ‘Implicit and explicit higher order time integration schemes for structural dynamics and fluid-structure interaction computations’, *Computers and Structures* **83**, 93–105.
- Walters, R.W. (2003), Towards stochastic fluid mechanics via polynomial chaos, in ‘Proceedings of the 41st AIAA Aerospace Sciences Meeting and Exhibit’, AIAA paper 2003–0413, Reno(NV), United States.
- Walters, R.W. and Huyse, L. (2002), Uncertainty analysis for fluid mechanics with applications, Technical Report No. 2002–1, ICASE Report.
- Wan, X. and Karniadakis, G.E. (2005), ‘Beyond wiener-askey expansions: Handling arbitrary pdfs’, *J. Sci. Comput.* **27**(1-3), 455–464.
- Wan, X.L. and Karniadakis, G.E. (2006), ‘Long-term behavior of polynomial chaos in stochastic flow simulations’, *Comput. method Appl. M.* **195**, 5582–5596.
- White, F. M. (2006), *Viscous Fluid Flow*, 3rd edn, McGraw-Hill.
- Wiegardt, K. and Tillman, W. (1951), On the turbulent friction layer for rising pressure, Technical Report TM–1314, NACA.
- Wiener, N. (1938), ‘The homogeneous chaos’, *Amer. J. Math.* **60**, 897–936.
- Wilcox, D.C. (1993), *Turbulence modeling for CFD*, second edn, La Canada: DCW Industries.
- Wilcox, R.C. and Ayyub, B.M. (2003), Uncertainty modeling of data and uncertainty propagation for risk studies, in ‘Proceedings of the 4th int. symposium on uncertainty modeling and analysis’.
- Williamson, C. H. K. and Brown, G. L. (1998), ‘A series in  $1/\sqrt{Re}$  to represent the strouhal-reynolds number relationship of the cylinder wake’, *Journal of Fluids and Structures* **12**, 1073–1085.
- Wisler, D. C. (1993), CFD code assessment in turbomachinery - author’s information package. unpublished ASME note.
- Witteveen, J.A.S. (2009), Efficient and robust uncertainty quantification for computational fluid dynamics and fluid-structure interaction, PhD thesis, Delft University of Technology.
- Witteveen, J.A.S. and Bijl, H. (2006a), Modeling arbitrary uncertainties using gram-schmidt polynomial chaos, in ‘Proceedings of the 44th AIAA Aerospace Sciences Meeting and Exhibit’, AIAA paper 2006–896, Reno (NV), United States.
- Witteveen, J.A.S. and Bijl, H. (2006b), Using polynomial chaos for uncertainty quantification in problems with nonlinearities, in ‘Proceedings of the 47th AIAA/ASME/ASCE/AHS/ASC Structures, Structural Dynamics and Materials Conference’, AIAA paper 2006–2066, Newport(RI), United States.

- Witteveen, J.A.S. and Bijl, H. (2009), ‘Effect of randomness on multi-frequency aeroelastic responses resolved by unsteady adaptive stochastic finite elements’, *Journal of Computational Physics* **228**, 7025–7045.
- Witteveen, J.A.S., Loeven, G.J.A. and Bijl, H. (2007a), Long-term stochastic behavior of aeroelastic systems, in ‘Proceedings of NATO RTO-AVT-147 symposium on Computational Uncertainty’, Athens, Greece.
- Witteveen, J.A.S., Loeven, G.J.A. and Bijl, H. (2007b), Quantifying the effect of physical uncertainties in unsteady fluid-structure interaction problems, in ‘Proceedings of the 48th AIAA/ASME/ASCE/AHS/ASC Structures, Structural Dynamics and Materials Conference’, AIAA paper 2007–1942, Honolulu (HI), United States.
- Witteveen, J.A.S., Loeven, G.J.A. and Bijl, H. (2009), ‘An adaptive stochastic finite elements approach based on newton-cotes quadrature in simplex elements’, *Computers and Fluids* **38**(6), 1270–1288.
- Witteveen, J.A.S., Loeven, G.J.A., Sarkar, S. and Bijl, H. (2008), ‘Probabilistic collocation for period-1 limit cycle oscillations’, *Journal of Sound and Vibration* **311**(1-2), 421–439.
- Xiu, D. and Hesthaven, J. (2005), ‘High order collocation methods for differential equations with random inputs’, *SIAM J. Sci. Comput.* **27**(3), 1118–1139.
- Xiu, D. and Karniadakis, G.E. (2002), ‘The Wiener-Askey polynomial chaos for stochastic differential equations’, *SIAM J. Sci. Comput.* **24**(2), 619–644.
- Xiu, D., Lucor, D., Su, C.H. and Karniadakis, G.E. (2002), ‘Stochastic modeling of flow-structure interactions using generalized polynomial chaos’, *J. Fluids Eng.* **124**, 51–59.
- Zang, T.A., Hemsch, M.J., Hilburger, M.W., Kenny, S.P., Luckring, J.M., Maghami, P., Padula, S.L. and Stroud, W.J. (2002), Needs and opportunities for uncertainty-based multidisciplinary design methods for aerospace vehicles, Technical Report NASA–TM–2002–211462, NASA Langley Research Center.
- Zingg, D.W. (1991), ‘Grid studies for thin-layer Navier-Stokes computations of airfoil flowfields’, *AIAA Journal* **30**(10), 2561–2564.



---

# List of publications

---

## Journal publications

- Loeven, G.J.A. & Bijl, H. (2008), ‘Probabilistic collocation used in a two-step approach for efficient uncertainty quantification in computational fluid dynamics’, *CMES Computer Modeling in Engineering & Sciences* **36**(3), 193–212.
- Witteveen, J.A.S., Loeven, G.J.A. & Bijl, H. (2009), ‘An adaptive stochastic finite elements approach based on Newton-Cotes quadrature in simplex elements’, *Computers & Fluids* **38**(6), 1270–1288.
- Sarkar, S., Witteveen, J.A.S., Loeven, G.J.A. & Bijl, H. (2009), ‘Effect of uncertainty on the bifurcation behavior of pitching airfoil stall flutter’, *Journal of Fluids and Structures* **25**(2), 304–320.
- Witteveen, J.A.S., Loeven, G.J.A., Sarkar, S. & Bijl, H. (2008), ‘Probabilistic Collocation for period-1 limit cycle oscillations’, *Journal of Sound and Vibration* **311**(1-2), 421-439.

## Conference proceedings

- Loeven, G.J.A. & Bijl, H. (2010), The Application of the Probabilistic Collocation Method to a Transonic Axial Flow Compressor, *in* ‘Proceedings of the 51th AIAA/ASME/ASCE/AHS/ASC Structures, Structural Dynamics and Materials Conference’, AIAA paper 2010–2923, Orlando(FL), United States, April 2010.

## *List of publications*

Onorato, G., Loeven, G.J.A., Ghorbaniasl, G., Bijl, H., Lacor, C. (Accepted), Comparison of intrusive and non-intrusive polynomial chaos methods for CFD applications in aeronautics, *in* 'Proceedings of the ECCOMAS-CFD Conference', Lisbon, Portugal, June 2010.

Loeven, G.J.A. & Bijl, H. (2009), Application of the Probabilistic Collocation method to transonic turbulent flow around a RAE2822 airfoil, *in* 'Workshop on Quantification of CFD Uncertainties', Brussels, Belgium.

Loeven, G.J.A. & Bijl, H. (2008*a*), An efficient framework for uncertainty quantification in CFD using Probabilistic Collocation, *in* 'Proceedings of the 50th AIAA/ASME/ASCE/AHS/ASC Structures, Structural Dynamics and Materials Conference', AIAA paper 2009-2275, Palm Springs(CA), United States.

Bijl, H., Witteveen, J.A.S. & Loeven, G.J.A. (2008), Uncertainty quantification in computational fluid dynamics and fluid-structure interaction, *in* 'Proceedings of the 13th International Conference on Computational and Applied Mathematics, ICCAM', Ghents, Belgium.

Loeven, G.J.A. & Bijl, H. (2008), Radial basis functions applied to uncertainty propagation in cfd, *in* 'Proceedings of the 5th European Congress on Computational Methods in Applied Sciences and Engineering, ECCOMAS', Venice, Italy.

Loeven, G.J.A. & Bijl, H. (2008*a*), Airfoil analysis with uncertain geometry using the probabilistic collocation method, *in* 'Proceedings of the 49th AIAA/ASME/ASCE/AHS/ASC Structures, Structural Dynamics and Materials Conference', AIAA paper 2008-2070, Schaumburg(IL), United States.

Platteeuw, P.D.A., Loeven, G.J.A. & Bijl, H. (2008), Uncertainty quantification applied to the  $k - \epsilon$  model of turbulence using the probabilistic collocation method, *in* 'Proceedings of the 49th AIAA/ASME/ASCE/AHS/ASC Structures, Structural Dynamics and Materials Conference', AIAA paper 2008-2150, Schaumburg(IL), United States.

Loeven, G.J.A., Witteveen, J.A.S. & Bijl, H. (2007), A probabilistic radial basis function approach for uncertainty quantification, *in* 'Proceedings of NATO RTO-AVT-147 symposium on Computational Uncertainty', paper no. 35, Athens, Greece.

Witteveen, J.A.S., Loeven, G.J.A. & Bijl, H. (2007), Long-term stochastic behavior of aeroelastic systems, *in* 'Proceedings of NATO RTO-AVT-147 symposium on Computational Uncertainty', Athens, Greece.

Loeven, G.J.A., Witteveen, J.A.S. & Bijl, H. (2007), Efficient uncertainty quantification in computational fluid-structure interactions: The probabilistic collocation method in a two step approach, *in* 'International Workshop on Coupled Methods in Numerical Dynamics, IUC', Dubrovnic, Croatia.



- Loeven, G.J.A., Sarkar, S., Witteveen, J.A.S. & Bijl, H. (2007), Dynamic stall flutter analysis with uncertainties using multi-element probabilistic collocation, *in* 'Proceedings of the 48th AIAA/ASME/ASCE/AHS/ASC Structures, Structural Dynamics and Materials Conference', AIAA paper 2007-1964, Honolulu(HI), United States.
- Witteveen, J.A.S., Loeven, G.J.A. & Bijl, H. (2007), Quantifying the effect of physical uncertainties in unsteady fluid-structure interaction problems, *in* 'Proceedings of the 48th AIAA/ASME/ASCE/AHS/ASC Structures, Structural Dynamics and Materials Conference', AIAA paper 2007-1942, Honolulu (HI), United States.
- Loeven, G.J.A., Witteveen, J.A.S. & Bijl, H. (2007), Probabilistic collocation: an efficient non-intrusive approach for arbitrarily distributed parametric uncertainties, *in* 'Proceedings of the 45th AIAA Aerospace Sciences Meeting and Exhibit', AIAA paper 2007-317, Reno(NV), United States.
- Loeven, A., Witteveen, J. & Bijl, H. (2006), Efficient uncertainty quantification using a two-step approach with chaos collocation, *in* 'Proceedings of the ECCOMAS CFD Conference', Egmond aan Zee, The Netherlands.
- Loeven, G.J.A., Witteveen, J.A.S. & Bijl, H. (2006), Efficient uncertainty quantification in computational fluid-structure interaction, *in* 'Proceedings of the 47th AIAA/ASME/ ASCE/AHS/ASC Structures, Structural Dynamics and Materials Conference', AIAA paper 2006-1634, Newport(RI), United States.

## **Others**

- Alex Loeven (2009), Do you trust your CFD results? The next step to reliable Computational Fluid Dynamics, *in* 'Leonardo Times', 15-17, Delft, the Netherlands.
- Loeven, G.J.A. (2005), Efficient Uncertainty Quantification in Computational Fluid-Structure Interaction, 'Master thesis at Delft University of Technology', Delft, the Netherlands.



---

# Samenvatting

---

Bij het modelleren van fysische systemen zijn er vele bronnen van onzekerheid aanwezig. Variabiliteit in randvoorwaarden zoals de snelheid of luchtdruk zijn altijd aanwezig. Verder spelen onzekerheden in geometrie een grote rol. Deze zijn het resultaat van bijvoorbeeld productietoleranties, slijtage of onbekende deformaties tijdens de belasting. Onzekerheid hebben in de numerieke stromingsleer (Computational Fluid Dynamics, CFD) een significante invloed op de aerodynamische prestaties die uitgerekend worden. Omdat CFD simulaties erg veel rekencapaciteit vragen, is het belangrijk de onzekerheden op een efficiënte manier aan te pakken.

Het hoofddoel van dit onderzoek is het ontwikkelen en onderzoeken van een efficiënte aanpak voor het kwantificeren van onzekerheden in CFD simulaties. Er is gefocust op het efficiënt propageren van onzekerheden door de CFD modellen en de praktische toepassing op een breed scala aan testproblemen.

De Probabilistische Collocatie methode is ontwikkeld als een efficiënte, niet-intrusieve methode voor het propageren van onzekerheden. De methode is gebaseerd op het polynomische chaos principe en laat spectrale convergentie zien ten opzichte van de orde van de benadering. De effectiviteit is aangetoond voor diverse CFD simulaties waarbij gebruik is gemaakt van een commercieel CFD programma.

Voor gevallen met een discontinuïteit in de respons of in instationaire gevallen, dient de methode te worden aangepast om de onzekerheden efficiënt te kunnen propageren. Een multi-element formulering is succesvol toegepast op een stall flutter model. Verder is een tijdsafhankelijke parametrisatie van de oplossing gebruikt om onzekerheden efficiënt te propageren in het geval van wervelafschudding achter een ronde cilinder.

Uit de resultaten is gebleken dat geometrische onzekerheden een grote invloed kunnen

## Samenvatting

hebben op de aerodynamische prestaties. Omdat geometrische onzekerheden de vorm van het model beïnvloeden, is er een nieuw rekenrooster voor elk collocatie punt in de Probabilistische Collocatie methode nodig. Om geometrische onzekerheden efficiënt mee te nemen in CFD simulaties, is een roosterdeformatietechniek toegepast.

Bij het oplossen van de Reynolds-averaged Navier-Stokes vergelijkingen in CFD simulaties, is een turbulentiemodel vereist om het systeem van vergelijkingen te sluiten. Parameters van een turbulentiemodel worden gevonden aan de hand van experimenten of berekeningen aan versimpelde stromingsproblemen, wat een bron van onzekerheden in het model introduceert. Onzekerheidskwantificatie is toegepast op de parameters van het  $k-\epsilon$  model inclusief wandfuncties voor stroming over een vlakke plaat en om een NACA0012 profiel. De wandfunctieparameters  $\kappa$  en  $C$  en de modelparameter  $C_\mu$  hebben de grootste invloed op de oplossing, met een variatie van 3-4% van de weerstand. Algemene conclusies vereisen echter meer onderzoek naar bijvoorbeeld een schuiflaag of vrije straal.

Compressorrotors zijn componenten van een gasturbine die erg gevoelig zijn voor operationele en geometrische onzekerheden. Operationele onzekerheden zoals de statische druk bij de uitlaat en het totale druk profiel aan de inlaat zijn in beschouwing genomen. De massastroom door de turbine is het meest gevoelig voor operationele onzekerheden gebleken.

Indien er meerdere onzekere parameters in het probleem aanwezig zijn, is een twee-stappen aanpak een goede manier om het effect van onzekerheden te kwantificeren. De eerste stap bestaat uit het filteren van de parameters met behulp van een gevoeligheidsstudie. In de tweede stap worden alleen de effecten van de meest belangrijke parameters meegenomen.

De Probabilistische Radiale Basis Functie methode is ontwikkeld voor gevallen waarbij veel onzekere parameters tegelijkertijd gepropageerd moeten worden. Radiale basis functies staan bekend om de goede eigenschappen in het benaderen van functies in hoge dimensies. Voor de CFD simulaties blijken voor een nauwkeurigheid van 0.1 tot 1%, slechts 10 tot 35 ondersteuningspunten voldoende te zijn. Er is een goede overeenkomst tussen de resultaten van de Probabilistische Radiale Basis functie methode en een Monte Carlo simulatie met 10,000 Latin Hypercube samples, voor turbulente transone stroming rond een RAE2822 profiel met 3 onzekere parameters.

Er kan worden geconcludeerd dat de Probabilistische Collocatie methode en aangepaste versies efficiënt onzekerheden propageren in CFD simulaties. De ontwikkeling van de Probabilistische Radiale Basis Functie methode geeft een efficiënt alternatief voor gevallen met meerdere onzekere parameters. Gebaseerd op de uitgevoerde simulaties blijkt dat de meest efficiënte methode af hangt van het testprobleem.

Onzekerheidskwantificatie verhoogt de betrouwbaarheid van CFD simulaties, omdat de invloed van onzekerheden op de oplossing gekwantificeerd worden. In sommige gevallen was er zelfs sprake van een grote variabiliteit van de oplossing, terwijl er kleine onzekerheden aanwezig waren. Het meenemen van onzekerheden in CFD simulaties is daarom van groot belang en met de huidige middelen haalbaar voor veel gevallen.

---

# Acknowledgements

---

Performing the research presented in this thesis was done in the past four years. I could not have succeeded in finishing this work without the help and support of many people. I would like to say thank you to all of them.

Many thanks go to my supervisor Hester Bijl, who gave me the opportunity to accomplish this PhD work in an interesting project. Her open way of advising and regular meetings were a good encouragement to perform my research. Next I would like to thank the partners from the NODESIM-CFD project for providing insight in the practical applicability of this work.

I want to thank the co-workers, who contributed to the work in this thesis. Firstly, Jeroen Witteveen, for the discussions we had about uncertainty quantification and our visits to many conferences together. Secondly, Sunetra Sarkar for our pleasant collaboration on the dynamic stall flutter problem. And finally, Pieterjan Platteeuw, who I supervised during his work on uncertainty in the  $k-\epsilon$  turbulence model.

Furthermore, I thank all my colleagues at the Aerodynamics Department for the enjoyable time. And especially Frank Bos and Peter Lucas for being, apart from colleagues, good friends as well.

I would like to acknowledge my parents, Joop en Anita Loeven, for the support during my Ph.D. track. And also I wish to show my gratitude to my in-laws, Jan en Tineke van Leeuwen, who occasionally took care of Carlijn to give me an additional day to work on my thesis in the final months.

Special thanks go to my wife Marieke for keeping me motivated and productive. Without her I would have never been able to perform this research and complete it on time. In October 2008, our beautiful daughter Carlijn was born. Watching her grow up constantly reminds me that there is more in life than CFD.

Alex Loeven  
Delft, May 2010



---

# Curriculum Vitae

---

- December 17, 1979    Born in Steenwijk, the Netherlands.
- 1992 - 1998        Pre-university education (VWO) at the St. Ludgercollege in Doetinchem.
- 1998 - 2005        Master's degree in Aerospace Engineering at Delft University of Technology, specialized in Aerodynamics. Graduated *cum laude* with the thesis: "Efficient uncertainty quantification in computational fluid-structure interaction: overview and comparison".
- 2006 - 2010        Ph.D. researcher at the Aerodynamics Department of Aerospace Engineering at Delft University of Technology. Dissertation title: "Efficient uncertainty quantification in computational fluid dynamics". This research was partly funded by the project 'NODESIM-CFD', which is part of the 6<sup>th</sup> framework program of the European Union.

